Development of ZnO-FTO nanocomposites for the use in transparent conductive thin films

Christelle Habis

Ecole Doctorale C2MP

« Chimie Mécanique. Matériaux Physique » - n° 606

Laboratoire Matériaux, Optique, Photonique et Système LMOPS,
Université de Lorraine, Metz, France.

DOCTOR of UNIVERSITE de LORRAINE
Speciality: Physics

Presented by

Christelle HABIS

Development of ZnO-FTO nanocomposites for the use in transparent conductive thin films

November 25, 2022

Jury Members :

President :	**Patrice BOURSON**	**Pr, LMOPS, Université de Lorraine, Metz, France**
Reporter :	**Maggy COLAS**	**Dr CNRS, IRCER, Université de Limoges, Limoges, France**
	Anne KAMINSKI-CACHOPO	**Pr, IMEP-LAHC, Université de Grenoble-Alpes, Grenoble, France**
Supervisor :	**Michel AILLERIE**	**Pr, LMOPS, Université de Lorraine, Metz, France**
Examiner :	**Maria-Carmen JIMENEZ AREVALO**	**Dr CNRS, LMGP, Université de Grenoble-Alpes, Grenoble, France**
	Baptiste COLIN	**Dr, LERMAB, Université de Lorraine, Epinal, France**
Invited :	**Jean-Pierre CHARLES**	**Pr, LMOPS, Université de Lorraine, Metz, France**

Ecole Doctorale C2MP

« Chimie Mécanique. Matériaux Physique » - n° 606

Laboratoire Matériaux, Optique, Photonique et Système LMOPS,
Université de Lorraine, Metz, France.

DOCTEUR de l'UNIVERSITE de LORRAINE
Spécialité: Physique

Presentée par

Christelle HABIS

Développement de nanocomposites ZnO-FTO pour des couches minces conductrices transparentes

25 novembre 2022

Membres du Jury :

Président de jury :	**Patrice BOURSON**	**Pr, LMOPS, Université de Lorraine, Metz, France**
Rapporteurs :	**Maggy COLAS**	**Dr CNRS, IRCER, Université de Limoges, Limoges, France**
	Anne KAMINSKI-CACHOPO	**Pr, IMEP-LAHC, Université de Grenoble-Alpes, Grenoble, France**
Directeurs de thèse :	**Michel AILLERIE**	**Pr, LMOPS, Université de Lorraine, Metz, France**
Examinateurs :	**Maria-Carmen JIMENEZ AREVALO**	**Dr CNRS, LMGP, Université de Grenoble-Alpes, Grenoble, France**
	Baptiste COLIN	**Dr, LERMAB, Université de Lorraine, Epinal, France**
Invité :	**Jean-Pierre CHARLES**	**Pr, LMOPS, Université de Lorraine, Metz, France**

Acknowledgments

At the end of my PhD journey, I would like to express my sincere gratitude to all the people who had a contribution to this work and made it possible through their support and advice.

I sincerely thank Professor Michel Aillerie, the supervisor of this thesis, for his help and support to overcome all the difficulties and put together all the pieces to make this project finally work. I would like thank Prof Aillerie not only for his enlightening advice and generous support, but also for his extreme kindness, on personal and professional level as well, and precious time he gave me for scientific discussion throughout this work.

I spent most of my time in LMOPS where I completed the majority of the work in this thesis. Everyone in LMOPS has supported me in a way or two. I thank Stéphanie Vergerio for her help concerning administrative issues; I thank David Chapron, Patrice Bourson, Thomas Kauffmann, Maryne Crouzet, Queny Keiffer, Jean-Claude Petit and Mario Fernandes-Lanfranchi for their help on experimental setup, technical issues and sample characterizations as well as the many fruitful scientific discussions. Their time and efforts were indispensable for my thesis to proceed. I'm also thankful for all the other members of LMOPS who have contributed to my work via different manners.

I would also like to sincerely thank and express my deep gratitude to Professors Carmen Jimenez and Daniel Bellet from Université de Grenoble-Alpes, France for their invitation to the LMGP laboratory for the deposition of FTO thin films and many fruitful and long scientific discussions that made a major contribution in the progress of this work. Thanks to Matthieu Jouvert for the technical support during my stay at the LMGP.

I would like to also thank Dr. Baptiste Colin from LERMAB, at University of Lorraine, Epinal for his invitation and help concerning the TGA/DSC experiment. His kindness and availability for many scientific discussions had an important contribution in the progress of this work.

I am also grateful to all my friends at LMOPS: Sadaqat, Rodolph, Xin, Waqar, Louis, Carmen, Fatima Zohra. You made working environment more enjoyable and hard times easier.

I am very grateful to my parents and two brothers for their support, encouragement and above all their unconditional love which has always been a motivation source. Your prayers for me was what sustained me this far.

Last but not least, I would like to give my warmest thanks to my husband, Jean Zaraket, for being the loving and caring partner. I would like to thank him for showing me the positivity in every encountered problem, beauty of life and for making my mind relax during the hard times of my thesis.

Table of Contents

List of abbreviations and symbols

AFM : Atomic Force Microscopy
AZO : Aluminum doped zinc oxide
DSC : Differential Scanning Calorimetry
DSSC : Dye Sensitized Solar Cell
EDX : Energy Dispersive X-ray
Eg : Energy gap
FESEM : Field Emission Scanning Electron Microscopy
FoM : Figure of Merit
FTIR : Fourier Transform Infrared Spectroscopy
FTO : Fluorine doped tin oxide
HF : Haze factor
IR : Infrared
ITO : Tin doped indium oxide
MCR-ALS : Multivariate Curve Resolution- Alternating Least Squares
NREL : National Renewable Energy Laboratory
PV : Photovoltaic
PVA : Polyvinyl alcohol
PVP : Poly vinyl pyrrolidone
SEM : Scanning Electron Microscopy
TCM : Transparent Conductive Material
TCO : Transparent Conductive Oxide
T_{diff} **:** Diffuse transmittance
TEM : Transmission Electron Microscopy
TGA : Thermogravimetric Analysis
T_{spec} **:** Specular transmittance
T_{tot} **:** Total transmittance
USP : Ultrasonic Spray Pyrolysis
XRD : X-Ray Diffraction
XRF : X-Ray Fluorescence
ZnAc : Zinc acetate
ZnO : Zinc oxide

List of Figures

List of Tables

Preface

My thesis work entitled “Development of ZnO-FTO nanocomposites for the use in transparent conductive thin films” is supervised by Professor Michel Aillerie at University of Lorraine. This work was mainly made at the “Laboratoire des Matériaux Optiques, Photoniques et Systèmes” LMOPS in Centrale Supélec, Metz.

Although this work forms a whole in the elaboration of transparent conductive oxides, it is divided into two parts. The first part consists on identifying the properties of bulk materials (ZnO and FTO) deposited in the form of thin film. Whereas, the second part is about the elaboration and characterization of Zinc Oxide (ZnO) and Aluminum doped Zinc Oxide (AZO) nanofibers, then associated to FTO thin films to form nanocomposite. The main objective of this work is to make flexible electrodes using low cost and abundant material, but also improving the optical properties and more specifically the haze factor of the nanocomposite layers.

Transparent conductive oxides (TCOs) are technologically significant class of materials extensively used in thin film solar cells due to their ability to transmit light and collect charge carriers. In addition to the fundamental qualities of transparency and conductivity, the TCOs are frequently desired to have a certain degree of surface roughness (i.e., texture) in order to effectively scatter transmitted light into the active materials, therefore lengthen the optical path and, as a result, enhance the performance of the cell and light absorption.

This thesis focuses on the development of low-cost fabrication techniques for transparent oxide layers using non-polluting materials to enable the functionalization of operational devices with high efficiency for renewable energy production.

The choice was made to study tin-based TCO layers doped with fluorine, F:SnO_2, known as FTOs for "Fluor Tin Oxides". FTOs are wide band gap oxides, like ZnO, TiO_2, Al_2O_3, pure or doped. In principle, these layers have a high scattering factor, as defined above, in order to improve the optical path and absorption. In addition, the optical texture of TCOs can be easily controlled by depositing suspensions of nanostructures before the film deposition.

Generally, these nanostructures are nanoparticles or even carbon nanowires or metallic nanowires (silver, copper, ...) and more recently nanowires of TiO_2 (presenting the disadvantage of the titanium element) or of undoped ZnO which unfortunately decrease the conductivity due to the increase of the interface resistance with the concentration of the nanoparticles.

Therefore, we propose the study of FTO thin films, pure and also in the presence of ZnO and AZO nanofibers by electrospinning from a PVA-based solution in order to have a nanostructured layer with improved transparency and electrical conductivity properties to be integrated as transparent electrodes in photovoltaic cells, meeting the performance criteria defined above. With the characterization techniques available in the LMOPS laboratory and the University of Lorraine (SEM, Raman, EDX, XRD, UV-vis Spectro, TGA, AFM, profilometer) the growth will be followed by morphological and structural studies of the layers. Finally, electrical and optical properties, in particular absorption and scattering factor, will also be extensively investigated on selected layers with the best structural and morphological properties and the minimum of interface defects when deposited on a PV structure.

This manuscript is organized as follows:

Chapter I starts with a general approach about the TCOs, their properties and applications along with the most commonly used techniques for the elaboration of these materials specifically for photovoltaic modules are discussed. Recent expectations on TCOs shifted beyond fundamental transparency and conductivity and are now requiring increased performance and varied roles that are compatible with scalable, cost-effective, and environmentally friendly procedures. The varied and programmable characteristics of nanomaterials combined with TCO thin films showed to create new functional capabilities. Therefore, this feature is discussed in the second part of this chapter. Within the presentation of different nanomaterials, we specifically focus on the ZnO and AZO nanofibers which appear to have great potential to be considered as transparent electrodes in the photovoltaic research domain.

In Chapter II, a detailed characterization of FTO and ZnO thin films deposited on glass substrate by the spray pyrolysis and sputtering techniques are presented respectively. The characterizations were carried on by Atomic Force Microscopy and Raman spectroscopy. The purpose of this study is to establish a reference results for the bulk thin films before the integration of nanostructures in the coming chapter. Moreover, a link between the position of the substrate during the deposition process and the structural properties of the deposited layer was also established.

Chapter III begins with a presentation of the electrospinning technique, its history and evolution, applications, and general processing parameters. Along this chapter, the experimental procedure used to produce zinc oxide nanofibers by electrospinning technique is detailed. The properties of the obtained ZnO nanofibers were investigated by optical microscopy and SEM for morphological characterizations and TEM for the structural one. ZnO nanofibers were used to make nanocomposite samples along with FTO thin films deposited by spray pyrolysis technique. Upon morphological, optical and electrical characterizations the nanostructured samples presented improved properties compared to their bulk counterparts.

In Chapter IV we concentrate on producing the precursor solutions required to make aluminum-doped zinc oxide nanofibers with PVA serving as the polymer matrix. We also go over an optimization process to produce well-shaped and structured nanofibers as well as the many implications this doping has on various levels. Finally, preliminary findings from morphological and thermal characterizations of the resulting TCO are also provided.

Finally, the most important results of this thesis have been selected and addressed in the general conclusion, as well as future perspectives based on this doctoral thesis are suggested in the end.

Résumé en Français

Résumé en Français

Cette thèse s'inscrit dans le cadre de développement de couches d'oxyde transparentes (TCO) avec des techniques à faible cout, basées sur des matériaux non polluants permettant de fonctionnaliser des dispositifs opérationnels efficace, donc à haut rendement pour la production d'énergies renouvelables.

Notre choix s'est porté plus particulièrement sur l'étude des couches TCO à base d'étain et dopés au fluor, F :SnO_2, dénommées FTO pour « Fluor Tin Oxydes ». Les FTO sont des oxydes à large bande interdite, à l'instar du ZnO, TiO_2, Al_2O_3, purs ou dopés. Ces couches possèdent en principe un facteur de diffusion, élevé afin d'améliorer le chemin optique et l'absorption. De plus, la texture optique des TCO peut être facilement contrôlée par dépôt de suspensions de nanostructures avant le dépôt de la couche. Généralement, ces nanostructures sont des nanoparticules voire nano-fils de carbone ou nano-fils métalliques (argent, cuivre, …) et plus récemment des nano-fils de TiO_2 (présentant l'inconvénient de l'élément titane) ou de ZnO non-dopés qui diminuent, malheureusement la conductivité du fait de l'augmentation de la résistance d'interface avec la concentration des nanoparticules.

C'est pourquoi, nous proposons l'étude de couches de FTO, pures et également en présence de nanofibres de ZnO et ZnO:Al par électrofilage à partir d'une solution à base de Polyvinyl Alcool (PVA) afin d'avoir une couche nanostructurée ayant des propriétés de transparence et de conductivité électrique améliorées pour être intégrés comme électrodes transparentes dans les cellules photovoltaïques (PV), répondant aux critères performatifs définis ci-dessus. Les croissances des couches seront suivies par des études morphologiques et structurales, en utilisant des techniques de caractérisations disponibles au sein du laboratoire LMOPS et de l'Université de Lorraine (tel que: MEB, Raman, EDX, DRX, spectroscopie UV-vis, ATG, AFM, profilomètre). Enfin, les propriétés électriques et optiques, en particulier l'absorption et le facteur de Haze, seront aussi largement investies sur les couches sélectionnées présentant les meilleures propriétés structurales et morphologique.

Chapitre I : Etat de l'art

Ce chapitre présente les différents types d'oxydes conducteurs transparents (TCO), leurs propriétés requises comme une haute conductivité associée à une haute transparence et de l'impact de l'élément de dopage approprié ainsi que la concentration sur les propriétés du matériau. En outre, une description des différentes techniques possibles pour la croissance de TCO à intégrer comme électrodes transparentes dans les modules photovoltaïques est également présentée. En effet, les nouvelles générations de cellules solaires nécessitent l'optimisation des TCO avec une conductivité et une transparence améliorées en fonction du type de cellules PV et des conditions d'utilisation. Ainsi, les familles de TCOs considérées dans ce chapitre seront: l'oxyde d'étain et d'indium (ITO), l'oxyde de zinc et particulièrement celui dopé aluminium (ZnO-AZO), et l'oxyde d'étain particulièrement dopé au Fluore (SnO_2-FTO). Cependant, les attentes récentes concernant les TCO se sont éloignées de la transparence et de la conductivité fondamentales, exigeant des performances accrues et des rôles variés compatibles avec des procédures évolutives, rentables et respectueuses de l'environnement. En raison des caractéristiques variables et programmables des nanomatériaux [1], [2], la combinaison de couches minces de TCO avec des nanomatériaux pour obtenir de nouvelles capacités fonctionnelles est un défi fascinant. Cette nouvelle approche est abordée dans la deuxième partie de ce chapitre avec une présentation de la nanostructuration des couches minces de TCO spécialement dédiée aux dispositifs et applications photovoltaïques. Pour la nanostructuration, une attention particulière sera accordée aux nanofibres, notamment aux nanofibres d'oxyde de zinc qui semblent avoir un grand potentiel pour être considérées comme des électrodes transparentes dans le domaine de la recherche photovoltaïque.

Chapitre II : Élaboration et caractérisation de couches minces ZnO et FTO

Dans ce chapitre, nous présentons l'élaboration et la caractérisation des couches minces d'oxyde de zinc et d'oxyde d'étain dopé au fluor déposés par deux techniques différentes et

caractérisés morphologiquement par microscopie à force atomique (AFM) et l'étude de la structure par spectroscopie Raman.

Tout d'abord, une couche mince d'oxyde de zinc a été déposée sur un substrat de verre par pulvérisation cathodique, la distance par rapport au centre du support étant le paramètre de changement. La morphologie de la surface a été étudiée par AFM . Au fur et à mesure que la distance varie, l'épaisseur, la taille et la forme des grains changent comme montré dans la Figure 1. La distance par rapport au centre du support montre qu'elle a un effet sur la forme, la distribution et la taille des grains qui déterminent la texture de la couche. Principalement, nous avons remarqué que lorsque cette distance augmente, la rugosité diminue, la taille des grains augmente et la forme des grains passe de sphérique à pyramidale.

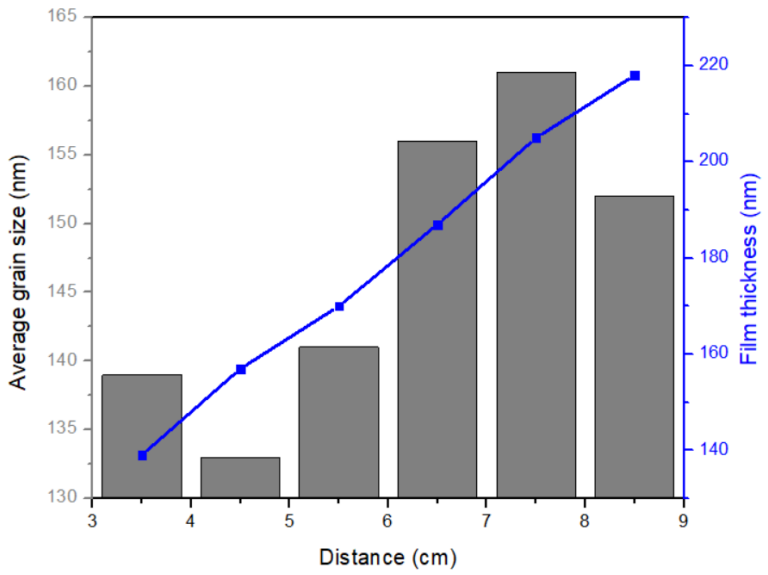

Figure 1. Tracé de la variation de la taille des grains et de l'épaisseur en fonction de la distance du centre.

Par conséquent, le contrôle de la texture est bénéfique pour améliorer le facteur de Haze, et donc la génération d'excitons avec la lumière, avec une influence directe sur l'absorption optique, donc sur la transmission optique de la couche et finalement sur l'efficacité du dispositif ainsi construit, surtout si l'on considère ces substrats comme des électrodes transparentes dans les applications photovoltaïques.

Dans la deuxième partie, deux couches minces de FTO ont été préparées par pyrolyse par pulvérisation à ultrasons (USP) en modifiant le débit du gaz porteur entre deux séries d'échantillons. La qualité de ces couches a été comparée à celle d'un substrat FTO commercial. Deux procédés expérimentaux ont été utilisés pour la caractérisation des couches. La morphologie de la surface de la couche et la taille moyenne des grains ont été caractérisées par microscopie à balayage AFM. Les images AFM des couches minces de FTO montrent que toutes les couches sont denses et nano-cristallisés. Les surfaces présentent des pics et des vallées et les grains ont une forme pyramidale. Les calculs de rugosité ont montré que l'échantillon déposé au débit le plus faible présente la plus grande rugosité par rapport aux autres échantillons. En effet, une rugosité plus élevée signifie un meilleur piégeage de la lumière et donc une meilleure efficacité de la cellule solaire.

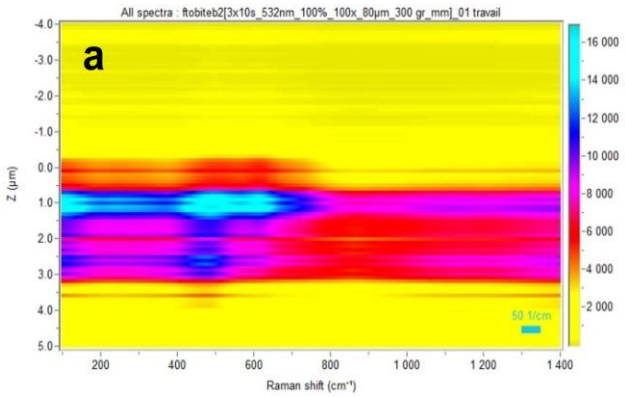

Figure 2. Cartographie en profondeur d'un échantillon FTO préparé par USP pour un débit de 6,22 l.min^{-1}

En outre, les propriétés cristallographiques et les épaisseurs des couches (voir la Figure 2) ont été étudiées par spectroscopie Raman associée à la méthode MCR-ALS (Multivariate Curve Resolution-Alternating Least Squares) permettant la discrimination des contributions des couches de FTO et du substrat dans les spectres Raman moyens. Grâce à la spectroscopie Raman réalisée en profondeur de la structure à travers les couches jusqu'aux substrats, la qualité des couches a été identifiée. En effet, nous mettons en évidence dans les spectres moyens des couches, les pics typiques et bien définis du FTO pour les échantillons déposés par USP en conformité avec les spectres de l'échantillon commercial et des travaux précédents sur le SnO_2. Les pics principaux des réponses Raman sont bien positionnés avec

une position fixe du pic à 626 cm^{-1} et un décalage vers le bleu pour le pic dans la gamme 480-510 cm^{-1} pour les deux échantillons expérimentaux. Ce décalage vers le bleu de ce pic pourrait être une indication d'une augmentation de la contrainte longitudinale induite par l'interface substrat-FTO et liée à l'épaisseur des couches comme également déterminé lors des caractérisations Raman.

Chapitre III : Nanofibres de ZnO par électrofilage pour électrodes transparentes

Ce chapitre est divisé en trois parties : tout d'abord une présentation de la technique d'électrofilage, de son principe et des différents paramètres à prendre en compte lors du dépôt, puis l'élaboration de nanofibres d'oxyde de zinc par électrofilage et enfin la fabrication du nanocomposite constitué d'une couche mince de FTO et de nanofibres de ZnO combinés.

L'électrofilage est considéré comme l'une des techniques de dépôt les plus simples et les moins coûteuses. Depuis l'observation d'une goutte d'eau de forme conique en présence d'un champ électrique dans les années 1600, le concept d'électrofilage a commencé à se développer au fil des ans jusqu'à atteindre les installations dont nous disposons aujourd'hui, qu'il s'agisse de machines de laboratoire ou même de machines fonctionnant à l'échelle industrielle. Ce développement massif a rendu les nanofibres fabriquées par électrofilage d'une grande utilité pour une variété de domaines d'application. Bien que cela semble simple, de nombreux paramètres doivent être considérés simultanément pendant le processus de filage car ils ont une grande influence sur les nanofibres produites. Des nanofibres d'oxyde de zinc ont été déposées avec succès par électrofilage dont l'image par MEB est illustré dans la Figure 3 (a). Ces fibres ont montré des diamètres fins, autour de 40 nm (voir Figure 3 (b)), et une structure hexagonale compatible avec celle du ZnO. Différents ensembles d'échantillons de nanofibres ont été élaborés en augmentant le temps de déposition, ce qui signifie le taux de recouvrement.

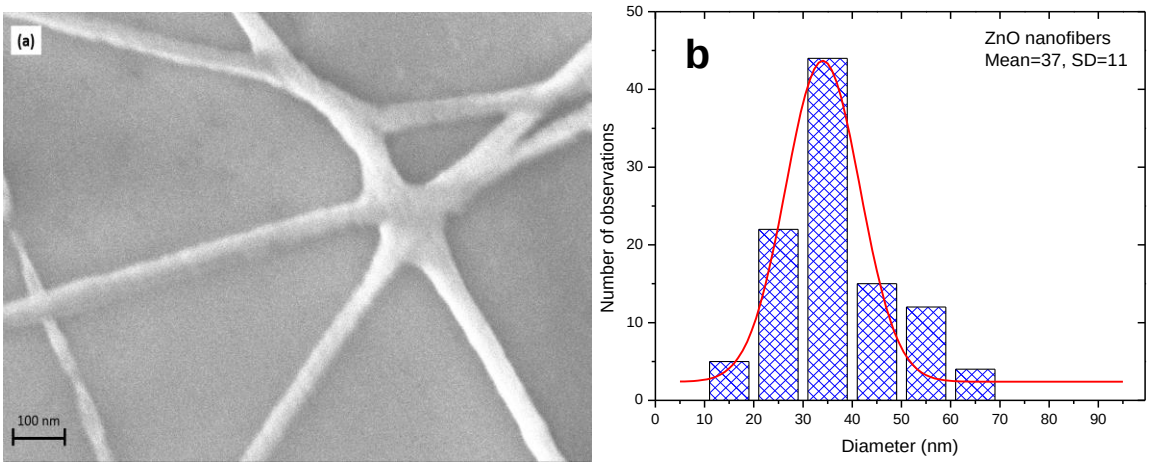

Figure 3. (a) Images MEB montrant la morphologie de la surface des nanofibres de ZnO après recuit à 450 °C pendant 1 heure. (b) Histogramme montrant la distribution de la taille du diamètre des nanofibres de ZnO.

Ensuite, une couche mince d'oxyde d'étain dopé au fluor a été déposée sur l'échantillon de nanofibres pour former les échantillons de nanocomposites FTO_ZnO. Les échantillons obtenus ont été soumis à des caractérisations morphologiques, optiques et électriques. Sur les images MEB (Figure 4), les échantillons ont montré un aspect nanostructuré avec une distribution uniforme de la taille des grains, même en comparaison avec le FTO de référence standard. Les propriétés optiques, plus précisément la transmission et le facteur de Haze, ont été mesurées par spectrophotomètre UV-vis.

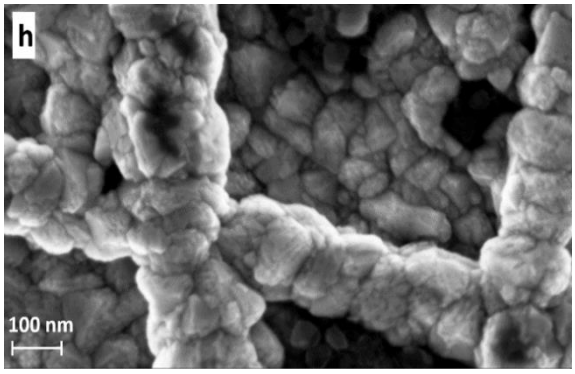

Figure 4. Images MEB des nanocomposites FTO_ZnO.

Une comparaison entre différentes configurations d'échantillons a été effectuée. Les échantillons ont montré de bonnes valeurs de transmission indépendamment du temps de dépôt des nanofibres dans le cas où la couche était déposée sur les nanofibres. Cependant,

les spectres enregistrés pour les deux cas où les nanofibres ont été déposées sur un substrat en verre et un FTO commercial n'ont pas montré de contribution significative causée par les nanofibres ; au contraire, les résultats étaient similaires à ceux du substrat de référence correspondant. En outre, une amélioration des valeurs de facteur de Haze calculées a également été enregistrée (Figure 5), ce qui signifie que nous avons réussi à augmenter la longueur du trajet de la lumière dans les échantillons nanocomposites sans affecter leur transparence. Quant aux propriétés électriques, il a été possible de mesurer la résistivité des échantillons nanocomposites où on a remarqué une augmentation des valeurs de résistivité après l'intégration des nanofibres de ZnO avec la couche mince de FTO, mais encore les valeurs obtenues de l'ordre de 10^{-3} reste acceptable.

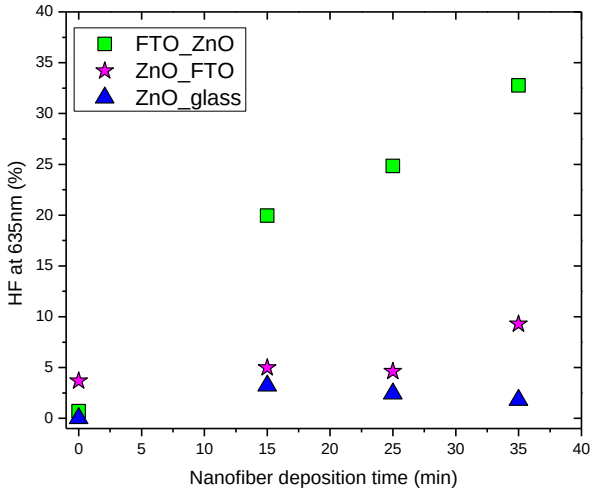

Figure 5. Facteur de Haze à 635 nm en fonction du temps de dépôt des nanofibres pour les trois configurations d'échantillons.

On conclut que la fabrication d'échantillons nanocomposites de FTO_ZnO a montré une amélioration remarquable du facteur de Haze de la couche de FTO ou de nanofibres de ZnO, néanmoins une petite dégradation de la conductivité de ces échantillons a été notée.

Le ZnO étant connu pour sa résistivité élevée, l'ajout d'un élément dopant à ce matériau est efficace pour augmenter sa conductivité. Dans ce contexte, le chapitre suivant sera consacré à la fabrication de nanofibres d'oxyde de zinc dopées aluminium, qui seront également utilisées comme nanocomposites avec une couche mince de FTO, dans l'intention

d'améliorer les propriétés électriques, principalement la conductivité qui a montré une dégradation pour les fibres non dopées.

Chapitre IV : Développement de nanofibres AZO par électrofilage

Dans le but d'améliorer la conductivité des nanofibres d'oxyde de zinc, l'approche du dopage aluminium a été abordée dans ce chapitre. Dans un premier temps, le chlorure d'aluminium a été utilisé comme précurseur ; il a été ajouté en différentes concentrations à la solution initiale de précurseur utilisée pour la fabrication des nanofibres d'oxyde de zinc. Les fibres déposées sont passées par le processus de recuit pour découvrir, après imagerie MEB, que les fibres avaient complètement disparu du substrat. Il s'est avéré que le précurseur utilisé pour le dopage (chlorure d'aluminium) était à l'origine de ce phénomène. En effet, les milieux acides provenant de l'utilisation d'un précurseur de chlorure, affectent directement la formation des nanofibres d'oxyde de zinc puisque ces dernières restent intactes dans un pH neutre mais sont immédiatement dissoutes dans un milieu acide, ce qui était notre cas. Par conséquent, un changement de précurseur pour l'acétate d'aluminium a été fait pour maintenir autant que possible une solution au pH presque neutre. Après le changement de précurseur, un affinement de la morphologie des nanofibres a été observé : forme parfaite avant recuit et structure améliorée après recuit.

Le comportement thermique d'une série d'échantillons de nanofibres produits par la méthode d'électrofilage a été étudié. A partir d'une solution de PVA, ces nanofibres sont de l'oxyde de zinc et de l'oxyde de zinc dopé avec 1%, 2%, 3% et 4% d'aluminium.

L'objectif principal était d'analyser le comportement des nanofibres pendant la phase de recuit post-croissance. C'est pourquoi, au-delà de la méthode d'électrofilage utilisée pour la croissance des fibres, la microscopie électronique à balayage qui a permis une analyse qualitative des échantillons, et des études complémentaires qui contribuent à la compréhension de la structure modifiée lors du traitement thermique ont été réalisées, précisément l'analyse thermogravimétrique (ATG) et la fluorescence X (XRF).

Le rôle particulier du dopage en aluminium dans la solution avec une forte dépendance de la température par rapport à la concentration a été mis en évidence. Ces variations de la

température de dégradation en fonction du zinc et de l'aluminium peuvent être expliquées par une forte interaction à l'interface du ZnO et du PVA, atténuée par l'aluminium dans les nanofibres dopées.

Ces analyses montrent également que la température de dégradation est relativement basse par rapport à la température nécessaire à la cristallisation des nanofibres à base de ZnO et de ZnO-Al, mais aussi que la masse résiduelle dans les fibres dopées se rapproche de la masse résiduelle du PVA pur. Ainsi, nous constatons que le ZnO étant vaporisé au-delà de cette température de fusion, la production de nanofibres ZnO-Al (AZO) est particulièrement difficile voire impossible par la méthode d'électrofilage avec recuit à l'air.

Conclusions et Perspectives

Le travail abordé durant cette thèse, a porté sur le développement de nanocomposites à base de ZnO et de FTO pour leur utilisation comme électrodes conductrices transparentes. Les nanocomposites utilisés durant ce travail ont deux configurations différentes et sont conçus comme suit : nanofibres de ZnO avec une fine couche de FTO. Le choix des nanofibres comme nanostructure offre la possibilité de réaliser des électrodes transparentes, conductrices et flexibles en même temps.

Après une introduction sur les propriétés générales des TCO, on présente les trois TCO les plus utilisés de nos jours : ITO, ZnO et FTO. Néanmoins, les propriétés requises des TCO vont au-delà de la transparence et de la conductivité, pour atteindre des performances rentables et respectueuses de l'environnement. Pour cela, l'intégration de nanomatériaux pour obtenir des capacités fonctionnelles se présente comme solution possible pour répondre à ces critères. Par conséquent, nous discutons dans la deuxième partie de ce chapitre de cette approche en accordant une attention particulière aux nanofibres d'oxyde de zinc.

Pour le deuxième chapitre, on commence par étudier des couches minces de FTO et de ZnO. Cet étude servira d’une étape intermédiaire, mais de base aussi, pour comprendre le comportement des couches avant l’intégration de nanofibres. Les propriétés morphologiques et structurales sont alors exploitées par AFM et spectroscopie Raman.

La nanostructuration des échantillons se fait avec des nanofibres d'oxyde de zinc élaborés par la technique d'électrofilage. Cette technique consiste à envoyer une solution de précurseur vers une aiguille placée au-dessus d'une plaque collectrice. Sous l'effet d'un champs électrique appliqué entre ces deux derniers, la solution se transforme en nanofibres qui se dépose sur les substrats. Les nanofibres obtenues ont montré une bonne cristallisation ainsi qu'une structure uniforme et continue avec un diamètre d'environ 40 nm. Après le dépôt d'une couche de FTO sur les nanofibres, les propriétés optiques surtout le facteur de haze subit une amélioration remarquable. Ceci montre que la lumière est bien diffusée à l'intérieur de la couche nanostructuré. Cependant, une régression de la conductivité a été noté en comparaison avec des couches minces de FTO, ce qui été attendue puisque l'oxyde de zinc est connu pour sa faible conductivité.

Le dopage des nanofibres avec de l'aluminium est une solution possible pour remédier à cet effet. Alors dans le dernier chapitre nous présentons une approche pour produire et optimiser les conditions d'obtention des nanofibres d'oxyde de zinc dopées aluminium par plusieurs étapes : précurseur utilisés pour la solution, conditions de traitement thermique et état structurale des nanofibres obtenues. Par ces approches, nous avons aboutis à améliorer et mieux comprendre la forme et structure des nanofibres AZO, qui s'est avéré particulièrement difficile.

Plusieurs perspectives et solutions se présentent à cette problématique :

- Utiliser la même méthodologie et la même technique en essayant différents types de dopants pour les nanofibres d'oxyde de zinc
- Le soudage à froid des nanofibres d'oxyde de zinc avant le dépôt d'une couche mince de FTO pourrait être un moyen possible d'améliorer la conductivité des échantillons nanostructurés. Cette technique a montré des résultats prometteurs dans le cas des nanofils d'argent.
- Utilisation éventuelle de la structure réalisée pour un autre type d'application (capteurs par exemple)

Chapter I: Introduction

This chapter is a presentation of the properties and applications of transparent conductive oxides (TCO), their required properties as high electrical conductivity associated with high transparency and the impact of the appropriate doping element and concentration on the properties of the material. Moreover, a description of the various possible techniques used for the growth of TCO to be integrated as transparent electrodes in photovoltaic modules is also presented. Indeed, new generations of solar cells need optimizing TCO with improved conductivity and transparency depending on substrate, type of PV cells, and conditions of use. Thus, Indium Tin Oxide (ITO), Zinc Oxide and Aluminum Zinc Oxide (ZnO-AZO), and Tin Oxide and Fluoride Tin Oxide (SnO_2-FTO) TCO families are considered. However, recent expectations on TCOs have shifted away from fundamental transparency and conductivity, requiring increased performance and varied roles that are compatible with scalable, cost-effective, and environmentally friendly procedures. Due to the variable and programmable features of nanomaterials [1,2] combining TCO thin films with nanomaterials to obtain new functional capabilities is an intriguing challenge. This new approach is discussed in the second part of this chapter with a presentation of the TCO thin films nanostructuration especially dedicated to Photovoltaic devices and applications. For nanostructuration, specific attention will be given to nanofibers particularly to Zinc Oxide nanofibers which appear to have great potential to be considered as transparent electrodes in the photovoltaic research domain.

1. Generalities on transparent conductive oxides

1.1 History and evolution of transparent conductive oxides

The original known discovery of Transparent Conductive Oxide, TCO was in 1904 when Badeker [3] observed an oxidation of cadmium (Cd) metal thin films deposited in a glow discharge chamber. He observed that after oxidation, the Cd films became transparent while conserving their electrical conductivity. Ever since, the value of these films grew commercially and the list of TCO expanded to other oxide materials as zinc oxide (ZnO), titanium oxide (TiO_2), tin oxide (SnO_2), indium oxide (In_2O_3), pure or doped with elements as Fluor or Alumina, and many more.[4] Currently, at the date of this contribution, the properties of TCO layers and their optimization remain a subject of intense research all around the word and the number of publications concerning TCO continues to grow to reach 250,000 (Google Scholar, 2021) publications in rank A journals. It is to be of note that oxide are not the only transparent conductive materials (TCM) but they are the most studied due to their advantageous set of properties. [5–7]

This enthusiasm is justified by the unique properties of these TCO layers which are jointly directly linked to their transparency and electrical conductivity. TCO thin films have a wide range of applications including transparent heaters, heat mirrors, smart windows, and optoelectronic devices in particular the market for transparent electrodes used in touch panels, flat panel displays or lamps, and thin film solar cells which is still expending linked to the increase of new emerging solar cells technologies and devices as organic and perovskite ones. Based on the precursor tin oxide, SnO_2, applications can be classified into two dominant markets: architectural applications such as energy efficient windows which currently employ fluorine doped tin oxide, FTO, deposited by pyrolytic process, thanks to its efficiency in preventing radiative heat loss due to tin oxide low emissivity. Such coated windows are ideal for low temperature applications as, for example, doors of glass freezer or windows of airplane cockpit. The second current application domain of TCO is flat panel applications such in the case of PV modules, touch screens and plasma displays which, currently, mainly employ indium doped tin oxide, ITO as external surface transparent

electrodes. [8] Beside ITO, and for many technological and environmental reasons discussed below, ZnO becomes for PV applications also a major material used for such applications.

These last decades, an emergent third market is linked to the development of renewable energies and more specifically to the production of electricity from photovoltaic, PV solar cells, modules or panels. The resulting increase in the need for PV panels, flat or not, rigid or more recently flexible, leads to technological new developments with the development of thin-film PV panels requiring the replacement of the surface electrodes made up of metal ribbons with transparent electrodes and therefore based on TCO layers.

Among all studied materials, ITO was the most employed for TCO applications, mainly for large surface due its advantageous and unique set of electrical and optical properties. Moreover, as ITO is a non-friendly material, over the years and with the increasing demand, the conception of employed TCO started to change. The change in the basic material opens the way to overcome limitations and improve the devices performance of new TCO as the already mentioned ZnO and FTO. Indeed, the development of new friendly materials, deposited or growth with low cost techniques for TCOs allowing the development of large area and/or flexible photovoltaic cells and display devices is a urgent need in the way of sustainability. This development is accompanied by the need to increase their conductivity and transparency, which is made possible by a better understanding of the relationship between their structure and their electrical and optical properties.

1.2 General properties of transparent conductive oxides and their relevance to some applications

The requirements for TCO are good electrical conductivity and high transparency in the visible spectrum of light. These properties are achieved in wide band gap oxides made degenerated by the introduction of dopants. [9] However, a lot of parameters influence the choice of a TCO depending on the application to which it is intended to be used for. These parameters include stability (physical, chemical, thermal), etchability, conductivity, plasma wavelength, thickness, deposition temperature, uniformity, toxicity and cost. Table I.1 shows the most important property of the most important transparent conductive materials

studied in various works around the word. Hence, for a given application, performance is defined by a number of electrical and optical but also by physical and chemical properties.

Table I. 1. Summarizing table of the most important property for different Transparent Conductive Materials (TCM).[10]

Property	Material
Highest transparency	ZnO:F, Cd_2SnO_4
Highest conductivity	In_2O_3:Sn
Lowest plasma frequency	SnO_2:F, ZnO:F
Highest plasma frequency	Ag, TiN, In_2O_3:Sn
Highest work function, best contact to p-Si	SnO_2:F, $ZnSnO_3$
Lowest work function, best contact to n-Si	ZnO:F
Best thermal stability	SnO_2:F, TiN, Cd_2SnO_4
Best mechanical durability	TiN, SnO_2:F
Best chemical durability	SnO_2:F
Easiest to etch	ZnO:F, TiN
Best resistance to H plasmas	ZnO:F
Lowest deposition temperature	In_2O_3:Sn, ZnO:B, Ag
Least toxic	ZnO:F, SnO_2:F
Lowest cost	SnO_2:F

Generally, a compromise must be found by researchers, manufacturers and designers of systems between all these properties in order to find the best material allowing to obtain the electrode adapted to the intended application. As an example, buildings with conventional glass windows allow visibility to the outside (visible wavelength range: 380–750 nm), but infrared energy from the sun (> 750 nm) enters the building and warms it up. In order to create comfort, infrared radiation from the outside to the inside must be blocked or minimized (in warm weather) or from the inside to the outside (in cold weather). As a result, the fundamental requirements for an excellent low-e coating for glass windows are good transmittance in the visible and high reflectance in the infrared wavelength ranges. For this application FTO is the best material because it has the convenient plasma wavelength along with excellent durability and low cost. On contrary, for hot weather, a short plasma wavelength is better so that the near IR is reflected out of the substrate. For this application silver and titanium nitrides are suitable, however silver nitride has a poor durability, so it needs to be sealed inside double-glazed panes for protection against moisture and air. [11]

1.2.1 TCO Electrical and optical properties

The first interest to control the charge carriers concentration and mobility in the TCO film is to offer the possibility of an optimization of its electrical properties. This possibility is closely related to the intrinsic material of the TCO and the type and concentration of dopant. Indeed, the conductivity of thin film is highly dependent on the carrier concentration and mobility which are related by the following relation:

$$\sigma_{n,p} = nq\mu \qquad \textit{Equation 1}$$

Where n is the density of electron (hole) in the conduction band (valence band), q is the charge of the electron (1.6×10^{-19}) and μ is the mobility of charge carriers. It can therefore be seen that to become conductive, the films must either deviate from stoichiometry or by intrinsic doping such as oxygen vacancies, or more generally, be doped with appropriate external impurities to form an extrinsic doping. According to Equation 1, the possibility of increasing the conductivity of the films consists either in improving the concentration of carriers by doping, or in improving the electronic mobility μ.

Depending on material or on type of dopant, the doping can be realized by substitution, vacations or interstitial implantations. Considering the valence of the dopants or of the type of implantation on acceptor or donor sites, the doping will induce n or p type conductivity. Thus, with the TCO presented in this contribution, the doping can be done by substitution of cation (metal ion) or anion (oxygen).

However, the increase in the dopant concentration is limited by the fact that at high concentration, the ionized dopant atoms can play the role of diffusion centers reducing the mobility of electrons but also can deteriorate the optical properties by an increase of the absorption of the film mainly at long wavelengths (near infra-red). Thus, as far as possible, it is preferred to improve the conductivity by increasing the electronic mobility μ. Grain boundary scattering and ionized impurity scattering are generally considered to be the two main interacting mechanisms in conductivity. These two phenomena will then depend directly on the quality of the layers, on their thickness and therefore also on the growth or deposition methods. In particular, Minami et al. [12] for ZnO films obtained by different

methods, and Rey et al. [13] for FTO films have shown that the conductivity is primarily affected by grain boundaries scattering in thin films while for thicker films the ionized impurities scattering dominates.

Direct bandgap and high exciton energy are basic requirements for materials to be used in optical emitting devices. Whereas for TCO to be used as electrodes in solar cells, they have to exhibit a minimum carrier concentration of the order of 10^{20} cm^{-3} and a band gap greater than 3.2 eV to avoid absorption of light over most of the solar spectra. [14] In the optoelectronic field especially for photovoltaic devices, it is preferable to have low resistivity to facilitate current transport. Experimentally, Hall Effect measurements and I-V measurements are performed to determine the electrical properties of TCO thin films. This characterization method permits to find the resistivity, charge carrier density and mobility.

The second interest for doping TCO concerns its optical properties. The first concerned optical effect is related to the Burstein Moss effect which shifts the transparency limit of a semiconductor towards short wavelengths with the increase in energy required to produce an interband electronic transition. [15] However, the increase in the density of carriers has the effect of increasing the Fermi energy and therefore of decreasing the transparency limit when the doping level increases. Nevertheless, corresponding to the second optical effect, the doping of TCO will strongly influence the interaction of photons and excitons. Below the higher wavelength limit of the transparency band (called plasma wavelength), but above the lower transparency limit, TCO is transparent and has a dielectric type behavior. Beyond the plasma wavelength, it behaves like a metal and absorbs or reflects light. The effect of the doping is then a shift in the plasma wavelength and therefore a reduction in the transparency of the TCO in the infrared. A compromise must then be found for the TCOs used in photovoltaic applications as a function of the spectral response of the absorber. Thus, in general, with TCOs whose plasma wavelength is typically between 1 and 2 μm, the type of oxide and its doping are optimized to have a transparency range ranging from near UV to near infrared depending on the material used and its doping. Experimentally, absorption-transmission (and/or FTIR) spectroscopy measurements are performed to determine the optical properties of TCO thin films.

To compare the performance of transparent conductive materials, TCM quantitatively, a pertinent figure of merit, FoM is defined as the ratio of the electrical conductivity (σ) on the visible absorption (α) and is given by Equation 2

$$\frac{\sigma}{\alpha} = -[R_s ln(T + R)]^{-1} \qquad \textit{Equation 2}$$

where R_s is the sheet resistance in ohms per square, T the total visible transmission, and R is the total visible reflectance. A larger value of FoM indicates better performance and quality of the TCM.[16] Another expression of FoM was proposed by Jain et al. [17] but without taking into account the reflection. It will not be considered here. Based on Equation 2, Table I.2 lists the FoM for different TCO materials.

Table I. 2. Figure of Merit for some transparent conductors. [10]

Material	Deposition method	FoM (x10^{-2} Ω^{-1})	Ref
ITO	Commercial	5.9	[18]
ITO	Atomic Layer Deposition	1.3	[19]
AZO	Pulsed DC magnetron sputtering	1.99	[20]
FTO	Ultrasonic Spray Pyrolysis	0.9	[21]

It is to be noted that the FoM is not the only qualification criteria occurring in the development of TCO on an industrial scale. All the production processes need to be considered and the whole life of the product, i.e. in case of TCM as other devices, the chemical and toxicity of the constituting elements and the environmental aspects for the production and treatment at the end of life. From the industrial point of view, currently the most used material for TCO is indium tin oxide (ITO). Despite its flaws imperfections and instability of purchasing price, ITO, having a unique set of properties, is still dominating the transparent and conductive oxide industry. As a result, effort is made in order to find a competitive transparent material having similar or overpassing performance. Indeed, Indium is a rare element on earth, which is found in small quantities in the zinc, and lead mines. Indium is then produced in much smaller amount compared to zinc and tin.

Table I. 3. Abundance of Indium, Tin and Zinc in ppm. [22]

Element	Abundance (ppm)
Indium (In)	0.049
Tin (Sn)	2.2
Zinc (Zn)	75

Due to its rarity and the world increasing demand from the photovoltaic panel industry, its price has incredibly risen. For this reason, a renewed interest has grown in finding replacements for ITO. With today's environmental challenges, using natural and renewable resources or abundant elements became prior for sustainable development of efficient TCO and systems. [23]

1.2.2 TCO Thermal stability

The deposition temperature is decisive during a deposit by Chemical Vapor Deposition (CVD) because it defines the kinetics of the various reactions between the chemical species present and the deposition regime. It follows a link between this temperature and the thermal stability of the so-grown layer.

Table I. 4. Thermal stability of some transparent conductors. (LPCVD and APCVD are Low and Atmospheric pressure CVD, respectively). [10]

Deposition method and material	Deposition temperature (°C)	Stability temperature (°C)
LPCVD ZnO:B	200	<250
APCVD ZnO:F	450	<500
APCVD SnO_2:F	650	<700

Generally, thermal stability of TCO is tested by heating the material to temperature greater than the deposition temperature. Generally, it leads to an increase in the resistance of the TCO if heated for a long period of time. Tests were made and reported in the literature to check the thermal stability of several TCOs and the results are shown in Table I.4. The tested materials remained stable with no increase in sheet resistance for temperatures slightly above the deposition temperature.

1.3 Doping transparent conductive oxides

In this part, the influence and interest of extrinsic doping on the properties of TCO is presented and discussed taking into account the two doping types; n- and p-type.

As previously shown a double interest exists in the doping of a TCO allowing the improvement of optical and electrical properties, respectively. Internal electronic, chemical and physical parameters of the components such as the size and the electronic charge of the dopant ion and external growing process and technique parameters such as the solid solubility of the dopant in the host material crystalline lattice influence the possibility of doping and the final quality of the film. We report in Table I.5 the ionic radius of the main elements considered in TCOs either as constituent elements of pure TCMs or as dopants, it is obvious that the substitution will be facilitated by ions having similar diameters.

Table I. 5. Table representing the ionic radii of the elements used as TCO. [24]

Element	Ionic radius (Å)	Ionic charge
Oxygen (O)	1.40	-2
Zinc (Zn)	0.74	+2
Tin (Sn)	0.69	+2; +4
Fluorine (F)	1.33	-1
Aluminum (Al)	0.53	+3
Chlorine (Cl)	1.81	-1
Gallium (Ga)	0.62	+3
Antimony (Sb)	0.76	+3; +5
Indium (In)	0.80	+3

Thus, we will see below that the size of the different ions involved in the doping process will be taken into consideration in the choice of the dopant in addition to the consideration of the electronegativity, the crystal structure and other optical and electronic parameters of host and dopants.

1.3.1 N-type doping

Many doping are based on cation substitutions. For example, indium oxide can be doped with transition metal ions as molybdenum, titanium or tin ions giving the well-known

indium tin oxide, ITO, already mentioned for its intensively used as TCO for photovoltaic cells of new generation. Zinc oxide ZnO is currently doped with metallic elements such as Al, Ga, In [25–27] and tin oxide SnO_2 with elements such as Sb, Nb, or metal ions such as F, Cu, Fe and Co.[28–31] The list of dopant candidates presented above, as example is not exhaustive and there is a great deal of works on many kinds of doping. Moreover, co-doping of TCO was already studied to enhance some specific properties and results can be found in literature, such as for the Al-Ti co-doping of ZnO. [32,33]

Doping TCO by substitution of the oxygen anion is rare. However, since oxygen and fluorine have relatively close ionic radius (mentioned in Table I.5), this substitution process is still applied for SnO_2 with fluorine dopant substituting oxygen.

All dopants mentioned above are associated with the creation of an intermediary energy level under the conduction band of the host. The increase in dopant concentration develops an energy band overlapping the conduction band which reinforce the n type nature of the host semiconductor TCOs. Thus, compared to a pure undoped TCO, by doping, a larger number of electrons will participate to the circulation of the charges yielding to an increase in conduction.

1.3.2 P-type doping

All the TCOs mentioned above are n-type semiconductors and the interest of p-type doping for TCO applications currently remains discussed and controversial. In fact, in literature, the difficulty of creating transparent conductive oxides of p-type has been attributed to the significant localization of the holes in the oxygen levels and to the ionicity of the metal atoms. As a result, these holes are confined and require a considerable amount of energy to overcome a large barrier height to migrate inside the crystal lattice, causing poor hole mobility and conductivity. [34,35] Despite that, the first attempt to make a p-type TCO was achieved by Sato et al. [34] in 1993. They reported a p-type semi-transparent TCO (40% visible transmission) and the possibility to form acceptor levels through doping ZnO. It was then until 1997 when Kawazoe et al. [36] reported the properties of an oxide material ($CuAlO_2$) that combines p-type conductivity up to 1 $S.cm^{-1}$ with a satisfactory optical transparency. According to the authors, this value is not comparable to the best n-type conducting oxides,

but is sufficient for some applications. In recent years, more and more experimental works have focused on TCO thin films of p-type more specifically on ZnO doping with Ga, N, Al, and Sb. [37–41] Nevertheless, the challenge to grow p-type TCO having a resistivity in the order of 10^{-3} Ω.cm or better still exists.

1.4 Development and growth of transparent conductive oxides

In this section, we highlight a variety of used methods for the deposition of oxide thin films. These different deposition conditions and methods affect significantly the optical and electrical properties of TCO thin films. We finally discuss the link between the process temperature and the stability and properties of the TCO.

1.4.1 Generalities of growth techniques for thin films

Initial developments of TCO layers on a substrate such as glass, silicon or photovoltaic cells were low-cost techniques of liquid chemistry, such as electrochemical deposits [42] hydrothermal growth [43] or even deposition by the Sol-gel process. [44] In order to improve the control of the growth process and therefore the quality of the layers, the first methods of producing TCO layers on a substrate by sputtering [45,46] and spray pyrolysis were used in the 1970s. The spray pyrolysis is also called atmospheric pressure deposition or aerosol-assisted chemical vapor deposition technique. More sophisticated techniques have emerged in recent decades, such as pulsed laser assisted deposition [47] or molecular beam epitaxy. [48] The development of these latter methods was motivated by the development of large-scale commercial TCOs requiring better control of the reproducibility of the layers while improving their crystallinity, or even obtaining monocrystalline films and allowing the integration of dopants.

Furthermore, it should be noted that the development of nanostructured layers based on nanoparticles, nanowires or nanofibers have been recently developed to respond either to an improvement in the electrical and optical performance of TCO layers and / or to new applications such as for example photovoltaic on a flexible substrate. Some of the techniques mentioned above can also be used for the growth of nanostructured layers such as the

deposition technique in a chemical bath, or in the vapor phase, others are then more specific such as for example the electro-spinning technique, as developed for this purpose in this work for the development of ZnO nanofibers.

In the following part, we describe the main deposition and growth techniques of TCO thin films, illustrated by various examples relating to particular TCO films, especially ITO, FTO and ZnO, in order to highlight the experimental and growth considerations to be taken into account. On a side note, the operating principle of the spray pyrolysis growth technique will be given into details in Chapter II, in the following section it will be presented briefly along with some examples related to ZnO thin films.

1.4.2 Sputtering

Sputtering is a widely used technique for the deposition of TCO thin films. Sputtering includes a variety of techniques that can be used in a wide range of temperature such as radio frequency (RF) or direct current (DC) sputtering, or at only high temperature as magnetron reactive and ion beam sputtering. Out of the mentioned techniques, RF and DC were found to be interesting for the industrial field since they offer high deposition rates, reproducibility and large area sputtering systems. But, the major drawback of RF deposition at room temperature is the poor electrical and structural properties since the temperature is not enough for the crystallization of oxide layers as ITO films. Additionally, ITO films deposited by DC magnetron sputtering at room temperature, are most of the time amorphous with high electrical resistivity as reported by Quaas et al. [49] and Teixeira et al. [50] The deposition temperature of oxides by magnetron sputtering generally ranges from room temperature up to a few hundred degrees as for ITO up to 500°C [51,52]. Nevertheless, solar cells or electronic systems on plastics are types of substrates or applications requiring a low deposition temperature because higher temperatures could directly damage them or even damage the structure of the electronic device. [53]

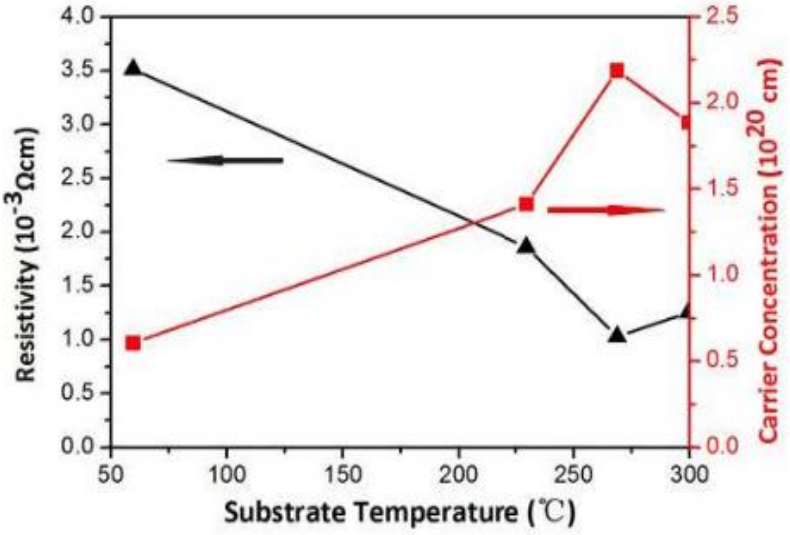

Figure I. 1. Variation of resistivity and carrier concentration in ITO layers with temperature grown by RF magnetron sputtering .[54]

As an example, we report in Figure I.1 the evolution of the resistivity and of the carrier concentration with the substrate temperature during the RF magnetron sputtering process made in discharge plasma modes. We can see at first, that resistivity and carrier concentration are inversely correlated.

1.4.3 Electron beam and direct thermal evaporation

For the growing of ITO films, electron beam and direct thermal evaporation methods use powders of metallic Sn and In. Indium will be favorably vaporized altering the composition of alloys caused by the higher vapor pressure of In relative to Sn. Diniz et al. [55] investigated the effect of various post deposition heat treatments on the microstructure, electrical and optical properties of In_2O_3:Sn (ITO) thin films deposited by electron beam evaporation. The thin films were deposited on microscope glass substrates and silicon single crystal wafer. After deposition, the samples were annealed in air for 30 minutes at temperatures of 200, 250, 300, 350, 400, 450, 550°C. They observed that at low temperature, the film was amorphous while the crystallite size remarkably increases with the temperature. It was noted that for a temperature of 300°C the average grain size was about 10 to 25 nm, whereas it increases to reach 15 to 50 nm for higher temperatures. This link between temperature

and structure was also reported in literature and is attributed to the fact that for a given driving force, the migration rate increases as the temperature increases. [56,57], [58]

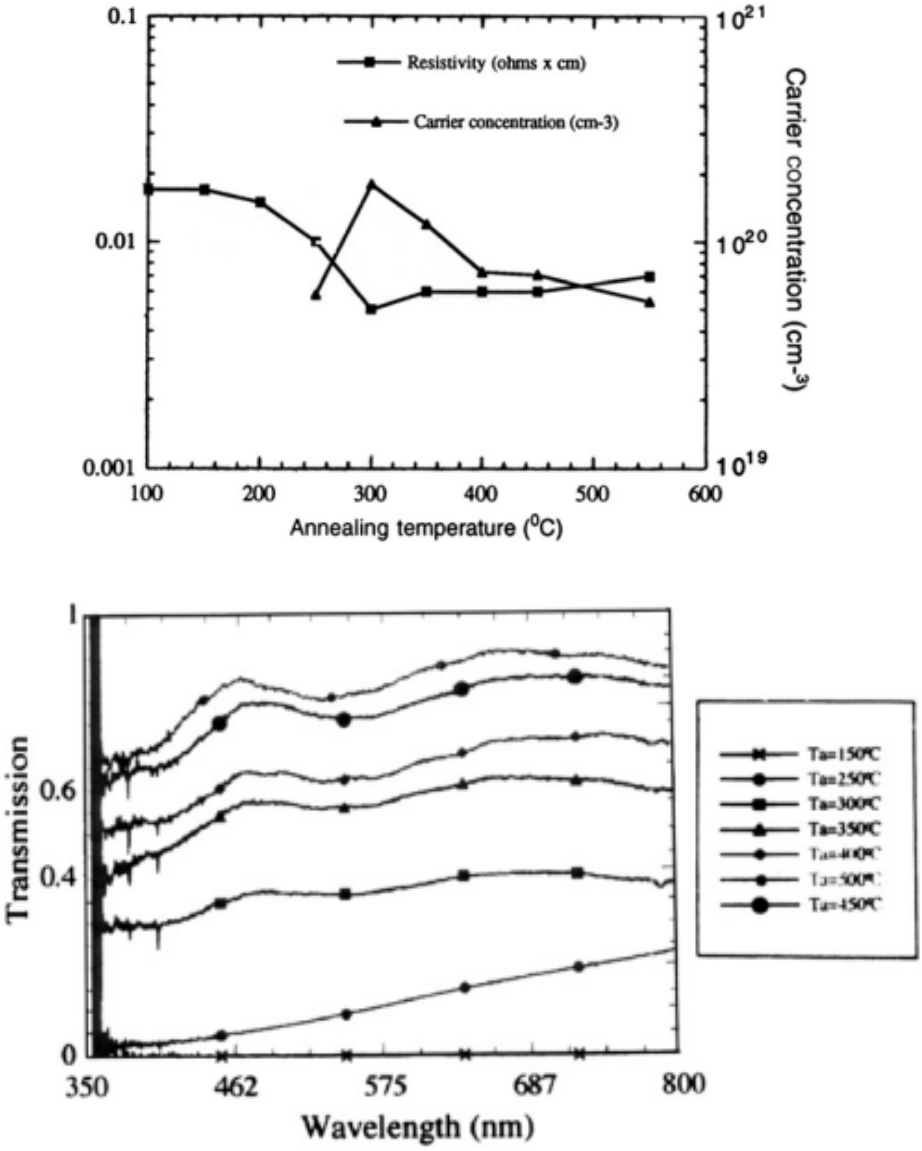

Figure I. 2. (a) Variation of electrical resistivity and carrier concentration as function of annealing temperature for ITO films. (b) Optical transmission curves for a series of ITO/glass films annealed at different temperatures.

Figure I.2 (a) summarizes the electrical properties (resistivity and carrier concentration) of the ITO films at various temperatures. At the annealing temperature of 300°C a sharp decrease in film resistivity as well as an increase in carrier concentration are observed. The

increase in film resistivity as we go further in annealing temperature is explained by the diffusion of more oxygen into the film that contribute to the decrease in the concentration of oxygen vacancies. This reduces the carrier concentration and hence the film resistivity. It is noted that optical transmission increases with increasing annealing temperatures since one of its effects is film crystallization as seen in Figure I.2 (b). Many earlier works explained the decrease of transmission for $\lambda<400$ nm by the absorption of ITO band gap which may vary in the range of $3.5\ eV < Eg < 3.8\ eV$. [59,60] Higher annealing temperatures resulted in improvement in optical transmission is a result of the transition from amorphous to microcrystalline then polycrystalline. This transition reduces the disorder level and assists the incorporation of tin atoms into the indium oxide lattice so that Eg becomes more defined.

1.4.4 Spray pyrolysis

In the spray pyrolysis (also called atmospheric pressure deposition or aerosol-assisted chemical vapor deposition technique), a chemical reaction of gaseous species takes place with a heated substrate surface. The advantages of this technique, are the relatively low cost of the deposit frame done at a low temperature allowing the possibility to be deposited on various substrates, and the possibility of depositing over large surfaces. All these advantages render this technique quite common for the development of transparent electrodes for a large amount of applications. For the experimental point of view, an additional advantage is that it enables the production of coatings having good properties on different substrate shapes with no need of vacuum use. Moreover, it is considered to be relatively cheap with respect to the apparatus. However, in the case of ITO films, the main drawback is the lack of volatile and thermally stable material source.

Numerous research for ZnO thin films deposition on glass substrates by the spray pyrolysis technique was made in the purpose to investigate the change in properties of the films with varying deposition parameter.

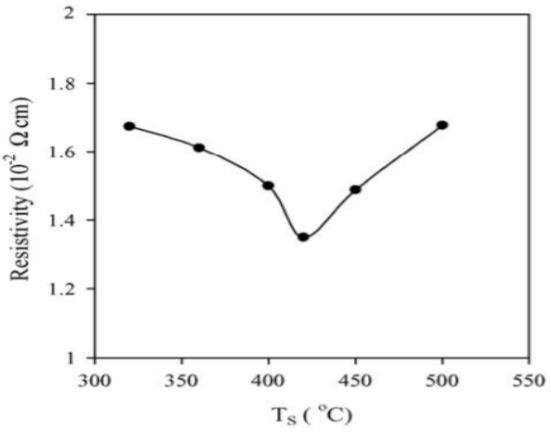

Figure I. 3. Dependence of the resistivity of ZnO films on the substrate temperature deposited by spray pyrolysis. [61]

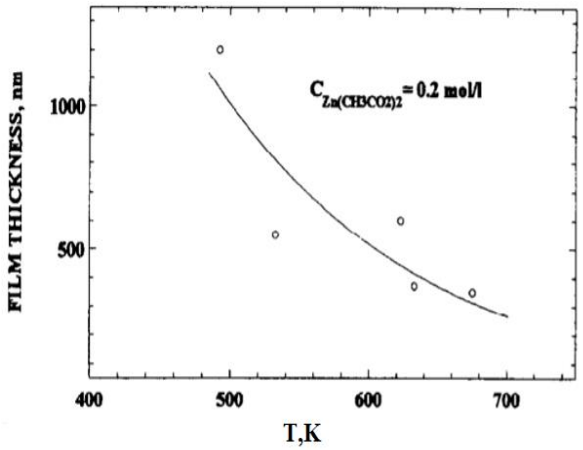

Figure I. 4. Dependence of ZnO film thickness on the growth temperature. [62]

ZnO thin films deposited on glass substrates with different thickness and different deposition temperature revealed the dependence of the resistivity on the substrate temperature and spraying rate shown in Figure I.3. In addition, Figure I.4 shows the effect of the substrate temperature during the deposition process on the film thickness; [62] it was found to decrease with increasing temperature. This decrease is explained by the decrease in mass transport to the substrate at higher temperature and by the increase of reevaporation rate.

2. The three main transparent conductive oxides for photovoltaic applications

As mentioned in the Introduction paragraph, following this general review of structural, electrical and optical properties of TCOs related to the growth techniques, the materials and their dopants, the three main families of transparent conductive materials, ITO, ZnO-AZO, and SnO_2-FTO, used as electrodes in PV cells and modules will be presented in the section below.

Over the years and with the increasing demand, the conception of employed TCO started to change and new materials were considered for transparent electrodes such as ZnO and SnO_2 with their dopants. Currently, these oxides showed to be more favorable and could compete some of the ITO properties. The change in the basic material has opened the way to overcome limitations and improve the devices performance. Indeed, the urgent need for new material comes with the need to increase conductivity and transparency i.e. a better understanding the relationship between structure and electrical and optical properties, allowing to develop flexible and/or large area display devices and PV cells.

2.1 Indium oxide (In_2O_3) and Indium Tin Oxide (ITO)

Indium Tin Oxide, ITO is a mixture of indium oxide (In_2O_3) and tin oxide (SnO_2) typically in a ratio of 90/10 wt%. [63] It is widely used in transparent heating elements of aircraft and car windows, antistatic coatings over electronic instrument display panels, heat reflecting mirrors and antireflection coatings, high temperature gas sensors. ITO is also widely integrated in other electro-optic devices as transparent electrodes for solar cells, light emitting diodes, phototransistors and lasers. In addition, until now, ITO offers the best available FoM, i.e. best performance in terms of conductivity and transparency along with excellent environmental stability, reproducibility and good surface morphology.

Indium oxide In_2O_3 presents a bixbyite structure, which can be described as a fluorite-type structure where a quarter of the anions are missing; a periodic structure that produces structural vacancies. [64] It crystallizes in a cubic structure as reported in Figure I.5. To obtain the indium tin oxide, doping with Sn replaces by substitution the In^{3+} ion forming an

interstitial bond between Sn and oxygen atoms. Tin is present with a dual valence and exists as either SnO or SnO_2 which gives a direct impact on the conductivity of ITO. For lower valence state, a drop in carrier concentration occurs caused by the creation of holes acting as traps and thus reducing conductivity.

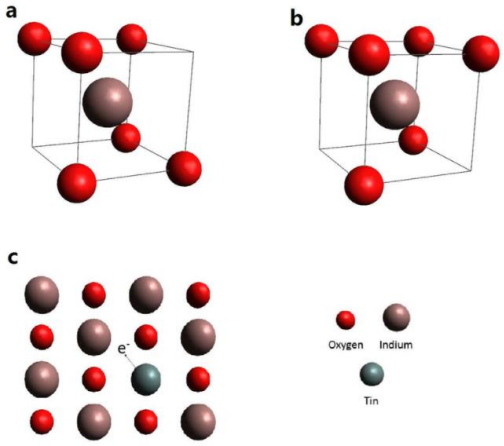

Figure I. 5. Indium oxide bixbyite structure. (a) Eight oxygen atoms situated within a compressed octahedral and have six equidistant oxygen atom neighbors. (b) Eight In atoms situated at the corners of a distorted octahedron. (c) Sn doping sites in In_2O_3 lattice. [65]

However, for the case of SnO_2 state, Sn^{4+} releases electrons to the conduction band, thus acting as n-type donor. Moreover, ITO films have lattice parameters close to that of In_2O_3 and are in the range 10.12 Å to 10.31 Å. [66]

Tuna et al. [67] reported the effect of substrate temperature and film thickness on the electrical, optical and structural properties of ITO thin films deposited by RF and DC magnetron sputtering on glass substrates. In their study they found out that the substrate temperature mostly affects the crystallization and resistivity of the samples. The characteristic peak (222) indicating the crystallization of ITO was observed starting from the annealing temperature of 150 °C up to 300 °C.

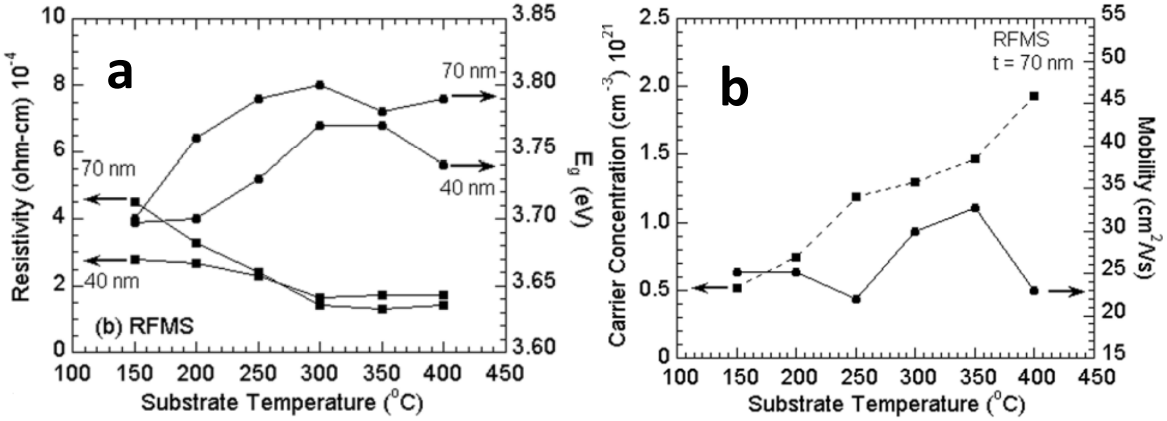

Figure I. 6. (a) Variation of resistivity and band gap as function of substrate temperature for ITO films. (b) Substrate temperature dependence of carrier concentration and Hall mobility of ITO 70 nm thickness. [18]

Generally, the resistivity of the ITO layer was noted to decrease as the substrate temperature increases due to the increment in carrier concentration, crystallization and grain size. Nevertheless, the resistivity of the films at 400°C is found to be slightly higher than the obtained resistivity at 350°C as reported in Figure I.6 (a). This small variation might be the result of the growing number of oxygen vacancies with increased substrate temperatures. In addition, Nisha et al. [18] previously reported that the diffusion of alkali ions from the substrate into the film structure at higher temperature might have a negative effect on the mobility. Figure I.6 (b) shows the increase in mobility for temperatures above 250 °C is attributed to the higher degree of crystallinity resulting in less grain boundary scattering. However, the increase of carrier concentration for temperature above 350 °C limits the mobility which by consequence suddenly decreases. Therefore, to get the optimum electrical properties, the preferable growth temperature for ITO films is experimentally found around 350 °C.

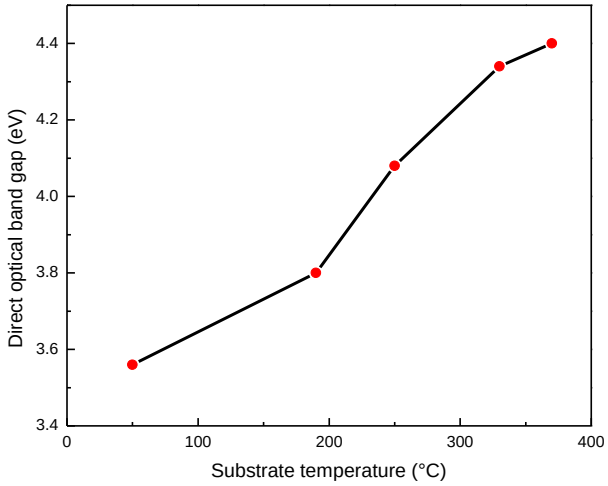

Figure I. 7. Variation of optical band gap with different substrate temperature for ITO thin films deposited by magnetron sputtering. [68]

High conductivity of ITO films is assumed to be owed to high carrier concentration rather than high mobility of hole. Compared to In_2O_3, the low mobility of hole in ITO and its dependence on substrate temperature is attributed to scattering mechanisms by ionized impurities or grain boundaries. At higher substrate temperature, an enhancement of the crystallinity contributes to the increase of the carrier mobility.

The band gap of ITO ranges from 3.50 eV to 4.40 eV depending on the growth method and conditions as illustrated in Figure I.7 with the dependence of the band gap with the temperature of the substrat for ITO thin films. [68] It has generally a value greater than 3.7 eV.

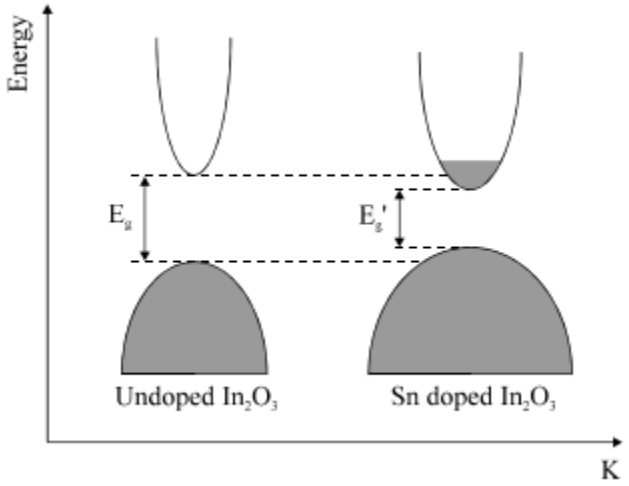

Figure I. 8. Assumed parabolic band structure of pure In_2O_3 and mixed In_2O_3-SnO_2 (ITO) compound. [69]

The doping with elements as tin indium oxide, contributes to the formation of donor states at a level below the conduction band. With increasing the doping density up to a critical density, these states merge with the conduction band as illustrated in Figure I.8. The ITO film becomes degenerate when the density of free electrons from the donor atom exceeds this critical value. By consequence, the columbic interactions shift up the valence band and shift down the conduction band which narrows the bandgap as illustrated in Figure I.8. This shift partially compensates the Burstein Moss effect.

In an attempt to identify the effect of grain size on the optical and electrical properties of ITO thin films under different annealing temperatures, Ahmed et al. deposited ITO thin films by high frequency magnetron sputtering. After deposition, the films were annealed at 250, 350, 450 and 550 °C for 1 hour.[58]

Table I. 6. Table showing the increase in grain size as the annealing temperature increases. [55]

Temperature (°C)	Average crystallite size D (nm)
As grown	35.05
250	40.98
350	41.17
450	41.54
550	51.62

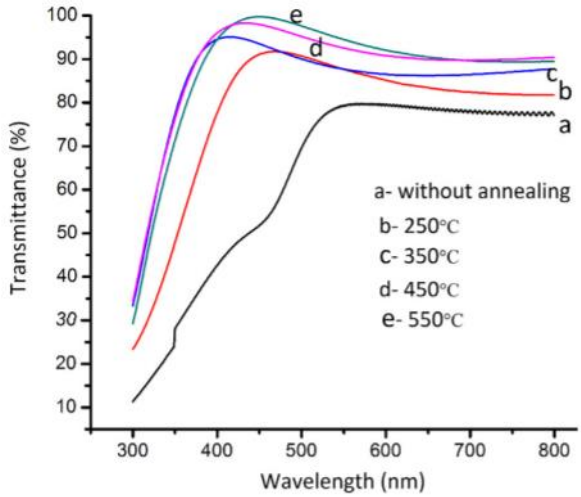

Figure I. 9. Optical transmittance spectra of ITO thin films deposited by high frequency magnetron sputtering. [58]

The study showed that as the annealing temperature increased, the microstructure of the ITO films improved and caused a decrease in the band gap of the film. This change is attributed to the possibilities of oxidation, higher realignment and strong interaction between film and substrate. It results, as shown in Figure I.9 an increase of the transmission response with the increase of the annealing temperature. In addition, as shown in Table I.6, authors in reference [58] observed an increase of the grain size (calculated from XRD spectra using Scherrer's formula) with the increase of the annealing temperature. Finally, the main output of this study displayed that at an annealing temperature of 450°C, an optimum set of characteristics of the ITO film were obtained.

Finally, it should be noted that indium tin oxide (ITO) thin films are also mainly used as transparent electrodes for most different types of liquid crystal displays (LCDs) and that ITO is not widely considered as transparent electrodes for traditional silicon photovoltaic sources or panels, but only for certain thin-film solar cells. For the latter, substitutes for ITO have already been developed, such as Al-doped ZnO (AZO) or Fluorine-doped SnO_2 (FTO). However, the properties of TCOs used for flat screens require improved optical and electronic qualities. It is for these reasons that, in applications such as flat screens, the ITO has not yet been replaced. Nonetheless, the total consumption of indium used for flat screens and alkaline batteries has dramatically increased in recent years and it is widely believed that a shortage of indium may arise in a near future. Currently, researchers in various fields are intensively focused on possible alternatives to the transparent ITO electrodes used in displays, focusing on the development or optimization of materials that can be produced with non-toxic and abundant materials and at low cost. Among them, we note the transparent conductive oxides (TCO) and particularly the importance of zinc oxide, mainly when it is doped with metal ions as Al or Ga (AZO or GZO) and tin dioxide mainly doped with fluorine (FTO).

Thus, for photovoltaic applications as concerned in the current contribution, it is therefore these two oxide-based materials in the ZnO and SnO_2 families, which will attract our attention.

2.2 Zinc oxide (ZnO) and Aluminum doped Zinc oxide (AZO)

ZnO doped with metal ions is often chosen as an alternative to ITO in optoelectronic devices properties as its functional properties achieved currently a good level of performance and as, in addition to being a very abundant element which makes it relatively cheap. By else, it possesses an interesting set of properties that can be individually used, manipulated and optimized in many application types. [70] For example, the large excitonic binding energy of ZnO about 60 meV at room temperature makes this material an efficient light emitter in the UV spectral region interesting in some optoelectronic applications. Its high conductivity and transparency, i.e. yielding to an interesting FoM, makes it important for applications, not only as transparent conducting oxides (TCO) but also as thin-film transistors (TFT). Furthermore, crystalline transparent and highly conductive ZnO thin film production can be deposited by various techniques on large scale and at room temperature making it compatible with a lot of substrate types: rigid or flexible, crystalized or amorphous, plastic, glass, silicon…, organic and inorganic ones. Moreover, optical, electrical, magnetic, piezoelectric, catalytic and gas sensing properties make ZnO specifically attractive for nanoelectronic, optoelectronic and piezoelectric devices, and of course for photovoltaic applications.

2.2.1 General properties of Zinc Oxide

In zinc oxide crystal lattice, the atoms are arranged in tetrahedral geometry where each Zn atom is surrounded by four Oxygen atoms and vice versa. ZnO generally crystallizes in wurtzite form, but depending on the growth conditions, other crystal forms like zinc blende and rock salt also exist for ZnO. The zinc oxide structure in wurtzite form is illustrated in Figure I.10.

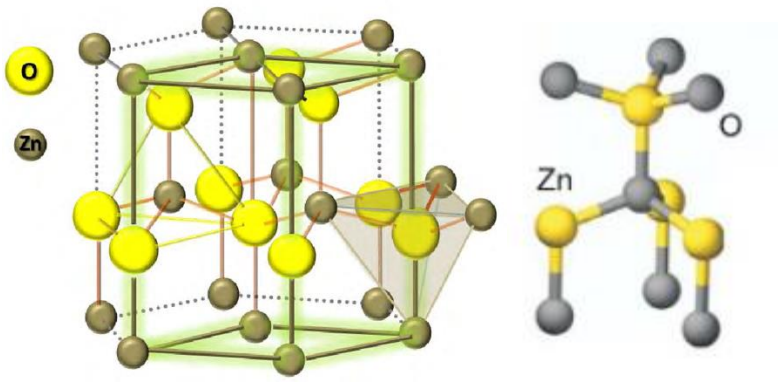

Figure I. 10. Zinc oxide structure: crystallizes in wurtzite form. [71]

Table I. 7. Basic properties of zinc oxide. [72]

Parameters	Value
Bandgap	3.4eV
Density	5.606g.cm^{-3}
Crystal structure	Wurtzite, rock salt, zinc blend
Stable phase at 300K	Wurtzite
Melting point	1975°C
Nature of oxide	Amphoteric oxide
Lattice constants at 300K	a_0= 0.32495nm c_0= 0.52069nm
Relative dielectric constant	8.66
Refractive index	2.0041
Solubility in water	0.16mg 100mL^{-1}
Intrinsic carrier concentration	10^{20}cm^{-3}

Zinc oxide is a direct band gap semiconductor with a high refractive index (~2) having Eg = 3.4 eV at room temperature. The concentration and mobility of electrons in ZnO were found to be in the range 10^{16}~10^{17} cm^{-3} and 20~400 cm^{2}V^{-1}s^{-1}, respectively. The resistivity of ZnO extends over several orders of magnitude, with values ranging from 10^{-4} Ω.cm to 10^{12} Ω.cm. [73] According to the processes used for the deposition of ZnO, a low resistive (ρ = 10^{-4} Ω.cm) or high resistive (ρ = 10^3 Ω.cm) i.e. respectively, high or low conductive films can be developed.

However, regardless of the processes used for the deposition of ZnO, the relatively low electrical conductivity of pure ZnO when compared to ITO is noted as a drawback, but doping

by foreign elements can offer possibilities for huge improvement of the conductivity with a lower sheet resistance down to values of 4.3 x 10^3 Ω/cm and 3.3 x 10^3 Ω/cm for Al and Ga doping, respectively. [74] In addition, ZnO having good physical, it is perfectly suited for applications as gas sensor for air pollution control, fire detection, leaks of harmful gases or tests for alcohol and other substances. ZnO having a high grain density and porosity, thus makes it possible to easily manufacture very sensitive gas sensors.

Various techniques can be used for the deposition of ZnO. The choice of a given technique will be drive by some practical criteria and of course, function of the targeted applications. Thus, TCO thin films must be prepared using appropriate deposition techniques that can produce low resistivity films at high deposition rates on large surface area substrates. Table I.8 summarizes some deposition techniques along with the resulting associated ZnO properties. In addition, for specialized ZnO thin film materials, it is necessary to use deposition techniques that can achieve the lowest resistivity. Table I.9 shows a number of deposition techniques that are usable for ZnO based thin film growth and their applications.

Table I. 8. Electric properties of ZnO for different deposition methods.

Deposition method	Temperature (°C)	ρ (Ω.cm)	n_V (cm^{-3})	μ ($cm^2.V^{-1}.s^{-1}$)	Ref
Spray	350	$2.70x10^3$	$2.4x10^{15}$	0.34	[75]
	450	$2.40x10^{-2}$	-	-	[76]
Sputtering	150	$1.00x10^3$	-	3	[76]
PLD*	400	3	$1.6x10^{17}$	12.3	[77]
ALD**	250	$5x10^{-2}$	$3x10^{19}$	5.5	[78]

***Pulsed Laser Deposition **Atomic Layer Deposition**

Table I. 9. Zinc oxide thin film growth methods and features.

Deposition method	Large area deposition	Applications
Magnetron sputtering deposition	Yes	LCDs, solar cells, touch panels
PLD	No	LEDs
Molecular beam deposition	No	LEDs
Spray pyrolysis	Yes	Solar cells
Chemical vapor deposition	Yes	Solar cells

2.2.2 Doping Zinc Oxide

As mentioned above, for applications in optoelectronic devices, especially photovoltaic cells, doping ZnO is mandatory. This is how the conductivity of zinc oxide can be increased, or even optimized for the intended application thanks to the existence of intrinsic defects (vacancies and presence of interstitial atoms) allowing the introduction of doping ions, not only on these defect sites but also possible by substitution of zinc or oxygen. The presence of such intrinsic defects leads to n-type conduction. To improve its properties as transparent conductive oxide, ZnO must be doped by group III elements (B, Al, Ga, In…) or group IV element (Pb, Sn). Aluminum, indium and fluorine are the most common doping elements for ZnO. [79] The use of different dopants leads to remarkable changes in the film properties.

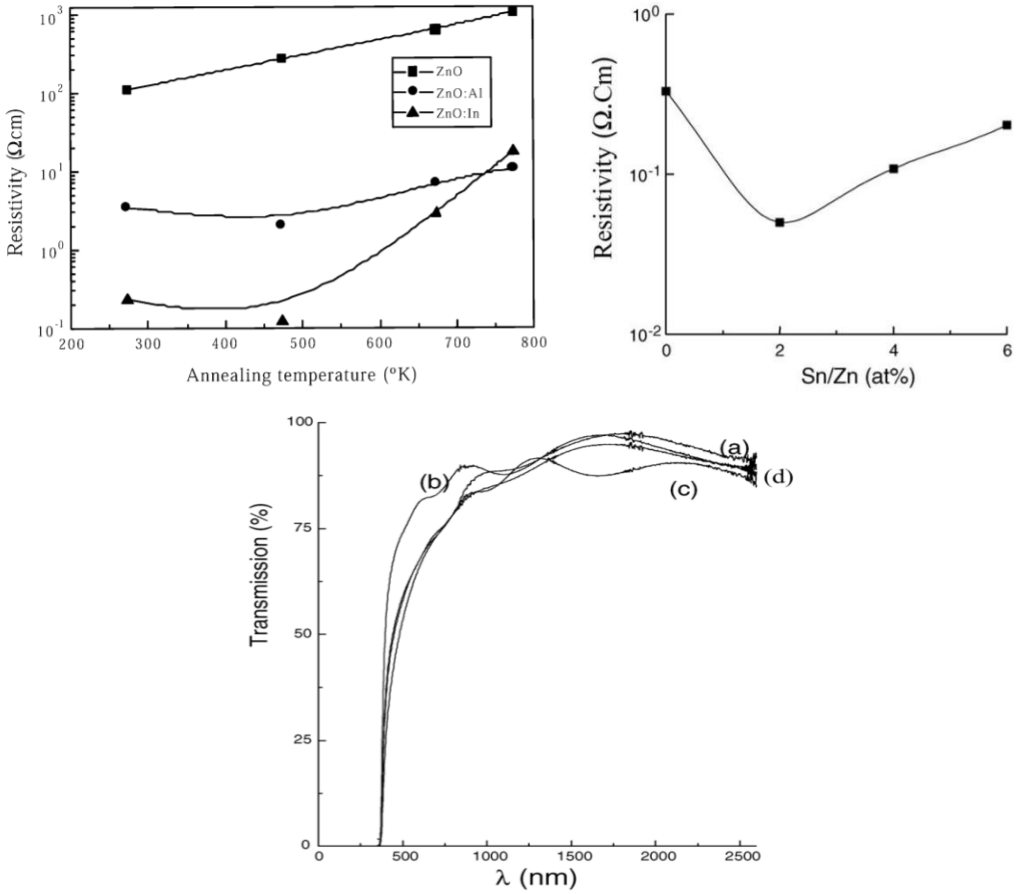

Figure I. 11. Resistivity variation of (a); doped and pure ZnO at different annealing temperatures. (b); ZnO:Sn at different concentrations. (c) Optical transmission of the ZnO:Sn as function Sn/Zn ratio: (a) 0 at.%, (b) 2 at.%, (c) 4 at.% and (d) 6 at.% [80 81]

Numerous studies have been carried out on properties of ZnO layers doped with different elements depending on the nature of dopant, its concentration and the deposition techniques. For several decades, these studies have made it possible to improve the structural, electrical and optical behavior of thin films. The works have been carried out mainly for ZnO dopants such as Al, Ga, In and Sn. As example of the change in the ZnO properties, we report in Figure I.11 (a) the dependence of the resistivity with the annealing temperature of pure, Al and In doped ZnO films grown by the spray pyrolysis technique.[80] We also report in Figure I.11 (b) the huge influence of the resistivity with the concentration of dopant (here with Sn ions) in the film allowing large possibilities of optimizations.[81] Within these two examples, it is obvious that doping ZnO hugely influence the electrical and optical properties, and additionally with a nonlinear dependence with the concentration of dopant. These studies have shown that the conductivity could be improved by adding Aluminum as dopant. Obviously, the optical properties are also modified by doping and growth techniques. It was also reported in Figure I.11 (c) that for these ZnO films, the transmission can vary between 70% and 95% observed for different concentrations of dopants thicknesses and deposition or annealing temperatures. [82]

Originally, for ZnO applications as gas sensors, aluminum and gallium were the most studied dopants. These two dopants remain the most used today even for other applications due to their abundance and its high electrical conductivity. [83,84] Moreover, the deposition method also influences the choice of dopant specifically when high doping concentration is expected. For example, in ZnO films doped with metallic ions, these dopants substitute preferably Zn sites. In this case, the growing of metallic doped ZnO based TCO by spray pyrolysis technique, give films having more efficient optical and electrical properties with indium and gallium than with aluminum. This can be explained by looking at the ionic radius of each element; the ionic radii of Ga and In are 0.62 Å and 0.80 Å respectively which is close to that of Zn being equal to 0.74 Å. Since the doping element replaces a Zn ion, the similarity in these values cause less lattice distortion at high concentration, when compared to the Al doping having 0.53 Å as ionic radius. Within this technique, the lowest resistivity of the doped ZnO film was obtained with In dopant at a concentration of 1 at%, but for a doping concentration above 2 at%, a weakening of the film properties occurs. [85]

2.2.2.1 Focus on Aluminum doped ZnO (AZO)

Despite the better performance of TCOs based on indium and gallium doped ZnO compared to aluminum doping, it is the latter which is the most studied and developed, thanks in particular to its abundance and its comparatively attractive cost. Aluminum doped ZnO (AZO), with its current and expected in a near future electrical and optical characteristics, is the potential candidate to replace the expending ITO and FTO in TCO applications.

Table I. 10. Comparative table of ITO and AZO properties required to be used as TCO.

Property	ITO	AZO
High conductivity	✓	-
High carrier mobility	✓	-
High transparency	✓	✓
Suitable refractive index	✓	✓
Ease of processing	✓	✓
High stability	-	✓
Low toxicity	-	✓
Low cost	-	✓

In the attempt to find a material having comparable properties to that of ITO, AZO appears to be a good candidate since it has a good balance regarding the last six properties listed in Table I.10. Whereas, AZO is not poor in completing the first two criteria, ITO has a good balance in fulfilling the first five but it fails with stability, toxicity and cost. [86] In this scope, many research works are carried on to sort out limitations of AZO considering different approaches to treat this material. Different approaches are adopted to overcome the limitations in AZO. Some researchers changed the doping concentration of Al in ZnO. [87] Others used different annealing temperatures,[88] or annealing duration,[89] and atmospheres.[90] While others focused on changing the substrate temperature and precursor concentration.[91] As already mentioned in the first part of this presentation, each of these parameters has a specific influence on the electrical and optical properties of the material.

It was reported in Figure I.12 that the incorporation of Al dopant enhances the transparency of the deposited film compared to the undoped ZnO. The transmittance observed to increase up to a certain concentration limit where it will slightly reduce due to

the increase in scattering and absorption photons by the crystal defects and free charge carriers. [92] Therefore, the upgrade in transmittance is attributed to the Al- induced crystal defects rather than the reduction of surface roughness. [93]

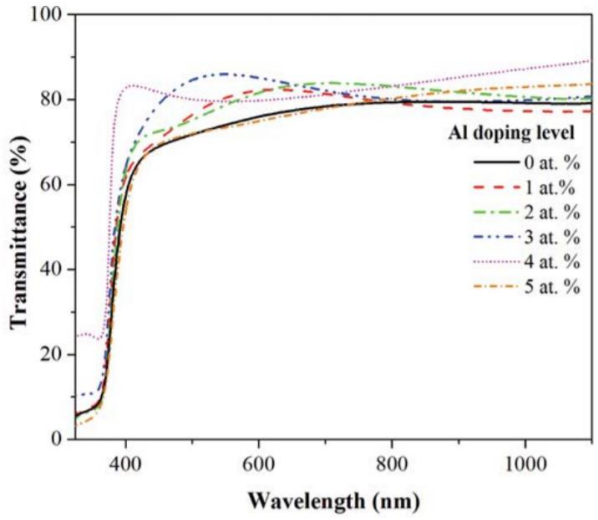

Figure I. 12. Transmittance of as deposited AZO thin films. [94]

Moreover, the choice of substrate also showed to have an influence on the optical properties of AZO films where glass and quartz substrates showed better optical transparency in the visible range. [95,96]

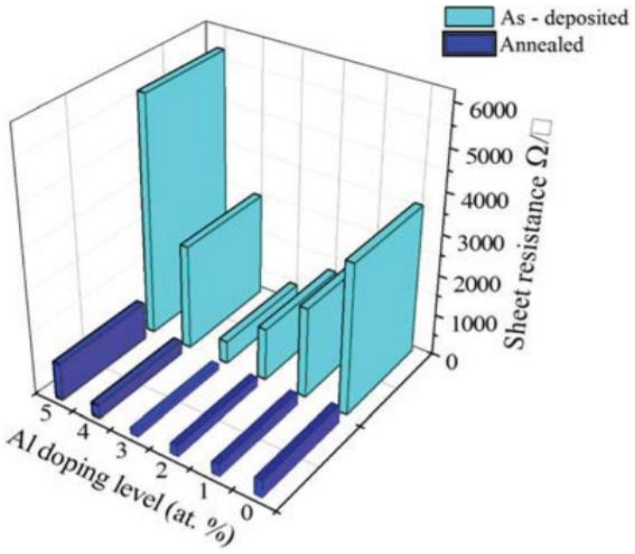

Figure I. 13. The variation of the sheet resistance of ZnO thin films as a function of Al doping level for as-deposited and annealed films.[94]

Besides the good transparency, conductivity is the second crucial property considered by researchers. Thus, they study the impact of different process parameters on the electrical properties of AZO films, as is shown in Figure I.13 the studied parameter is the heat treatment. Concerning the annealing process of AZO films, a decrease in the resistivity value to half of that of the as deposited films was observed.[97] An explanation of this phenomenon is given by some studies suggesting that annealing causes Al atoms to migrate from the grain boundaries to electrically active sites and this leads to an increase in the concentration of free carriers. Nonetheless a certain annealing temperature limit should be respected above which a reevaporation of the film occurs, inducing an increase in resistivity caused by the creation of zinc vacancies or antisite defects. [97]

2.3 Tin oxide (SnO_2) and Fluorine doped Tin Oxide (FTO)

2.3.1 General properties of Tin Oxide

There are two main forms of tin oxide: the stannic oxide (SnO_2) and the stannous oxide (SnO). The existence of these two oxides reflects the dual valence of tin, with oxidation states of 2+ and 4+. Stannous oxide is not as well characterized as the stannic form of the stannous oxide. Currently, the electronic band gap of the stannous oxide is not accurately known but lies somewhere in the range of 2.5 eV to 3 eV. Thus, SnO exhibits a smaller band gap than SnO_2, for which, the band gap is commonly quoted to be 3.6 eV. Also, there are no single crystals of stannous oxide available that would facilitate more detailed studies. Stannic oxide possesses the rutile structure and stannous oxide has the less common litharge structure (tetragonal crystal system). [98] Finally, stannic oxide is the more abundant form of tin oxide and is thus, by extension, commonly named tin oxide.

Tin oxide is a material having a big technological importance. Thus, SnO_2 have been studied for a wide range of applications such as rechargeable lithium batteries, storage of solar energy, and it is the one of technological significance in gas sensing applications and oxidation catalysts. This variety of applications depends on the morphology, phase, crystallinity, and size of the nanocrystals of the material. But in fact, dedicated to various applications, many geometrical structures and forms of tin oxide were produced like spherical particles, thin films, networks of ribbons and sheets.

In ambient conditions and atmospheric pressure, SnO_2 crystallizes in tetragonal rutile structure with space group P42/mnm (Table I.11), where the tin ions are at the center of the octahedral site formed by the oxygen ions as shown in Figure I.14.

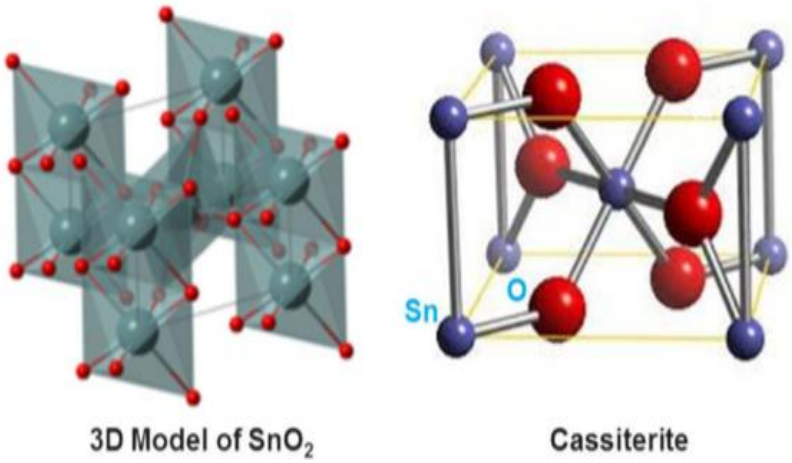

Figure I. 14.Crystal structure of SnO_2.[99]

Table I. 11. Tin oxide properties.

Property	**SnO_2**
Mineral name	Cassiterite
Crystal structure	Tetragonal, rutile
Space group	$P4_2mnm$
Lattice constant	a=0.474 c=0.319
Band gap [eV]	3.6
Common n-type dopants	Sb, F, Cl

Nanostructured SnO_{2-x} thin films are usually prepared by chemical vapor deposition and by reactive DC-magnetron sputtering techniques. As for other materials deposited in film shapes, its crystallographic phase will be conditioned by the substrate temperature during the growth process. Thus, for SnO_2 films growth by DC magnetron sputtering technique, the pure tetragonal phase at low temperatures (below 90°C) and a mixture of tetragonal and

orthorhombic phases at temperatures above was found. In this temperature range, the films present a wider band gap than that of a pure tetragonal phase. [100]

2.3.2 Doping of Tin Oxide

As for previous presented TCO, a great variety of dopants, mainly Al, In, Li was selected for tin oxide for the improvement or specialization of the SnO_2 layer properties optimized to specific applications. For TCO applications, the most commonly used dopants for tin oxide are Sb, Cl and F. In the case of Sb doping, antimony (+V) substitutes tin (+IV) ion. For high doping levels, the coexistence of Sb (+V) and Sb (+III) makes the later act as an acceptor by compensation of charge carriers liberated by Sb (+V). In addition, always for high doping levels, the ions mobility decreases attributed to formation of micelles, and, the thin film color changes to darker shades reducing the transparency and leading to a low Figure of Merit. [101]

Fluorine and chlorine doping share many similarities. Cl and F ions replace oxygen by releasing a charge carrier. The incorporation of these dopants also leads to the formation of uncharged micelles. Unlike Sb doping, the micelles do not carry an electrical charge, which does not cause disturbance of the tin network. In addition, films obtained by doping with chlorine or fluorine have better transparency compared to doping with antimony. Finally, fluorine doping offers an advantage over chlorine doping because of the close values of the ionic rays for fluorine (0.133 nm) and for oxygen (0.132 nm) while the ionic radius of chlorine is 0.181 nm. The consequence is that unlike the incorporation of Cl but also of Sb, the doping F can be incorporated into the tin oxide network without disturbance, thus making it possible to ensure better conductivity.

2.3.2.1 Focus on Fluorine doped SnO_2 (FTO)

Many deposition methods are adopted for the preparation of fluorine doped tin oxide such as chemical vapor deposition, [102] sputtering, [103] and most commonly spray pyrolysis [104] using tin chlorides as precursors. As expected, the fluorine doping concentration influences the properties of the film. Increasing the F-doping level leads to an increase in the Fermi energy until reaching the conduction band edge. Hence the optical band gap exceeds 4 eV and the transparency of the film in the ultraviolet (UV) range is improved.

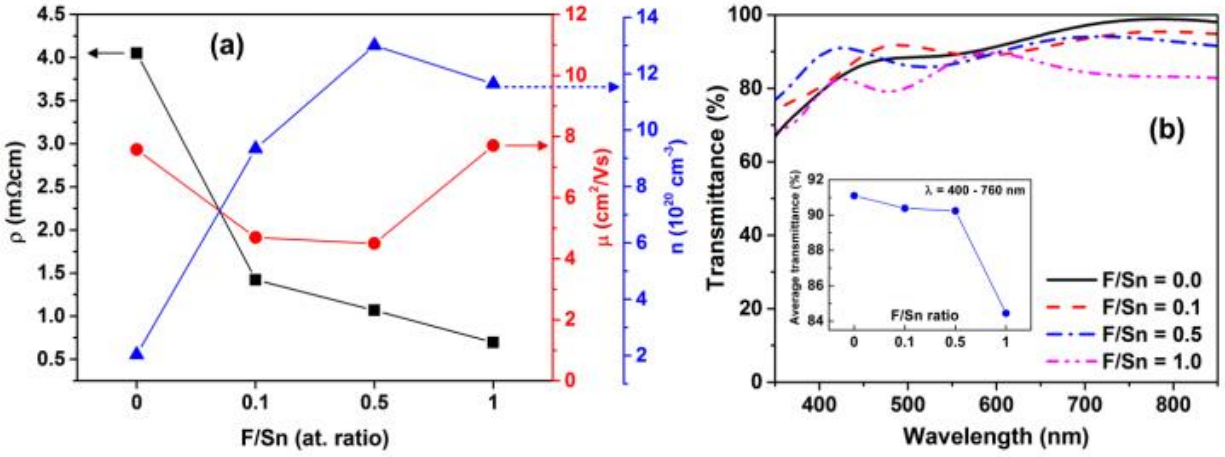

Figure I. 15.(a) F/Sn ratio-dependent resistivity, carrier concentration, and carrier mobility of FTO thin films. (b) Transmission spectra of FTO thin films for different F/Sn ratios. Inset in (b): average optical transmittance (%) of the films in the visible range. [105]

The effect of F/Sn atomic ratio on the structural, optical and nano-mechanical properties of FTO films grown by Ultrasonic Spray Pyrolysis on glass substrate was recently investigated by Tuyen L et al.. [105] The films showed tetragonal rutile structure of SnO2 with preferred orientation of (110) and an increased grain size with increasing F/Sn ratio. An important result of their study is the demonstration for the electrical and optical properties of FTO of a critical concentration of the fluorine dopant located approximately at a ratio F/Sn = 0.5. We present in Figure I.15 the results of their studies of FTO as a function of fluoride concentration. Below the critical concentration, a sharp increase in the concentration of free charge carriers is clearly observed, leading to a decrease in resistivity. However, beyond this critical concentration, there is a decrease in the concentration of charge carriers attributed to the fact that the excess fluorine no longer being able to replace the oxygen ions, it is expelled to segregate at the grain boundaries. Moreover, FTO films are acceptable have interesting transmittance (around 90% in the visible range) below the concentration threshold, whereas it appears to be reduced above the threshold (down to 80% for F/Sn=1). Authors explained this decrease by the scattering effect due to the increase of the surface roughness.

Since their discovery, Transparent Conductive Oxides were the subject of intense studies and researches in view of the diversity of materials, their important features and the

multitude of application fields mainly as detectors and as transparent electrodes in various optoelectronic devices and for photovoltaic cells and modules of new generation. Among these TCOs, Indium doped Tin Oxide (ITO), Zinc Oxide (ZnO) with its many dopants mainly aluminum (AZO) and tin oxide mainly fluorine doped (FTO), possess excellent transparency combined with high electrical conductivity. They are widely studied and were found to be the most suited for photovoltaic purposes. The continuous increasing need for energy resources have pushed research into the domain of materials for energy and particularly photovoltaic conversion. Currently, photovoltaic cells are mostly Silicon based. However, the price for a kilowatt from a solar origin source remains high when compared to fossil fuels prices which makes it a less competitive substitute. Hence, a reduction in the price of solar energy conditions the big scale development of renewable energies. In this instance, it becomes of priority for the research community to increase photovoltaic cells efficiency and hence decreasing the cost. Thereby, a 2nd generation of PV cells based on thin films of thickness less than 2 µm enables a significant fabrication price reduction by lowering the use of photoactive materials but also increasing the efficiency of photovoltaic conversion. [106]

3. Nanostructuration of TCO for photovoltaic cells

Throughout the years, new innovative concepts and ideas have been proposed in the photovoltaic conversion domain which led mainly to 3 different generations of solar cells according to the NREL classification. [107] The evolution of this domain can be seen on Figure I.16. [108] Nanostructures have been successfully employed in the manufacturing process of solar cells permitting an improvement of the conversion efficiency compared to a conventional solar cell using inexpensive materials with low cost production. So far, a wide range of nanomaterials including bulk nanostructured materials (3D), quantum wells, (2D) nanowires (1D) quantum dots/nanoparticles (0D), semiconducting oxides and nanocarbons, materials have been employed in buffer layers, interfacial modification layers, and photoactive layers. [109]

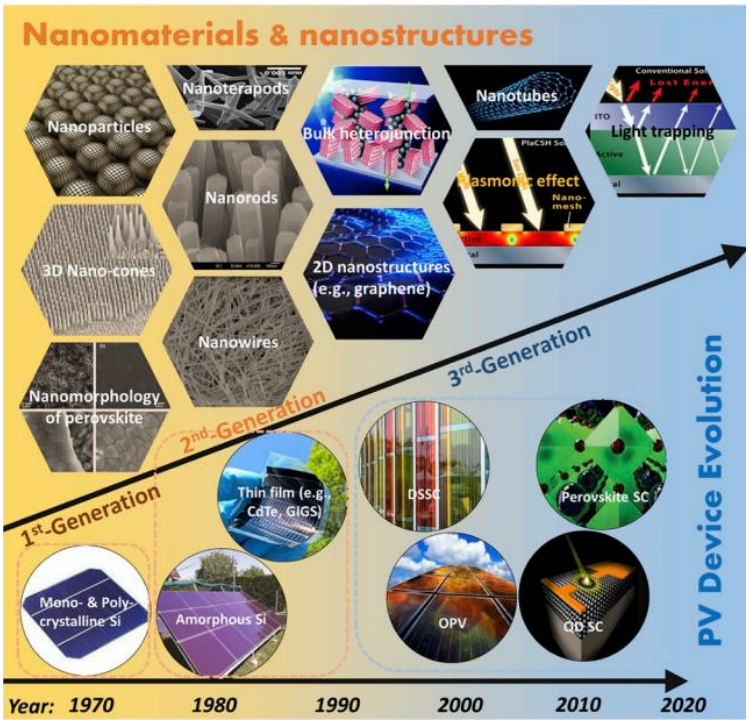

Figure I. 16. Timeline of the three PV generations along with multiple nanomaterials and nanostructures that have been successfully employed in the PV 3rd generation. [108]

An emerging concept in the field of science and technology is the study of nanomaterial. The numerous applications of nanoscale materials is the key to new technological and environmental challenges as solar energy conversion, energy storage and water treatment. TiO_2, MnO_2, NiO, ZnO and SnO_2 are semiconducting nanomaterials that attracted much attention due to their applications in electronics, optoelectronics, photovoltaics, photocatalysis and many more.

3.1 Various types of nanocomposites for TCO

3.1.1 Nanoparticles

The importance of nanoparticles relies in the big domain where they can be used as applications. Nanoparticles can be found anywhere around us, as they have a wide range of applications such as drugs and medications, manufacturing and materials, they are also found in electronics, energy harvesting systems, mechanical industries and also environmental applications.

They are now being used in the manufacture of scratchproof eyeglasses, crack-resistant paints, anti-graffiti coatings for walls, transparent sunscreens, stain-repellent fabrics, self-cleaning windows and ceramic coatings for solar cells.

Generally, two routes are adopted for the synthesis of metal oxide nanoparticles. Both routes are shown in the schematic of Figure I.17 and their classification is as follows: chemical methods such as hydrothermal synthesis, chemical vapor deposition, sol-gel process, co-precipitation method, etc. and physical methods like mechanical milling, electron beam evaporation, sputtering, laser ablation and electrospraying. In the chemical synthesis approach, the formation of nanoparticles distribution of different size occurs by the assembly of atoms or molecules while for the physical approach, synthesis starts from the bulk counterpart of a material which gets depleted systematically generating fine nanoparticles. Among the mentioned synthesis methods, chemical approach and specifically sol-gel technique is the most commonly used technique. The main bonus of the chemical synthesis technique is that nanoparticles of controlled size, dimension, composition and structure can be produced. The ability of obtaining such defined properties is very useful for many applications in electronic devices as well as catalysis and sensing. Moreover, the sol gel technique uses less energy for carrying out the synthesis and low processing temperature which makes it more economical technique compared to physical methods.[110]

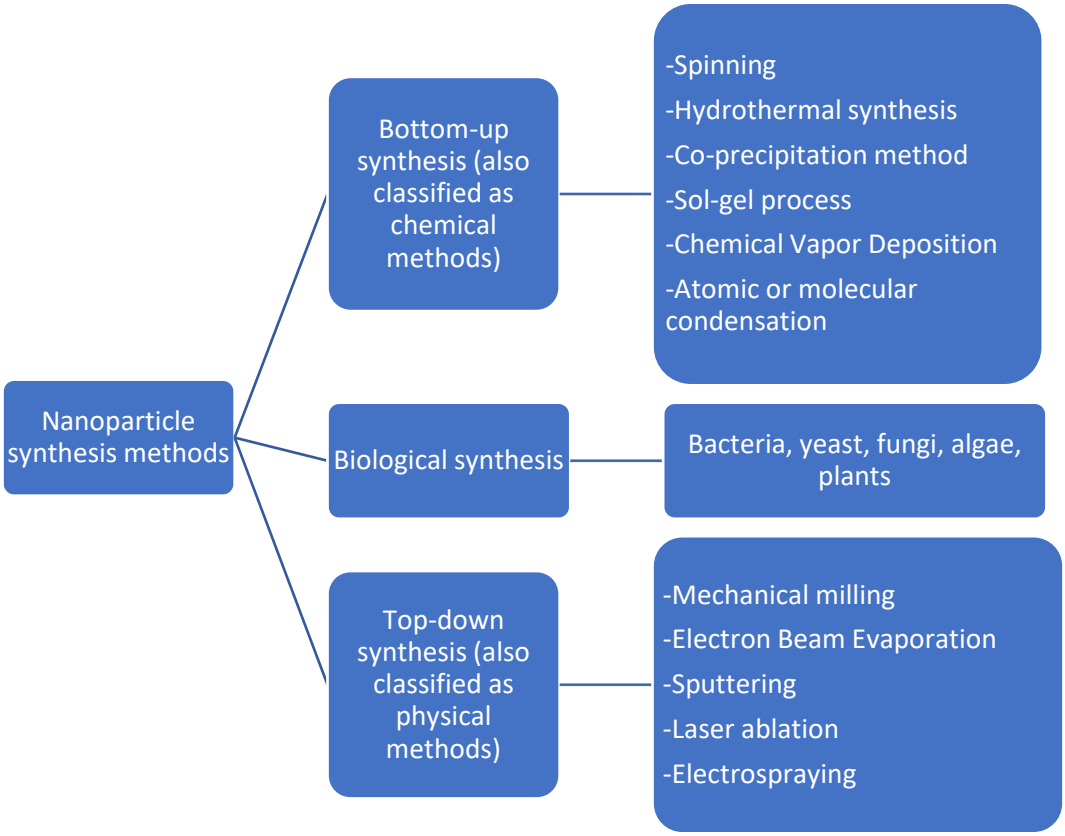

Figure I. 17. Scheme showing the bottom-up and top-down methods of nanoparticle synthesis. [111]

3.1.2 Nanowires and nanorods

Nanowires, tubes, rods and belts are one dimensional nanostructures with dimensions from 1 to 100 nm. By definition, a nanowire, as the name suggest it, is a solid material in the form a wire having a diameter less than 100 nm. Whereas, a nanotube is a hollow nanowire with a wall thickness of the order of molecular dimensions up to the thickness of a 2D single sheet of graphene type.

The growth along one direction of nanostructures is based on the synthesis by promoting the crystallization of solid state structures in this chosen direction. Thus, two types of one dimensional structure can be formed: longitudinal and coaxial structures. Longitudinal refers to nanowires composed of different stoichiometries along the length of the nanowire, while coaxial structure refers nanowire material having different core shell compositions.

Vapor phase synthesis is a method for nanowire growth where gas species are the starting reactants to form wires. Many techniques were used to prepare precursors into the gas

phase for thin film growth including; laser ablation, chemical vapor deposition molecular beam epitaxy and sputtering. The concentration of gaseous reactants is an important parameter to be regulated for the nanowire synthesis to predominate and suppress secondary nucleation phenomena. Vapor-liquid-solid (VLS), mechanism is a vapor based technique considered to be the most successful in generating large quantities of single crystalline structured nanowires. The process begins by the dissolution of gas reactants into nanosized liquid droplets of a catalyst metal, then the nucleation and crystalline growth of rods starts to happen to finally form a nanowire as presented in Figure I.18. VLS is the mostly used for the synthesis of nanowires. [112] Since it uses a gaseous precursor reactant to synthesize nanowires, it is easier to organize and manipulate the nanostructures to obtain crystalline and defect free nanowires.

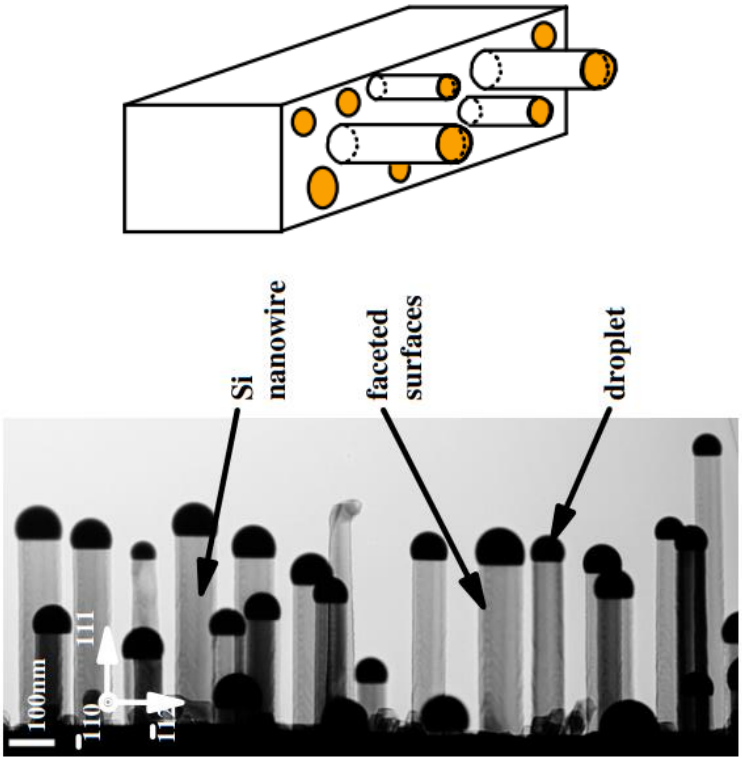

Figure I. 18. (a) Scheme showing the nanowire growth from Au droplets. (b) TEM image showing Si nanowires in growth process. [113]

Nanowires (specifically ZnO nanowires) could be synthesized by a variety of methods, which are classified into two big categories: vapor phase synthesis and solution phase synthesis. Details on each category are found in the chart of Figure I.19. [114]

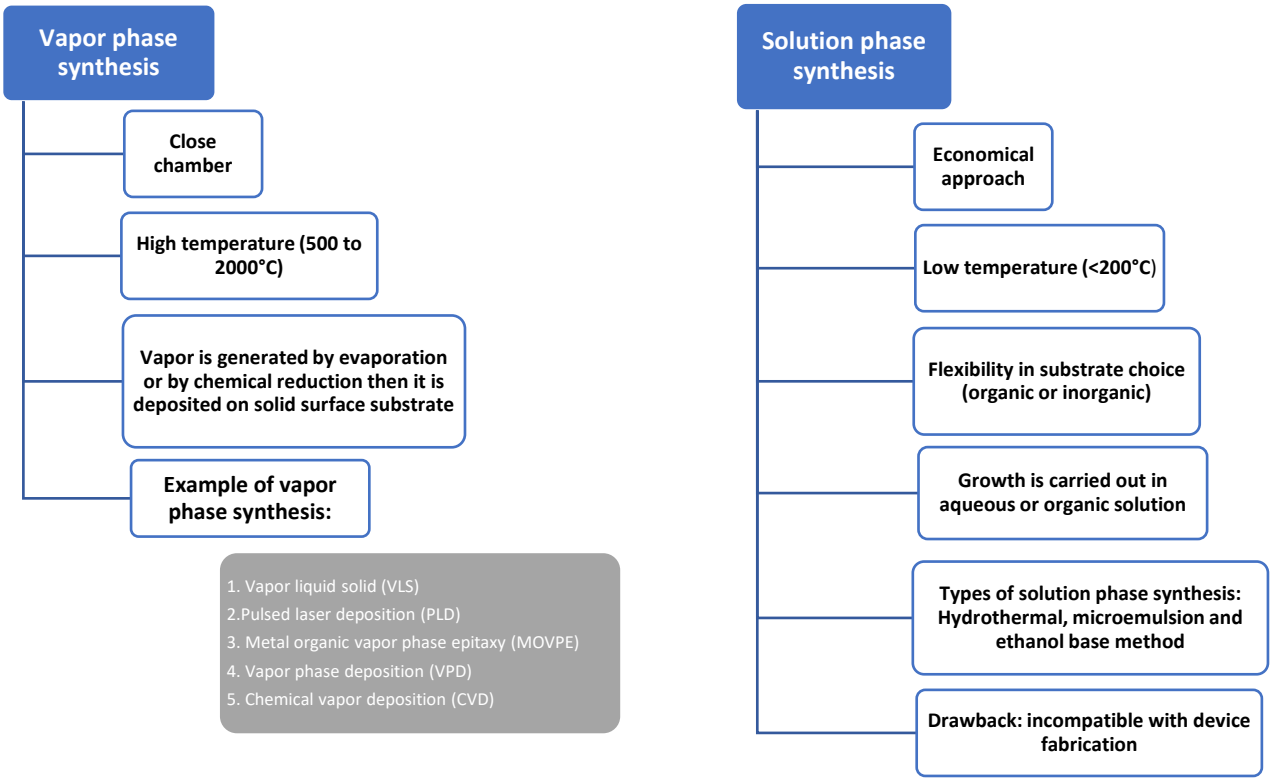

Figure I. 19. Classification of nanowires synthesis methods.

3.1.3 Nanofibers

Nanofibers are very long filaments in cylindrical shape having a diameter in the order of some hundreds of nanometers. The only way to make nanofibers (to our knowledge) is electrospinning. It consists of producing fibers by charging and ejecting a polymer melt or solution through a spinneret under a high-voltage electric field which results in the solidification and formation of the filament. Nanofibers are famous for their high porosity, flexibility, high surface area and controllable morphology. In fact, their high surface area to volume ratio makes them very interesting for applications where large surface area is necessary. [115] Moreover, they are stable in terms of macroscopic properties; for instance, nanoparticles tend to agglomerate in aqueous medium which will alter their properties. [116]

Another difference between nanoparticles and nanofibers is in terms of aspect ratio, and with nanotubes in crystallographic properties.

In this paragraph we only presented the nanofibers in a general and broad approach, more details along with convenient examples specifically related to our topic will be presented in the following section. Also, a specific section will be dedicated to the electrospinning process in the third chapter.

3.2 ZnO and AZO nanofibers

Electrospinning allows for the creation of long nanofibers with diameters ranging generally from 10 to 100 nm from a variety of materials. Because of its high surface-to-volume ratio, nanofibers produced by electrospinning mats could be used in a variety of applications where a significant contact area with the environment is required, [117] such as filter materials, wound dressings, tissue engineering, and other cell growth applications. [118–120]

Besides polymeric fibers created from the electrospinning of polymer solution or melts, blends of polymers and other materials can also be prepared by this technique. [121,122] For instance, nanofibers with semiconducting or metallic nanoparticles could be added to a chemical solution to permit complete mixing of all the components. Hence, pure ceramic or non-polymeric nanofibers are obtained after calcination. By such techniques, the applications can be extended as compared to pure nanofiber mats.

High attentiveness is growing for zinc oxide nanofibers since the material is useful for gas sensing applications, microwave absorption, supercapacitor electrode, photocatalytic degradation and also for light emitting electrochemical cells. [123–127]

Among all kinds of nanofibers and as concerned by this work, ZnO nanofibers grown by electrospinning from a melt of zinc acetate in PVA show the possibility to be used as electron transport layers in organic photovoltaic devices. F. Mohtaram et al. [128] studied the effect of annealing and electrospinning time on electrospun ZnO nanofibers. They showed that annealing time reduces the nanofibers diameter as presented in Figure I.20 as a result of the PVA decomposition in the as-grown fibers. Different characterization techniques (SEM, AFM,

XRD) showed that pure ZnO nanofibers obtained from the electrospinning process after annealing are well crystallized. Moreover, layer thickness and fibers concentration on the electrode surface was dependent from the electrospinning time.

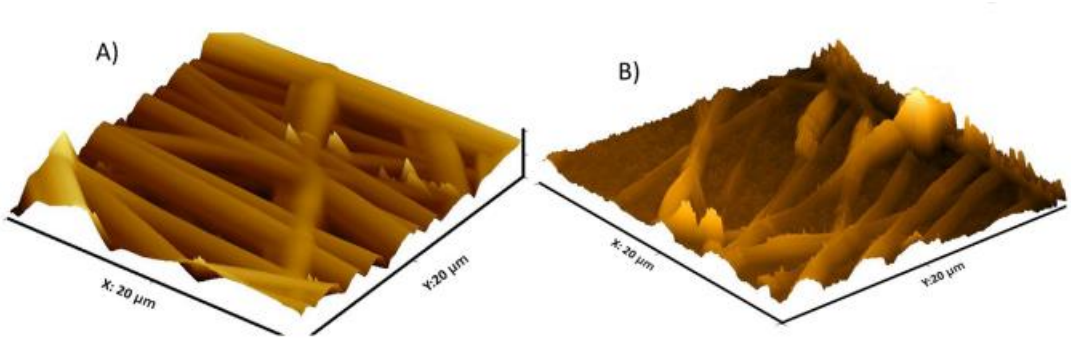

Figure I. 20. 3D AFM images of the ZnO nanofiber layer before (A) and after annealing (B) for 3h at 500°C.

3.2.1 Morphological properties of ZnO and AZO nanofibers

ZnO and AZO nanofibers prepared by electrospinning showed to have morphology properties depending on the concentration of precursors or some processing parameters. Generally, beadless and smooth nanofibers are obtained regardless of the precursor concentration (Zn or Al doping concentration generally under their acetate form). However, the precursor content showed to have an effect on the diameter of as spun fibers (before annealing) where it was found to increase of about 50 to 100 nm if more Zn precursor content was added to the starting solution. Moreover, the increase of Zn precursor in the starting solution increases the viscosity of the solution leading to a non-uniform ejection of the jet making the diameters distribution broader. Moreover, the authors [129] have shown that this dependence of the diameter with zinc concentration in the initial melt is linear as reported in Figure I.21. This variation could be described by the following linear equation $AFD= mx + D0$, where $D0$ is the average fiber diameter of pristine PVA, x the zinc acetate concentration in wt.% and m a constant proportionality coefficient. [129,130]

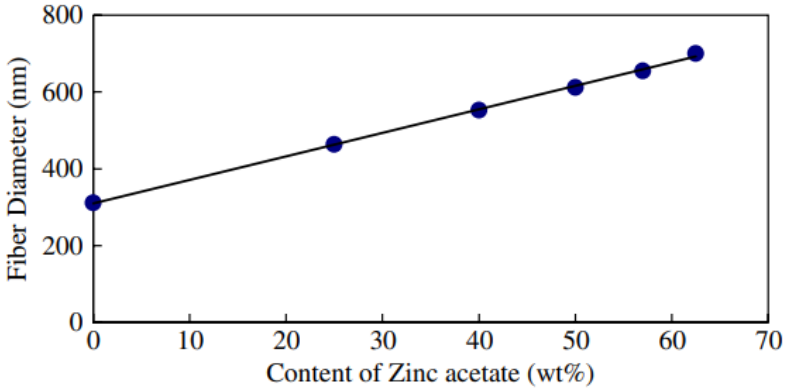

Figure I. 21. Average fiber diameter–zinc acetate ratio curves of the zinc acetate/polyvinyl alcohol precursor fibers. [129]

At a starting point of the electrospinning process, spun nanofibers contain not only zinc and aluminum elements but also a lot of organic compounds coming from the polymer used in the solution, and acetate or chloride precursors as zinc acetate, and aluminum acetate/chloride. For this reason, calcination is an essential step to decompose all the organic material and to end up with well crystallized zinc oxide or aluminum doped zinc oxide. The annealing process usually takes place in air with a range of temperature starting from 400°C to 800°C. AFM images of samples annealed at increasing temperature, presented in Figure I.22, show a decrease in the diameter size with increasing temperature. Moreover, the reduction in fibers diameter with temperature with some remaining traces of burnt organics was visible in SEM images of Figure I.23. The shrinkage of the diameter above 500°C was attributed to the shrinkage of ZnO by sintering while the smaller diameter below 500°C is attributed to the decomposition of organic compounds.

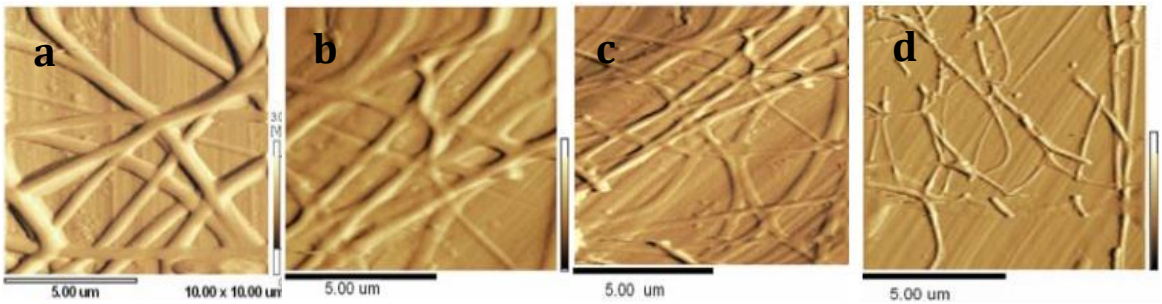

Figure I. 22. AFM images of: (a) PVA/zinc acetate composite fibers of size 400-500nm; (b) ZnO fiber of size 200-300 nm calcinated at 400°C and (c) 600°C; (d) ZnO fiber of size 100-200 nm calcinated at 800°C.[131]

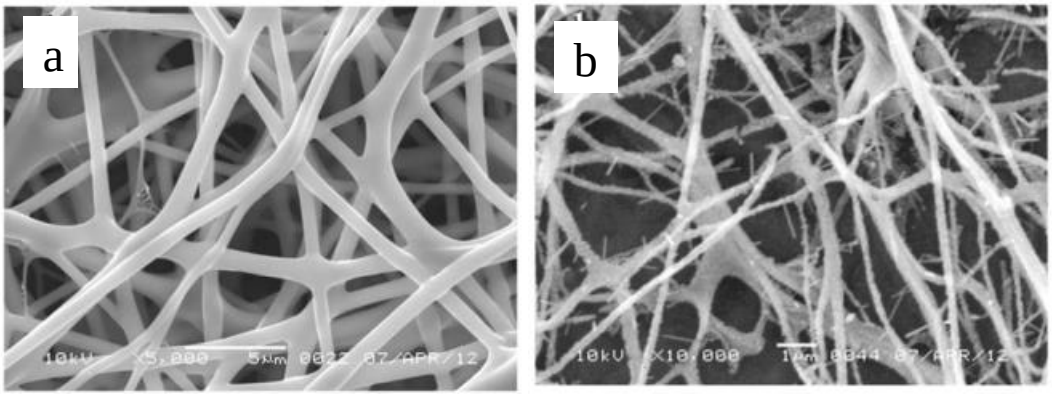

Figure I. 23. SEM images of 5 wt.% zinc acetate/PVA nanofibers (a)before and (b) after calcination.[132]

Electrospun nanofibers have a limited applicability in electrical devices due to their weak adherence to conductive substrates. To help with this, a seed layer (SD) is deposited on the FTO substrate before the electrospun composite nanofibers are deposited. This improves the interfacial adherence of the AZO nanofiber films to the FTO substrate and promotes the release of interfacial tensile stress during calcination. Sining Yun et al. [133] deposited AZO nanofibers used as photoelectrodes for DSSC. The introduction of a seed layer between the conducting substrate and the spun fibers helped in better adhesion of the fibers on the substrate as well as showing an improved energy conversion efficiency.

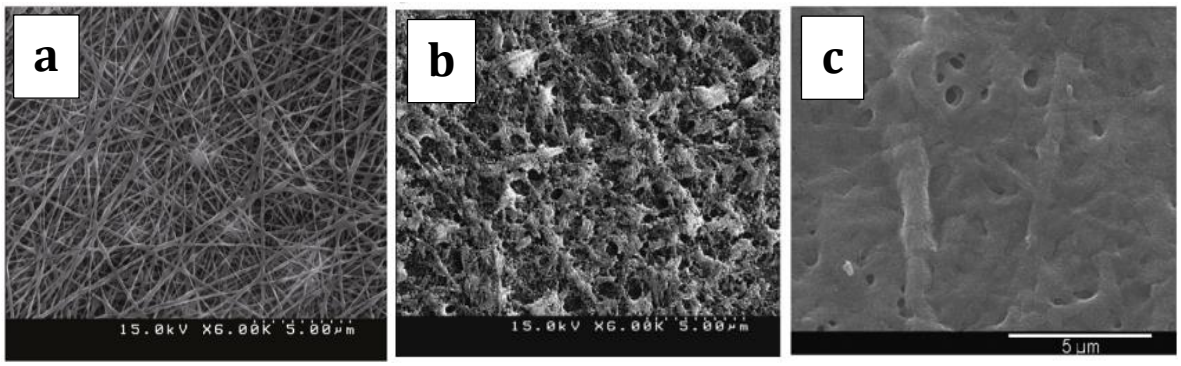

Figure I. 24. (a)FESEM images of as spun AZO PVAc composite nanofibers (b)cracked and peeled off AZO nanofibers after calcination. (c) AZO nanofibers after calcination deposited on seed layer treated substrate. [133]

Smooth and uniform nanofibers with diameter 58 to 106 nm before calcination as seen in Figure I.24. The morphology of the fibers changed after calcination to become as linked crystallite particulate form which is explained by the decomposition of residual organics and crystallization during the calcination process. Moreover, the calcination process generates

strong stress leading to the shrinkage and roughness of the AZO fibers film changing the properties of the nanofibers in addition to causing the cracking and peeling of the fibers from the substrate as explained by the same study.

3.2.2 Structural and Thermal properties of ZnO and AZO nanofibers

The solutions used for the electrospinning of nanofibers contain polymer and organic materials in order to increase the viscosity and act as a holding matrix for the main precursor. Once the fibers are formed and deposited on the substrate, the role of the polymer is over. Thus, the as spun nanofibers undergo heat treatment to crystallize the material and get rid of all organic compounds.

Comparing the weight loss of Zinc Acetate and polyvinyl alcohol nanofibers in a range of temperature from 0 °C to 600 °C, presented in Figure I.25, Imran et al. [132] noted that 63% of weight loss occurred until 324 °C and the second degradation until 595 °C with a weight loss of 21% for the PVA nanofibers. Whereas, for the zinc acetate/PVA nanofibers four stages of degradation were recorded. The first weight loss occurred until 71°C with a degradation of 5% corresponds to water evaporation and the final until 480°C. The intermediate weight loss of 68% was attributed to the decomposition of organic components of the zinc acetate and PVA polymer. And finally, a stability in the weight loss beyond 480°C suggests the presence of only pure inorganic material.

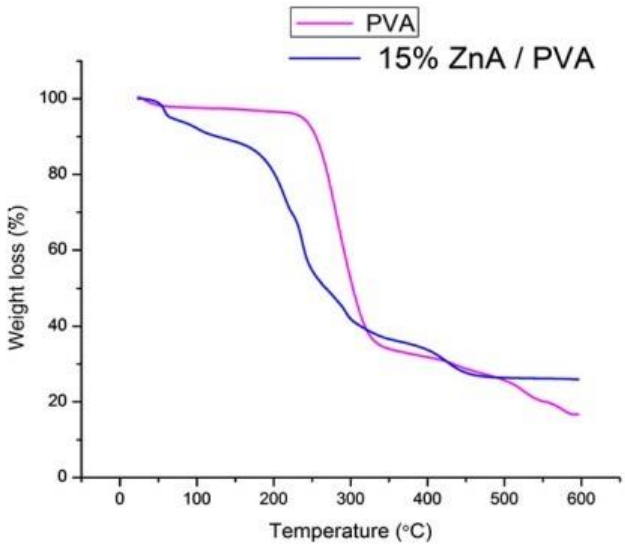

Figure I. 25. Thermogravimetric analysis for PVA and 15 wt.% zinc acetate/PVA nanofibers.

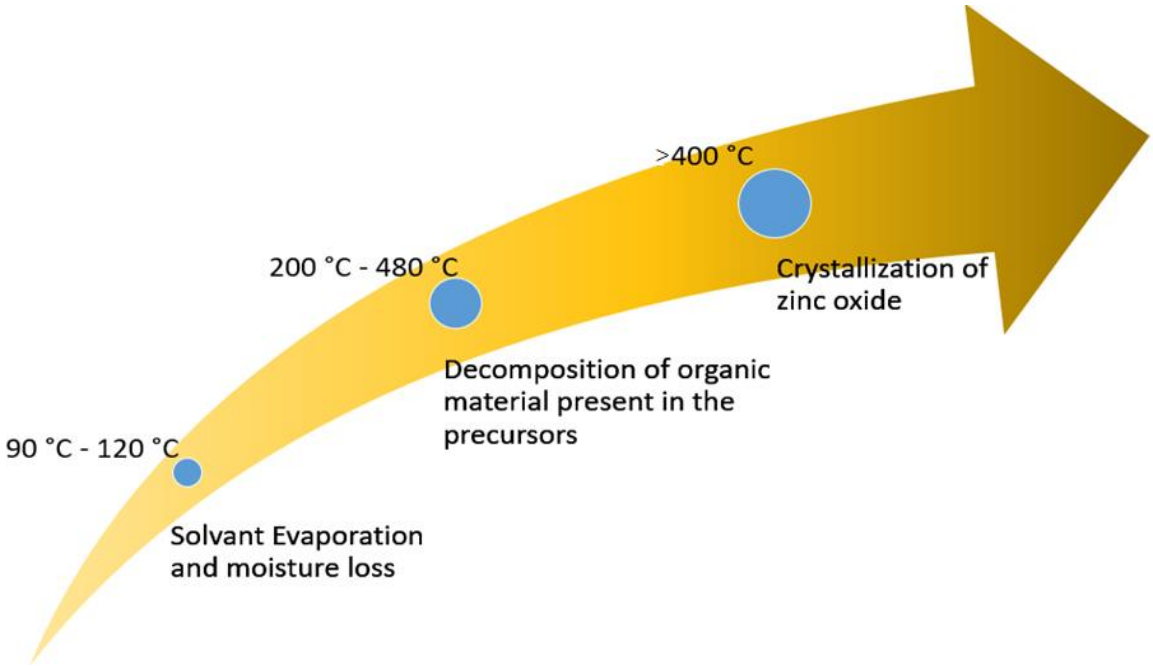

Figure I. 26. Scheme showing the different stages of degradation (for PVA, PVA-Zn nanofibers) with increasing temperature.

Generally, different temperatures for calcination of nanofibers were used ranging from 300°C to 900°C. [134–137] In fact, along with the increasing temperature, the degradation stages of the fibers is observed and could be classified in three categories: solvant evaporation and moisture loss, decomposition of organic material found in the precursors used for electrospinning solution preparation and finally the crystallization phase. [129,131,132,138–140] A summarization of the different stages of degradation and corresponding temperatures recorded by many research groups who worked on zinc oxide nanofibers by electrospinning are shown in Figure I.26.

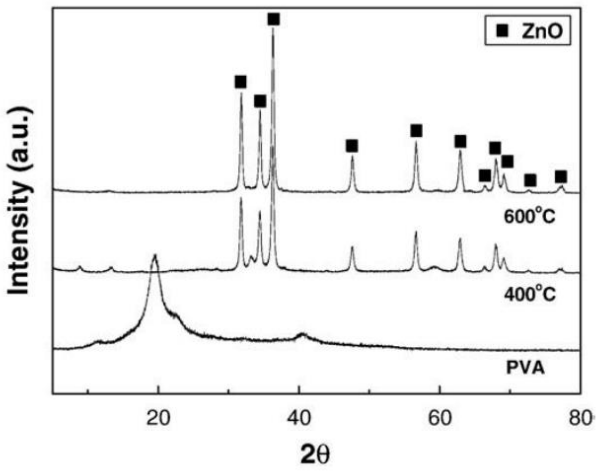

Figure I. 27. XRD patterns for dried PVA for 24 hours at 80 °C; and annealed (1at.%) AZO gels for 2 hours. [140]

Structural characterizations carried by XRD and FTIR for the fibers before and after calcination at different temperatures, showed a difference in the recorded spectrum in terms of the materials characteristic peaks. In fact, no distinct peaks were observed before for the samples before the calcination process since the material is amorphous. However, after heat treatment, the specific pattern with intense peaks of the zinc oxide wurtzite structure was detected. Even for the Al doped zinc oxide nanofibers, the wurtzite structure was detected after calcination proving that the Al was incorporated homogeneously in the ZnO matrix as seen on the XRD graphs of Figure I.27. Moreover, FTIR analysis for ZnO nanofibers showed the disappearance of the peaks assigned to H_2O, CH and OH organic groups after calcination. These results complete what was discussed previously and is an evidence that the calcination process is an essential tool to crystallize the nanofibers and to remove all the organic groups coming from the precursors being used in the fabrication process.

3.2.3 Optical and electrical properties of ZnO and AZO nanofibers

ZnO is perhaps the most structurally and physically diverse of all metal oxides. As a result, researchers have looked at the optical characteristics of ZnO NPs embedded in polymers including PVA and PVP.

Authors investigated the effect of Zinc precursor concentration on the optical properties of electrospun nanofibers. Figure I.28 demonstrate the UV–Vis transmittance, absorbance and reflectance spectra of ZnO/PVP nanocomposite fibers, respectively. The ZnO/PVP nanocomposite fibers' transmittance spectra reveal a pronounced absorption edge in the wavelength range 300–420 nm. The produced fibers' transmittance spectra show two distinct effects: a change in average transmittance in the visible range, and a variation in the beginning of transmittance with wavelength that switches to longer wavelengths as the molar ratio increases. This indicates that the absorption edge varies with the amount of ZnO NPs present.

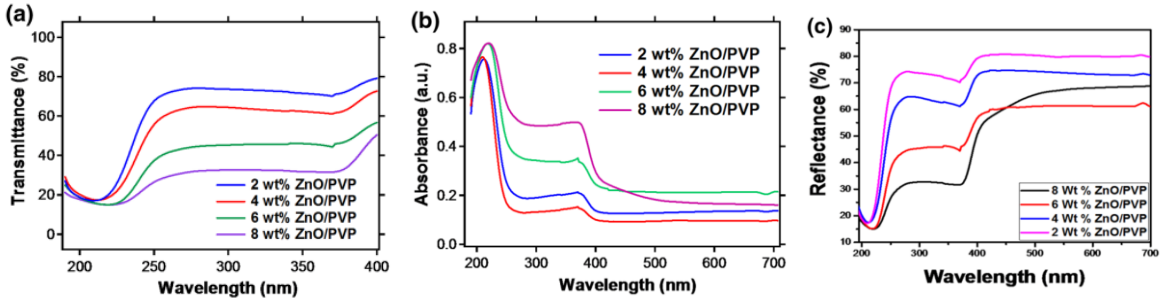

Figure I. 28. UV–Vis spectra of the prepared ZnO/PVP nanocomposite fibers: (a) transmittance; (b) absorbance (c) reflectance.[141]

I–V measurements were used to evaluate the electrical properties of the AZO nanofibers. The electrical contacts were difficult to attach because the ceramic fibers were fragile. The AZO nanofibers were ground into powder and formed into disks for these tests. Due to the geometry of the disk structure, measured conductivity may differ from that of actual fiber mats. Electrical current may preferentially follow the fiber axis in fiber form. The fiber mat structure is random, and grinding may or may not have a major influence, but more interest is given to the magnitude change in conductivity relative to the doping concentration.

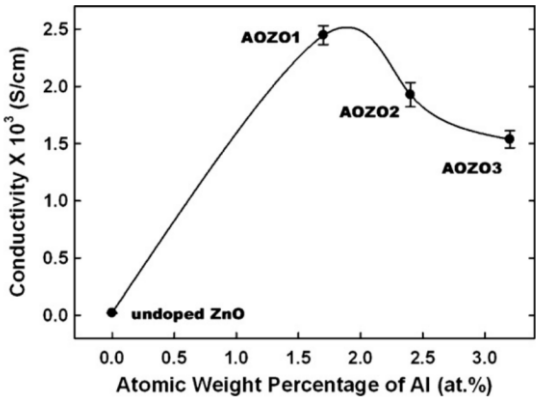

Figure I. 29. Electrical conductivities of undoped and aluminum oxide doped zinc oxide (AOZO) nanofibers (calcined at 600°C for 5 h).[142]

At room temperature, the conductivity of the nanofiber samples dropped as the aluminum content increased above 2 at% as seen on the graph of Figure I.29. This propensity can be interpreted in the following way, based on the inclusion of Al atoms into the ZnO lattice during the crystal formation process. More Al atoms can occupy Zn sites as the Al concentration in the solution rises, and an electron is contributed for every Al atom, raising the carrier concentration. Furthermore, aluminum concentration in ZnO has a solid solubility limit of roughly 2%. As a result, one potential explanation is that at higher aluminum concentrations (AOZO2 and AOZO3), segregation of aluminum compounds, most likely as aluminum oxide, occurs in the grain boundaries of AOZO materials, acting as carrier traps and contributing to the drop in conductivity. Percolation is a second probable mechanism. The increase in metallic Al could create additional conduction pathways by percolation.

It is to be noted that not a big number of researches considered the optical and electrical properties of the Aluminum doped Zinc Oxide nanofibers, rather they focused on the morphological properties as fibers diameter and structural properties as crystallization. However, further in the coming chapters, optical and electrical properties investigations will be considered for the elaborated nanofibers in addition to structural and morphology analysis.

4. Conclusions

This chapter is composed of two parts. The first part, dedicated to general statements about transparent conductive oxides, with a specific focus on TCO families integrating photovoltaic cells and modules. Among these TCOs, Indium doped Tin Oxide (ITO), Zinc Oxide (ZnO) with its many dopants mainly aluminum (AZO) and tin oxide mainly fluorine doped (FTO), possess excellent transparency combined with high electrical conductivity. They are widely studied and were found to be the most suited for photovoltaic purposes. The second part treats the aspect of nanostructures used in the layers of PV modules with an emphasis on the ZnO nanofibers where they showed promising results regarding their use as transparent electrodes in PV modules. After a general presentation of structural, electrical and optical properties of TCO layer applied in photovoltaic cells and modules, the second chapter will be devoted to the elaboration of Zinc oxide and Fluorine doped tin oxide by two deposition methods with further morphological and structural investigation.

Chapter II: Elaboration and characterization of ZnO and FTO thin films

After the presentation of TCO more specifically three oxide materials used for photovoltaic devices in the form of thin films and nanocomposites, this chapter will provide a detailed morphological for FTO and ZnO thin films and structural investigation of FTO thin films deposited on glass substrate by spray pyrolysis and magnetron sputtering.

This first study is considered as a building block (step) in this work since it enables us to establish reference results without any nanostructuration, coming in the next chapters, for the materials that will be used along this work.

The process, i.e. spray pyrolysis used for the deposition and the material, i.e. ZnO are already well-known and numerous reports can be found in literature associating this process with this material for layer deposition. The originality of the contribution achieved during the thesis and presented in the following chapter is the link established between the position of the substrate during the deposition process and the structural properties of the deposited layer.

The morphological characterization was carried out by atomic force microscopy and Raman spectroscopy was used for the determination of structural properties of FTO thin films.

1. Elaboration and characterization of Zinc Oxide thin film by Magnetron Sputtering

1.1 Experimental procedure

Sputtering is one of the most commonly used plasma process techniques for the deposition of thin films. An ionized species (argon) forms a plasma in a chamber which undergoes a secondary vacuum. The substrate and the material to be deposited are respectively connected to the mass and to an anode in the chamber. The Ar^+ ions go towards the material (which is therefore negatively charged) and extract atoms. These atoms go towards the substrate which is positioned just above the target. Figure II.1 represents the schematic diagram of the sputtering process. The particularity of this technique relies in the form of supplied energy, since it is provided by the ionized argon in the form of plasma and not by heating in thermal form. [143]

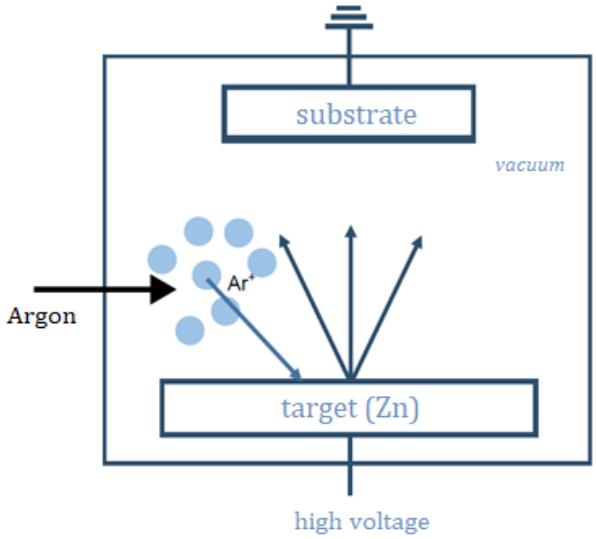

Figure II. 1. Schematic diagram of sputtering.

A thin film of Zinc Oxide was deposited by magnetron sputtering at Institut Jean Lamour (IJL) of the Université de Lorraine in Nancy under the supervision of Mr. Davis Horwat from the Department of Chemistry and Physics of Solids and Surfaces. The process took place at room temperature with the deposition parameters mentioned in Table II.1. Morphology of

the deposited thin film was investigated by Atomic Force Microscopy (AFM). Surface scanning was made along the different sections of the sample.

Table II. 1. Deposition parameters used for the growth of ZnO thin film by sputtering.

Deposition parameters			
Substrate	Glass	Power	100 W
Deposition time	40 min	Voltage	330 kV
Temperature	Room temperature	Oxygen volume flow rate	6 sccm
Target-substrate distance	5cm	Argon volume flow rate	50 sccm
Initial pressure	1.12×10^{-4} mbar	Current pressure	42×10^{-4} mbar

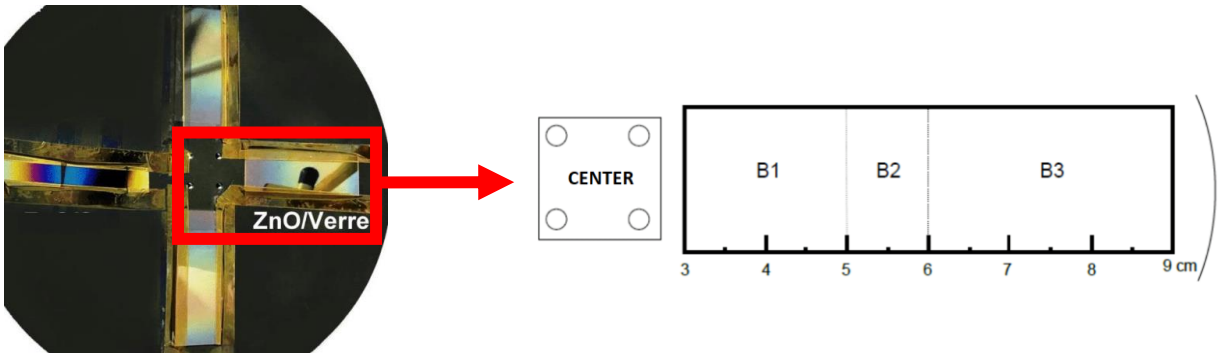

Figure II. 2. Photo and scheme of the sputtering position of ZnO substrate.

The target glass slide was divided into three sections called B1, B2 and B3 as shown in Figure II.2. These areas are delimited by their distance from the center of the substrate holder with zone B1 from 3 cm to 5 cm, zone B2 from 5 cm to 6 cm and zone B3 from 6 cm to 9 cm.

1.2 Surface imaging by Atomic Force Microscopy

1.2.1 History and evolution

Gerd Binning and Heinrich Rohrer won the Nobel Prize in Physics (1986) after creating the Scanning Tunneling Microscope (STM) and discovering its ability to image individual surface atoms. [144] After the success of the STM other Scanning Probe Microscopes

were invented, all of them rely on the mechanical scanning of a sharp tip over a samples' surface. [145]

Whatever the type of the force, all force microscopes have five essential components:

- A sharp tip mounted on a soft cantilever spring
- A way of sensing the cantilever's deflection
- A feedback system to monitor and control the deflection (and, hence, the interaction force)
- A mechanical scanning system (usually piezoelectric) that moves the sample with respect to the tip in a raster pattern
- A display system that converts the measured data into an image.

While scanning in contact mode, the tip is in contact with the sample. Being similar to a stylus profilometer, it measures the topography of surface atoms with an atomic imaging resolution. The concept of applying a force to a surface for the purpose of imaging may seem unreasonable specially when considering the macroscopic size of AFM tips. Actually, the high resolution achieved by AFM is due to a very small loading force on the tip (10^{-7} to 10^{-11} N) making the contact area between the tip and the sample extremely small. [145]

1.2.2 Operating principle

Atomic force microscopes (AFMs) are a type of microscope that provides pictures of surface atoms. AFM can resolve features as small as an atomic lattice, for either conductive or non-conductive samples. Like the Scanning Electron Microscope (SEM), the purpose of the AFM is to look at objects on the atomic level.

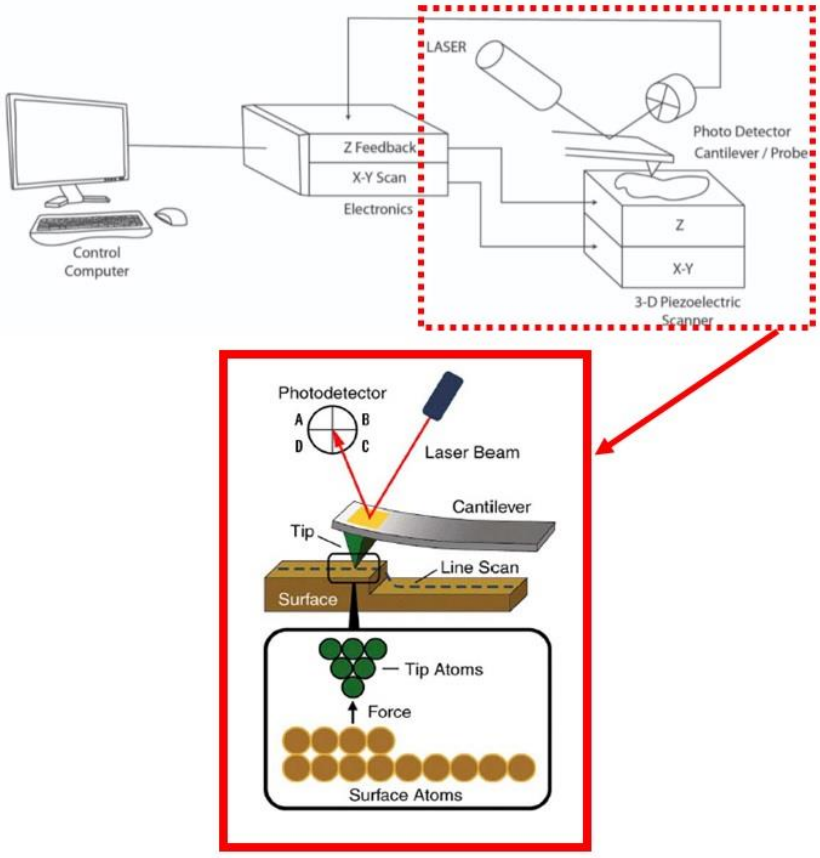

Figure II. 3. Schematic illustration of the main components of an AFM. [146]

In addition to the higher resolution that AFM can provide comparing to SEM, it gives three-dimensional information, with little sample preparation. The technique makes it possible to image in fluid, under controlled temperature and in other controlled environments. The AFM does not need to operate in a vacuum, so it can be used to see surfaces of biological samples like living cells.

In AFM, as shown in Figure II.3, a sharp tip at the free end of a cantilever (the "probe") is brought into contact with the sample surface. The tip interacts with the surface, causing the cantilever to bend. A laser spot is reflected from the cantilever onto a position-sensitive photodiode detector. As the tip moves up and down due to the surface, the cantilever deflects causing a change in the angle of incidence for the laser beam. The cantilever displacement is measured by detecting the deflection of the laser beam which is reflected off its backside. This deflection is sensed with a position-sensitive detector. In this way, an image may be created revealing the configuration of the surface being imaged by the machine.

Figure II.4 shows the force interaction as the tip approaches the sample. At the right side of the curve the tip and sample are separated by large distance. As they approach, tip and sample atoms first weakly attract each other. This zone of interaction is known as the "non-contact" regime. Closer still, in the "intermittent contact" regime, the repulsive van der Waals force predominates. When the distance between tip and sample is just a few angstroms, the forces balance, and the net force drops to zero. When the total force becomes positive (repulsive), the atoms are in the "contact" regime. The various AFM techniques described below, can be generally described by their function within these three domains (Figure II.4).

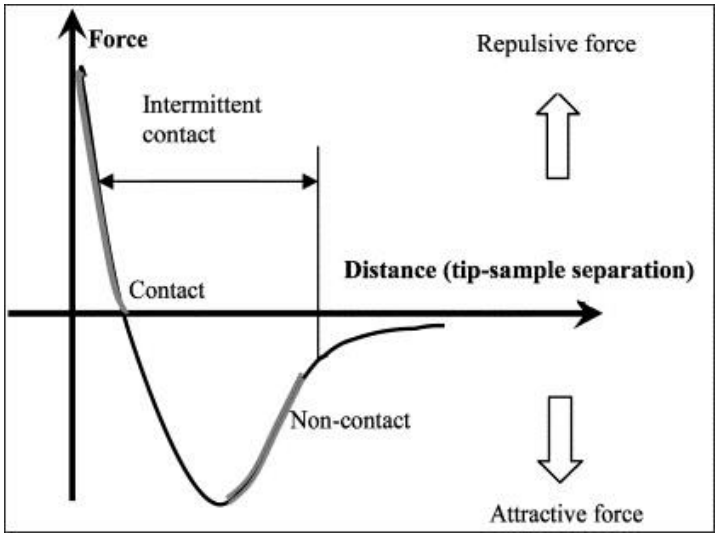

Figure II. 4. Zones of interaction as the tip approaches the sample.[147]

The tip-sample interaction is complicated by additional forces, including strong capillary and adhesive forces that attract the tip and sample. The capillary force arises when water, often present when imaging in the ambient environment, wicks around the tip, holding the tip in contact with the surface. As long as the tip is in contact with the sample, the capillary force should be constant because the fluid between the tip and the sample is virtually incompressible. The total force that the tip exerts on the sample is the sum of the capillary, adhesive and van der Waals forces. The van der Waals force counters almost any force that attempts to push the atoms closer together. When the cantilever pushes the tip against the sample, the cantilever bends rather than forcing the tip closer to the sample atoms. The deflection, therefore, can be used as a reliable indicator of surface topography.

1.3 Morphology investigation of the ZnO thin films

The AFM apparatus used to investigate the surface morphology of the samples is an Agilent Technologies 5420 Scanning Probe Microscope. The scanning is made in contact mode with a speed of 1.7 lines/s for all the measurements. The scanned area is of 2x2 μm^2 for all the sections of the sample and the average grain size was calculated after many random grain choice measurements with Gwyddion software. The scanning parameters are illustrated in Table II.2.

Table II. 2. AFM Scanning parameters for ZnO thin films.

Scanning parameters	
Mode	Contact mode
Scan speed	1.7 lines/s
Scanning area	2x2 μm^2
Software for image treatment	Gwyddion

We report in Figure II.5 the AFM topography images in 3D and 2D form of the ZnO thin films for a distance of (a) 4.5 cm (zone B1) and (b) 7.5 cm (zone B3) from the holder's center of the sputtered target. The 3D images show the topography of the surface on a 2x2 μm^2 area with the z-axis representing the distance between the lowest and the highest point on the scanned area. This means that the values appearing in Figure II.5 (22 nm and 10 nm) do not represent in any form the roughness or the grain size. However these topics will be discussed in details below.

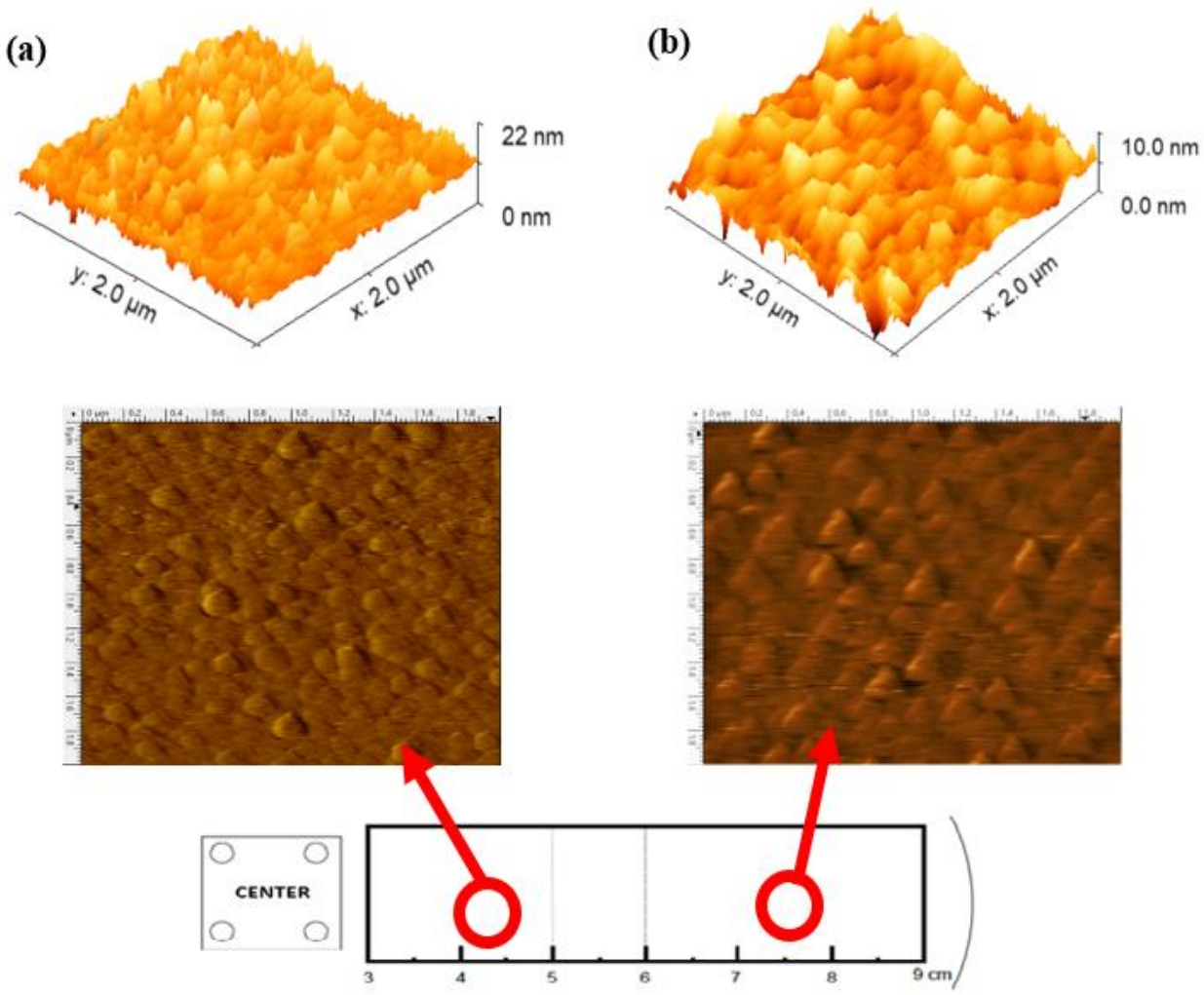

Figure II. 5. AFM topography images of the ZnO thin film for a distance of (a) 4.5cm and (b) 7.5cm in 3D and 2D form.

The plot of grain sizes along with the thickness of the film as function of the distance from the holders' center is represented in Figure II.6. It shows an increase in grain size with distance as well as a linear increase in the thickness of the film. In addition to the increase in grain size, also the grain shape was reformed; the grains transformed from spherical to pyramidal shapes as it is clearly shown in the pictures of the surfaces reported in Figure II.2. This pyramidal structure of grains was already observed and reported in literature which align our obtained results with the previous published work. [20]

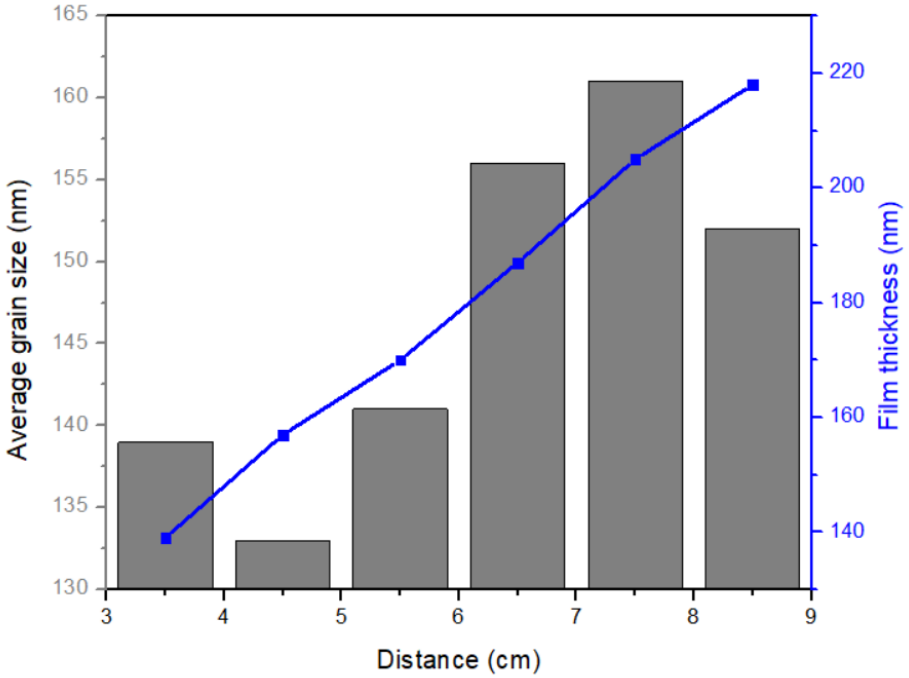

Figure II. 6. Plot of the grain size and thickness variation as function of the distance from the center.

It is well-known that the morphology of the surface of a TCO layer has an important role in improving light scattering and thus energy conversion efficiency (ECE) (for thin film transistors, solar cells…) by increasing the light path-length through reflection and scattering of the incident light with different angles leading to increased light trapping [148,149]. This contributes in increasing the ECE's factor which became highly requested by industrials and consumers in order to provide a compact system with the highest possible harvesting amount of clean energy.

Finally, as we have shown that the position of substrate from the center of the substrate holder has a direct influence on the morphology, also it is useful to mention that it has an indirect influence on the Haze factor of the TCO layer, where this Haze factor will increase as the spray distance increases. Furthermore, we have seen that the thickness of the layer also increases with the increase in the spray distance. This will also have a direct impact on the absorption of the layer. [150]

From all the above we need to find an optimal conditions in the development of electrodes for applications in photovoltaic cells between the increase in the Haze factor, i.e. the

collection of excitons, i.e. electrons in case of ZnO layer, and the optical transmission to the internal layers of the photovoltaic cells in particular their absorbent layer.

2. FTO by spray pyrolysis

2.1 Ultrasonic Spray Pyrolysis

The spray pyrolysis is another method of elaboration used during this work. Pyrolysis is the thermal decomposition of materials at elevated temperatures in an inert atmosphere. It involves the change of chemical composition in an irreversible way to form a stable structure on the substrate. A precursor solution is placed over a piezoelectric ceramic which vibrates at its resonance frequency. Due to the strong vibration of the underlying piezo-ceramic, an aerosol is formed and sent to the hot substrate by compressed air. The growth temperature was set at 420 °C in our case and the moving heating plate results in large area deposition.

2.1.1 Processing parameters

This method is a process in which a thin film is deposited by spraying a solution on a heated surface, where the constituents react to form a chemical compound. The chemical reactants are selected such that the products other than the desired compound are volatile at the temperature of deposition. The process is particularly useful for the deposition of oxides and has long been a production method for applying a transparent electric conductor as SnO_2 based materials onto glass. [151]

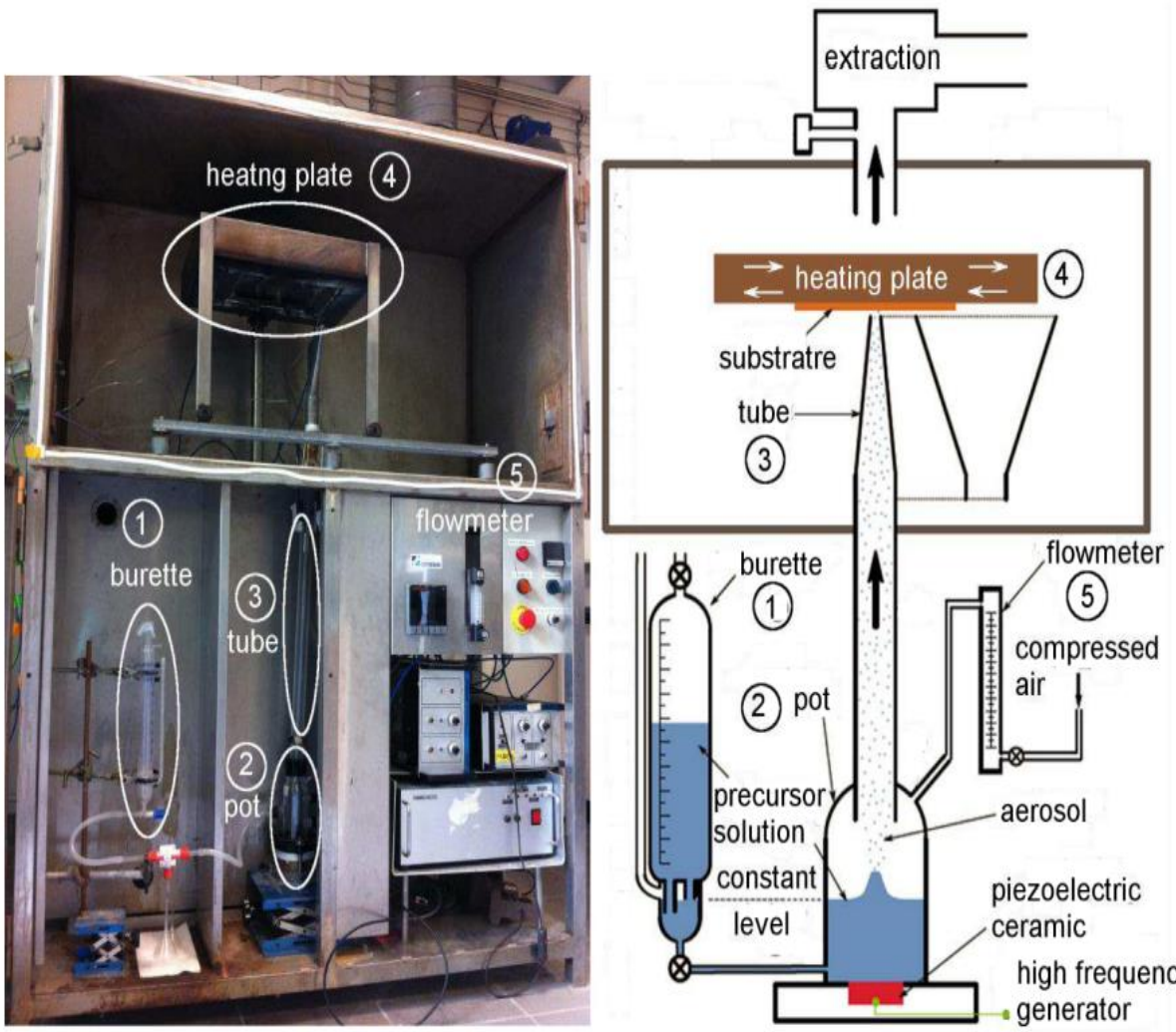

Figure II. 7. The setup of ultrasonic spray pyrolysis together with its schematics drawn for clarification at LMGP laboratory. [152]

The setup required for the spray pyrolysis consists of five essential elements; (1) burette, (2) pot, (3) tube, (4) flowmeter and (5) heating plate. Figure II.7 shows the Spray Pyrolysis setup used to deposit FTO layers on glass substrate in the LMGP laboratory (Laboratoire des Matériaux et du Génie Physique) of the Université de Grenoble, Grenoble INP - Minatec, France under the supervision of Pr. Daniel Bellet, Pr. Carmen Jimenez and Mr. Matthieu Jouvert.

2.2 Experimental procedure

A first set of commercial samples from Solaronix Company – Switzerland is used as reference. A second set of experimental FTO thin film layers deposited on glass substrates was provided by the LMGP laboratory. These samples were prepared by the Ultrasonic Spray Pyrolysis explained above. The experimentally obtained thin films were characterized, as well as the commercial ones, and the results obtained from both series were compared.

2.2.1 Solution Preparation

Polycrystalline F:SnO_2 thin films were grown by Ultrasonic Spray Pyrolysis (USP) on a Corning 1737 substrate. The substrate was previously cleaned in ultrasonic acetone bath for 15 minutes then transferred to a boiling isopropanol bath for 15 minutes and finally dried by a flow of argon gas. The precursor solution was prepared by adding tin chloride pentahydrate ($SnCl_4.5H_2O$) and tin diethyldiacetate (DDSn) having a chemical formula $C_{12}H_{24}O_4Sn$ to a certain volume of methanol as solvent. The mixture was stirred for 24 hours at room temperature, then a small amount of ammonium fluoride (NH_4F) was added to the mixture and stirred again for about 24 hours to obtain a clear and homogenous solution.

2.2.2 Deposition of Thin Films

The Spray pyrolysis is a simple and inexpensive thin film synthesis technique since the deposit is carried out at atmospheric pressure and at a temperature close to 400°C. Thus, this deposition temperature is fairly low as compared to the melting temperature of tin oxide at 1630°C. Chemical and structural composition of the obtained thin layers is of good quality, making this technique a good candidate for the development of low cost solar cells. In addition, this deposition method is already used on a large scale in the industry and as no vacuum is necessary, the process can be carried out continuously. The parameters used for the deposition of the FTO laboratory samples are summarized in Table II.3.

Table II. 3. Deposition parameters.

Processing parameters	
Carrier gas flow	6.22 / 9.05 $l.min^{-1}$
Nozzle-heating plate distance	15 mm
[Sn] in the solution	0.16 $mol.l^{-1}$
Volume of sprayed solution	20 ml
Substrate temperature	420 °C
Sprayed solution flow	1.25 $ml.min^{-1}$
[F]/([Sn]+[F])	0.2
Nature of the tin precursor	$SnCl_4 . 5H_2O$

2.3 Morphology investigation by AFM

Atomic Force Microscopy (AFM) is a high-resolution non-optical imaging technique providing accurate and non-destructive measurements of the topography, electrical, magnetic and mechanical properties of a sample surface with very high resolution. It is recognized that

for surface imaging, (AFM) is considered as a versatile, high-resolution instrument to provide a powerful tool in microelectronics for topography inspection and distribution measurement of nanoparticles on the surface.[153] Moreover, no previous treatment is needed to characterize sample surfaces by this technique.

In the current study, the samples were scanned using Agilent Technologies 5420 Scanning Probe Microscope. The software “Gwyddion” was used as a visualization and analysis tool for the registered AFM data. Each sample undergoes scanning at random positions with 3 different scanning dimensions (10x10 μm^2, 5x5 μm^2 and 2x2 μm^2). Constant scanning speed of 1.7 lines/s was maintained throughout the measurements. The grain size of samples is determined within images of 4 μm^2 area and the roughness with image having 25 μm^2 area. The scanning parameters are shown in Table II.4.

Table II. 4. AFM scanning parameters for FTO thin films.

Scanning parameters	
Mode	Contact mode
Scan speed	1.7 lines/s
Scanning area	10x10 μm^2
	5x5 μm^2
	2x2 μm^2
Software for image treatment	Gwyddion

The morphology of FTO thin film was characterized by analysis of the AFM pictures of the surface topography of one commercial FTO thin film in Figure II.8 (a), (b) and two samples with FTO thin film being deposited by USP with different carrier gas flow rate of 9.05l.min^{-1} and 6.22 l.min^{-1} in Figure II.8 (c), (d) and Figure II.8 (e), (f) respectively.

All AFM images of FTO thin films show that films are dense and nano-crystallized. For all the samples, the distribution of the grain sizes and shapes appear uniform.

The average grain size measured for the commercial sample was found to be 246 nm while that of the sprayed FTO samples is 230 nm and 269 nm for the carrier gas flow rate of 9.05 l.min^{-1} and 6.22 l.min^{-1}, respectively.

These first experimental results obtained by AFM show that the average grain size is comparable regardless of the origin of the samples and in fact, the techniques and conditions of deposits used from the moment they are well mastered. These results also clearly indicate that the quality of the samples deposited in the laboratory are up to commercial standards.

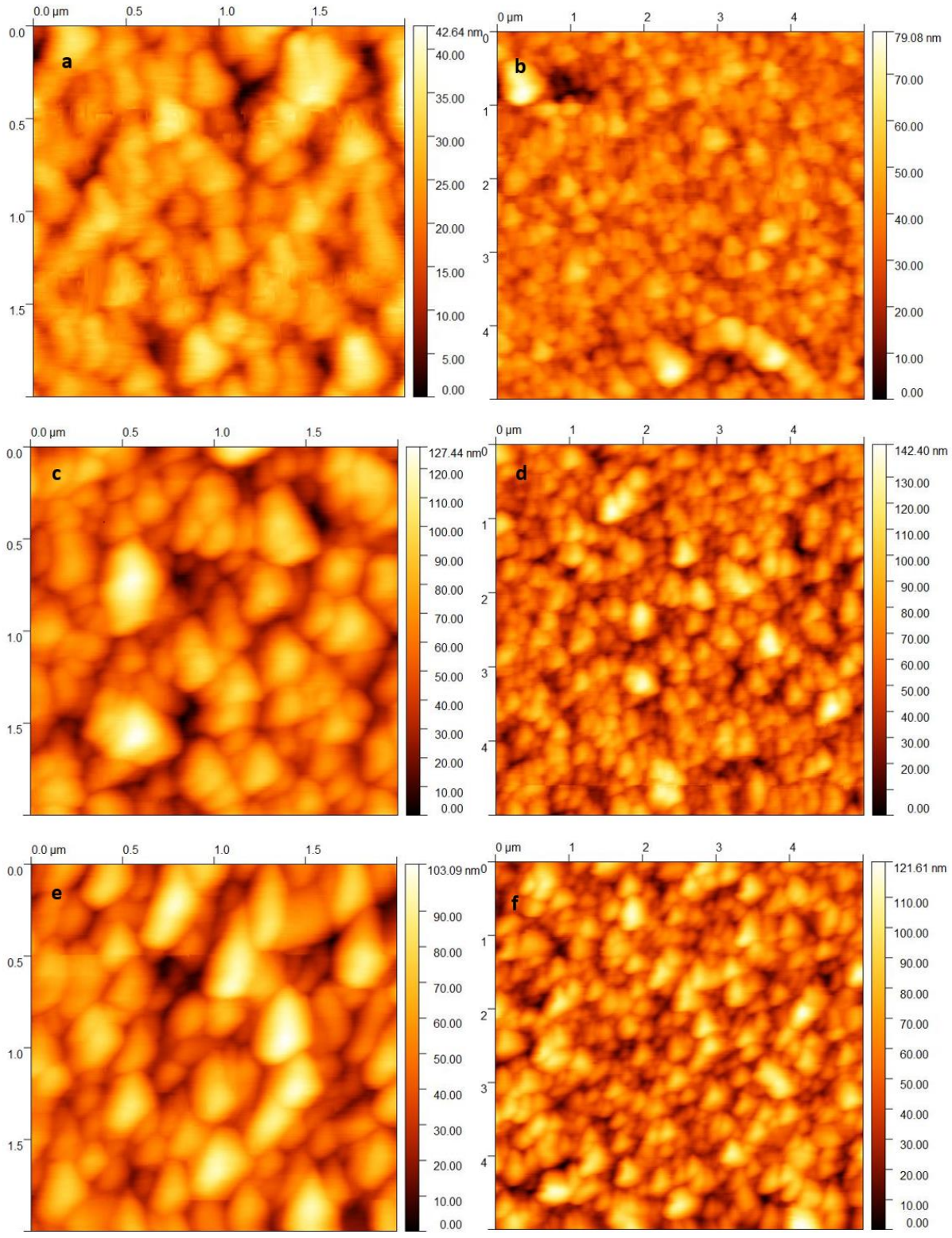

Figure II. 8. AFM topography images of (a-b) commercial and (c-d-e-f) sprayed FTO samples. the carrier gas flow for the sprayed samples is 9.05 l.min^{-1} and 6.22 l.min^{-1} respectively for (c-d) and (e-f).

For all samples and as enlighten by the photo in Figure II.9 for sample prepared by USP at a carrier gas flow rate of 6.22 l.min^{-1},the grains show a pyramidal shape.

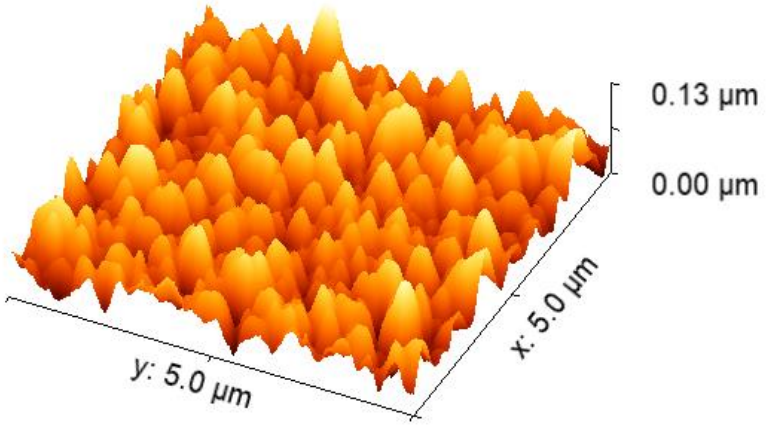

Figure II. 9. 3D topography of FTO by USP for a carrier gas flow rate of 6.22 l.min^{-1}.

The surfaces present high peaks along with deep valleys which contributes in increasing surface roughness to higher values. The values of roughness calculated through the Gwyddion software were found to be 18 nm for sprayed samples compared to 11 nm for commercial samples.

By referring to the previous section, in the case of ZnO the sample was placed at a fixed position during the whole process but for the case of FTO deposition the sample was placed on a moving heating plate above the spraying nozzle. Hence the variation of distance from the center in the case of FTO could not be considered taking into account the slim rectangular shape of the nozzle. This variation in geometry of placed samples makes the roughness values incomparable between both samples.

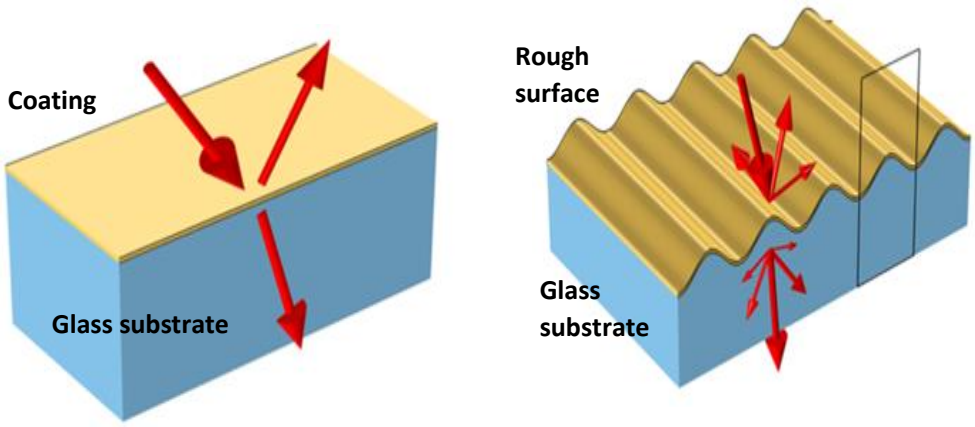

Figure II. 10. Schematic representation of light scattering for smooth vs rough TCO coating thin film.

A rough or even a naturally structured surface in a free or forced way is often preferable in various applications because it improves the light scattering and thus, increases the Haze factor defined as the ratio of the diffused light on the direct light. This happens because such kind of surface texture increases light trapping by increasing light path length and scattering the incident light with different angles as shown in the illustration of Figure II.10. In photovoltaic applications, when this layer is deposited as electrode, the increase of the Haze factor will correspond to an increase of the energy conversion efficiency [154].

2.4 Raman Spectroscopy

2.4.1 Brief overview and theory of Raman spectroscopy

Raman spectroscopy is a nondestructive fast and effective analysis technique which provides access to vibrational and rotational levels of atoms and molecules. The process involved is linked to a variation in the polarizability during a vibrational transition. Within this technique, sample preparation can be reduced to a minimum since it is possible to work in the liquid, gaseous or solid state. It allows the determination of the nanocrystallite sizes and the chemical species and crystalline quality of the material. Typically, a sample is illuminated with a laser beam. Electromagnetic radiation from the illuminated spot is collected with a lens and sent through a monochromator. Elastic scattered radiation at the wavelength corresponding to the laser line (Rayleigh scattering) is filtered out by either a notch filter, edge pass filter, or a band pass filter, while the rest of the collected light is dispersed onto a detector.

Raman scattering is very sensitive to the main structure as well as the concentration and nature of intrinsic and extrinsic defects in a crystal. Furthermore, Raman spectroscopy is well suited for obtaining information on the quality of samples as the crystallinity of samples, i.e. the order-disorder in the lattice, and finally, with a confocal lens, some information on the quality of the interface between layers or between films and substrate. It allows the width determination for various layers in a complex structure.

The operational principle of Raman spectroscopy is based on the inelastic scattering, or Raman scattering, of a monochromatic excitation source by the sample under probe. Upon interaction with the excitation source (usually lasers) the sample will be polarized (electrically deformed).

The vibration is termed Raman active when Raman scattering occurs. That is to say, part of the incident photon energy is used to excite the vibration of the sample, thus the scattered photon would have lower energy compared to the incident ones. This lower frequency is termed as Stokes frequency while in some cases a higher frequency can be obtained termed as Anti-Stoke frequency (when excessive energy of excited Raman-active mode is released). For non-Raman-active modes, a Rayleigh scattering may happen when photons of exact energy with the incident photons are observed. The IR-active and Raman active modes are schematically illustrated in Figure II.11.

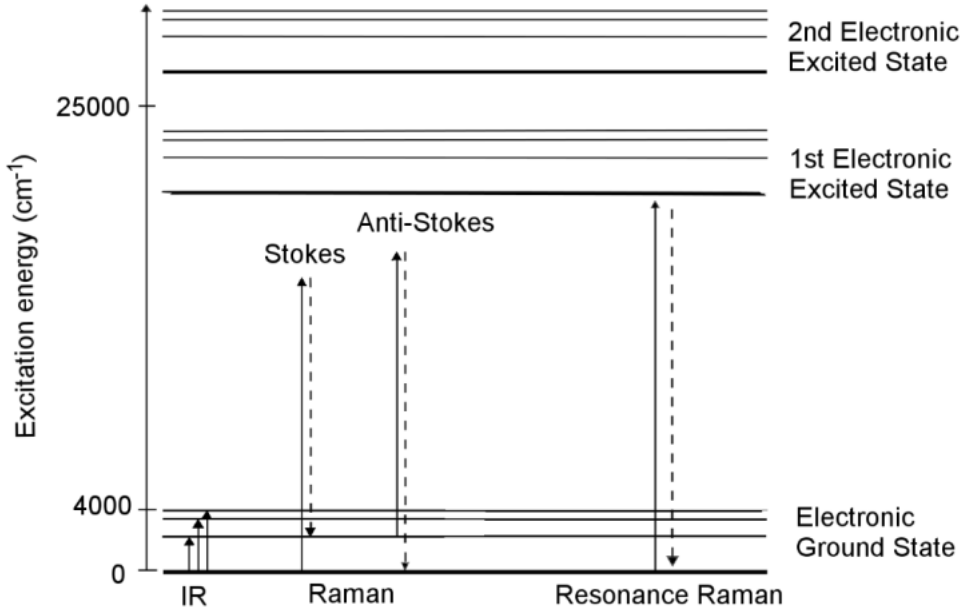

Figure II. 11. The IR, Raman, and resonance Raman modes represented in energy level scale. [152]

2.4.2 Structural analysis of FTO thin films by Raman spectroscopy

Raman scattering measurements were performed in a backscattering configuration at room temperature using the Horiba Jobin-Yvon Confocal Raman HORIBA LabRAM HR Evolution spectrometer of Figure II.12, at the spectroscopy platform at LMOPS . The excitation source was a diode-pumped solid-state laser emitting 50 mW at 532 nm, focused on the external surface of the films. The typical resolution used was 3 cm^{-1}, with optical grating 300 line/mm for an acquisition time of few seconds. The samples undergo surface scanning in addition to in-depth mapping.

Different spectra collection methods were used in the purpose of finding the crystalline quality as well as the film thickness. Analysis of the evolution of some typical peaks in the Raman spectra relative to the material under study can be considered as its signature.

In a complex structure composed by multi-layers of material, the evolution of the signature of the different films and of the substrate can be directly relied to the crystalline quality and the various thicknesses of the films. Among the discriminant methods used for the analysis and identification of the different Raman signatures along the longitudinal depth of the structure, we used the Multivariate Curve Resolution-Alternating Least Squares (MCR-ALS) method. We chose this method for the quality of the extractions it offers and its great adaptability widely applied to spectroscopy and separation techniques. MCR-ALS is thus an efficient method for the analysis of the wide data collection resulting of accurate Raman scattering measurements.

Figure II. 12. LabRAM HR Evolution spectrometer at the spectroscopy platform of LMOPS.

To obtain complementary information on the quality of the samples given at the surface by the AFM topography, and to evaluate the internal quality of the films, we have thus performed Raman spectroscopy on the two sets of samples.

In this study we have considered two independent variables related in MCR-ALS method for the film and the substrate, respectively.

Raman spectra of the FTO films are reported in Figure II.13 (a) and (b) for the commercial sample and in Figure II.13 (c) to (f) for samples of the second set.

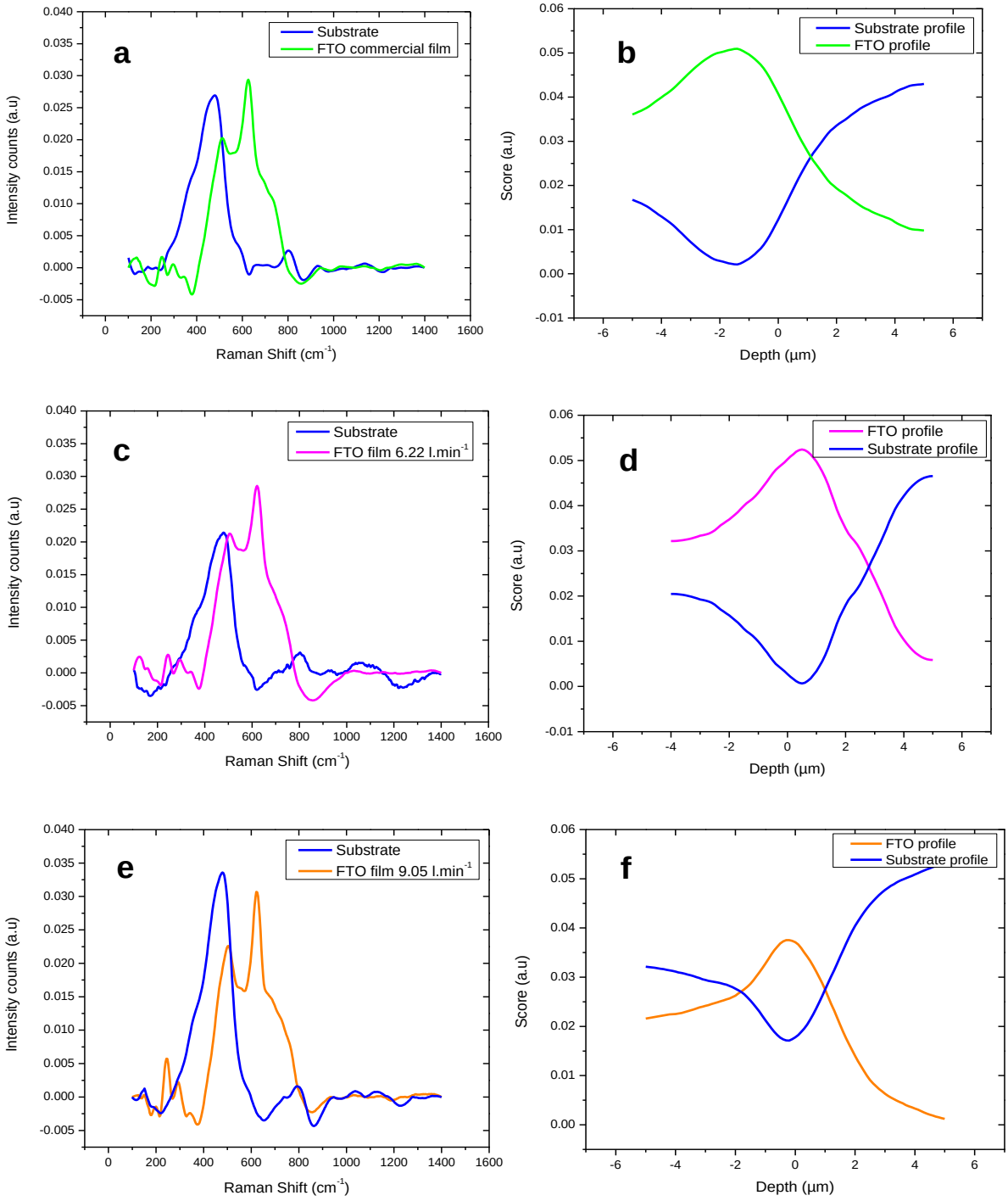

Figure II. 13. Raman spectra of: commercial FTO sample (a), FTO deposited by spray pyrolysis with a carrier gas flow rate of 6.22 l.min⁻¹ (c) and 9.05 l.min⁻¹ (e). Multivariate Curve Resolution of: commercial FTO sample (a), FTO deposited by spray pyrolysis with a carrier gas flow rate of 6.22 l.min⁻¹ (c), and 9.05 l.min⁻¹ (e).

The MCR-ALS method reveals on the average Raman spectra of the FTO layers and the substrates, Figure II.13 (a) (c) and (e), thus for all the samples, the same families of lines. Spectra associated with FTO films (green, pink and orange curves) show 2 main lines, one at 626 cm^{-1}, and a second in the range 480-510 cm^{-1}. [155] A remarkable third part of the Raman spectrum of FTO films shows a set of lines in the range 260-290 cm^{-1}. The spectra associated with the substrate (blue curve) show a main line positioned at 470 cm^{-1} and quite identical for all the samples, thus validating the possibility of discriminating the analysis by considering only the FTO film.

The analysis of the average Raman spectra by the MCR-ALS method, allowed us to establish the profile of the Raman response, represented in Figure II.13 (b), (d) (f)., as a function of the depth in the samples. A regular profile of the FTO layer is observed for the three samples. For the sample deposited by spray pyrolysis with a carrier gas flow rate of 6.22 $l.min^{-1}$, the width of the profile is in the same range that for the commercial one and larger than for the sample deposited by spray pyrolysis with a carrier gas flow rate of 9.05 $l.min^{-1}$. It is of note that from these results, an estimation of the layer thickness can be obtained by dividing the width of the Raman profile by the value of the refractive index. This idea is confirmed by the mappings extracted from the Raman spectra of the samples as reported in Figure II.14 for the two experimental samples.

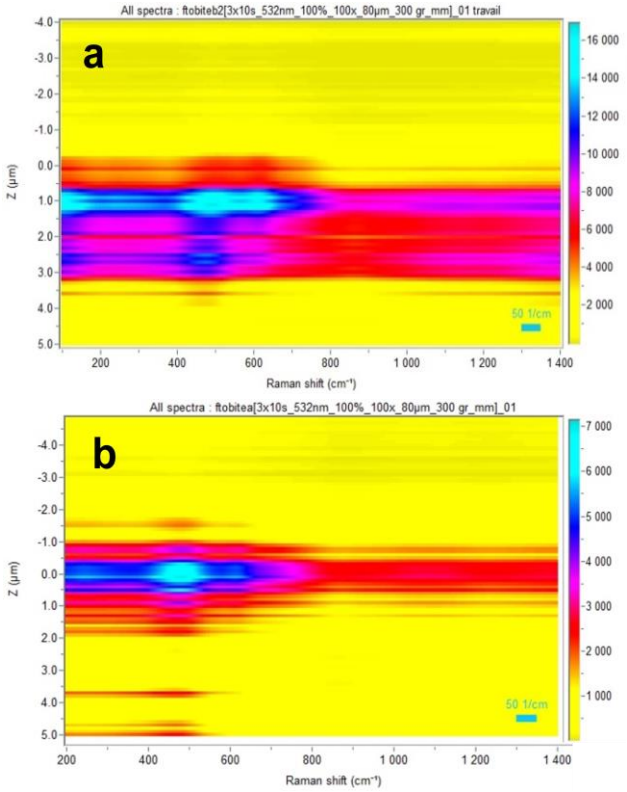

Figure II. 14. In depth mapping of the sprayed samples at 6.22 l.min^{-1} (a) and 9.05 l.min^{-1} (b).

We observed in Figure II.14, that the sample deposited by spray pyrolysis with a carrier gas flow rate of 9.05 l.min^{-1} has the lowest thickness (about 1µm) than that deposited with a flow rate of 6.22 l.min^{-1} having a thickness above 3µm. Moreover, these mappings show that the thinner sample is almost better merged with the substrate at the interface than the thicker one.

Finally, we point out that the quality of the FTO films can be also highlighted by considering the position and width of some peaks in Raman spectra. The peaks detected in the range of 260-290 cm^{-1} and 480-510 cm^{-1} in the FTO thin films are associated to some specific phonon modes in Raman spectra which are directly linked to the presence of defects originating at the oxygen vacancies present in the lattice. [156,157] As a reminder, among these modes, totally symmetrical vibrations (denoted A, A1, A1', A1g) are always active in Raman, for all symmetry groups. The corresponding lines are polarized and often intense, which facilitates their identification in the Raman spectrum. The A1g vibration is a non-degenerate total symmetry vibration, that is, it is symmetric under all symmetry operations (rotation,

mirror plane, center of inversion). In the SnO_2 samples, the symmetric mode of vibration A1g, as well as the much less intense mode of asymmetric vibration B2g, are both vibrations related to the expansion and contraction of Sn-O bonds. Thus, their position and mainly their width indicates the presence of defects caused by oxygen vacancies and the scattering peaks due to local vibration of Sn atoms around defects. The peak at 626 cm^{-1} corresponds to the A1g vibrational mode. The position of this peak is sensitive to the nanoparticle size. [158]

We compared, Figure II.15, the spectra of the FTO layers of the 3 samples. In the inset of this figure, we have specifically zoomed in on the line in the range 480-510 cm^{-1} and 623 cm^{-1}.

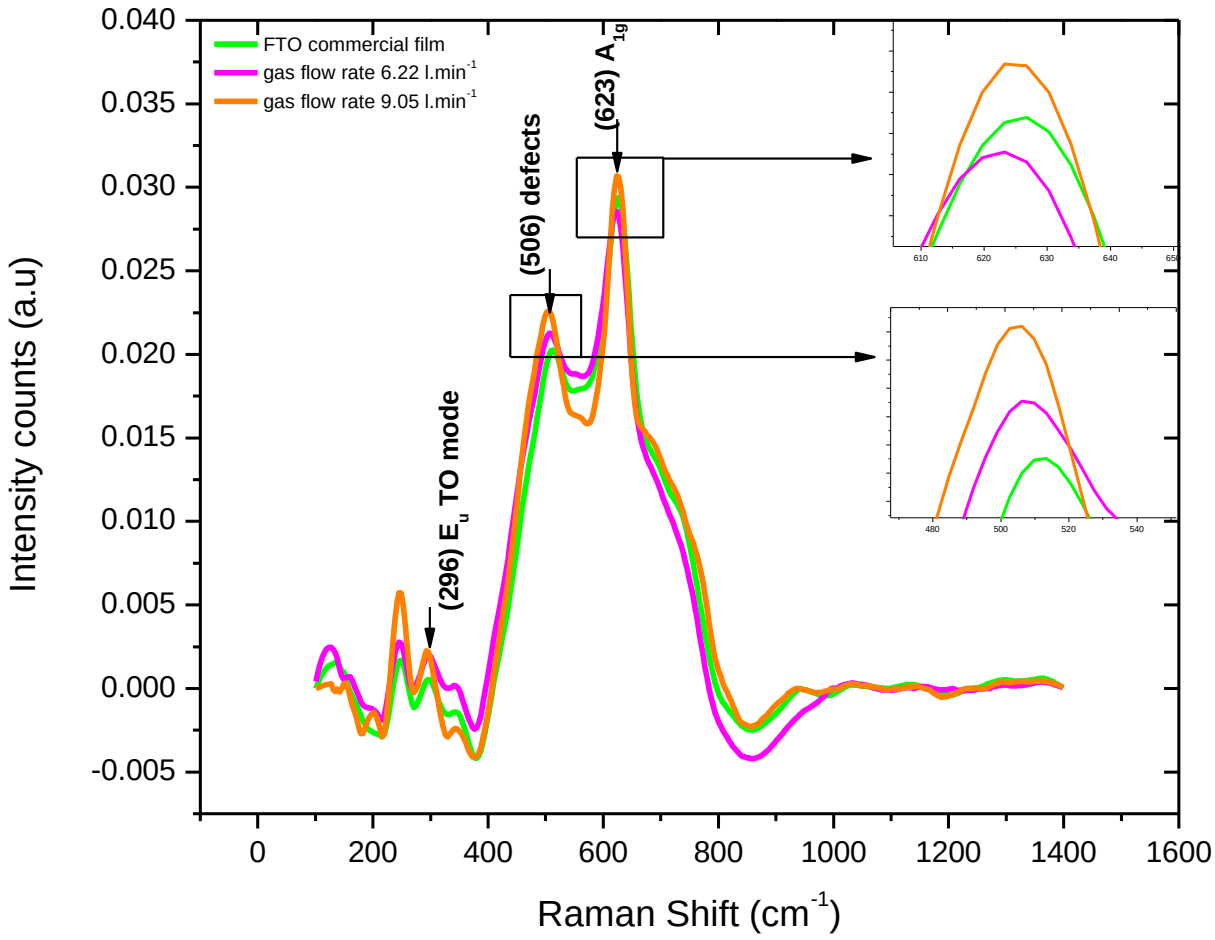

Figure II. 15. Superposition of the Raman spectra of the three samples. Insert: Zoom of the peak at 480-510 cm^{-1} and 623 cm^{-1}.

The position of the peak at 626 cm^{-1} has a slight blue shift for the different samples. Compared in literature to the Raman spectra of undoped SnO_2, the doped sample presents a broader peak which is induced by the size effect of crystallites and is very sensitive to the nanoparticle size. Besides, the peak in the range 480-510 cm^{-1} presents a blue shift for the two experimental samples that increases with the intensity of the gas flow used during the deposition process. This shift in the peak position to lower frequencies observed in the spectra of the samples indicates the presence of a compressive stress in the bonds of the material lattice. It is recalled that the MCR-ALS method applied in this study uses the mean Raman spectra. Thus, the shift of this line and therefore the increase in the observed stress can be attributed to an increase in the stress generated by a greater quality of interface with the substrate as observed previously thus blocking the longitudinal vibrations, mainly in the third sample having a relatively thin layer.

3. Conclusions

In this chapter we present the elaboration and characterization of Zinc Oxide and Fluorine doped tin oxide thin films deposited using two different techniques and characterized morphologically by AFM and structure investigation by Raman spectroscopy.

Firstly, a Zinc Oxide thin film was deposited on glass substrate by Sputtering with the distance from the center of the holder being the changing parameter. The surface morphology of the film was investigated by Atomic Force Microscopy. As the distance varies, the thickness, grain size and shape appear to change. The distance from the holder center shows to have an effect on the form, distribution and size of the grains which determine the texture of the film. Mainly, we noticed that as this distance increases, the roughness decreases, the grain size increases and the shape of the grains changes from spherical to pyramidal.

Hence, controlling the texture is beneficial for improving the Haze factor, and thus the generation of excitons with light, with a straightforward influence on the optical absorption, thus on the optical transmission of the layer and finally on the efficiency of the so-built device specially when considering these substrates as transparent electrodes in photovoltaic applications.

In the second part, two FTO thin films were prepared by Ultrasonic Spray Pyrolysis (USP) by changing the carrier gas flow rate between two sets of samples. The quality of these films was compared with a commercial FTO substrate. Two experimental processes were used for the characterizations of the films. The surface morphology of the film and the average grain size were characterized by AFM scanning microscopy. The AFM images of FTO thin films show that all the films are dense and nano-crystallized. The surfaces present high peaks along with deep valleys and the grains possess a pyramidal shape. The roughness calculations showed that the sample deposited at the lowest flow rate has the higher roughness compared to other samples. This parameter is important specially when considering these substrates as transparent electrodes in photovoltaic applications. In fact

higher roughness means more light trapping and thus the efficiency of the solar cell is improved.

Besides, the crystallography properties and the thicknesses of the layers was investigated by Raman spectroscopy associated to the Multivariate Curve Resolution-Alternating Least Squares (MCR-ALS) method allowing the discrimination of the contributions of the FTO films and the substrate in the average Raman spectra. With the Raman spectroscopy performed in depth of the structure through the films down to the substrates, the quality of the films was identified. Indeed, we enlighten in the average spectra of the films, the typical and well-defined peaks of FTO for the samples deposited by USP in compliance with the spectra of the commercial sample and previous work on SnO_2. The main peaks of the Raman responses are well positioned with a fix position of the peak at 626 cm^{-1} and a shift to the blue for the peak in the range 480-510 cm^{-1} for the two experimental samples. This blue shift of this average peak could be the signature of an increase of the longitudinal stress induced by the interface substrate-FTO film and linked to the thickness of the films as also determined during the Raman characterizations.

In the upcoming chapter, we will outline the electrospinning process with all the parameters taken into account for the ZnO nanofiber deposition in addition to the deposition of FTO thin film to have nanostructured samples and investigate their morphological, optical, structural and electrical properties.

Chapter III: ZnO nanofibers by electrospinning for transparent electrodes

In chapter III, the morphology, structural, optical and electrical properties of ZnO nanofibers and FTO_ZnO nanofibers are discussed in details.

Firstly, a presentation of the electrospinning technique, its history and evolution, applications, and general processing parameters is furnished. Electrospinning is a technique that enable the production of fibers to the order of few nanometers with large surface area and superior mechanical properties that are useful for various purposes. Along this chapter, electrospinning is used to produce zinc oxide nanofibers. Since these nanofibers will be used to make FTO_ZnO nanocomposite layers using fluorine doped tin oxide thin films deposited by spray pyrolysis technique, it became important to control the parameters of electrospinning and annealing, then make structural characterization for these nanofibers. A focus on the surface morphology of the obtained nanofibers is provided by optical microscopy as well as SEM images in addition to structural characterization by TEM.

As mentioned in chapter I, the combination of nanostructures with thin films for the transparent electrodes is showing promising improvement in the terms of electrical and optical properties. Although, in many research teams all around the word, a lot of nanocomposite configurations has been investigated, including nanowires, nanoparticles and nanotubes. Nevertheless, the amount of published work concerning the use of nanofibers specifically ZnO and AZO for the application as transparent electrodes remains low. In this context, the second part of this chapter treats the fabrication of FTO_ZnO nanocomposites sequentially combining the electrospinning technique and the spray pyrolysis method detailed in chapter II.

Careful discussion of morphological, optical and electrical properties of the resultant nanocomposites is detailed and presented in the third section of this chapter.

Finally, conclusion and future perspectives of this approach to realize high-performance transparent electrodes in terms of structural, electrical, optical and mechanical properties are summarized in section IV.

1. Electrospinning: Principle and parameters

Electrohydrodynamic process is the study of the dynamics of electrically charged fluids. This process is also known as electro-fluid-dynamics or electrokinetics. More precisely, it is the study of the motion and interaction of ionized particles and molecules with an applied electric field.[159] Electrospinning and electrospray are examples of two simple, cost effective and flexible electrohydrodynamic processes for creating various materials in layered or more massive forms depending on the processing time or the number of additional layers created.. Both of them use an electrically charged jet of solution for the fabrication of nanofibers and nanoparticles. The main setups used for electrospinning and electrospray are quite the same; a charge is induced on the droplets by the means of an electric voltage. At a certain value, the liquid droplet can no longer carry the amount of charge so it changes into a jet. This phenomenon is known as “Rayleigh-Taylor criteria”. In addition to the electric field, other operating and solution parameters should be regulated to obtain the desired product. During this thesis, we used the electrospinning method for the elaboration of ZnO and AZO nanofibers. [160] During the thesis work, I was in charge of starting up the electrospinning bench at the LMOPS laboratory with the implementation of the procedures and protocols necessary for the production of ZnO and AZO nanofibers.

1.1 Discovery and applications

1.1.1 History

Fibers in the form of elongated objects or continuous filaments have always existed in nature. We can cite natural animal fibers such as spider webs and silkworm cocoons, natural plant fibers such as cotton and linen. The man then strived to use them in many everyday objects such as clothing, or industrial objects such as filters. However, it was not until the 1600s that the observation and design of the electrospinning process as we know it today was introduced. [161]Some important dates are listed in Table III.1:

Table III. 1. History presentation of the discovery and evolution steps of the nowadays known electrospinning.

Year	Development history
1600	*William Gilbert* reported the formation of a cone-shaped water droplet in the presence of an external electric field. [162]
1700	*Stephen Gray* observed the electrohydrodynamic atomization of a water droplet. [163]
1744-1747	*George Mathias Bose, Abbé Nollet* performed the electrospraying experiment during which water could be sprayed as an aerosol by applying high electric potential to the droplets at the end of a glass capillary tube. [164]
1887	*Charles Boys* generated electrospun fibers from a viscoelastic liquid. [165]
1902	*John Cooley* and *William Morton* filed two patents to describe a prototype of the setup for electrospinning. [166]
1938	Electrospun nanofibers were first implemented for the development of aerosol capturing air filters. [167,168]
1964-1969	*Geoffrey Taylor* reported the formation of a Taylor cone. [169], [170–172]
1980s	*Donaldson Company Inc*. produced and sold filters comprised of electrospun fibers for air filtration.
1990s	*Darrell Reneker* and *Gregory Rutledge* demonstrated that many different organic polymers could be electrospun into fibers. [15]– [19]
2000s	First depositions of ZnO composite nanofibers and development of ceramic fibers, core sheath and hollow fibers, aligned fibers and continuous yarns of fibers. [178–182]
2010s	Industrial production lines based on multiple needle electrospinning and needless electrospinning. [183–185]

i. Applications of electrospinning

Electrospinning is considered as a simple and low-cost technique generally used for the fabrication of fibers with a very small diameter ranging from micrometers to nanometers using a high voltage power supply. Electrospinning could be used for many purposes to begin with the domain of biomedical engineering then, for wound dressing and drug delivery carrier. Electrospinning could also be of use for the fabrication of air filters, vehicle cabin filters and liquid filtration. Furthermore, electrospun nanofibers are also used for protective clothing and cosmetics in addition to electrical applications and renewable energies.

However, the majority of the published work related to nanofibers field are for the biomedical engineering and filtration applications. Depending on the application, the polymer and materials used for the fabrication of fibers changes, a summary of the material precursors used for the variety of application domains are listed in Table III.2. Different domains where electrospun nanofibers are used, are summarized in the following paragraphs and shown into categories in the scheme of Figure III.1.[186]

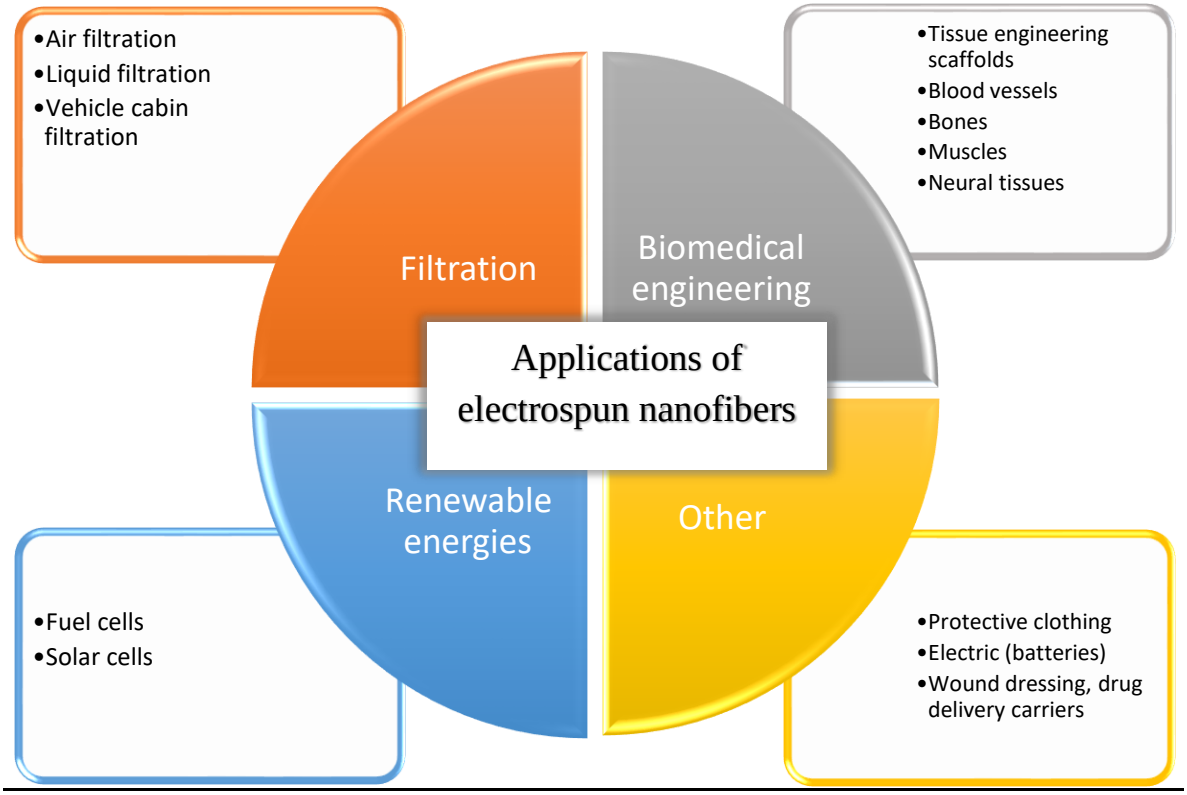

Figure III. 1. Diagram showing the different application domains of electrospun nanofibers.

Air filtration: For the purpose of eliminating solid particles from liquid or air, filtration is a common process used in both domestic and industrial settings. Nanofibers have an advantageous filtering feature because of properties such a high surface area to volume ratio, high porosity, and large interconnected pores that are useful for applications like air filtration and water purification. [187] The porous structure of the nanofibrous mat can be stabilized utilizing chemical and physical crosslinking procedures, resulting in long-term flotation performance.

Biomedical engineering: Recent years have seen an increase in the electrospinning of natural polymers, synthetic polymers and hybrid blends of these two that are biodegradable and non-biodegradable. They are employed in tissue engineering applications for the regeneration of blood vessels, skin, bones, neural tissues, and muscles as well as for the support of cells that need to replace extracellular matrix that has been destroyed by disease or trauma.[188]

Renewable energies: Having unique properties such as low density, high porosity and extremely high surface area to weigh ratio, electrospun nanofibrous material offer a greater energy conversion compared to their bulk counterparts. The two most popular applications for electrospun nanofibers in the renewable energy field are fuel cells and solar cells.[189,190] For example in the case of DSSC, one dimensional electrospun nanofibers having the properties previously listed, can significantly boost photocurrent generation by increasing the penetration of viscous polymer gel electrolyte in dye-sensitized solar cells. [191]

Table III. 2. Table representing the different polymer types used depending on the application domain.

Application category	Application field	Material precursor	Ref
Biomedical engineering	Drug delivery	Polyethylene-co-vinyl acetate, PEVA Polylactic acid, PLA	[192]
	Wound healing, tissue engineering	Collagen-PEO Cellulose acetate	[193,194]
Renewable energies	Photovoltaic and conductive polymers	Polyacrylonitrile (PAN)	[195]
	Light emitting diodes	PVA	[196]
Filtration	filter	Polyamide, PA Polyvinyl-carbazole	[197,198]
Other	Conductive fiber	Polyaniline (PANI) /PEO blend Polyaniline (PANI)/ Polystyrene (PS)	[199,200]
	Sensors	Polyvinyl-carbazole polyacrylic acid-polypyrene methanol, PAA-PM	[198,201]
	Protective clothing	Polybenzimidazole, PBI Polycarbonate, PC	[202]

Other applications include but are not limited to protective clothing, batteries and wound healing. Due to its distinct qualities, electrospun nanofiber membrane makes a strong choice for a wound dressing. Particularly, the small pores and extremely high specific surface area properties, not only prevent the entry of external microorganisms but also help regulate fluid drainage. Add to that, during the electrospinning process drugs can be added to the precursor solution to serve as a possible medical treatment or antibacterial purposes. [203] Furthermore, electrospun nanofiber membrane acts as a sponge-like electrode as they will have high discharge current and capacity, and a porous separator between the electrodes can effectively stop the short circuit, but allow the exchange of ions freely. [204]

1.2 Electrospinning process

The electrospinning technique works by applying a high voltage power source to a polymer solution and adjusting the volume feed rate. The electric field must reach a precise value for the polymer solution to be expelled from the tip to the collector. The repulsive electric force beats the surface tension of the precursor solution at this critical value, and the solution is repelled from the tip. The solvent evaporates as it travels to the collector, solidifying the solution and depositing it on the collector. The electrospinning process is illustrated in Figure III.2. [205,206]

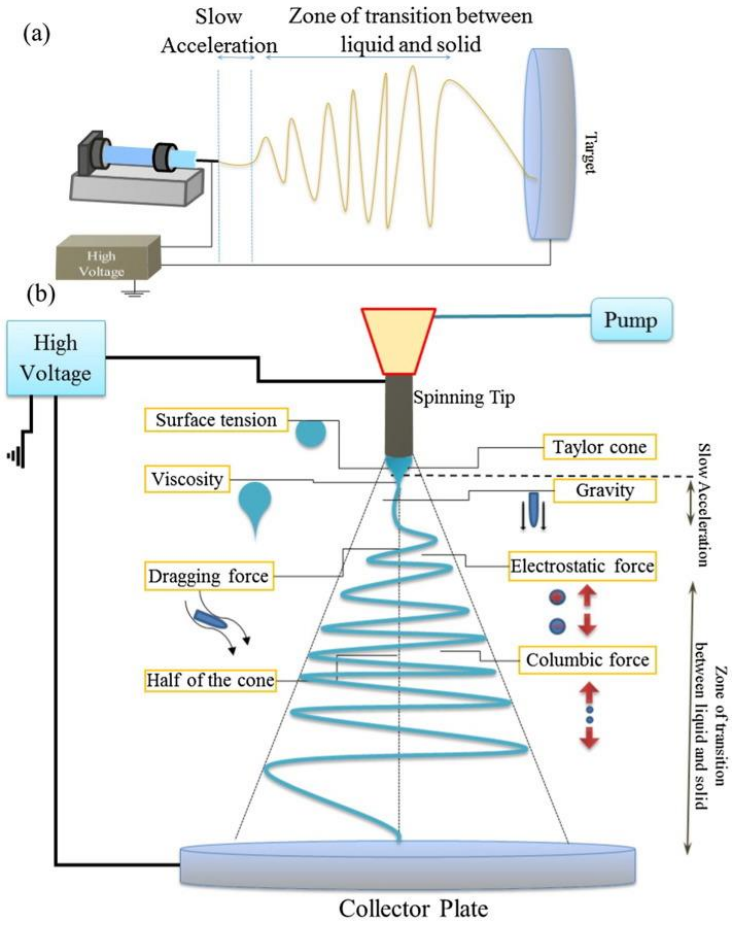

Figure III. 2. Typical electrospinning setup (a) horizontal, (b) vertical. (b) schematic diagram showing the electrospinning process with Taylor cone formation.[207]

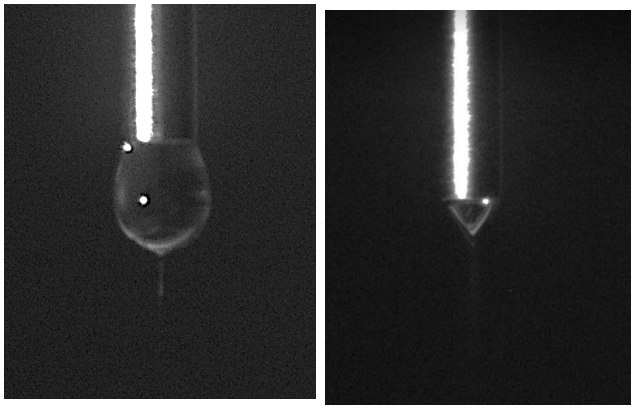

Figure III. 3. Actual footage of a droplet subjected to an electric field during the deposition of zinc oxide nanofibers.

An electrospinning setup consists of four parts mainly: a syringe to hold the solution, a needle usually metallic, an applied voltage and a metallic collector sometimes having different morphology. A high voltage is applied to the metallic needle causing electric charges to transfer to the polymeric solution leading to an instability of the droplets. The charges are repelled from each other causing the generation of a force opposite to surface tension. Hence these forces make the polymer solution move with the direction of the electric field. An increase in the electric field imposes the spherical droplets to distort into a conical shape called "Taylor cone" as shown in Figure III.3 which is an actual footage of a droplet at the needles tip undergoing an electric field during the deposition of zinc oxide nanofibers. At this stage, nanofibers appear from the Taylor cone and they are assembled on the collector.

1.3 General processing parameters

After describing how the electrospinning process works, it is important to mention the factors that affect this process and should be considered during the experiments. These factors are classified in two categories [208,209] operating parameters and solution parameters. The operating parameters are fundamental and they include: applied voltage, working distance (distance between needle and substrate) and solution flow rate. However, electrical conductivity viscosity, surface tension and dielectric constant are considered as solution parameters.

1.3.1 Process parameters:

Applied voltage effect: Applied voltage is an essential element in carrying out the experiment. Indeed, this force will oblige the solution to transform into a jet by a traction phenomenon, this phenomenon comes from the electrostatic field which is observed on the Taylor cone and which results in a reduction in the diameter of the fiber due to the resulting high speed of ejection. [210] However, we observe a multiplication of the jets but also fiber breakage and formation of pearls resulting from the instabilities of the forces (brief alternation of surface tension and electric tension). Furthermore, many studies have shown that an increase in applied voltage causes a change in the jet initiating point which by consequence affects the

structure and morphology of the fibers. Figure III.4 shows the different electrospinning jet mode.

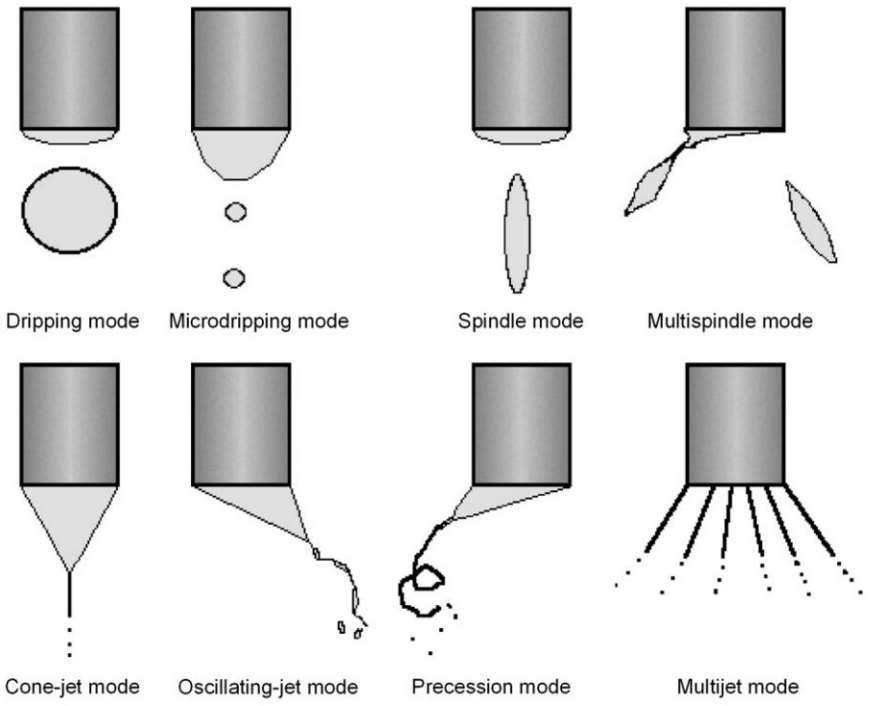

Figure III. 4. Scheme of different electrospray jet modes.[211]

Solution flow rate: The optimization of the flow rate mainly depends on two characteristics of the solution: the vapor pressure of the solvent and the electrical conductivity of the solution. They break down into several parameters: conductivity, molar mass, viscosity, concentration, and surface tension. Thus, the intrinsic parameters are important to be considered in the process parameters. They need to be experimentally adjusted as they are specific to each polymer and solvent and process temperature. Lower flowrates are preferable for the formation of a stable Taylor cone. This allows the uncharged drop at the tip of the needle to have sufficient time to polarize and form a stable Taylor cone. Conversely, a high flow rate causes dripping of droplets due to gravity. In addition, it is important to couple the flow rate with voltage so that a balance is maintained between the leaving solution and the replacement of that solution with new one.[160] Moreover, this will also allow the creation of a continuous cone jet. This balance avoids the breaking of fibers and creating disparities in the fiber's diameter.

Needle-Collector distance: The distance between the needle tip and the collector is important for achieving a suitable value of the electric field and for the formation of a stable Taylor cone. Hence an optimized distance is required so that the fibers have sufficient time to stretch and dry before reaching the collector since for too short or too far distances, the quality of the fibers is altered with the formation of beads, fiber breakage, a change in diameter and morphology, even the deposition of a liquid film instead of nanofibers.[212–214]

1.3.2 Solution parameters

Solution conductivity: This parameter is the important electrical factor to look after since it affects the diameter size of the obtained fibers. It was shown in a study that the fiber radius was inversely proportional to the conductivity of the solution. [215] This is simply explained by the fact that when the solution is highly conductive, the stretching of the jet will be fast and powerful which will result in smaller fiber sections. However, up to a certain limit of solution conductivity, fiber breakage and bead formation could occur. [216 217]

Solution viscosity and concentration: The concentration of the polymeric solution is linked to its viscosity and depending of the final composition and desired physical, electrical and optical properties, a compromise between possible viscosity and concentration need to be respected. If the solution is too concentrated, the jet will be too viscous and larger filaments will be observed. If the concentration of the solution is low, it will be less viscous and production of beads appears in the fibers. Thus, it is necessary to adjust the concentration in solvent in order to obtain a good spinning. In addition, the viscosity is also linked with the particle's dispersion influencing the conductivity in the volume of the jet. This implies that the viscosity will influence the electrical tension to be regulated in order to get Taylor phenomenon.

Surface tension: surface tension is the result of repulsive and attractive forces present in a material. Indeed, the forces located inside the material tend to attract each other while the connections on the periphery and its contact with the enclosure, i.e. syringe and needle will induce a phenomenon of repulsion. For the solution used in electrospinning, the surface tension will come mainly from the solvent. The more the solvent has a strong surface tension, the more energy it will take (electric voltage) to create the jet. Thus, the surface tension must

be considered in the electrospinning as a strong electric tension will lead to breakage of the fibers due to their heating originate of the motion and the sudden disorganization of the polymers.

Consequently, although electrospinning is a promising, simple and low-cost technique that has the potential to be used in many applications, a lot of parameters should be controlled and optimized during the spinning process to obtain homogenous and defect free fibers.

This optimization, with the various parameters presented above, was one of the contributions that I had to consider during my thesis work knowing that the LMOPS laboratory had just acquired the electrospinning bench on which I developed the ZnO nanofibers. This optimization phase is intrinsically linked to the material to be drawn in fiber form, as in this work for the development of ZnO-based nanofibers. Hence, for time management purposes, only process parameters were considered in the following section concerning zinc oxide nanofibers elaboration. But this experimental skill acquired on a family of materials could be profitable for the drawing, then the analysis, of nanofibers based on other materials. Thus, with regard to the contributions that this thesis should bring, this optimization work has indeed been carried out, more precisely on process parameters, in order to obtain the sought-after pure ZnO fibers. As we will see in the rest of this manuscript, material and deposition parameters still need to be improved for the printing of AZO nanofibers.

In fact, few published works on the zinc oxide and aluminum doped zinc oxide nanofibers by electrospinning for the use as transparent electrodes could be found. After thorough literature examination, experimental and solution preparation method was adapted from a group of Indonesian researches.[218–220] Modifications were applied to this method in order to fit with our project.

2. Fabrication of ZnO nanofibers

2.1 Experimental details

2.1.1 The electrospinning experimental setup at LMOPS

Figure III. 5. Electrospinning machine used during my thesis at LMOPS.

The electrospinning set up was from Spraybase company. As seen on Figure III.5, it is composed of a high frequency generator, syringe pump, metallic needle and a collector plate. The solution was transferred to a syringe placed in the pump of electrospinning machine. The needle was connected to the positive terminal of high voltage supplier while the collector plate was connected to the negative terminal.

2.1.2 General procedure for the solution preparation for ZnO fibers deposition.

First, a polyvinyl alcohol PVA $[CH_2CH(OH)]_n$ solution was prepared using 10 g of polyvinyl alcohol (MW= 70.000, Merck Ltd., Germany) and then mixing with 50 ml of distilled water. The solution was stirred at 70 °C for 4 h and was allowed to settle at room temperature for 24 h. To produce a zinc acetate (ZnAc) solution, 12.5 g of zinc acetate dihydrate $Zn(CH_3COO)_2{\cdot}2H_2O$ (Merck Ltd., Germany, M=219.49 g/mol) was mixed with 50 ml of distilled water and stirred for 1 h at 70 °C then the solution was set to rest for 24 h. ZnAc and solution was mixed with the PVA solution at a weight ratio of 1:4, stirred at 70 °C for 6 h, and

allowed to settle at room temperature for 24 h. In this way, the ZnAc/PVA precursor solution used for electrospinning was produced.

2.1.3 Substrate choice and cleaning

The techniques used in work to elaborate the nanocomposite samples are Spray pyrolysis and electrospinning. The spray pyrolysis setup permits the deposition of thin films over any substrate type providing that it has a constant thickness and is resistant to the deposition temperature. The choice of the substrates type depends on many parameters; usually alumina borosilicate is privileged for the deposition of oxide thin films since it has less alkaline compared to classical glass which will diffuse into the layer and deteriorate its electrical properties. For these reasons, the choice was corning glass slides of size 75x25 mm^2 to be used as substrates for the whole elaborated samples. Before their use, the substrates were cleaned ultrasonically with acetone for 15 minutes then with ethanol during 15 minutes and finally dried under purified air flux.

2.1.4 Nanofibers deposition parameters by Electrospinning

Detailed experimental parameters are showed in Table III.3. These optimized parameters were finally fixed after several tries. During all this work, three sets of samples were deposited indexed by the deposit time, i.e. 15 min, 25 min, 35 min.

The distance between the needle and the collector was fixed at 13 cm, the electrostatic field of 16kV generated between the two terminals transforms the solution ejected with a flow rate of 0.12 ml/h from the needle into nanofibers on the collector plate. The obtained fibers were calcined at 450 °C for 1 hour.

Table III. 3. Detailed experimental parameters used for the nanofiber deposition.

Elaboration parameters	
Deposition time	15 min; 25 min; 35 min
Voltage (kV)	16
Distance (cm)	13
Flowrate (ml/h)	0.12
Annealing	450°C for 1 hour
Number of samples for each deposition time	3
Individual sample size	75x25 mm

2.2 Morphological and structural properties of ZnO nanofibers

2.2.1 Sample imaging by optical microscopy

As well-known, an optical microscope only using light and geometric optical systems to visualize objects of small size doesn't compete laser-based microscope as AFM and electron-based microscopes as SEM and TEM. Yet, in optical microscopy no prior sample preparation is needed, in addition, it enables the acquisition of large area images providing a non-invasive way of imaging (i.e. the sample doesn't suffer from charging issues). Therefore, this approach served as a good way for a first qualitative check on sample morphology on large scale, more specifically in this study to check the nanofibers continuity and aspect.

An Olympus SC30 camera of a Horiba Jobin-Yvon Raman spectrometer was used in this study to map the surface morphology of nanofibers substrates. All the images were taken with the magnification (x50) and (×100).

The surface of ZnO nanofiber substrate prepared as described in section (2.1) is presented in Figure III.6 where the large area morphology is illustrated by optical microscopic images with low magnification (x100). Local surface details will be revealed below in corresponding SEM images of Figure III.9 taken at higher magnification.

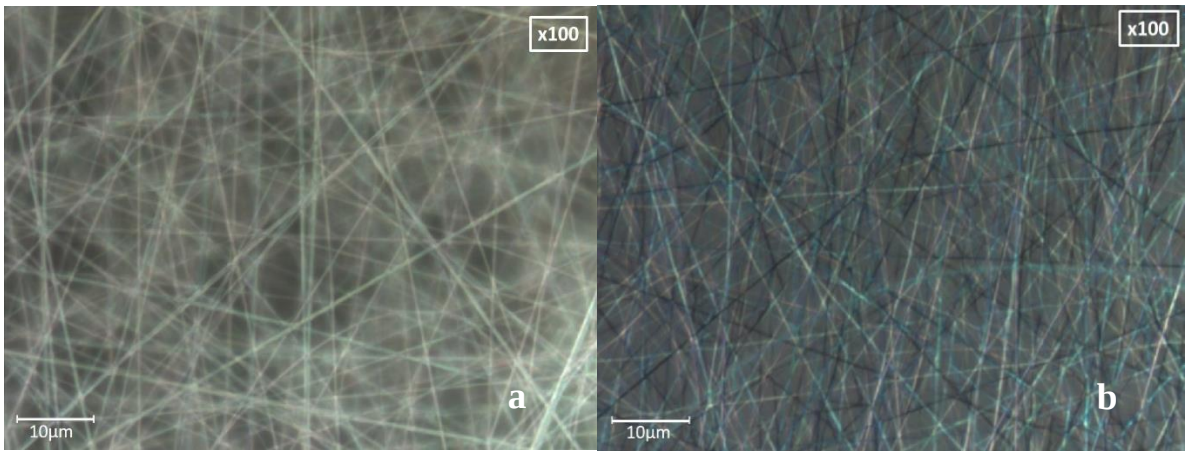

Figure III. 6. Microscopic images of Zinc Acetate fibers for a deposition time of 35 min;(a) before annealing with magnification of x100; (b) after annealing at 450°C with magnification x100.

Basically, right after deposition and before annealing, the nanofiber mat has a white color as can be seen on Figure III.6 (a) and is observed in the form of a peelable sheet. However, after annealing, sample color becomes transparent with no mat aspect visible to bare eye. Moreover, in Figure III.6 (b) it can be seen that the fibers are continuous with no beads and uniform shape.

Before annealing as seen in the images of optical microscope the zinc oxide nanofibers appear to be white against the glass substrate which appears as the black background, while after annealing the aspect changed to look darker. The nanofibers as seen in the images, form a mat-like surface with fibers in random directions that do not completely cover the substrate. Also, we note that the deposition of nanofibers results in a piled-up structure which can be observed as well in the microscopic images as blurred fibers. In fact, the fibers situated in the focal plane are seen with clear shape while the foggy fibers are located beyond that plane.

2.2.2 Scanning Electron Microscopy (SEM)

Scanning electron microscopy (SEM) is a technique based on electron-matter interactions to give information about topography, morphology, composition and crystallographic indications of the examined sample. The beam of electron irradiating the surface of a sample, penetrate the material at various depth in the sample in the form of teardrop-shaped volume, illustrated in Figure III.7, known as the interaction volume. The remitted signals are collected on a detector to provide many types of information. The most common signals are secondary electrons (SE), backscattered electrons (BSE) and Auger electrons. BSE refers to beam electrons that are reflected from the sample by elastic scattering, while SE refers to electrons kicked out of the atom by primary high electron beams. Because the BSE signal is highly related to the atomic number (Z) of the specimen, BSE pictures can provide information about the distribution of different elements in the sample. The SE signal can provide images of a sample surface with extremely high resolution.

A scanning electron microscope is essentially composed of an electron gun and an electron column whose function is to produce a fine electron probe on the sample, a chamber in which there is an object stage to move the sample in all three axes and detectors to detect and

analyze the radiation emitted by the sample. In addition, the apparatus must be equipped with a vacuum pump system.

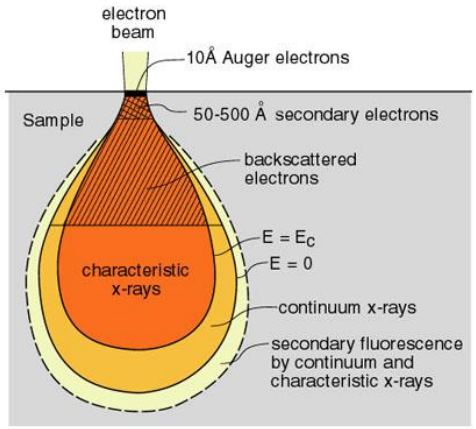

Figure III. 7. Schematic representation of the interaction volume with the different signals produced in depth length.

In the scanning electron microscopes used in this study, a Schottky field emission gun (FEG) was used to create electron beams in high vacuum by posing a sufficiently high potential gradient at the emitter to generate field electron emission by decreasing the energy barrier.

Scanning electron microscopy (SEM) is an essential characterization method for imaging method for imaging nanostructures. Several scanning electron microscopes were used to characterize the samples:

- SEM FEG GeminiSEM 300 from Zeiss Equipped with a field effect gun and 4 detectors: 2 for the secondary electrons (an InLens detector in the column and an Everhart & Thornley detector in the chamber) as well as 2 for the backscattered electrons (an ESB detector with energy filtering in the column and a retractable 6-sector BSD detector in the chamber). It provides a resolution of 0.7 nm at 15 kV.
- Environmental SEM FEG QUANTA 250 ESEM FEG from FEI with an SDD/ Bruker 30mm^2 detector. Equipped with a field effect gun (Field Effect Gun / FEG) it allows the visualization of details down to 30 nm.

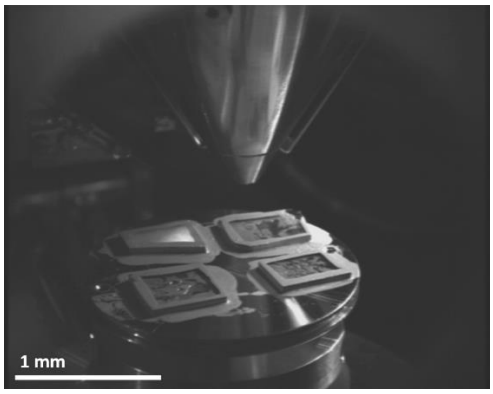

Figure III. 8. ZnO nanofiber samples placed in the SEM chamber.

All these microscopes have a field effect tip to reduce the size of the electron source and therefore the size of the electron beam, in order to have a better spatial resolution. In addition, these microscopes allow observations to be made using a low accelerating voltage, which is essential for imaging coatings on glass substrates. In order to achieve high spatial resolution and to limit aberrations due to the accumulation of electric charges, most observations were made with the secondary electron detector located in the lens or column, a working distance of 4 to 10 mm and an accelerating voltage of 3 to 5 kV.

Although SEM offers more beneficial images for showing surface details, they are limited by the maximum visible surface. Also, it is difficult to obtain good quality SEM images of the nanofiber substrates since the insulating glass substrate induces fast sample charging. Hence, to reduce the charging effect, prior the placement of the ZnO nanofibers in the SEM chamber, the samples were placed on the substrate holder with silver varnish on the edges of the substrate to serve as conducting connection between the holder and the nanofibers on top of the isolating substrate as shown in Figure III.8. The samples were ready for measurement after the silver varnish was left to dry for 12 hours.

Figure III.9 illustrates the SEM images of zinc oxide nanofibers deposited on glass substrate by the parameters of Table III.3 and annealed at 450°C for 1 hour. The samples were visualized at different magnification scales (x 100k; x 50k; x10k) for Figure III.9 (a), (b), (c) respectively.

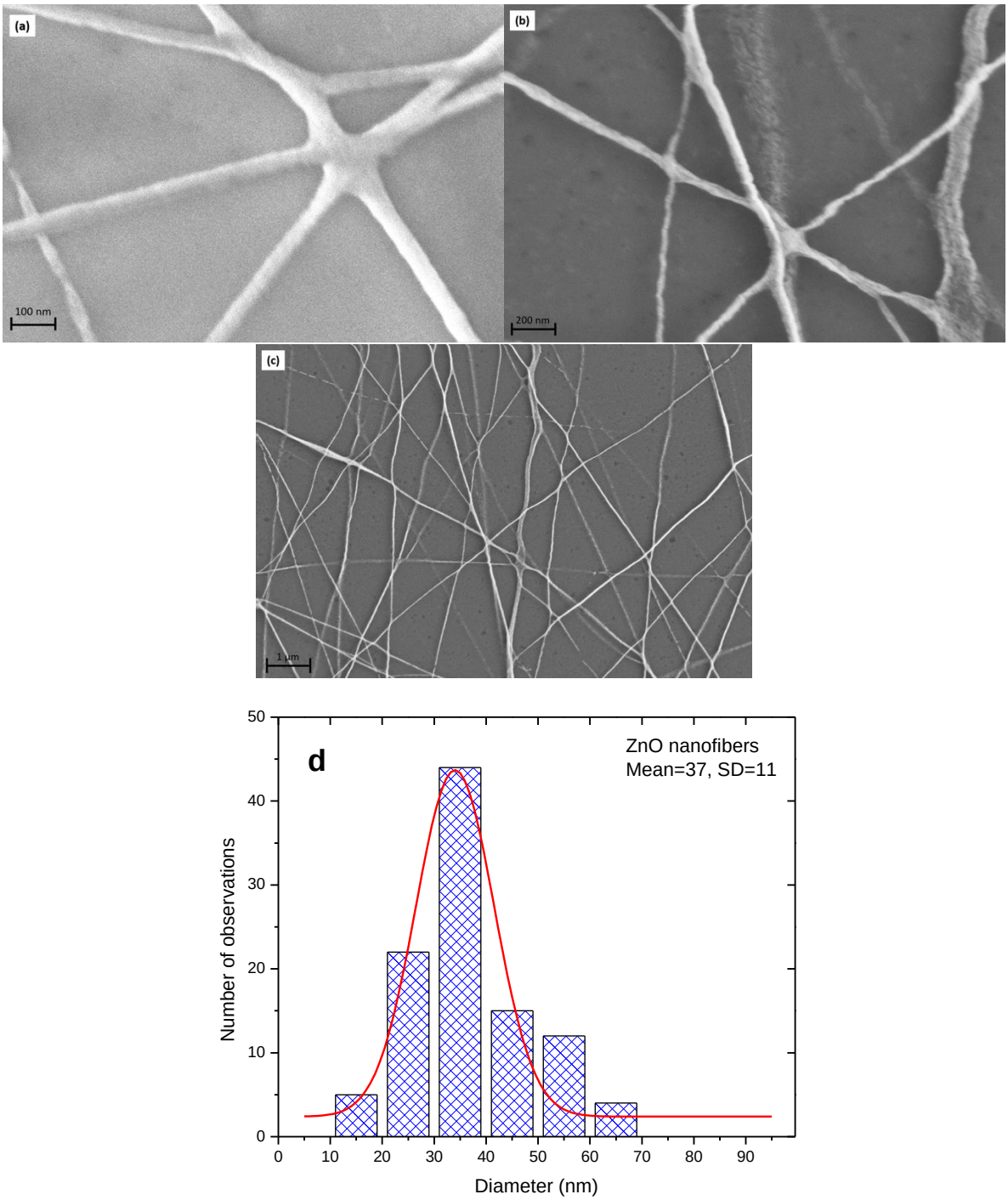

Figure III. 9. SEM images showing surface morphology of ZnO nanofibers after annealing at 450 °C for 1 hour. (d) Histogram showing the diameter size distribution for ZnO nanofibers.

The fibers show a continuous and homogenous aspect with some apparent difference in the diameter size. Measurement of the diameter size was performed over 100 distinct and different nanofiber by ImageJ software and the resultant statistics were illustrated in the

histogram of Figure III.9. The nanofibers showed to fit with a Gaussian distribution of diameter ranging from 10 nm to 70 nm with an average of 37 nm. Hence, the nanofibers have a very thin diameter which seems interesting for the improvement of optical properties. The advantage of this aspect will be detailed in section 3.3.

2.2.3 Transmission Electron Microscopy

As with scanning electron microscopy, transmission electron microscopy (TEM) also probes sample structure by making use of interaction with electrons. Although transmission electron microscopy (TEM) uses the interaction matter-electron as scanning electron microscope, this technique requires very thin samples (< 100 nm) for the electrons to be transmitted through for imaging and diffraction. Therefore, TEM is a destructive technique since it involves delicate sample preparation.

Transmission electron microscopy (TEM) observations were performed utilizing a Jeol 2010 instrument with a 200 kV acceleration voltage, LaB6 electron gun and 0.194 nm resolution. The samples were prepared by etching then they were deposited on the TEM grid using ethanol droplets. The nano-objects were disseminated in ethanol by ultrasonic for the observation of nanofibers. The suspension is then dropped onto a grid that serves as an observation support.

Single electrospun ZnO nanofibers were visualized by TEM and are shown in Figure III.10.

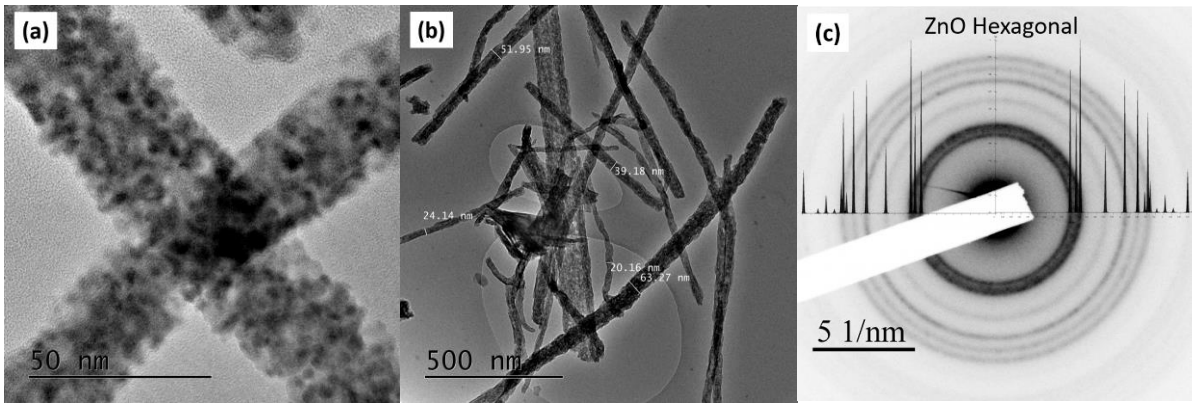

Figure III. 10. (a) (b) High resolution TEM images showing ZnO nanofibers morphology. (c) TEM diffraction pattern on ZnO nanofibers matching well with hexagonal wurtzite structure of zinc oxide.

High resolution images of the sample shown in Figure III.10 (a) and (b) indicate a polycrystalline structure of the annealed nanofibers consisting of nanosized ZnO grains of 5 nm dimension shown in the bright field TEM images of ZnO nanofibers. In addition, the measured diameter of some nanofibers ranged from 20 nm to 63 nm. Moreover, the electron diffraction pattern of Figure III.10 (c) indicates the hexagonal structure of the annealed zinc oxide nanofibers.

In this section, the structural and morphological properties of the zinc oxide nanofibers were studied since they will be the base of the nanostructured samples to be fabricated. Moreover, as the purpose of this study is to improve optical and electrical properties of the transparent electrode, after the initial characterizations, FTO thin film will be deposited in the next step on these nanofibers to form the nanocomposite samples.

3. Fabrication of nanocomposite samples

3.1 Deposition of FTO thin films by Ultrasonic Spray Pyrolysis

3.1.1 Sample preparation

The ZnO nanofiber substrates prepared by electrospinning were then coated conformally with FTO film by ultrasonic spray pyrolysis at the LMGP laboratory in Grenoble with the setup and schematic shown in Figure III.7 of Chapter II. The resultant samples are termed FTO_ZnO nanocomposites.

The ZnO nanofiber samples were placed in different batches for coating, two at a time with a reference sample of flat FTO in each batch as noted on Figure III.11. All the coatings were performed following the same deposition conditions.

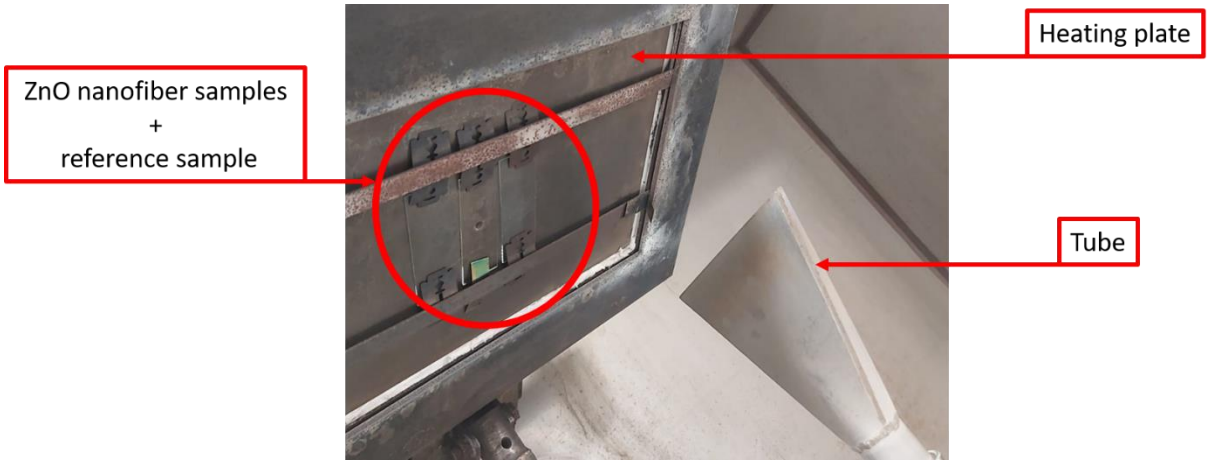

Figure III. 11. Samples in the Spray pyrolysis apparatus.

The precursor solution for FTO deposition was prepared by dissolving 0.16 M of $SnCl_4 \cdot 5H_2O$ (Sigma Aldrich) and 0.04 M of NH_4F (Sigma Aldrich) in methanol (VWR™). The precursor solution was placed over a piezoelectric ceramic which vibrates at its resonance frequency (700 kHz). Due to the strong vibration of the underlying piezo-ceramic, an aerosol was formed and sent to the hot substrate by compressed air (carrying gas) resulting in a constant flow rate of 1.36 mL/min. The growth temperature was 420 °C and the moving heating plate results in large area deposition. The resulting FTO thin film thickness is around 300 nm with deposition rate as high as 15-20 nm/min. A bare glass substrate was positioned in the same deposition batch of nanocomposites resulting in the reference flat FTO (named FTOstd_ref).

In the meantime, ZnO nanofibers were also deposited on commercial bought FTO samples (Solaronix-Switzerland). The ZnO nanofibers deposition conditions were identical to those mentioned in section 2.1. These samples provide the opposite configuration (termed as ZnO_FTO) and serves as a comparison to FTO_ZnO in optical and electrical characterizations.

3.1.2 Evaluating the thickness by profilometer of FTO thin films

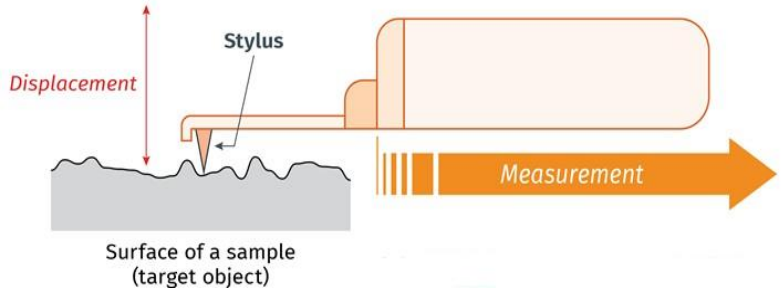

Figure III. 12. Scheme representing the working mechanism of a profilometer.

A profilometer is an instrument used to measure the profile and surface finish of a thin film on a small scale. During the measurement process, it provides information about height variation, depths and spacing as represented in Figure III.12. Film thickness measurement for the FTOstd samples with placed in the different deposition series was carried out by mechanical profilometer Bruker Dektak XT which makes a line scan of 2 mm and optical profilometer Profilm 3D which makes a surface scan of 400 µm x 400 µm.

Profile measurement performed on the edge of the deposited film was recorded for the three reference samples to make sure that all the nanocomposite samples have uniform FTO thickness.

Scans deeper into the samples, up to 2 mm, where made using a mechanical profilometer. The profiles for the three reference samples are reported in Figure III.13 (a). In Figure III.13 (b) we report a 3D image of the optical profile scanned at the edge of FTO thin film with a 400x400 μm^2 area.

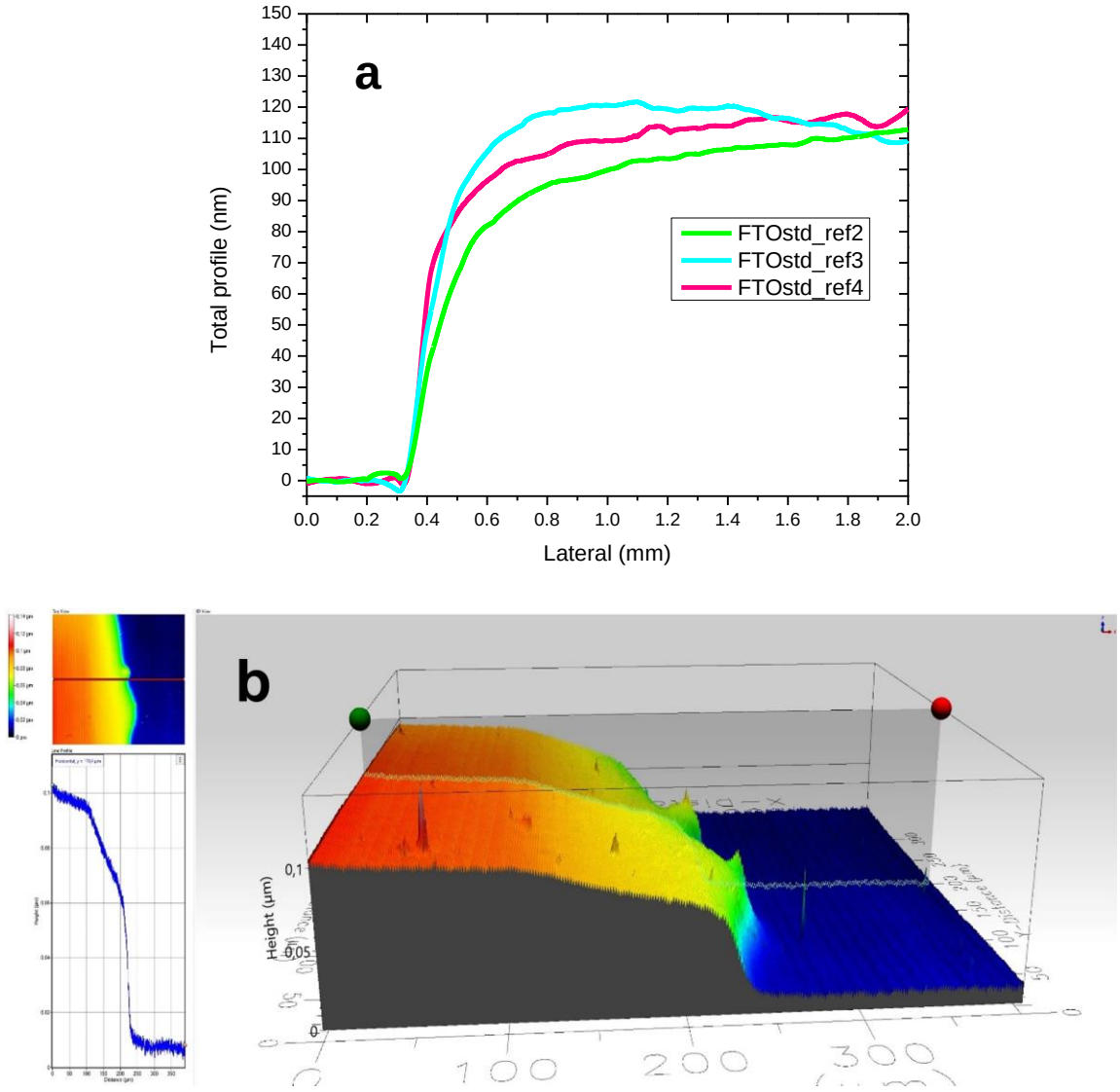

Figure III. 13. (a) Graph showing the thickness variation of FTOstd thin films with different deposition time. (b) Optical profilometer 3D profile of FTOstd_ref2 sample edge showing a thickness of 100nm.

As shown in Figure III.13 (a), a little variation in the thickness of the three samples turned out to be 115 nm. Moreover, in the 3D image in Figure III.13 (b) the measured thickness is about 100 nm.

This preliminary measurement confirmed that all the nanocomposite samples were covered by a uniform FTO film with almost no variation in thickness between different deposition series. In this way, the effect of nanofiber deposition time is considered to be the only changing parameter for the different samples.

3.2 Morphological characterization of FTO_ZnO nanocomposite samples

3.2.1 Sample imaging by Scanning Electron Microscopy

Morphological characterization was carried on by scanning electron microscopy for the group of elaborated samples. Figure III.14 (a), (b) shows the ZnO nanofibers deposited on glass substrate, the standard FTO deposited by spray pyrolysis as reference are represented in Figure III.14 (c), (d) and the nanocomposite samples FTO_ZnO are shown in Figure III.14 (e), (f), (g), (h) respectively. In this part we choose to represent the 15 min deposition time for ZnO nanofibers on glass substrate in Figure III.14 (a), (b) and for the nanocomposite samples, the 25 and 35 min nanofiber deposition time in Figure III.14 (e), (f) and (g), (h) respectively. All showed images were taken with low magnification (x10k) for a scale 1 µm and high magnification (x100k) for a scale 100 nm.

Prior to imaging, the samples were attached on the sample holder by conductive carbon adhesive tape specifically for SEM. The tape was placed on the back side of the substrate and a small connection was made between the deposited layer and the holder. Here we didn't use silver varnish as in the previous sample preparation for SEM imaging because it is easy to take off the carbon tape without causing any damage to the samples since they were also used for other characterization techniques.

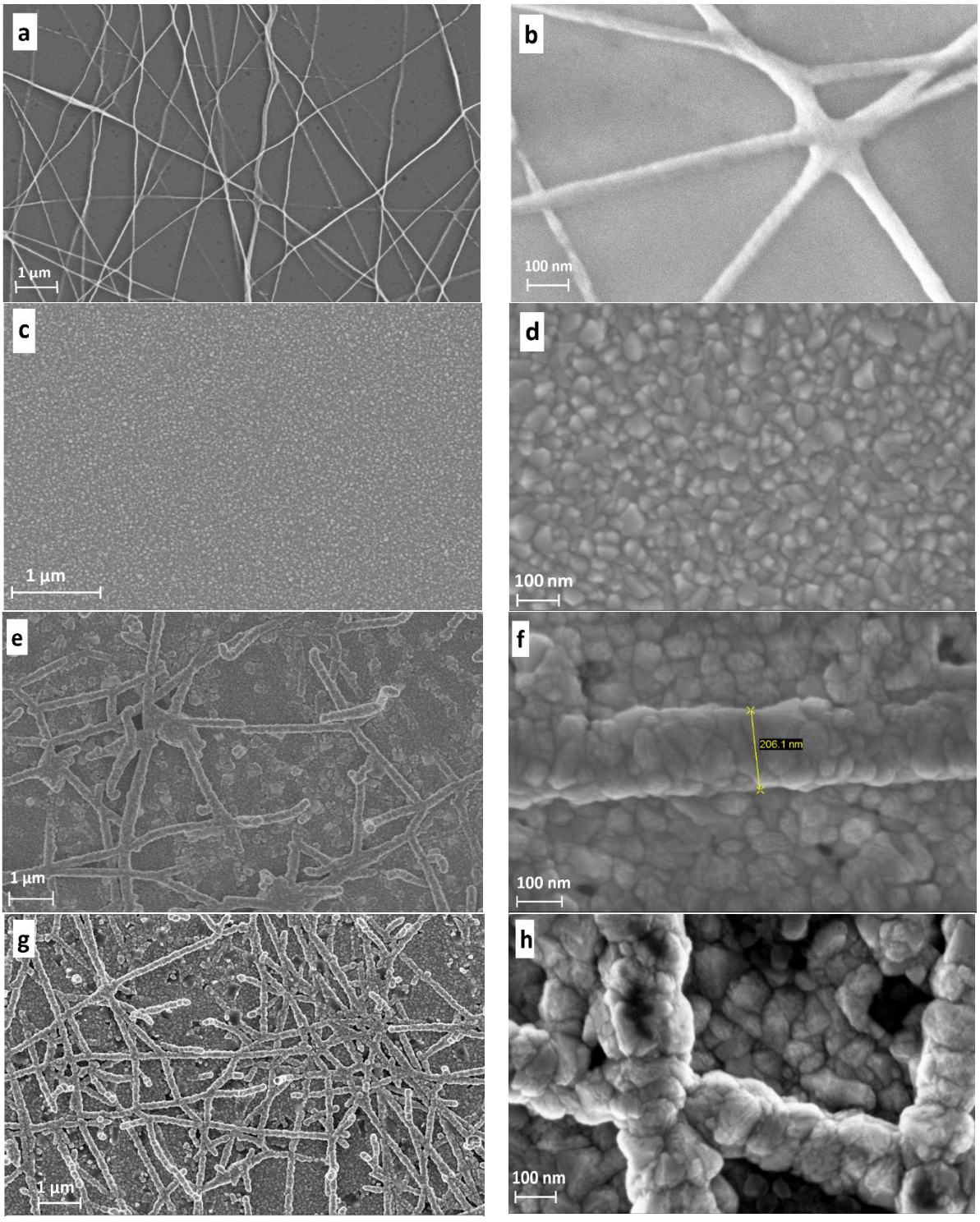

Figure III. 14. SEM images of FTO_ZnO nanocomposites with ZnO nanofibers deposited for: (a)-(b) 15min; (c)-(d) FTOstd reference sample; (e)-(f) 25 min and (g)-(h) 35 min.

The zinc oxide nanofibers present a homogeneous aspect on the substrate surface and show to have very low surface coverage; the sample is composed of bare areas where no presence

of nanofibers could be seen and of nanofibers that appear to be continuous nanofibers with long length having a lot of cross sections. For the FTO thin film deposited as reference, the grains have pyramidal shape with homogenous distribution on the substrate. Even when the deposition of FTO thin film is performed on the nanofiber substrates for nanostructuration, the grain shape and size remained unchanged. However, the nanofibers changed in form, they appear to be broken at some places and floating above the FTO thin film. It is also noticed that the nanofibers of Figure III.14 (g) are more dense then those of Figure III.14 (e) considering the increased deposition time of the zinc oxide nanofibers by electrospinning. In addition, we can also note that the nanofibers are all cover by the FTO thin film. This observation is normal and consistent with the measured layer thickness by profilometer of the FTOstd sample.

3.3 Optical properties of nanocomposite TCO

3.3.1 UV-Vis-NIR Spectrophotometer

A Perkin Elmer Lambda 950 spectrophotometer (Figure III.15) was used to study the optical properties of the composite samples which allows the measurement of transmittance and reflectance. The spectrophotometer is equipped with two light sources, a deuterium arc lamp for ultraviolet (UV) light and a tungsten-halogen lamp for visible and infrared (IR) light. Hence, a total wavelength range of 250 nm to 2500 nm is possible with this setup. This setup uses a set of optical elements to direct the incident light to the sample where it gets absorbed, reflected or transmitted. For the collection of transmitted and reflected light, the spectrophotometer is equipped by two detectors: one photomultiplier (PM) for UV and Visible regions of the spectrum and an InGaAs sensor for the near infrared range. The detectors switch at 850 nm. An additional 150 mm diameter integrating sphere covered with spectralon, can be mounted as accessory on the spectrophotometer, With the integrating sphere mounted, the total (T_{tot}) and specular (T_{spec}) transmitted light can be measured with the geometry shown in Figure III.16.

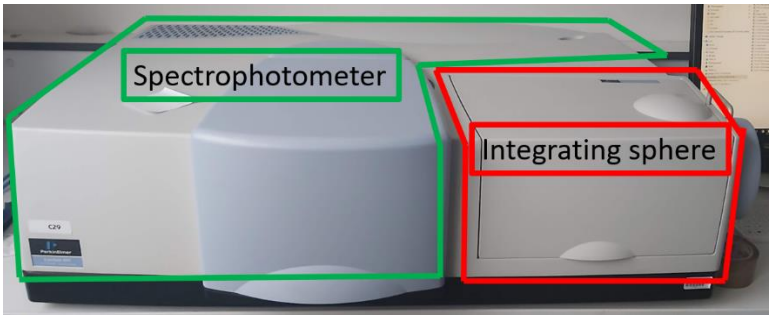

Figure III. 15. The Perkin Elmer Lambda 950 spectrophotometer equipped with integrating sphere.

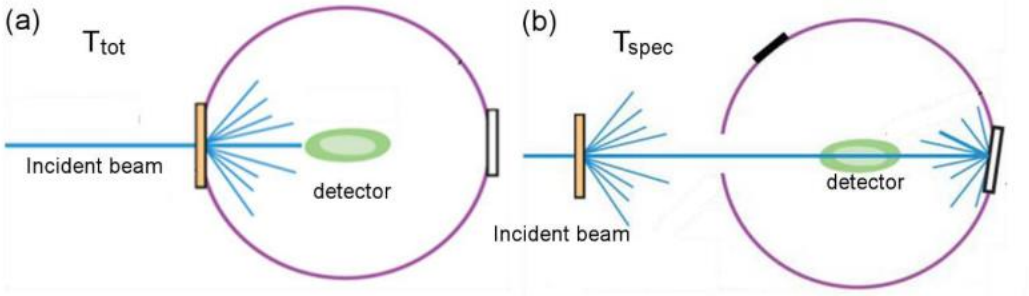

Figure III. 16. Schematic representation of the geometry for measuring (a) total transmittance (Ttot), (b) specular transmittance (Tspec). [152]

3.3.2 Optical transmission and Haze Factor (HF)

The total transmittance is particularly well suited to the transparent character evaluation of a layer to be integrated as electrode onto a solar cell. Indeed, for this type of application, all the light power transmitted to the absorber material should be considered. Besides, the Haze Factor is a quantification of the amount of incident light scattered towards the absorber layer, which enhances the light path length and thus the short circuit current density of the solar cell. For instance, the case of Ag nanowires was reported in literature. Research teams such as the LMGP in Grenoble-France [221,222] or else the teams of S. Suyitno et *al.* [219], and S. M. Bergin *et al.* [223] showed that the geometry of the nanowires and more precisely the diameter and the length are associated with the amplitude of light scattering in the nanowire layer of a transparent conductive material. For example, J. Ray showed that the performance of Ag nanowires was better optimized for the realization of transparent electrodes by large aspect ratios with wires having a large diameter-to-length ratio whereas larger diameter wires have larger scattering cross sections. Nevertheless, despite that transmittance of larger diameter

nanowires is less by 30% than the transmittance of smaller diameter nanowires, both have transparencies that are suitable for the use as transparent electrode. [224]

The measurement of total and diffuse transmittances was carried on for ZnO nanofibers deposited, FTO thin film and nanostructured FTO_ZnO samples; all the samples were deposited on the same type of glass substrate which was also analyzed. The total transmittance is particularly well suited to the transparent character evaluation of a layer to be integrated into a solar cell. Indeed, for this type of application, all the light power transmitted to the absorber material should be considered.

The Haze factor in the transmission range is calculated for the composite samples, the bare glass substrate and the FTOstd using the following equation [152] :

$$H_T(\lambda) = \frac{T_{diff}(\lambda)}{T_{tot}(\lambda)} \qquad \textit{Equation (1)}$$

where T_{tot} is the sum of specular and diffuse transmittance: $T_{tot}(\lambda) = T_{spec}(\lambda) + T_{diff}(\lambda)$

A coating that has a high haze factor will appear blurry, whereas a coating with a low haze factor will appear transparent due to low scattering.[225] The required value oh haze factor depends on the application of the material; for example low haze values are required for the fabrication of transparent electrodes to be used in touch displays and screens for them to give good clarity of the beneath display. Nonetheless, an increase in the light path length within the active layer reached by the increased scattering of the surface electrode is optimum for solar cells.[226] Consequently, a high haze value is preferable for applications relating to the production of devices associated with the conversion of light energy into electricity of the photovoltaic cell type. Therefore, the evaluation of the haze factor becomes of great importance for the design and characterization of transparent electrodes.

We report in Figure III.17 the total and diffuse transmittances of the nanocomposites in the 250-2500 nm range with the corresponding Haze factor calculated in the 350-1500 nm range for the ZnO nanofibers with different deposition time.

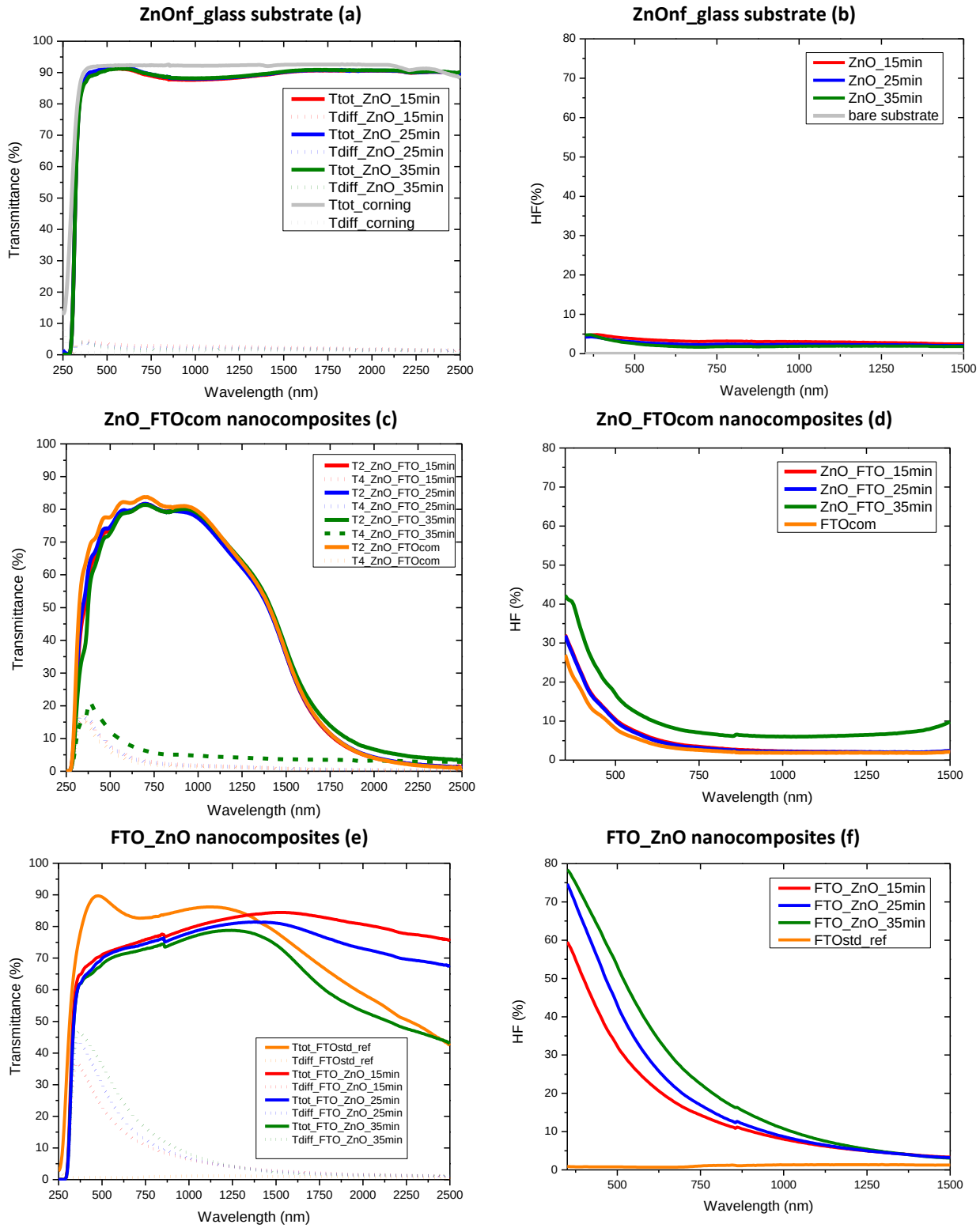

Figure III. 17. Total and diffuse transmittance of the nanocomposites in the 250-2500 nm range with corresponding Haze factor calculated in the 350-1500 nm range for the ZnO nanofibers at different deposition time. (a),(b) ZnO nanofibers deposited on glass substrate; (c),(d) ZnO nanofibers on commercial FTO substrate; (e),(f) FTO thin film by spray pyrolysis on ZnO nanofibers.

We first considered the transmittance of the so-built layers. The total and diffuse transmittance spectra for the ZnO nanofibers follow a similar behavior as the spectra recorded for the bare glass substrate in Figure III.17 (a). As previously seen and discussed in the previous section (Morphological properties of FTO_ZnO nanocomposites), the ZnO nanofibers do not ensure a total coverage of the glass substrate. In addition, the nanofibers are very small in size with an average diameter of 37 nm. All these factors explain the similar transmittance spectra for the ZnO nanofibers and the glass substrate no matter the electrospinning time. The same concept applies to the ZnO nanofibers deposited on the commercial FTO substrate where the contribution of the fibers goes discrete when compared to the transmittance and diffuse spectra of the commercial thin film. Hence, for the first two cases which graphs are in Figure III.17 (a), (b) and (c), (d), the detected transmittance and diffuse spectra could be considered as the response of the used substrate with no effect or contribution of the fibers no matter their deposition time.

For all the samples, the total transmittance increases sharply until reaching its maximum. This maximum for the nanocomposite samples achieves a value between 65 % and 85% in the visible range (> 400nm). For the FTOstd samples, we notice some oscillations in the spectra in the 300-750 nm range, these oscillations are due to the constructive and destructive interference effects caused by the multiple reflections at the air/thin film and thin film/substrate interfaces. However, in the presence of nanofibers, this effect is no longer observed since the specular reflectance is less privileged. [227] We also observed very low values of the total transmittance in the UV range, between 250 nm and 365 nm. This observation is attributed to the band gap absorption of the FTO thin film ($E_g \approx 3.7\ eV$) combined with the ZnO nanofibers ($E_g \approx 3.4\ eV$). Indeed, the presence of ZnO nanofibers increases the absorption for short wavelengths (UV range). In Figure III.17, we also notice a decrease in the transmittance beyond 1250 nm (IR range).

The drop-in transmittance at shorter wavelengths is due to the absorption of light by the glass substrate and FTO. The absorption of light in the UV range is linked to electronic transitions from the valence to the conduction band of the FTO thin film. As for the decrease in transmittance for longer wavelengths, in the infrared region, this is attributed to the interaction of photons with the free electrons of FTO.

The diffuse transmittance spectra increase gradually until reaching their maximum in the far UV then an exponential decrease is observed to occur for the whole remaining spectral range. The FTOstd samples have a very low Tdiff (being approximately 5%) while for the FTO_ZnO samples higher Tdiff values are recorded, between 10% and 45%. This is straightforwardly linked to the presence of nanofibers and is a common behavior for surface having random rugosity which is the case of FTO_ZnO nanocomposite samples.[228]

Now, consider the haze factor calculated in the range 350 nm to 1500 nm for all samples. For ZnO nanofibers deposited on glass substrates, HF is very low with maximum values of 5% at 350 nm. For all the sample types, HF is highest at 350 nm then consistently decreases until 1500 nm. This is a common observed behavior in the case of fixed size scattering centers that diffuse more effectively at shorter wavelengths owing to larger ratios of scatter size and the wavelength.[229] However, HF varies significantly with the ZnO nanofiber deposition time, as seen in Figure III.17 (d), (f), due to the increase in mass density of the nanofibers which will in its turn increase the light path length.

We report in Figure III.18 the haze factor at 635 nm plotted as function of nanofiber deposition time for the three sample types.

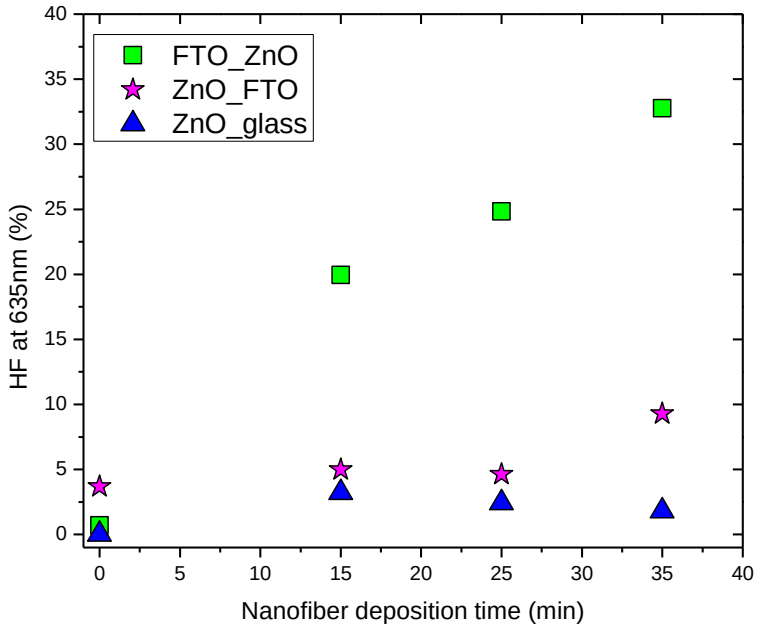

Figure III. 18. Haze factor at 635 nm plotted as function of nanofiber deposition time for the three sample types.

It is interesting to note that the ZnO nanofiber samples already show non-zero haze values (around 5%) even if when compared to their nanocomposite counterpart. In all ZnO nanofiber samples, the haze values are consistently lower. Similar observation can be noted for the ZnO_FTO nanocomposites with slightly increased haze factor. However, the FTO_ZnO samples record significantly higher values. This approves the assumption that rough surface morphologies in the FTO nanocomposites play a crucial role in light scattering. For the nanocomposites studied here, the nanofibers show a very thin diameter. Moreover, the resultant samples have different configurations. It is thus less proper to treat the three series of FTO nanocomposites as homogenous substrate. However, the ZnO nanofibers encapsulated by the FTO thin film exhibit the highest haze percentage among the other two sample configurations. Besides, we can consider that optical scattering of the nanocomposites can thus be modeled as collective scattering by all the present nanofiber. From this we can assume that HF is related to the surface coverage and density of the nanofibers present within the sample. This suggestion is supported by the quasi linear dependence between HF at 635nm and the nanofiber deposition time enlighten by the plots of Figure III.18.

Finally, the different configurations of nanocomposites used in this study have relatively high haze factor (specifically in the red and near infrared regions) and could be used to improve the performance of Si-based thin film solar cells by enhancing interface light scattering, hence increasing the light path length. [230]

3.4 Electrical properties of FTO_ZnO nanocomposites

3.4.1 Four-point probe measurements

The resistivity measurement of the samples was made using a Signatone 302 Resistivity Probe Stand. This apparatus is designed to measure sheet resistivity on flat surfaces with a requirement that the 4-point probe make even pressure on each point and move straight up and down. The main components of the setup are: a stand; the probe head mounting block and the sample chuck.

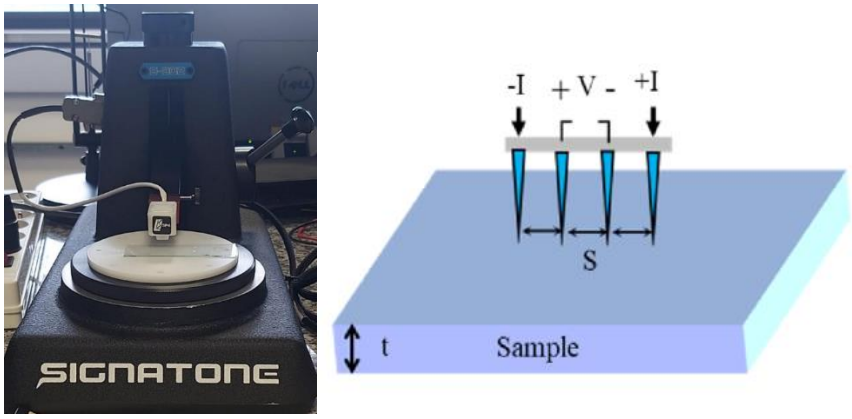

Figure III. 19. Schematic of the in-line 4point probe to measure Rs.

In theory, measuring the sheet resistivity of a sample applies the following formula:

$$R_s(\Omega/sq) = 4.5324\ \frac{V(V)}{I(A)} \qquad \textit{Equation 2}$$

The constant is derived from the original theory published in 1957 by LB Valdes in the article entitled "Resistivity measurements on Germanium for Transistors". The theory makes 6 assumptions that are important for consistent good measurements:

- The spacing between probe tips is the same between each probe tip.
- The contact pressure on all four probe tips is uniform.
- The edge of the sample is at least 10 times the spacing between probe tips.
- The thickness of the sample is less than 0.4 times the spacing between probe tips.
- The current is forced until a voltage reading between 1 and 100 mV is achieved.
- The measurement takes place at room temperature.

The current (I) is injected in the 2 outer probes, the voltage (V) in the 2 inner probes is then measured and Rs is calculated according to the given equation 2 (see the scheme in Figure III.15). For the FTO_ZnO nanocomposites, the sample size is 25x75 mm^2 and the probe spacing, much smaller than the sample size is s=1.02 mm.. The Rs of each sample in this study is averaged over nine measurements in different locations on the sample.

Table III. 4. Resistivity of the different configurations for nanocomposites samples.

Sample ID	***Resistivity (Ω.cm)***
FTOstd_ref	6.4 x10^{-04}
FTO_ZnO_15min	3.9 x10^{-03}
FTO_ZnO _25min	4.4 x10^{-03}
FTO_ZnO _35min	2.9 x10^{-03}
FTOcom	8.9 x10^{-05}
ZnO_FTO_15min	9.5 x10^{-05}
ZnO_FTO_25min	9.7 x10^{-05}
ZnO_FTO_35min	9.6 x10^{-05}

The resistivity of the FTO_ZnO nanocomposites with variation in the deposition time of the zinc oxide nanofibers (15, 25 and 35 min) and the resistivity of ZnO_FTO nanocomposites are plotted in Figure III.20. In the inset of Figure III.20, a zoom of the resistivity of the ZnO_FTO nanocomposites is proposed for clarity.

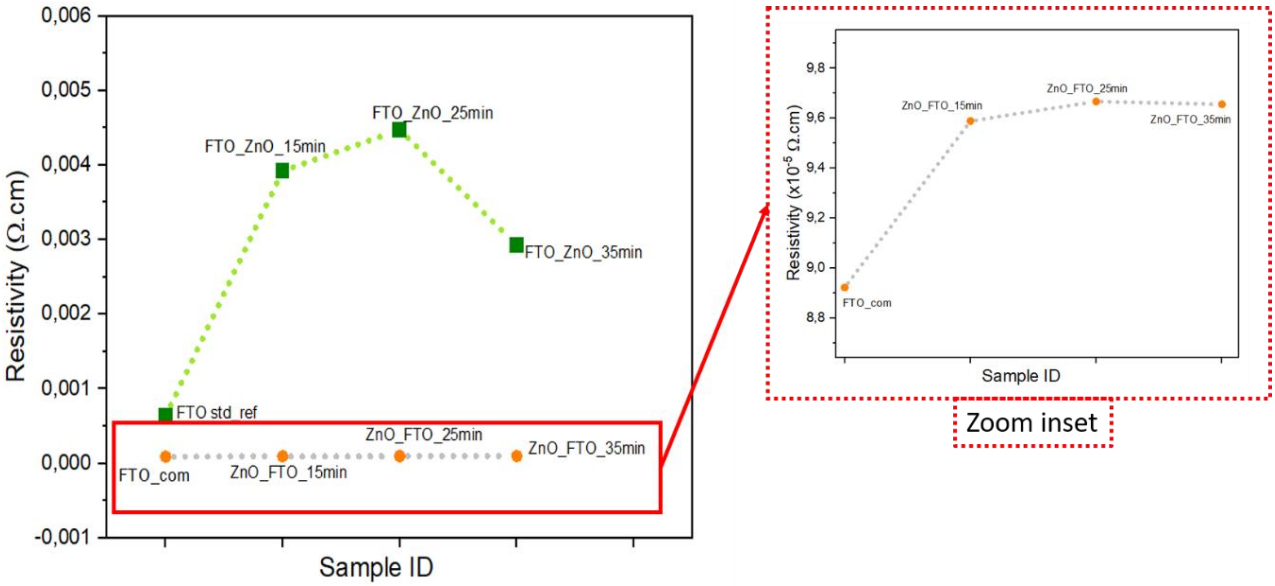

Figure III. 20. Resistivity of the FTO_ZnO and ZnO_FTO nanocomposite samples along with their corresponding reference samples.

For each series, the resistivity of the corresponding reference sample (FTOstd_ref and FTOcom) was also plotted.

For the samples where FTO thin film was deposited over the ZnO nanofibers the resistivity values increased from 6.4 $x10^{-04}$ Ω.cm for the standard reference to 3.9 $x10^{-03}$, 4.4 $x10^{-03}$ and 2.9 $x10^{-03}$ Ω.cm for the nanofiber deposition time of 15, 25 and 35 min respectively. However, regardless of the fiber deposition time, the presence of zinc oxide increased the resistivity of FTO thin film by a factor of 10. For the configuration where the ZnO nanofibers were deposited over a commercial FTO thin film for varying deposition time, almost no change in the resistivity was observed (check Table III.4 for detailed values); All the samples exhibit values in the order of 10^{-5} Ω.cm. Although in the zoom inset of Figure III.20, a slight difference is noticed between the nanocomposite samples and the commercial film. In both configurations, the presence of zinc oxide increased the resistivity when compared to the corresponding reference. As explained by Minami et al. [231] and Caglar et al. [232] this behavior is common with nanostructuration specifically in the case of zinc oxide nanostructure due to its high resistive properties. Besides, it is also important to mention that the case of nanofibers deposited on commercial films, the probe tips have more chance to assume a good electrical contact with the film then to be placed on the nanofibers as their diameter in very small. For this reason almost no variation in the resistivity is noted. However in the case where the nanofibers are covered by the thin film, an important increase in resistivity occurs. In fact, as explained by Zhang et al., [233,234] when the nanostructure (in our case ZnO nanofibers) are very resistive, the current has more tendency to flow through the FTO thin film. But, since the structure has a very rough aspect compared to a thin film, then the charges have to travel a longer path, that means higher resistance. Consequently, the following nanocomposites would have higher resistance than that of a simple thin film.

4. Conclusions

This chapter was divided into three main parts: the electrospinning technique with a presentation of its principle and different parameters to be considered during deposition, then the elaboration of zinc oxide nanofibers by electrospinning and finally the nanocomposite fabrication consisting of combined FTO thin film and ZnO nanofibers.

Electrospinning is considered one of the simplest and cheapest deposition techniques. Since the observation of cone-shaped water droplet in the presence of an electric field in the 1600s, the concept of electrospinning started its development through the years until reaching the setups that we have today either lab machines or even industrial scale operating machines. This massive development made the nanofibers fabricated by electrospinning of great usefulness for w variety of application domains. Although it appears simple, many parameters have to be considered simultaneously during the spinning process since they have big influence on the produced nanofibers. Zinc oxide nanofibers were successfully deposited by electrospinning and showed to have thin diameters, around 40 nm, and hexagonal structure compatible with that of ZnO. Different sets of nanofiber samples were elaborated by increasing the deposition time, meaning the surface coverage.

Afterwards, a thin film of fluorine doped tin oxide was deposited on the nanofiber sample to form the FTO_ZnO nanocomposites samples. The resultant samples were subject to morphological, optical and electrical characterizations. In the SEM images, the samples showed a nanostructured aspect with uniform grain size distribution even when compared to the standard reference FTO. Optical properties, more specifically, transmission and haze factor were measured by UV-vis spectrophotometer. A comparison between different sample configuration was made. The samples showed good transmission values regardless of the nanofiber deposition time for the case were the thin film was deposited over the nanofibers. However, the recorded spectra for both cases where nanofibers were deposited over glass substrate and commercial FTO showed no significant contribution caused by the nanofibers; instead the results were similar to the corresponding reference substrate. Moreover, an improvement in the calculated haze values was also recorded which means that we succeeded at increasing the light path length in the nanocomposite samples without

affecting its transparency. As for the electrical properties, it was possible to measure the resistivity of the nanocomposite samples where the values recorded an increase in resistivity values after the integration of ZnO nanofibers with the FTO thin film, but still the obtained values of the order 10^{-3} remains acceptable.

As final outcome, the fabrication of nanocomposite samples of FTO_ZnO showed to remarkably improve the haze factor of a simple FTO thin film or ZnO nanofibers, nevertheless a little degradation in the conductivity of such samples was noted.

Since ZnO is known for its high resistivity, adding dopant element to this material is efficient in increasing its conductivity. In this context, the next chapter will be dedicated for the fabrication of Al doped zinc oxide nanofibers, to be also used as nanocomposites along with FTO thin film, in the intention of improving the electrical properties mainly the conductivity that showed a downgrading for the undoped fibers.

Chapter IV: Development of AZO nanofibers by Electrospinning

The combination approach of nanostructures with thin films to give what we call nanocomposite samples was discussed in chapter III. The integration of zinc oxide nanofibers to a fluorine doped tin oxide thin film showed to have unique properties which are not achievable for the nanofibers or thin film alone. In fact, an improvement in the optical properties was noticed. Specifically the haze factor has been increased with the development of the nanocomposite samples compared with the bulk form of the samples. Nevertheless, the electrical behavior of the nanocomposite samples didn't show an upgrade. As a matter of fact, the integration of ZnO nanofibers reduced the conductivity of the FTO thin film.

It is known that zinc oxide, in the form of thin film or as nanomaterial, has poor conductivity compared to FTO and the previous findings concerning the electronic properties of the nanostructured pure ZnO-FTO electrodes that we have developed were expected. We remember that one main goal of the current work was the development of a simple technique for the creation of flexible TCO, what has been achieved and presented in the previous chapter. To overcome this aspect, many dopants of zinc oxides, as Al, Ga, Li, Mg, In, Cu, to name a few, [235–238] had been used to enhance its electrical properties. Particularly, aluminum is considered as one of the best doping elements to be associated to zinc oxide that render remarkable effects more precisely in terms of electrical properties. [239–241]

However, in the electrospinning process, the dopant addition into precursor solutions of PVA and zinc acetate and its effect on the morphological, structural and electric properties of ZnO nanofibers was poorly investigated by authors. [242–244]

In this chapter, we focus on the synthesis of precursor solutions for the fabrication of aluminum doped zinc oxide nanofibers with PVA as polymer matrix. We also discuss the different effects produced by this doping on many levels as well as an optimization process in order to have well shaped and structured nanofibers. First results of optical and electric characterizations of the so obtained TCO are finally also presented.

1. Experimental procedure for AZO nanofiber deposition

1.1 General principles used

The full methodology used for the fabrication and characterization of doped nanofibers is shown in Figure IV.1. Two aluminum precursors were used. After explanation of the reason in the paragraphs below, more details about each precursor and obtained samples are discussed in the next sections.

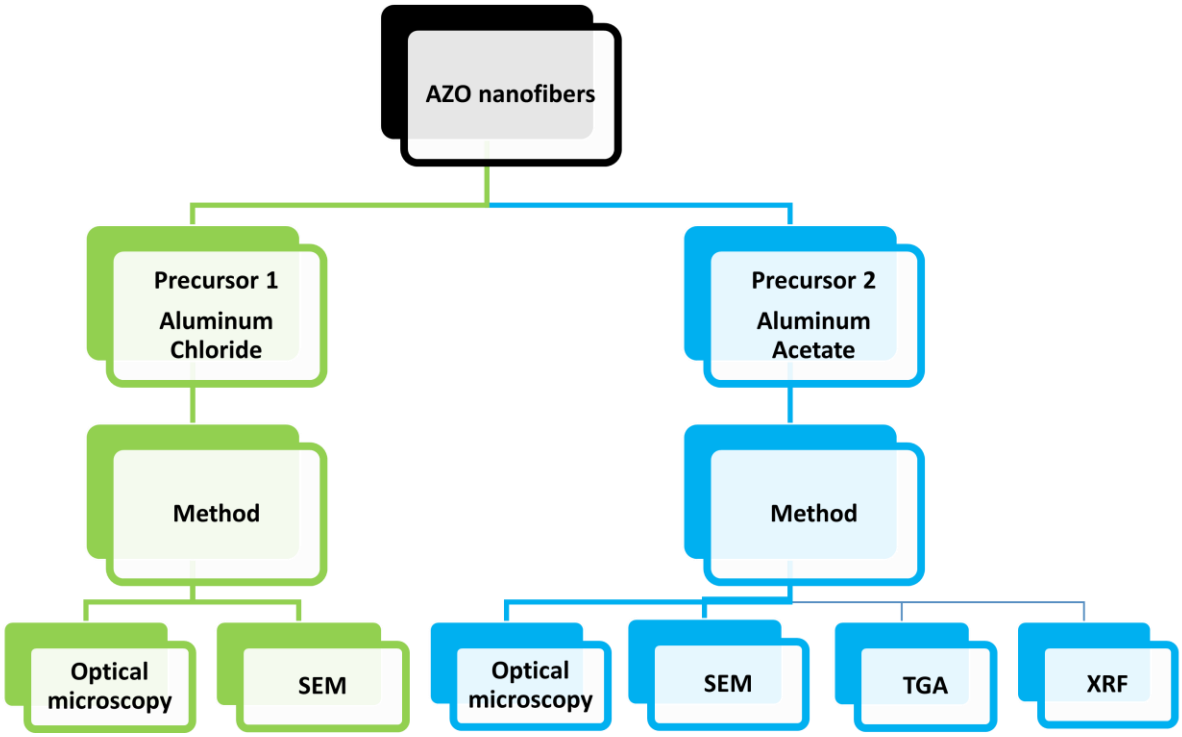

Figure IV. 1. Diagram showing the methodology used for Al:ZnO nanofibers.

For the doping of zinc oxide nanofibers, two precursors were tested during this work. At first, following the work of a team from the University of Surakarta in Indonesia [245,246]we

have started by the use of aluminum chloride hexahydrate ($AlCl_3.6H_2O$) as precursor, added into the initial solution at different weight concentrations.

$$ZnO + 2HCl \rightarrow ZnCl_2 + H_2O$$

$$ZnCl_2 \leftrightarrow Zn^{2+} + 2Cl^-$$

The after annealing result was a substrate with almost no nanofiber trace. After searching for the causes of the fibers disappearance, it turned out the presence of chloride makes the solution acidic and attacks the zinc oxide nanofiber hence ending up with residual random nanoparticles on the substrates. In fact, zinc oxide remains intact in a neutral media or biological pH, however, it rapidly dissolves and decomposes under acidic conditions as described by the chemical reactions above. [247,248]

Thus a replacement of the precursor was required. So, for the second phase, aluminum acetate was used for doping at same weight concentration as for aluminum chloride and with same procedure. An improvement in the fiber morphology was observed as it will be shown later on. After annealing, aligned nanoparticles were observed that could be linked visually to form nanofibers.

1.2 Materials and methods

To produce the aluminum doped zinc oxide nanofibers, we used the same procedure mentioned in chapter III for the production of zinc precursor. To introduce aluminum, aluminum chloride hexahydrate ($AlCl_3 \cdot 6H_2O$, Merck) as precursor 1 then aluminum acetate ($C_6H_9AlO_6$, Merck) as precursor 2 was mixed, at different weight % (1, 2, 3, and 4 wt%), with 4g of the zinc acetate solution (prepared as mentioned in chap III) and stirred for 2 hours at 70 °C. Homogenization of the zinc acetate-aluminum chloride (then aluminum acetate) solutions with PVA solution was carried out separately at a weight ratio of 1:4 and then stirred at 70 °C for 8 hours. The resulting solutions were allowed to rest at room temperature until the formed foam was clear and then used the next day for electrospinning. The electrospinning parameters used for deposition of AZO nanofibers are mentioned in Table IV.1.

It is important to note that after modification of the aluminum precursor, calculations were carried out to find whether the doping percentage is still the same. In other words, a change in the precursor means that a different molecule was used; although both of them contain only one aluminum atom per molecule, it is possible that upon adding the same mass one precursor may contain more molecule than the other (by considering the molecular mass of each). However, From the calculations it was found that the number of aluminum atoms in both precursors used with mass percentages of 1, 2, 3, and 4 wt%, is almost the same of the order of 10^{21} . Thus the change of precursor did not alter the amount of Al present in the fibers. Detailed values are shown in Table IV.2.

Table IV. 1. Elaboration parameters used for the electrospinning of AZO nanofibers.

Elaboration parameters	
Deposition time	35 min
Voltage (kV)	13
Distance (cm)	13
Flowrate (ml/h)	0.18
Annealing	400°C for 1 hour
Individual sample size	25x25 mm

Table IV. 2.Number of Al atoms in both precursor solution for each wt% of doping.

wt%	***Mass (g)***	***Number of Al atoms***	
		Aluminum Chloride	***Aluminum Acetate***
1	0.4	1.08×10^{21}	1.18×10^{21}
2	0.8	2.17×10^{21}	2.36×10^{21}
3	1.2	3.26×10^{21}	3.56×10^{21}
4	1.6	4.35×10^{21}	4.72×10^{21}

1.3 Pure ZnO nanofibers as reference

1.3.1 Morphological characterization of pure ZnO nanofibers

Morphological changes of pure and Al doped ZnO nanofibers before and after annealing were analyzed by Scanning Electron Microscopy, SEM. The images of pure ZnO nanofibers are

presented in Figure IV.2 as reference for the discussion. An image of ZnO nanofibers by optical microscope is also shown.

SEM experiments were done at LEM3, Université de Lorraine – France, and at LMGP, Université de Grenoble-Alpes – France.

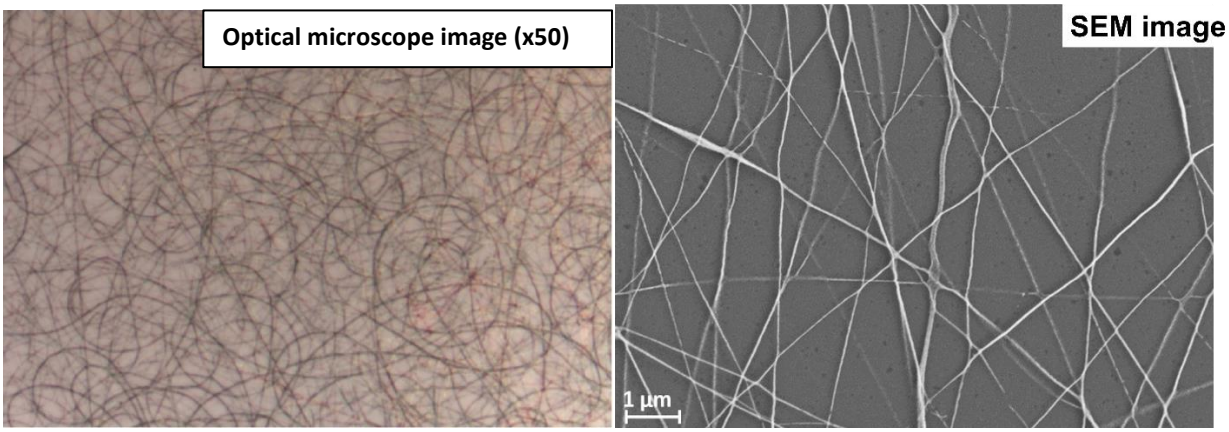

Figure IV. 2. Pure ZnO nanofibers after annealing.

In Figures IV.2, for PVA-ZnO fibers, we observe during all the experimental process a regular distribution of nanofibers on the surface. After annealing, we observe regular ZnO fibers with a mean diameter equal to 40 nm.

1.4 AZO nanofiber elaborated with precursor 1

1.4.1 Morphological characterization

Morphological changes of Al doped ZnO nanofibers obtained from aluminum chloride before and after annealing were analyzed by SEM. These SEM images of AZO nanofibers are presented in Figure IV.3 . (SEM image recordings for 3% Al doped ZnO nanofibers will be also reported later on in this section (Figure IV.4 and IV.5)). The images of Figure IV.3 show the doped nanofibers after annealing. We can observe the remaining traces of nanofibers having a nanoparticle like appearance. Moreover, the residuals are seen to be randomly dispersed on the substrate with no possibility of being visually linked back into lines of nanofibers.

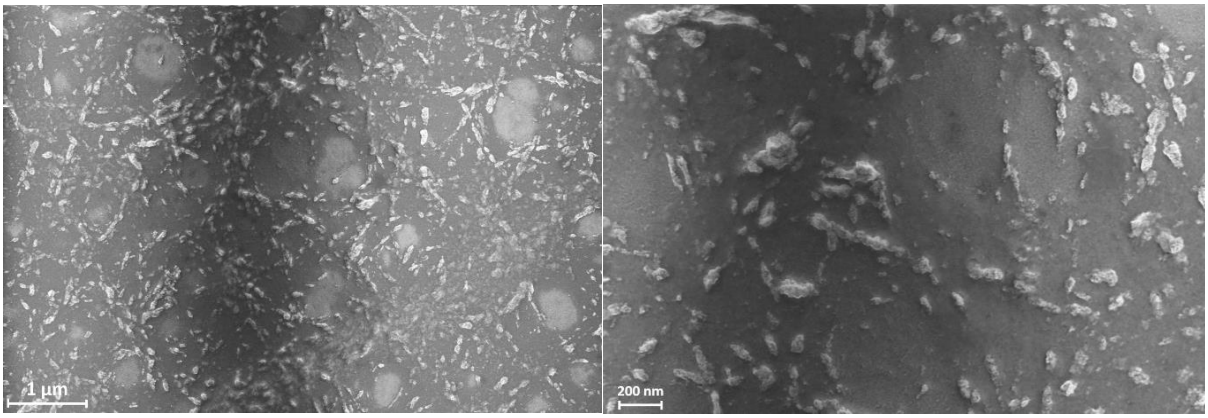

Figure IV. 3. SEM images of Al doped ZnO nanofibers after annealing (Aluminum chloride was used as precursor).

1.5 AZO nanofiber elaborated with precursor 2

1.5.1 Morphological characterization

Morphological changes of Al doped ZnO nanofibers obtained from aluminum acetate before annealing were analyzed by SEM. These SEM images of AZO nanofibers doped with 3 wt% are presented in Figure IV.4 at two scales.

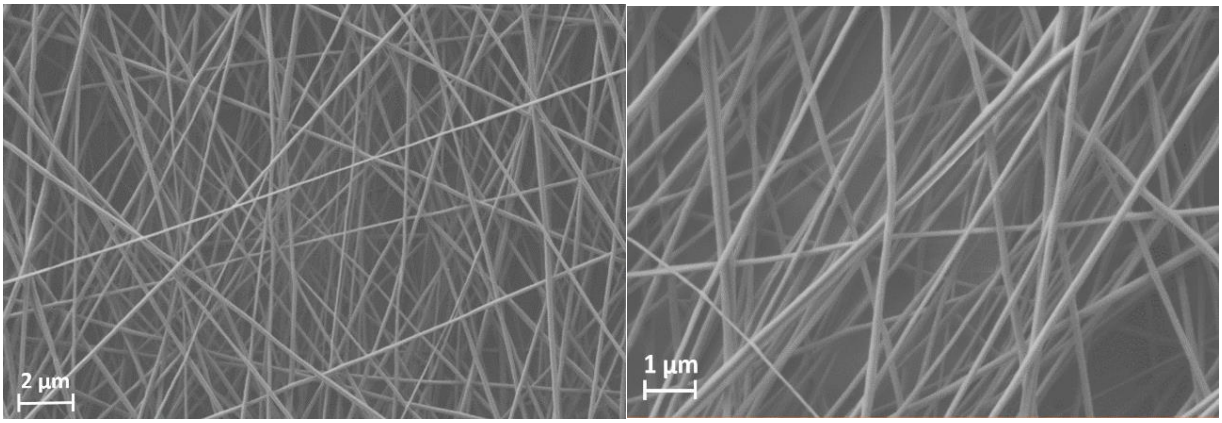

Figure IV. 4. ZnO:Al nanofibers Al[3%] before annealing (Scales: Left 2 µm, Right 1 µm)

In Figure IV.4, images of the doped nanofibers then before annealing are shown. We observe a regular distribution of the fiber on the substrate as observed previously with pure ZnO nanofibers. As for PVA-ZnO fibers, the images clearly indicate that all nanofibers exhibit a cylindrical, branched structure.

We present in Figure IV.5 SEM micrographs of ZnO:Al [3%]nanofibers after annealing deposited from precursor 2, at two scales.

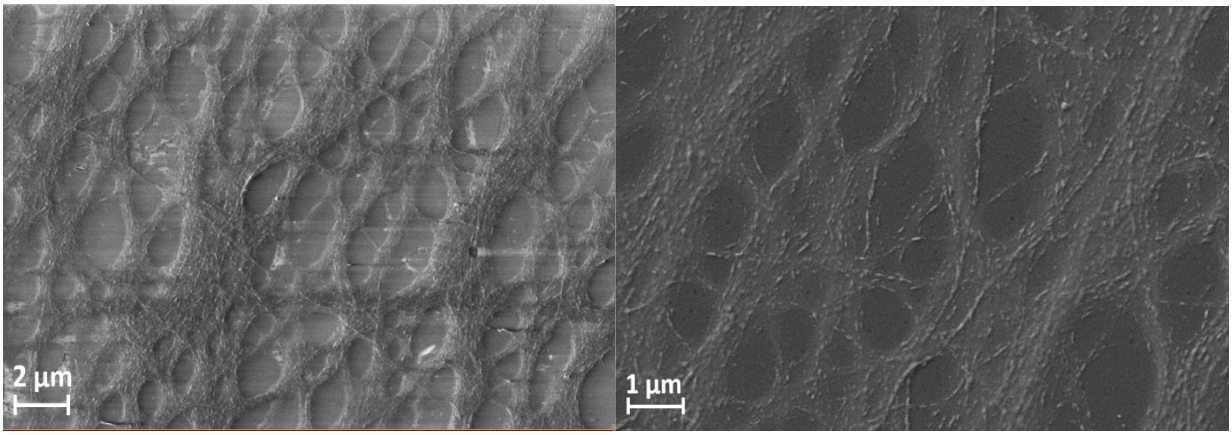

Figure IV. 5. ZnO:Al nanofibers Al[3%] after annealing (Scales: Left 2 µm, Right 1 µm)

On contrary, after the annealing process, in image of Figure IV.5, even if the general shape of fibers still exist, we observed a merge of the nanofibers between them with an enlargement and a rupture in the nanofiber structure of the layer giving rise to a highly irregular surface.

As a result, when we observe the SEM images obtained after annealing and when we compare with images obtained after annealing for pure ZnO, Figure IV.2 and Al doped ZnO, Figure IV.3 and IV.5, we clearly see the straightforward influence of aluminum in this annealing process and by consequence in the realization of nanostructured TCO even if the same process is used in both cases. It seems that Al opposes the crystallization phase of the expected crystalline nanofibers. Nevertheless, in Figure IV.5-right, at the scale of 1 µm, it is obvious that the fiber structure persists but discontinuously in the form of nanoparticles aligned along the fibers initially deposited. For these reasons, it is important to deepen the study in temperature in order to analyze the influence of aluminum in the process of creation of nanofibers by the technique of electrospinning.

2. Thermal analysis (TGA-DSC)

Thermogravimetric analysis (TGA) is an analytical technique used to determine a material's thermal stability and its fraction of volatile components by tracking the weight change that occurs as the sample is heated at a constant rate and is subjected to a controlled atmosphere

and temperature program. Differential Scanning Calorimetry (DSC) is an extensively used thermal analysis technique. It measures enthalpy shifts in samples as a result of changes in chemical and physical properties as a function of temperature and time. Thus, by using coupled techniques TGA-DSC both physical and chemical information could be provided by this measurement such as phase transitions or thermal decomposition.

Figure IV. 6. Apparatus used for TGA-DSC analysis of nanofibers at LERMAB.

Figure IV.6 show the coupled Thermogravimetric Analysis and Differential Scanning Calorimetry, TGA/ DSC apparatus used for the characterizations of AZO nanofibers performed at LERMAB, Université de Lorraine – France. The used apparatus is a simultaneous thermal analyzer *NETZSCH STA 449 F3 Jupiter* that allows the measurement of mass changes and thermal effects between -150 °C and 2400 °C. The six dried nanofiber samples were characterized from room temperature to 700°C under 50 mL/min of air with a constant heating rate of 10°C/min followed by a natural free temperature decrease. The weight loss and the heat flow were jointly recorded and results are presented in Figure IV.7 respectively.

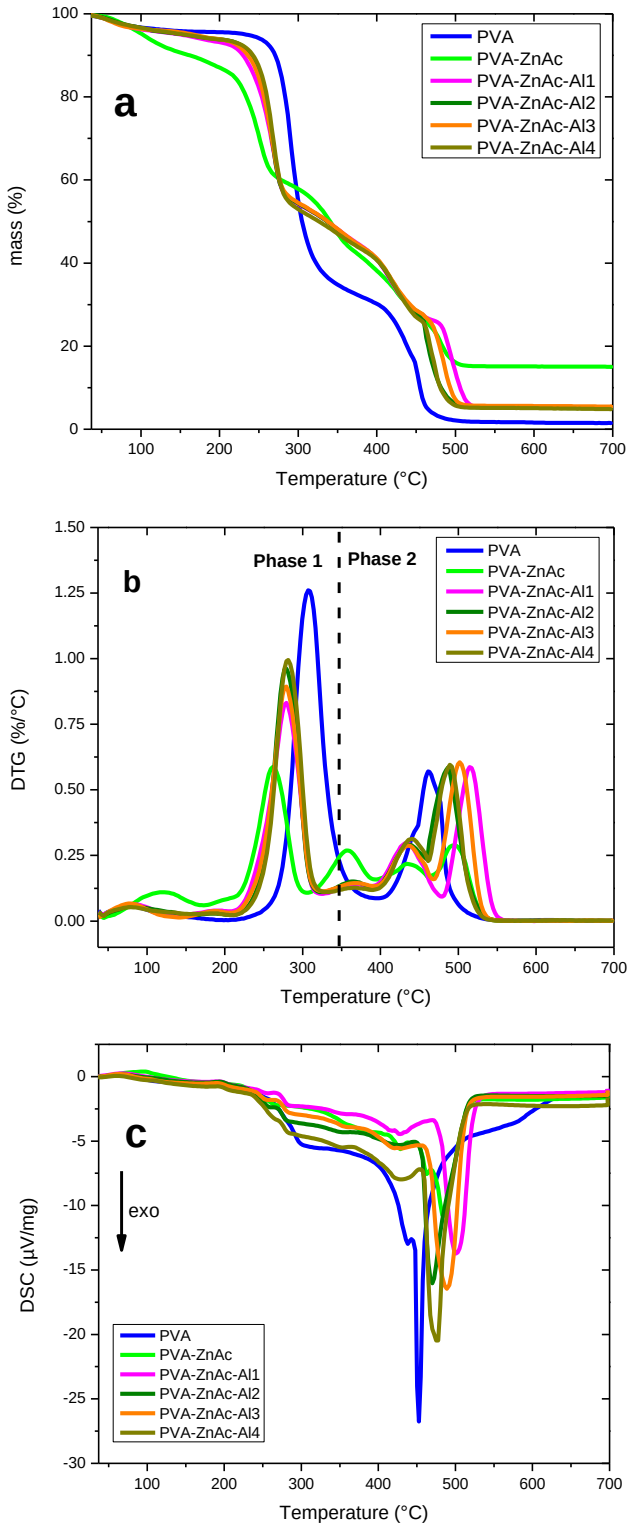

Figure IV. 7. (a) TGA; (b) DTG and (c) DSC graphs of dried PVA, PVA-ZnAc and PVA-ZnAc-Al composite nanofibers.

The general shapes of TGA and DSC characteristics confirm results of literature obtain with nanofibers of pure PVA [249], PVA-ZnO [250] and PVA-ZnO-Al [251]. For all samples we observed in TGA characteristics, Figure IV.7 (a), that the weight loss can be decomposed in three steps. However, some differences exist in the variation of the mass with the temperature between samples. Referred to the pure PVA sample, addition of ZnO induces a shift of the TGA characteristic to the low temperature whereas supplementary addition in PVA-ZnO samples of Al induces a shift to an intermediary temperature position for all PVA-ZnO-Al samples. It can be seen that the initial mass loss at low temperature is mainly due to the release of water (up to 125°C). Beyond this temperature, the weight loss corresponds to the decomposition of the polymer.

The DTG analysis, Figure IV.7 (b) shows that the observed degradation can be considered in 2 distinct phases. In phase 1, we observe that the degradation temperature of pure PVA is equal to 223°C and a shift of this degradation towards low temperatures when zinc acetate is added in the initial mixture. To explain this disparity, Chih-Cheng et al. [252] consider that the thermal process related to zinc acetate dihydrate can be considered as a phenomenon of dehydration favoring the vaporization/decomposition of the solution and thus, in phase 2, favoring the formation of crystalized ZnO. For this reason, adding zinc acetate to the initial PVA solution allows degradation to start faster and therefore at a lower temperature.

Now, when doping with aluminum acetate, the position of the DTG peaks of the first phase is located between those of PVA and PVA-ZnAc. Among this observation, the position of this peak and the rate of degradation appear to be relatively independent of Al concentration. Lopez-Juarez et al. [253] indicate that the decomposition of aluminum acetate by the formation of gamma alumina already begins in this first phase.

Finally, the positions of the DTG peaks in phase 2 for all, appear beyond 470°C within a range of a few degrees, except for PVA-ZnAc which is at a much lower temperature, 420°C, which would confirm the degradation process favored by the introduction of zinc acetate in the solution and then blocked with the introduction of aluminum acetate. In Ref. [254], Ayral et al. show that this shift is explained by the departure of carboxylate groups only up to a temperature of 475°C.

Thus, the TGA/DSC-DTG analyzes indicate that during annealing for the crystallization of nanofibers following electrospinning deposition, it is possible to obtain at lower temperature, in well-defined phases, ZnO nanofibers, in fact better crystallized than aluminum-doped ZnO nanofibers. This analysis thus confirms the observations made by SEM, shown in Figures IV.2 and IV.5, for ZnO and AZO nanofibers, respectively showing after annealing the quality of the nanofibers obtained in this study.

We plot in Figure IV.8 the residual mass % at 700°C and the temperature at which the mass% becomes stable for all the samples. Total residues, as reported in Figure IV.8, equal to 1.49%, 15.03%, 5.14%, 5.03%, 5.47% and 4.83% for pure PVA, PVA-ZnO, PVA-ZNO-Al samples at 1%, 2%, 3%, and 4%, respectively.

Thus, with reference of the pure PVA sample, we clearly observed in Figure IV.8 the influence of each added element in the solution on the residual mass and the associated temperature.

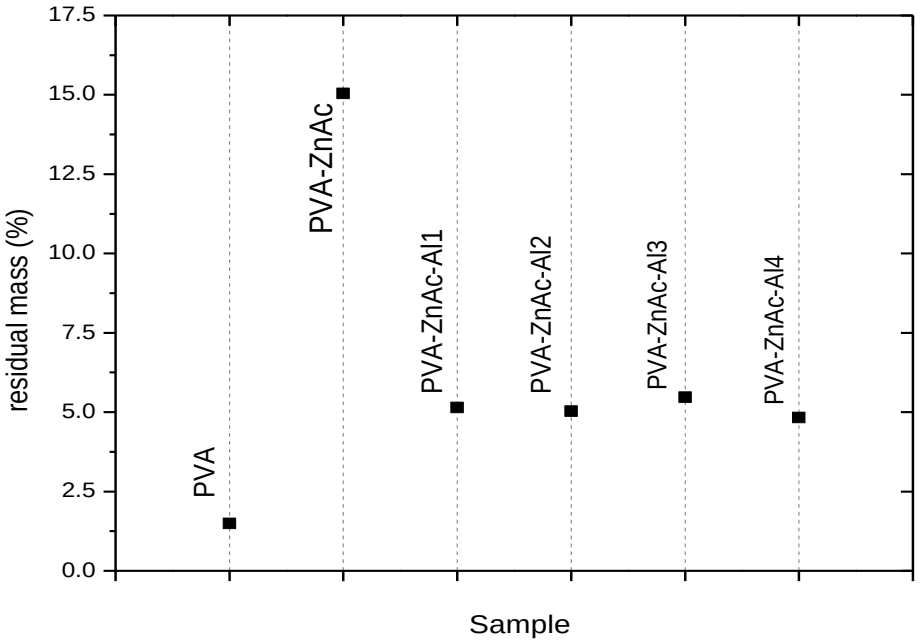

Figure IV. 8. Residual mass % of PVA, PVA-ZnAc and PVA-ZnAc-Al composite nanofibers at the end of heating process.

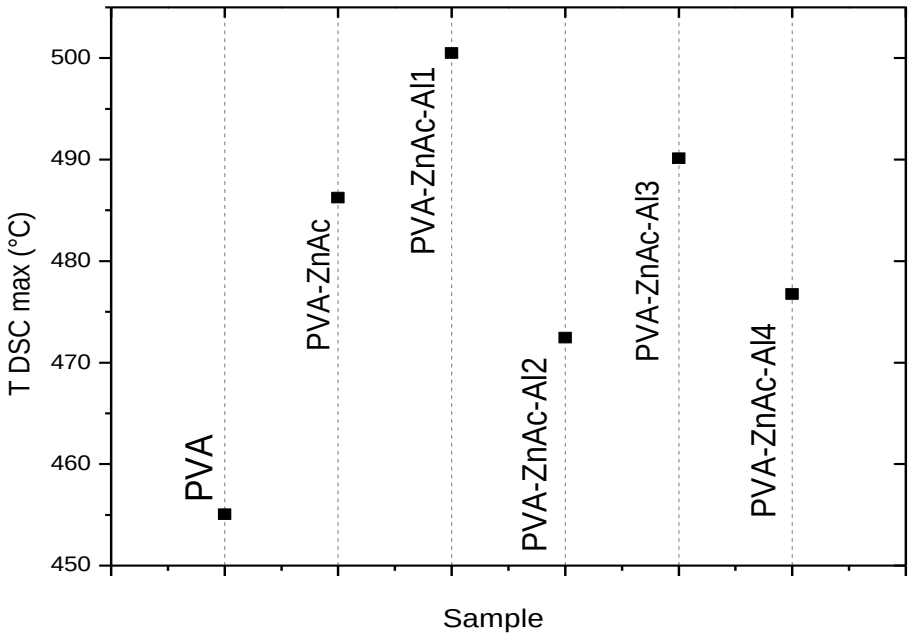

Figure IV. 9. Temperature of the main DSC peak for PVA, PVA-ZnO and PVA-ZnO-Al composite gels.

Consider as a reference the pure PVA sample. For this sample, at the end of the annealing process, the mass is associated to the residual elements of the initial PVA solution. This value has to be found in all samples as the same PVA solutions were used as precursor in the others samples. In the case of the PVA-ZnO sample, the residual mass hugely increases up to 4 times more than that of the pure PVA one. This difference corresponds to the contribution of the mass of ZnO remaining at the end of the annealing process. However and surprisingly, as soon as aluminum is added into the initial mixture, the residual mass is hugely reduced falling down for the sample with Al 2%. Beyond this threshold concentration, the residual mass increases again to reach 94% for the most aluminum-doped sample. The graph showing the residual mass of the samples is illustrated in Figure IV.8.

The weight behavior observed in the TGA characteristics can be analyzed by observation of the DSC characteristics, Figure IV.7 (c), with the consideration of the intensity and position of the endothermic or exothermic peaks with temperature. At low temperature, we observe an irregular decrease of the DSC response associated to the water evaporation.[250] We also observe a main exothermic peak in all samples corresponding to the combustion temperature. [251] The temperature related to this peak is plotted in Figure IV.9. It is noted that after the addition of zinc acetate, this temperature decreases remarkably to increase again

with the addition of aluminum doping. These peaks are simultaneous with the sudden decrease of mass % with increasing temperature and comes in compliance with decomposition of organic residues at the end of the process which seems to be the result of organic material combustion at high temperatures specifically that the measurement process is done under air atmosphere.

To summarize the main results obtained by TGA-DSC, it appears that the Zn element is only present in the undoped sample. As soon as Al is introduced into the fibers, whatever its concentration, it has no influence on the residual mass of the samples. The same is true for the peak temperature of DTG max which is not influenced by the Al concentration: the addition of Zn to pure PVA decreases the degradation temperature but the addition of Al decreases this effect. For the temperature of the DSC peak there is no particular trend except that when there is Zn or Al this temperature is higher than in the case of pure PVA.

This unexpected behavior and the new results that were never observed in literature before, raises a question concerning the doped samples. Logically, after the addition of Al, the residual mass after heat treatment should be equal or slightly higher than that of pure ZnO sample, and that was not observed within our experiments with the aluminum doped zinc electrospun nanofibers. To help understand this behavior, elemental analysis of the as spun fibers (immediately after deposition with no heat treatment) was performed by fluorescence X-ray to control the presence of Zn and Al in the fibers.

3. Elemental analysis by X-Ray Fluorescence (XRF)

After TGA-DSC characterizations of pure and doped nanofibers, the purpose of XRF analysis is to complete, understand and validate the results of TGA-DSC measurements. In fact, this new set of measurements was made for nanofibers immediately after deposition to detect the various element present in the samples before annealing.

X-Ray Fluorescence spectroscopy is a technique that identifies the elemental composition of a substance using the interaction of X-rays with the material. It is a non-destructive technique suitable for all kind of samples, solid, liquids and powders. XRF is thus an effective

technique for a qualitative and quantitative analysis of material composition. The range of detectable elements typically covers all elements from sodium to uranium.

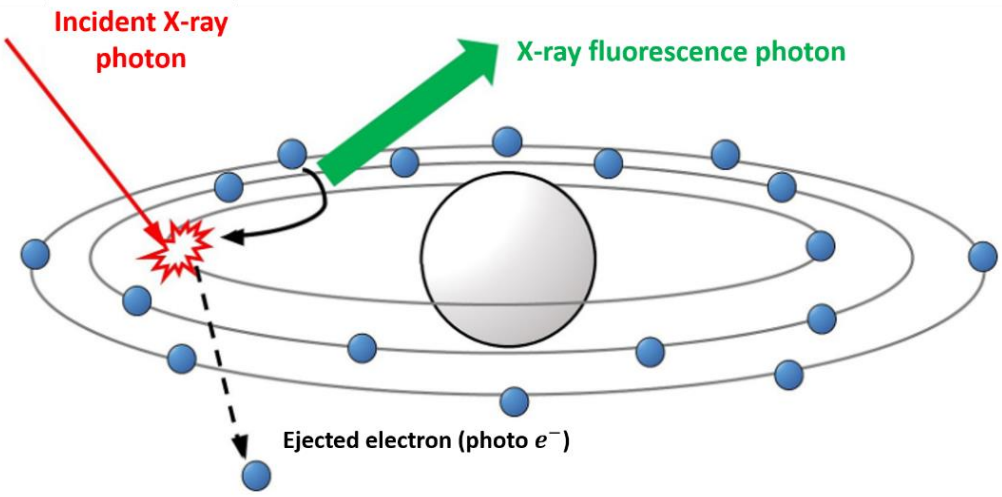

Figure IV. 10. Scheme showing XRF mechanism.

X-rays form part of the electromagnetic spectrum, and are characterized by energies lying between ultra-violet and gamma radiation. Wavelengths are typically in the range 0.01 to 10 nm, which is equivalent to energies of 125 keV to 0.125 keV. XRF describes the process where X-ray radiation excites atoms by pulling electrons from the innermost orbitals. When the atom expands, i.e. when outer electrons fill the inner shells, X-ray fluorescence radiation is emitted (Figure IV.10).

The radiation emitted looks very much like a fingerprint of the atom. Each element has a specific and unique fluorescence. This is why XRF is one of the simplest and most practical ways to find the elemental composition of a specimen and is currently used for a large number of industrial, research and educational applications.

The equipment used for the elemental qualification of the nanofiber samples is *Micro-fluorescence X : XGT – 7000* available at the LMOPS laboratory. It consists of the analysis unit and a computer for analysis process control. The analysis unit chamber is equipped by an X-ray source, detectors and sample holder controlling box. The XGT-7000 is made up of a silicon semiconductor detector which will capture the energy of each photon. This type of detector must be cooled with liquid nitrogen. It only consumes it when the machine performs

a measurement. The XGT-7000 has a 3L liquid nitrogen tank. A camera is located above the plate when it is on the edge. It gives an overall picture of the sample. A second camera is located in the center of the device, near the source X to view the sample in detail and a third camera is located in front of the user to control the height of the sample.

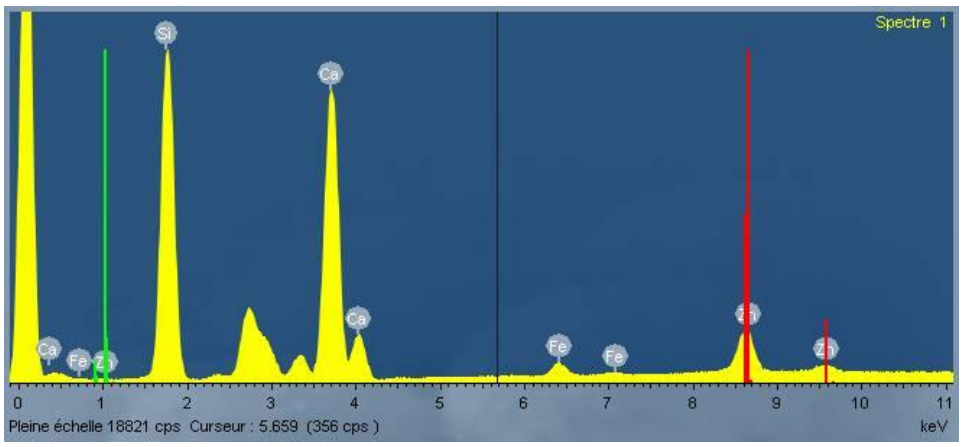

Figure IV. 11. As recorded spectrum for PVA-ZnAc sample.

As spun nanofibers of PVA-ZnAc, PVA-ZnAc-Al (1%, 2%, 3% and 4%) were deposited on glass substrates of size *1x1 cm^2* specifically prepared for the measurement. They were placed one by one in the chamber with identical measurement parameters: X-ray tube voltage (30 kV) and acquisition time 900 s. Figure IV.11 shows the spectrum as recorded and displayed by the software for the PVA-ZnAc sample. For clarity, the obtained spectra for all samples are plotted in one graph of Figure IV.12.

The atomic percentage of Zn and Al are reported in Table IV.3. They show barely detectable values in the samples. This is justified by the fact that the measurements were made before annealing, thus an important amount of water coming from the spinning solution is still present in the nanofibers. In addition, the measured samples are in the form of nanofibers and not uniform layers, thus the density of material is low. However, these results could be considered in a relative way.

Table IV. 3. Atomic percentage of zinc and aluminum present in the nanofibers samples.

	atomic %	
Sample	*Zn*	*Al*
ZnAc	0,14	0
ZnAc-Al1%	0	0,61
ZnAc-Al2	0	0,57
ZnAc-Al3	0,02	0,41
ZnAc-Al4	0,01	0,56

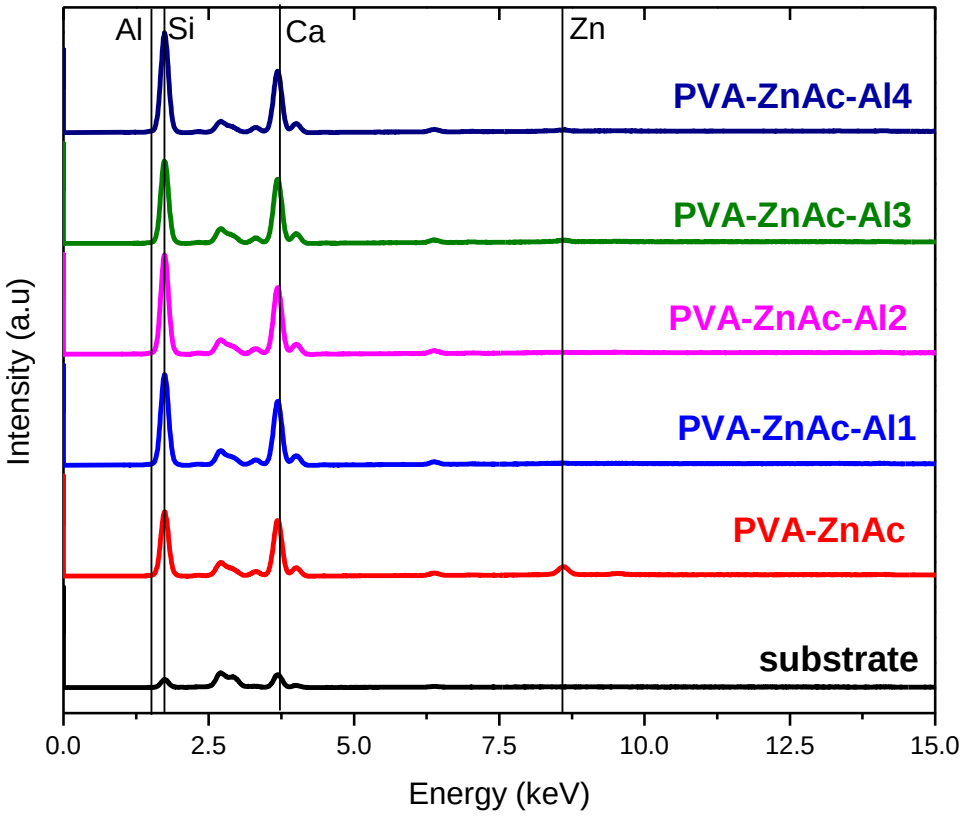

Figure IV. 12. Plotted data for all the samples with elemental identification.

The most significant elements detected in this measurement are Si and Ca originate from the glass substrate used for nanofibers deposition. In compliance with previous results, the XRF measurements showed that zinc disappeared and is no longer detectable as soon as the aluminum is added as precursor. Moreover, the Al presence appears to be independent of the initial dopant solution concentration.

The drop in Zn quantity measured by XRF could justify the mass loss observed at 700°C in the TGA-DSC measurements between the Al-doped Zn samples and the pure Zn sample. However, this does not give a complete explanation for what happens to the Zn in the presence of Al during the creation of the nanofibers.

For recall, electrospinning uses an electric field to eject the precursor solution from the needle to the collector plate. We suggest that the phenomena concerning the Zn and Al presence in the nanofibers could be related to the difference of conductivity for both elements (the conductivity of Al is twice that of Zn) which fully modify the elaboration process of nanofibers during deposition for pure ZnO and Al doped ZnO fibers. [255]

4. First approach by TEM for AZO nanofibers

In the previous chapter, we showed TEM characterization for the ZnO nanofibers performed in LMGP at University of Grenoble-Alpes. The apparatus was coupled with XRD which enabled the identification of the material crystal phase. In this chapter, the characterization of AZO nanofibers by TEM was made at LEM3 laboratory at the University of Lorraine. This microscope is not coupled with XRD. Nevertheless, as TEM apparatus is devoted for, these experiments were able to indicate the crystallization of the nanofibers after annealing, even if the nature of crystallized elements is not confirmed as when TEM characterization is coupled to XRD. Obtained results for AZO nanofibers as function of Al content are summarized in Figure IV.13.

As observed on the images of Figure IV.13, the ZnO nanofibers conserve their shape after annealing. That is not the case for AZO nanofibers as we can only observe random polycrystalline grains except for the lowest Al doping (Figure IV.13 (b)) where a small fiber shaped link is observed between two grain groups. The associated diffraction patterns of some samples illustrated in Figure IV.14 show that these grains, in some cases, are polycrystalline, but no clear link could be established for the influence of Al content on our observation.

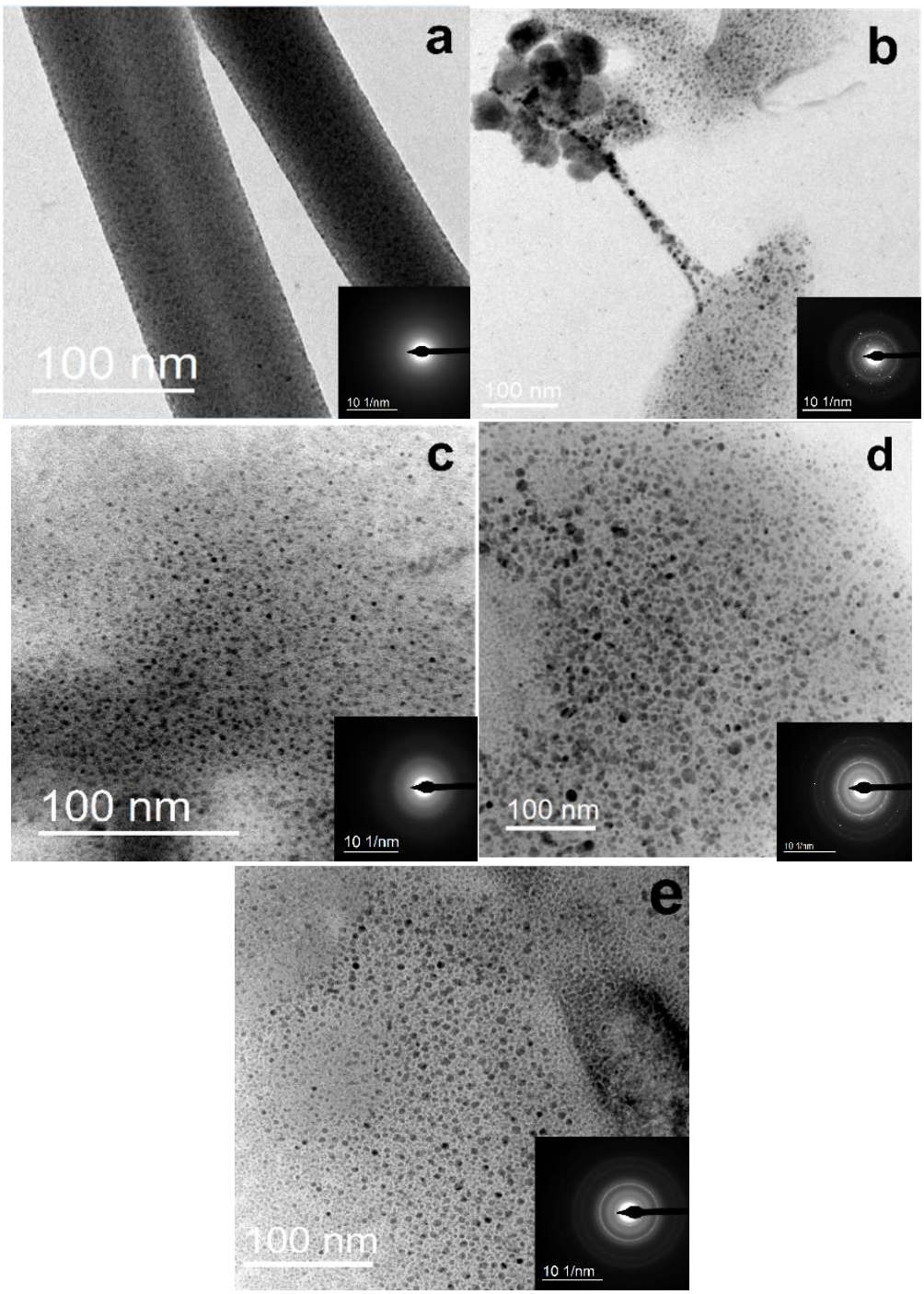

Figure IV. 13. TEM images of nanofibers after annealing; (a) ZnO, (b), (c), (d) and (e) for AZO 1wt%, 2wt%, 3wt% and 4wt% respectively.

4.1 Qualitative analysis of ZnO-AZO samples as function of substrate

During the elaboration process of doped nanofibers and in addition to the glass substrate used for all previous depositions, we made electrospinning deposition on silicon substrate.

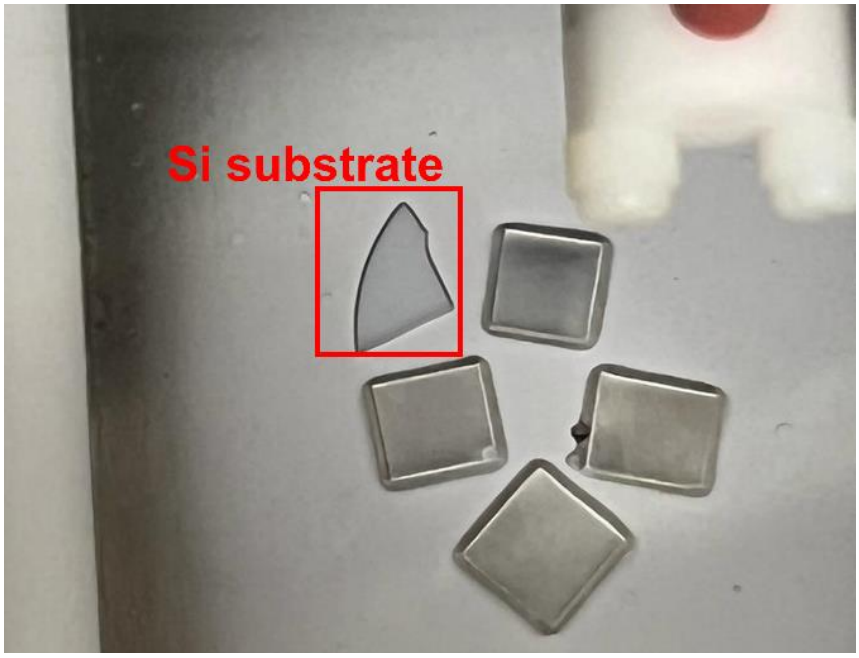

Figure IV. 14. Photo showing the difference in density for silicon and glass nanofibers during deposition.

For the spinning process to occur, a high voltage is applied between the needle and the collector plate where the substrates are placed for deposition. Since glass is an insulator, the electric field may not be homogenous and the deposition of fibers not uniform, on the contrary silicon substrates are conductive and do not cause any distortion of the electric field, thus the deposited fibers. By consequence, a remarkable difference is observed regarding the density of deposited fibers, when placing both silicon and glass substrate on the plate. This is observed in the images of Figure IV.14.

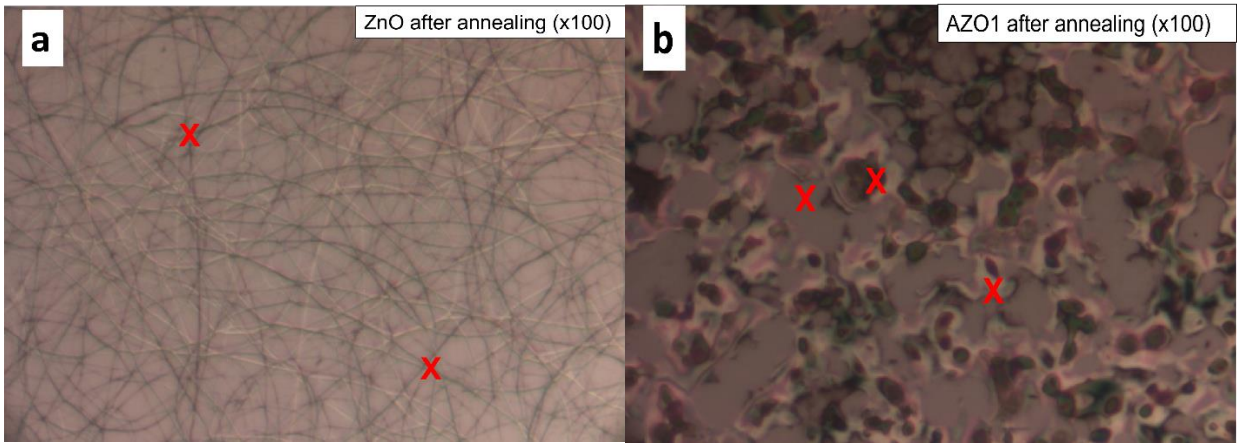

Figure IV. 15. Optical microscopy images at (x100) after annealing of (a) ZnO and (b) AZO 1% nanofibers. the red marks show the chosen places for spectra acquisition.

Concerning the fibers aspect deposited on silicon substrate, as observed by optical microscopy, no remarkable change was noted for the fibers aspect before annealing if compared to the ones deposited on glass substrate. In addition to the reasons mentioned above, the choice for depositing nanofibers on silicon substrate was planned for Raman structural characterization. Even though the density is more important on such substrate, the fibers do not ensure a complete coverage of the substrate, and in addition, the diameter of the fibers is still very thin. Moreover, during the spectra acquisition, whatever the place that we choose for measurement (dark or bright spots), the peak coming from the substrate was always dominant. In Figure IV.15 the red marks show the selected places of the spectra acquisition on a sample of ZnO nanofibers (a) and Al doped ZnO (b) after annealing. Whether the nanofibers were deposited on silicon or glass, the dominant peak was that of the substrate thus masking the possibility of going back to the structural properties of the fibers. Hence, the detection of zinc oxide peaks by Raman was unfortunately not successful and unable to provide any conclusive points.

5. Conclusions

In the purpose of improving the conductivity of zinc oxide nanofibers, the doping approach with aluminum was discussed in this chapter. At first, aluminum chloride was used as a precursor; it was added in different concentrations to the initial precursor solution used for the fabrication of zinc oxide nanofibers. The deposited fibers went through annealing process only to discover after SEM imaging that the fibers completely disappeared from the substrate. It turned out that the precursor used for doping (aluminum chloride) was at the origin of this phenomenon. In fact, the acidic media coming from the use of a chloride precursor, directly affect the zinc oxide nanofibers formation since the latter remains intact in around neutral pH but is immediately dissolved under acidic one, and that was our case. Hence, a swap for aluminum acetate was made to maintain as possible an almost neutral pH solution. After precursor change, a refinement in the nanofibers morphology was observed: perfectly shaped before annealing and improved structure after annealing.

The thermal behavior of a series of nanofibers samples produced by the electrospinning method has been studied. Starting from a PVA solution, these nanofibers are zinc oxide and zinc oxide doped with 1%, 2%, 3% and 4% aluminum.

The main objective was to analyze the behavior of nanofibers during the post-growth annealing phase. This is why, beyond the electrospinning method used for fiber growth, scanning electron microscopy which allowed a qualitative analysis of the samples, and complementary studies that contribute in the understanding of such modified structure upon heat treatment were carried on, precisely thermogravimetric analysis and X-ray fluorescence.

The particular role of aluminum doping in the solution with a strong dependence of the melting temperature on the concentration was showed. These variations in degradation temperature as a function of zinc and aluminum can be explained by a strong interaction at the interface of ZnO and PVA, attenuated by the aluminum in the doped nanofibers.

These analyzes also clearly show that the degradation temperature is relatively low compared to the temperature necessary for the crystallization of nanofibers based on ZnO

and ZnO-Al, but also that the residual mass in the doped fibers approaches the residual mass of the pure PVA. Thus, we point out that ZnO being vaporized beyond this melting temperature, the production of ZnO-Al (AZO) nanofibers is particularly difficult or even impossible by the electrospinning method with annealing in air.

General Conclusions and Perspectives

General Conclusions and Perspectives

In this manuscript, we have presented the work accomplished during my thesis at LMOPS. This work focused on the development of nanocomposites based on ZnO and FTO for their use as transparent conductive electrodes. The nanocomposites used during this work have two different configurations and are designed as follows: ZnO nanofibers with a thin layer of FTO. The choice of nanofibers as a nanostructure offers the possibility of realizing transparent, conductive and flexible electrodes at the same time. In this work, the targeted applications for the use of the as developed transparent conductive electrodes based on nano-fibers are those related to the recent development of sensors - photovoltaic cells, for example new perovskite or dye cells allowing their integration on flexible substrates.

The first chapter begins by a general introduction about the transparent conductive oxides that states their unique properties with the different types of applications that they can be used for in addition to the different elaboration methods used for their fabrication. More specifically, a presentation of three TCO families (ITO, ZnO and FTO) were chosen due to their potential as transparent electrodes and importance in the market of opto-electronic devices. Nevertheless, the required properties of TCO are going beyond transparency and conductivity, to increased performance, cost effective and environmental friendly. Fulfilling these new requisites demands some changes in the traditional conception of TCO. Hence the integration of nanomaterials to manage and control functional capabilities became a challenge of today. We discussed in the second part of this chapter this new approach by giving a specific attention to Zinc Oxide nanofibers which appear to have great potential for transparent electrodes.

The second chapter is considered as an intermediate step and building block since it enables us to establish reference results without the nanostructuration which will be discussed in the following chapters. In this chapter, we give a detailed morphological and structural characterization of two thin films (ZnO and FTO). Firstly, in the ZnO thin film, we showed the particular link between the substrate position during the deposition process and the morphological properties of the film notably the grain size and texture. These parameters have direct influence on the generation of excitons with light and hence the optical

properties, specifically absorption and transmission of the film. Secondly, we have experimentally developed FTO thin films deposited by ultrasonic spray pyrolysis with different carrier gas flow rate and used a commercial FTO sample as reference sample. The discussions on structural characterization by Raman spectroscopy and morphological by AFM were carried out in this part. Through these techniques, we showed that the films are dense nanocrystallized and rough. In addition well defined characteristic peaks of FTO were found in the Raman spectra which indicates the good quality of the developed samples during this work in compliance with commercial one.

The third chapter presents the various aspects occurring in the electrospinning technique used for the elaboration of transparent conductive electrodes developed on the basis of ZnO nanofibers. This technique, generally used for the manufacture of films in the form of polymer or organic nanowires, is an original and challenging technique for the development of transparent conductive electrodes. Indeed, as indicated in the manuscript, our work is based on a very limited number of publications relating to ZnO nanofibers from water based solutions, obtained by electrospinning.

First of all we give a presentation of the electrospinning technique with all parameters having influence on the nanofiber elaboration. Along this chapter, we successfully deposited Zinc Oxide nanofibers by the electrospinning technique and showed the nanometric diameter and well crystallized structure through Transmission Electron Microscopy (TEM). We also made nanostructured samples by covering the ZnO nanofibers with a FTO thin film by the spray pyrolysis technique. The resultant samples were subject to morphological, optical and electrical characterizations. In the SEM images, the samples showed a nanostructured aspect with uniform grain size distribution even when compared to the standard reference FTO. Optical properties, more specifically, transmission and haze factor were measured by UV-vis spectrophotometer. We realized two sample configurations: FTO_ZnO and ZnO_FTO. The samples showed good transmission values regardless of the nanofiber deposition time for the case were the thin film was deposited over the nanofibers. However, the recorded spectra for both cases where nanofibers were deposited over glass substrate and commercial FTO showed no significant contribution caused by the nanofibers; instead the results were similar to the corresponding reference substrate. Additionally, an

enhancement in the predicted haze values was also seen, indicating that we were successful in prolonging the light path in the nanocomposite samples without degrading their transparency. As for the electrical qualities, it was possible to test the resistivity of the nanocomposite samples where the results recorded an increase in resistivity values following the integration of ZnO nanofibers with the FTO thin film, but nevertheless the acquired values of the order 10^{-3} stays acceptable. Finally, even though we noted a degradation in the conductivity of the nanocomposite samples, that was expected and explained by the difference of conductivity between ZnO and FTO, we pointed out a remarkable increase in the haze factor for the nanocomposite FTO_ZnO samples.

To overcome this drawback related to conductivity, adding Aluminum as dopant to the ZnO nanofibers is suggested in the last chapter. The number of publications relating to these new works is still clearly reduced in the literature. The addition of doping elements showed to have efficient contribution in the increase of conductivity. However, in the electrospinning process, the dopant addition into precursor solutions of PVA and zinc acetate and its effect on the morphological, structural and electric properties of ZnO nanofibers was poorly investigated by authors. That being the case, we concentrate in this chapter on creating the precursor solutions needed to produce aluminum-doped zinc oxide nanofibers with PVA serving as the polymer matrix. We also go over an optimization procedure to produce well-shaped and organized nanofibers as well as the many implications this doping has on various levels. On a first level, we made a change in the aluminum precursor, initially aluminum chloride by aluminum acetate to maintain a solution pH suitable for ZnO nanofibers. After the precursor swap we observed a significant improvement in the nanofibers shape specifically after annealing. On another level, we made optimization through the annealing process and for this reason, we recorded the thermal behavior through TGA-DSC of nanofiber samples having different Al concentrations. This complementary study was chosen to contribute to the understanding of the modified nanofiber structure after heat treatment. Through this analysis we showed that the degradation temperature is relatively low compared to the temperature necessary for the crystallization of nanofibers based on ZnO and ZnO-Al, but also that the residual mass in the doped fibers approaches the residual

mass of the pure PVA. Thus, we point out that the production of ZnO-Al (AZO) nanofibers is particularly difficult or even impossible by the electrospinning method with annealing in air.

This final outcome opens up new doors for the future. Concerning the electrospinning part, knowing that our work has shown the disappearance of Zn in the nanofibers from the beginning of Al doping, it seems strongly necessary to have to deepen the study of the deposit to understand the fate of Zn in the Al doped fibers. In the work presented in this thesis, we have focused on the characterizations of nanofibers from their prints to their crystallization by annealing. Our next short-term work will consist in carrying out deeper characterizations of the precursor solution to verify its composition after addition of aluminum acetate. It is hoped that these new measurements will allow an adaptation of the methodology followed in the preparation of the initial solution with, at the end, many tests in temperatures, in controlled atmosphere or not, or other changes which could be highlighted. by these new measures.

Regardless of the final electrical and optical properties expected in the nanofibers, we propose to also try another metal dopant for the zinc oxide nanofibers, especially using the same methodology and approach presented here to understand if the phenomenon is bound only to aluminum. This new study, complementary to that proposed above in first perspective, should make it possible to understand the role of aluminum but also to consider a new dopant to improve the conduction of nanostructured electrodes by spun nanofibers.

In addition to the physico-chemical characterizations considered as perspectives, perspectives concerning more technical processes on nanofibers are also imagined for this work. One new approach was suggested by Pr. D. Bellet and Dr. C. Jiménez of the LMGP laboratory-Grenoble. As an alternative for doping to increase the conductivity, they have shown that cold welding is a promising technique for silver nanowires. It consists of applying moisture on the nanofiber film, without any technical support like the addition of materials or the use of specific facilities. This moisture induces a powerful driving capillary force which will be at the origin of fiber to fiber junction welding. This way a reduction of the junction resistance occurs by using a very simple technique without the need of doping elements. We

plan in a near future to use this cold welding technique to increase the conductivity of electrospun ZnO and ZnO nanofibers doped with metal ions.

Our work carried out during this thesis, is relatively upstream compared to the planned applicative purpose concerning the realization of photovoltaic cells. In the continuity, it is then considered to extend our work by moving towards the devices and in particular, by the realization of a photovoltaic cell of the perovskite type integrating this type of electrode. The cells could, for example, be produced in partnership with a laboratory such as XLIM in Limoges with which the laboratory collaborates.

Finally, as a new perspective opened by our work, zinc oxide nanofibers have the potential to be used in many devices and for many types of applications. We can cite, apart from their use as transparent conductive electrodes, they can be potentially interesting in biomedical applications where they can be used for dressing and healing (thanks to their non-toxicity) or as gas sensors for the detection of toxic substances and combustible gases. We do not plan to work directly on new developments, except within the framework of a collaboration, but the results that we have presented represent a possible contribution to this work by other teams.

References

References

(1) Kim, C.-L.; Jung, C.-W.; Oh, Y.-J.; Kim, D.-E. A Highly Flexible Transparent Conductive Electrode Based on Nanomaterials. *NPG Asia Mater* **2017**, *9* (10), e438–e438. https://doi.org/10.1038/am.2017.177.

(2) Bellet, D.; Lagrange, M.; Sannicolo, T.; Aghazadehchors, S.; Nguyen, V. H.; Langley, D. P.; Muñoz-Rojas, D.; Jiménez, C.; Bréchet, Y.; Nguyen, N. D. Transparent Electrodes Based on Silver Nanowire Networks: From Physical Considerations towards Device Integration. *Materials* **2017**, *10* (6), 570. https://doi.org/10.3390/ma10060570.

(3) Badeker, K. Concerning the Electricity Conductibility and the Thermoelectric Energy of Several Heavy Metal Bonds. *Annalen der Physik* **1907**, *22*, 749.

(4) Lewis, B. G.; Paine, D. C. Applications and Processing of Transparent Conducting Oxides. *MRS Bulletin* **2000**, *25* (8), 22–27. https://doi.org/10.1557/mrs2000.147.

(5) Li, D.; Lai, W.-Y.; Zhang, Y.-Z.; Huang, W. Printable Transparent Conductive Films for Flexible Electronics. *Advanced Materials* **2018**, *30* (10), 1704738. https://doi.org/10.1002/adma.201704738.

(6) Langley, D.; Giusti, G.; Mayousse, C.; Celle, C.; Bellet, D.; Simonato, J.-P. Flexible Transparent Conductive Materials Based on Silver Nanowire Networks: A Review. *Nanotechnology* **2013**, *24* (45), 452001. https://doi.org/10.1088/0957-4484/24/45/452001.

(7) Wu, Z.; Chen, Z.; Du, X.; Logan, J. M.; Sippel, J.; Nikolou, M.; Kamaras, K.; Reynolds, J. R.; Tanner, D. B.; Hebard, A. F.; Rinzler, A. G. Transparent, Conductive Carbon Nanotube Films. *Science* **2004**, *305* (5688), 1273–1276. https://doi.org/10.1126/science.1101243.

(8) TCO-Ginley2000.Pdf.

(9) Lewis, B. G.; Paine, D. C. Applications and Processing of Transparent Conducting Oxides. *MRS Bull.* **2000**, *25* (8), 22–27. https://doi.org/10.1557/mrs2000.147.

(10) Gordon, R. Criteria for Choosing Transparent Conductors. **2000**. https://doi.org/10.1557/MRS2000.151.

(11) Bianchi, C. Near Infrared Photothermoelectric Effect in Transparent AZO/ITO/Ag/ITO Thin Films. *Scientific Reports* **2021**, 11.

(12) Minami, T. New N-Type Transparent Conducting Oxides. *MRS Bulletin* **2000**, *25* (8), 38–44. https://doi.org/10.1557/mrs2000.149.

(13) Rey, G.; Ternon, C.; Modreanu, M.; Mescot, X.; Consonni, V.; Bellet, D. Electron Scattering Mechanisms in Fluorine-Doped SnO2 Thin Films. *Journal of Applied Physics* **2013**, *114* (18), 183713. https://doi.org/10.1063/1.4829672.

(14) Minami, T. Transparent Conducting Oxide Semiconductors for Transparent Electrodes. *Semicond. Sci. Technol.* **2005**, *20* (4), S35–S44. https://doi.org/10.1088/0268-1242/20/4/004.

(15) Burstein, E. Anomalous Optical Absorption Limit in InSb. *Phys. Rev.* **1954**, *93* (3), 632–633. https://doi.org/10.1103/PhysRev.93.632.

(16) Ginley, D.; Catalano, A.; Schock, H. W.; Eberspacher, C.; Peterson, T. M.; Wada, T. Thin Films for Photovoltaic and Related Device Applications. **1996**.

(17) Jain, V. K.; Kulshreshtha, A. P. Indium-Tin-Oxide Transparent Conducting Coatings on Silicon Solar Cells and Their "Figure of Merit." *Solar Energy Materials* **1981**, *4* (2), 151–158. https://doi.org/10.1016/0165-1633(81)90038-1.

(18) Nisha, M.; Anusha, S.; Antony, A.; Manoj, R.; Jayaraj, M. K. Effect of Substrate Temperature on the Growth of ITO Thin Films. *Applied Surface Science* **2005**, *252* (5), 1430–1435. https://doi.org/10.1016/j.apsusc.2005.02.115.

(19) Dugrenil, B.; Séguy, I.; Lee, H.-Y.; Camps, T.; Lin, Y.-C.; Doucet, J. B.; Chiu, Y.-S.; Salvagnac, L.; Bedel-Pereira, E.; Ternisien, M.; Lee, C. T.; Bardinal, V. AZO Electrodes Deposited by Atomic Layer Deposition for OLED Fabrication. In *Organic Photonics VI*; SPIE, 2014; Vol. 9137, pp 127–132. https://doi.org/10.1117/12.2052504.

(20) Sarma, B.; Barman, D.; Sarma, B. K. AZO (Al:ZnO) Thin Films with High Figure of Merit as Stable Indium Free Transparent Conducting Oxide. *Applied Surface Science* **2019**, *479*, 786–795. https://doi.org/10.1016/j.apsusc.2019.02.146.

(21) Benhaoua, B.; Abbas, S.; Rahal, A.; Benhaoua, A.; Aida, M. S. Effect of Film Thickness on the Structural, Optical and Electrical Properties of SnO2: F Thin Films Prepared by Spray Ultrasonic for Solar Cells Applications. *Superlattices and Microstructures* **2015**, *83*, 78–88. https://doi.org/10.1016/j.spmi.2015.03.017.

(22) *Reading: Abundance of Elements in Earth's Crust | Geology*. https://courses.lumenlearning.com/geology/chapter/reading-abundance-of-elements-in-earths-crust/ (accessed 2022-03-21).

(23) Lide, D. R.; Baysinger, G.; Chemistry, S.; Berger, L. I.; Goldberg, R. N.; Kehiaian, H. V. CRC Handbook of Chemistry and Physics. 2661.

(24) *Periodic Table of Elements: Sorted by Ionic Radius (EnvironmentalChemistry.com)*. https://environmentalchemistry.com/yogi/periodic/ionicradius.html (accessed 2021-10-14).

(25) Asemi, M.; Ahmadi, M.; Ghanaatshoar, M. Preparation of Highly Conducting Al-Doped ZnO Target by Vacuum Heat-Treatment for Thin Film Solar Cell Applications. *Ceramics International* **2018**, *44* (11), 12862–12868. https://doi.org/10.1016/j.ceramint.2018.04.096.

(26) Muchuweni, E.; Sathiaraj, T. S.; Nyakotyo, H. Effect of Gallium Doping on the Structural, Optical and Electrical Properties of Zinc Oxide Thin Films Prepared by Spray Pyrolysis. *Ceramics International* **2016**, *42* (8), 10066–10070. https://doi.org/10.1016/j.ceramint.2016.03.110.

(27) Chava, R. K.; Kang, M. Improving the Photovoltaic Conversion Efficiency of ZnO Based Dye Sensitized Solar Cells by Indium Doping. *Journal of Alloys and Compounds* **2017**, *692*, 67–76. https://doi.org/10.1016/j.jallcom.2016.09.029.

(28) Zhou, N.; Cheng, Q.; Li, L.; Zhou, H. Doping Effects in SnO2 Transport Material for High Performance Planar Perovskite Solar Cells. *J. Phys. D: Appl. Phys.* **2018**, *51* (39), 394001. https://doi.org/10.1088/1361-6463/aad685.

(29) Roy, S. S.; Podder, J. Synthesis and Optical Characterization of Pure and Cu Doped SnO2 Thin Films Deposited by Spray Pyrolysis. 7.

(30) Kaur, J.; Shah, J.; Kotnala, R. K.; Verma, K. C. Raman Spectra, Photoluminescence and Ferromagnetism of Pure, Co and Fe Doped SnO2 Nanoparticles. *Ceramics International* **2012**, *38* (7), 5563–5570. https://doi.org/10.1016/j.ceramint.2012.03.075.

(31) Halvani Anaraki, E.; Kermanpur, A.; Mayer, M. T.; Steier, L.; Ahmed, T.; Turren-Cruz, S.-H.; Seo, J.; Luo, J.; Zakeeruddin, S. M.; Tress, W. R.; Edvinsson, T.; Grätzel, M.; Hagfeldt, A.; Correa-Baena, J.-P. Low-Temperature Nb-Doped SnO2 Electron-Selective Contact Yields over 20% Efficiency in Planar Perovskite Solar Cells. *ACS Energy Lett.* **2018**, *3* (4), 773–778. https://doi.org/10.1021/acsenergylett.8b00055.

(32) Sun, Q.; Li, G.; Tian, T.; Zeng, J.; Zhao, K.; Zheng, L.; Barré, M.; Dittmer, J.; Gouttenoire, F.; Rousseau, A.; Kassiba, A. H. Co-Doping Effects of (Al, Ti, Mg) on the Microstructure and Electrical Behavior of ZnO-Based Ceramics. *Journal of the American Ceramic Society* **2020**, *103* (5), 3194–3204. https://doi.org/10.1111/jace.16999.

(33) Jiang, M.; Liu, X. Structural, Electrical and Optical Properties of Al–Ti Codoped ZnO (ZATO) Thin Films Prepared by RF Magnetron Sputtering. *Applied Surface Science* **2008**, *255* (5, Part 2), 3175–3178. https://doi.org/10.1016/j.apsusc.2008.09.012.

(34) Sato, H.; Minami, T.; Takata, S.; Yamada, T. Transparent Conducting P-Type NiO Thin Films Prepared by Magnetron Sputtering. *Thin Solid Films* **1993**, *236* (1), 27–31. https://doi.org/10.1016/0040-6090(93)90636-4.

(35) Kawazoe, H.; Yanagi, H.; Ueda, K.; Hosono, H. Transparent P-Type Conducting Oxides: Design and Fabrication of p-n Heterojunctions. *MRS Bulletin* **2000**, *25* (8), 28–36. https://doi.org/10.1557/mrs2000.148.

(36) Kawazoe, H.; Yasukawa, M.; Hyodo, H.; Kurita, M.; Yanagi, H.; Hosono, H. P-Type Electrical Conduction in Transparent Thin Films of CuAlO2. *Nature* **1997**, *389* (6654), 939–942. https://doi.org/10.1038/40087.

(37) David, T.; Goldsmith, S.; Boxman, R. L. Electro-Optical and Structural Properties of Thin ZnO Films, Prepared by Filtered Vacuum Arc Deposition. *Thin Solid Films* **2004**, *447–448*, 61–67. https://doi.org/10.1016/j.tsf.2003.09.023.

(38) Nasser, R.; Song, J.-M.; Elhouichet, H. Epitaxial Growth and Properties Study of P-Type Doped ZnO:Sb by PLD. *Superlattices and Microstructures* **2021**, *155*, 106908. https://doi.org/10.1016/j.spmi.2021.106908.

(39) Joseph, M.; Tabata, H.; Kawai, T. P-Type Electrical Conduction in ZnO Thin Films by Ga and N Codoping. *Jpn. J. Appl. Phys.* **1999**, *38* (11A), L1205. https://doi.org/10.1143/JJAP.38.L1205.

(40) Lu, J. G.; Ye, Z. Z.; Zhuge, F.; Zeng, Y. J.; Zhao, B. H.; Zhu, L. P. P-Type Conduction in N–Al Co-Doped ZnO Thin Films. *Appl. Phys. Lett.* **2004**, *85* (15), 3134–3135. https://doi.org/10.1063/1.1803935.

(41) Pan, X.; Ye, Z.; Li, J.; Gu, X.; Zeng, Y.; He, H.; Zhu, L.; Che, Y. Fabrication of Sb-Doped p-Type ZnO Thin Films by Pulsed Laser Deposition. *Applied Surface Science* **2007**, *253* (11), 5067–5069. https://doi.org/10.1016/j.apsusc.2006.11.014.

(42) Wellings, J. S.; Chaure, N. B.; Heavens, S. N.; Dharmadasa, I. M. Growth and Characterisation of Electrodeposited ZnO Thin Films. *Thin Solid Films* **2008**, *516* (12), 3893–3898. https://doi.org/10.1016/j.tsf.2007.07.156.

(43) Sahoo, T.; Jeon, J. W.; Kannan, V.; Lee, C. R.; Yu, Y. T.; Song, Y. W.; Lee, I. H. Hydrothermal Growth and Characterization of ZnO Thin Film on Sapphire (0001) Substrate with p-GaN Buffer Layer. *Thin Solid Films* **2008**, *516* (23), 8244–8247. https://doi.org/10.1016/j.tsf.2008.03.001.

(44) Znaidi, L. Sol–Gel-Deposited ZnO Thin Films: A Review. *Materials Science & Engineering B* **2010**, *1–3* (174), 18–30. https://doi.org/10.1016/j.mseb.2010.07.001.

(45) Takayanagi, S.; Yanagitani, T.; Matsukawa, M. Effect of Metal Mode and Oxide Mode on Unusual C-Axis Parallel Oriented ZnO Film Growth on Al/Glass Substrate in a Reactive Magnetron Sputtering of Zn Target. *Journal of Crystal Growth* **2013**, *363*, 22–24. https://doi.org/10.1016/j.jcrysgro.2012.09.016.

(46) Gao, W.; Li, Z. ZnO Thin Films Produced by Magnetron Sputtering. **2004**. https://doi.org/10.1016/J.CERAMINT.2003.12.197.

(47) Park, S.-M.; Ikegami, T.; Ebihara, K.; Shin, P.-K. Structure and Properties of Transparent Conductive Doped ZnO Films by Pulsed Laser Deposition. *Applied Surface Science* **2006**, *253* (3), 1522–1527. https://doi.org/10.1016/j.apsusc.2006.02.046.

(48) Rinaldi, F. *Basics of Molecular Beam Epitaxy (MBE)*. https://www.semanticscholar.org/paper/Basics-of-Molecular-Beam-Epitaxy-(-MBE-)-Rinaldi/c4b463caba1e85265210a62b5cb42b8dba4ce0fd (accessed 2022-01-10).

(49) Quaas, M.; Steffen, H.; Hippler, R.; Wulff, H. Investigation of Diffusion and Crystallization Processes in Thin ITO Films by Temperature and Time Resolved Grazing Incidence X-Ray Diffractometry. *Surface Science* **2003**, *540* (2), 337–342. https://doi.org/10.1016/S0039-6028(03)00850-1.

(50) Teixeira, V.; Cui, H. N.; Meng, L. J.; Fortunato, E.; Martins, R. Amorphous ITO Thin Films Prepared by DC Sputtering for Electrochromic Applications. *Thin Solid Films* **2002**, *420–421*, 70–75. https://doi.org/10.1016/S0040-6090(02)00656-9.

(51) Kurdesau, F.; Khripunov, G.; da Cunha, A. F.; Kaelin, M.; Tiwari, A. N. Comparative Study of ITO Layers Deposited by DC and RF Magnetron Sputtering at Room Temperature. *Journal of Non-Crystalline Solids* **2006**, *352* (9), 1466–1470. https://doi.org/10.1016/j.jnoncrysol.2005.11.088.

(52) Jung, Y. S.; Lee, S. S. Development of Indium Tin Oxide Film Texture during DC Magnetron Sputtering Deposition. *Journal of Crystal Growth* **2003**, *259* (4), 343–351. https://doi.org/10.1016/j.jcrysgro.2003.07.006.

(53) Liu, W.; Cheng, S. Photoelectric Properties of ITO Thin Films Deposited by DC Magnetron Sputtering. *J. Semicond.* **2011**, *32* (1), 013002. https://doi.org/10.1088/1674-4926/32/1/013002.

(54) Chityuttakan, C.; Chinvetkitvanich, P.; Chatraphorn, S.; Chatraphorn, S. Influence of Deposition Parameters on the Quality of ITO Films for Photovoltaic Application. In *AIP Conf. Proc*; 2019; Vol. 2091, p 3.

(55) Diniz, A. S. A. C. The Effects of Various Annealing Regimes on the Microstructure and Physical Properties of ITO (In2O3:Sn) Thin Films Deposited by Electron Beam Evaporation for Solar Energy Applications. *Renewable Energy* **2011**, *36* (4), 1153–1165. https://doi.org/10.1016/j.renene.2010.09.005.

(56) Rauf, I. A.; Walls, M. G. A Comparative Study of Microstructure (in ITO Films) and Techniques (CTEM and STM). *Ultramicroscopy* **1991**, *35* (1), 19–26. https://doi.org/10.1016/0304-3991(91)90040-D.

(57) Diniz, A. S. A. C.; Kiely, C. J.; Elfalla, I.; Pilkington, R. D.; Hill, A. E. The Effects of Post-Deposition Annealing on the Microstructure of Electron-Beam Evaporated Indium Tin Oxide Thin Films. *Renewable Energy* **1994**, *5* (1), 209–211. https://doi.org/10.1016/0960-1481(94)90373-5.

(58) Ahmed, N. M.; Sabah, F. A.; Abdulgafour, H. I.; Alsadig, A.; Sulieman, A.; Alkhoaryef, M. The Effect of Post Annealing Temperature on Grain Size of Indium-Tin-Oxide for Optical and Electrical Properties Improvement. *Results in Physics* **2019**, *13*, 102159. https://doi.org/10.1016/j.rinp.2019.102159.

(59) Hamberg, I.; Granqvist, C. G. Evaporated Sn-doped In2O3 Films: Basic Optical Properties and Applications to Energy-efficient Windows. *Journal of Applied Physics* **1986**, *60* (11), R123–R160. https://doi.org/10.1063/1.337534.

(60) Zhao, L.; Zhou, Z.; Peng, H.; Cui, R. Indium Tin Oxide Thin Films by Bias Magnetron Rf Sputtering for Heterojunction Solar Cells Application. *Applied Surface Science* **2005**, *252* (2), 385–392. https://doi.org/10.1016/j.apsusc.2005.01.033.

(61) Ashour, A.; Kaid, M. A.; El-Sayed, N. Z.; Ibrahim, A. A. Physical Properties of ZnO Thin Films Deposited by Spray Pyrolysis Technique. *Applied Surface Science* **2006**, *252* (22), 7844–7848. https://doi.org/10.1016/j.apsusc.2005.09.048.

(62) Krunks, M.; Mellikov, E. Zinc Oxide Thin Films by the Spray Pyrolysis Method. *Thin Solid Films* **1995**, *270* (1), 33–36. https://doi.org/10.1016/0040-6090(95)06893-7.

(63) Elements, A. *Indium Tin Oxide (ITO)*. American Elements. https://www.americanelements.com/indium-tin-oxide-ito-50926-11-9 (accessed 2022-01-09).

(64) Buchholz, D. B.; Ma, Q.; Alducin, D.; Ponce, A.; Jose-Yacaman, M.; Khanal, R.; Medvedeva, J. E.; Chang, R. P. H. The Structure and Properties of Amorphous Indium Oxide. *Chem. Mater.* **2014**, *26* (18), 5401–5411. https://doi.org/10.1021/cm502689x.

(65) Ma, Z.; Li, Z.; Liu, K.; Ye, C.; Sorger, V. J. Indium-Tin-Oxide for High-Performance Electro-Optic Modulation. *Nanophotonics* **2015**, *4* (2), 198–213. https://doi.org/10.1515/nanoph-2015-0006.

(66) Fan, J. C. C.; Goodenough, J. B. X-ray Photoemission Spectroscopy Studies of Sn-doped Indium-oxide Films. *Journal of Applied Physics* **1977**, *48* (8), 3524–3531. https://doi.org/10.1063/1.324149.

(67) Tuna, O.; Selamet, Y.; Aygun, G.; Ozyuzer, L. High Quality ITO Thin Films Grown by Dc and RF Sputtering without Oxygen. *J. Phys. D: Appl. Phys.* **2010**, *43* (5), 055402. https://doi.org/10.1088/0022-3727/43/5/055402.

(68) Ray, S.; Banerjee, R.; Basu, N.; Batabyal, A. K.; Barua, A. K. Properties of Tin Doped Indium Oxide Thin Films Prepared by Magnetron Sputtering. *Journal of Applied Physics* **1983**, *54* (6), 3497–3501. https://doi.org/10.1063/1.332415.

(69) Gupta, L.; Mansingh, A.; Srivastava, P. K. Band Gap Narrowing and the Band Structure of Tin-Doped Indium Oxide Films. *Thin Solid Films* **1989**, *176* (1), 33–44. https://doi.org/10.1016/0040-6090(89)90361-1.

(70) Özgür, Ü.; Alivov, Ya. I.; Liu, C.; Teke, A.; Reshchikov, M. A.; Doğan, S.; Avrutin, V.; Cho, S.-J.; Morkoç, H. A Comprehensive Review of ZnO Materials and Devices. *Journal of Applied Physics* **2005**, *98* (4), 041301. https://doi.org/10.1063/1.1992666.

(71) Ellmer, K.; Klein, A.; Rech, B. *Transparent Conductive Zinc Oxide: Basics and Applications in Thin Film Solar Cells*; Springer Science & Business Media, 2007.

(72) Johari, S.; Muhammad, N. Y.; Zakaria, M. R. Study of Zinc Oxide Thin Film Characteristics. *EPJ Web Conf.* **2017**, *162*, 01057. https://doi.org/10.1051/epjconf/201716201057.

(73) Bouderbala, M.; Hamzaoui, S.; Amrani, B.; Reshak, A. H.; Adnane, M.; Sahraoui, T.; Zerdali, M. Thickness Dependence of Structural, Electrical and Optical Behaviour of Undoped ZnO Thin Films. *Physica B: Condensed Matter* **2008**, *403* (18), 3326–3330. https://doi.org/10.1016/j.physb.2008.04.045.

(74) Jun, M.-C.; Park, S.-U.; Koh, J.-H. Comparative Studies of Al-Doped ZnO and Ga-Doped ZnO Transparent Conducting Oxide Thin Films. *Nanoscale Research Letters* **2012**, *7* (1), 639. https://doi.org/10.1186/1556-276X-7-639.

(75) Prasada Rao, T.; Santhosh Kumar, M. C.; Safarulla, A.; Ganesan, V.; Barman, S. R.; Sanjeeviraja, C. Physical Properties of ZnO Thin Films Deposited at Various Substrate Temperatures Using Spray Pyrolysis. *Physica B: Condensed Matter* **2010**, *405* (9), 2226–2231. https://doi.org/10.1016/j.physb.2010.02.016.

(76) Vimalkumar, T. V.; Poornima, N.; Kartha, C. S.; Vijayakumar, K. P. Effect of Precursor Medium on Structural, Electrical and Optical Properties of Sprayed Polycrystalline ZnO Thin Films. *Materials Science and Engineering: B* **2010**, *175* (1), 29–35. https://doi.org/10.1016/j.mseb.2010.06.012.

(77) Epurescu, G.; Dinescu, G.; Moldovan, A.; Birjega, R.; Dipietrantonio, F.; Verona, E.; Verardi, P.; Nistor, L. C.; Ghica, C.; Van Tendeloo, G.; Dinescu, M. P-Type ZnO Thin Films Grown by RF Plasma Beam Assisted Pulsed Laser Deposition. *Superlattices and Microstructures* **2007**, *42* (1), 79–84. https://doi.org/10.1016/j.spmi.2007.04.072.

(78) Nguyen, V. H.; Resende, J.; Jiménez, C.; Deschanvres, J.-L.; Carroy, P.; Muñoz, D.; Bellet, D.; Muñoz-Rojas, D. Deposition of ZnO Based Thin Films by Atmospheric Pressure Spatial Atomic Layer Deposition for Application in Solar Cells. *Journal of Renewable and Sustainable Energy* **2017**, *9* (2), 021203. https://doi.org/10.1063/1.4979822.

(79) Douayar, A.; Diaz, R.; Moursli, F. C. E.; Schmerber, G.; Dinia, A.; Abd-Lefdil, M. Fluorine-Doped ZnO Thin Films Deposited by Spray Pyrolysis Technique. *Eur. Phys. J. Appl. Phys.* **2011**, *53* (2), 20501. https://doi.org/10.1051/epjap/2010100364.

(80) Nunes, P.; Fortunato, E.; Martins, R. Influence of the Post-Treatment on the Properties of ZnO Thin Films. **2001**. https://doi.org/10.1016/S0040-6090(00)01577-7.

(81) Bougrine, A.; Addou, M.; Kachouane, A.; Bérnède, J. C.; Morsli, M. Effect of Tin Incorporation on Physicochemical Properties of ZnO Films Prepared by Spray Pyrolysis. *Materials Chemistry and Physics* **2005**, *91* (2), 247–252. https://doi.org/10.1016/j.matchemphys.2003.11.033.

(82) Hijazi, F. Etude Des Propriétés Physiques et de Transport Dans Des Films d'ITO et de ZnO (Dopé Ou Non) Pour Dispositifs Optoélectroniques Organiques = Study of Physical and Transport Properties of ITO and ZnO Films (Doped or Undoped) for Organic Optoelectronic Devices, Limoges, 2010.

(83) Hjiri, M.; El Mir, L.; Leonardi, S. G.; Pistone, A.; Mavilia, L.; Neri, G. Al-Doped ZnO for Highly Sensitive CO Gas Sensors. *Sensors and Actuators B: Chemical* **2014**, *196*, 413–420. https://doi.org/10.1016/j.snb.2014.01.068.

(84) Zhang, Y.; Jia, C.; Kong, Q.; Fan, N.; Chen, G.; Guan, H.; Dong, C. ZnO-Decorated In/Ga Oxide Nanotubes Derived from Bimetallic In/Ga MOFs for Fast Acetone Detection with High Sensitivity and Selectivity. *ACS Appl. Mater. Interfaces* **2020**, *12* (23), 26161–26169. https://doi.org/10.1021/acsami.0c04580.

(85) Nunes, P.; Fortunato, E.; Tonello, P.; Braz Fernandes, F.; Vilarinho, P.; Martins, R. Effect of Different Dopant Elements on the Properties of ZnO Thin Films. *Vacuum* **2002**, *64* (3), 281–285. https://doi.org/10.1016/S0042-207X(01)00322-0.

(86) Rombach, J.; Papadogianni, A.; Mischo, M.; Cimalla, V.; Kirste, L.; Ambacher, O.; Berthold, T.; Krischok, S.; Himmerlich, M.; Selve, S.; Bierwagen, O. The Role of Surface Electron Accumulation and Bulk Doping for Gas-Sensing Explored with Single-Crystalline In2O3 Thin Films. *Sensors and Actuators B: Chemical* **2016**, *236*, 909–916. https://doi.org/10.1016/j.snb.2016.03.079.

(87) Prajapati, C. S.; Kushwaha, A.; Sahay, P. P. Effect of Al Dopants on the Structural, Optical and Gas Sensing Properties of Spray-Deposited ZnO Thin Films. *Materials Chemistry and Physics* **2013**. https://doi.org/10.1016/J.MATCHEMPHYS.2013.07.015.

(88) Ng, Z.-N.; Chan, K.-Y.; Tohsophon, T. Effects of Annealing Temperature on ZnO and AZO Films Prepared by Sol–Gel Technique. *Applied Surface Science* **2012**, *258* (24), 9604–9609. https://doi.org/10.1016/j.apsusc.2012.05.156.

(89) Shu-Wen, X. A Study of Annealing Time Effects on the Properties of Al:ZnO. *Physics Procedia* **2012**, *25*.

(90) Lennon, C.; Kodama, R.; Chang, Y.; Sivananthan, S.; Deshpande, M. Effects of Annealing in N2 on Sputtered Al-Doped ZnO Thin Films. *Journal of Vacuum Science & Technology B: Microelectronics and Nanometer Structures Processing, Measurement, and Phenomena* **2009**, *27* (3), 1641–1645. https://doi.org/10.1116/1.3110020.

(91) Kim, D. S.; Park, J. H.; Shin, B. K.; Moon, K. J.; Son, M.; Ham, M. H.; Lee, W.; Myoung, J. M. Effect of Deposition Temperature on the Properties of Al-Doped ZnO Films Prepared by Pulsed DC Magnetron Sputtering for Transparent Electrodes in Thin-Film Solar Cells. *Applied Surface Science* **2012**, *259*, 596–599. https://doi.org/10.1016/j.apsusc.2012.07.082.

(92) Babu, B. J.; Maldonado, A.; Velumani, S.; Asomoza, R. Electrical and Optical Properties of Ultrasonically Sprayed Al-Doped Zinc Oxide Thin Films. *Materials Science and Engineering: B* **2010**, *174* (1), 31–37. https://doi.org/10.1016/j.mseb.2010.03.010.

(93) Muiva, C. M.; Sathiaraj, T. S.; Maabong, K. Effect of Doping Concentration on the Properties of Aluminium Doped Zinc Oxide Thin Films Prepared by Spray Pyrolysis for Transparent Electrode Applications. *Ceramics International* **2011**, *37* (2), 555–560. https://doi.org/10.1016/j.ceramint.2010.09.042.

(94) Ravichandran, K.; Begum, N. J.; Snega, S.; Sakthivel, B. Properties of Sprayed Aluminum-Doped Zinc Oxide Films—A Review. *Materials and Manufacturing Processes* **2014**.

(95) Benhaliliba, M.; Benouis, C. E.; Aida, M. S.; Juarez, A. S.; Yakuphanoglu, F.; Silver, A. T. A Comparative Study on Structural, Optical, Photoconductivity Properties of In and Al Doped ZnO Thin Films Grown onto Glass and FTO Substrates Grown by Spray Pyrolysis Process. *Journal of Alloys and Compounds* **2010**, *2* (506), 548–553. https://doi.org/10.1016/j.jallcom.2010.07.023.

(96) Manouni, A. E.; Manjón, F. J.; Mollar, M.; Marí, B.; Gómez, R.; López, M. C.; Ramos-Barrado, J. R. Effect of Aluminium Doping on Zinc Oxide Thin Films Grown by Spray Pyrolysis. *Superlattices and Microstructures* **2006**, *39* (1), 185–192. https://doi.org/10.1016/j.spmi.2005.08.041.

(97) Igasaki, Y.; Saito, H. Substrate Temperature Dependence of Electrical Properties of ZnO:Al Epitaxial Films on Sapphire (1$\bar{2}$10). *Journal of Applied Physics* **1991**, *69* (4), 2190–2195. https://doi.org/10.1063/1.348748.

(98) Batzill, M.; Diebold, U. The Surface and Materials Science of Tin Oxide. *Progress in Surface Science* **2005**, *79* (2), 47–154. https://doi.org/10.1016/j.progsurf.2005.09.002.

(99) Das, S.; Jayaraman, V. SnO2: A Comprehensive Review on Structures and Gas Sensors. *Progress in Materials Science* **2014**, *66*, 112–255. https://doi.org/10.1016/j.pmatsci.2014.06.003.

(100) *Characterization of nanostructured SnO2 films deposited by reactive DC-magnetron sputtering*. http://www.scielo.org.mx/scielo.php?script=sci_arttext&pid=S1665-35212013000300005 (accessed 2021-04-28).

(101) Rey, G. Etude d'oxydes métalliques nanostructurés (ZnO, SnO2) pour applications photovoltaïques notamment oxydes transparents conducteurs et cellules solaires à coloran. 250.

(102) Tavakoli, M. M.; Gu, L.; Gao, Y.; Reckmeier, C.; He, J.; Rogach, A. L.; Yao, Y.; Fan, Z. Fabrication of Efficient Planar Perovskite Solar Cells Using a One-Step Chemical Vapor Deposition Method. *Sci Rep* **2015**, *5* (1), 14083. https://doi.org/10.1038/srep14083.

(103) Banyamin, Z.; Kelly, P.; West, G.; Boardman, J. Electrical and Optical Properties of Fluorine Doped Tin Oxide Thin Films Prepared by Magnetron Sputtering. *Coatings* **2014**, *4* (4), 732–746. https://doi.org/10.3390/coatings4040732.

(104) Aouaj, M. A.; Diaz, R.; Belayachi, A.; Rueda, F.; Abd-Lefdil, M. Comparative Study of ITO and FTO Thin Films Grown by Spray Pyrolysis. *Materials Research Bulletin* **2009**, *44* (7), 1458–1461. https://doi.org/10.1016/j.materresbull.2009.02.019.

(105) Tuyen, L. T. C.; Jian, S.-R.; Tien, N. T.; Le, P. H. Nanomechanical and Material Properties of Fluorine-Doped Tin Oxide Thin Films Prepared by Ultrasonic Spray Pyrolysis: Effects of F-Doping. *Materials* **2019**, *12* (10), 1665. https://doi.org/10.3390/ma12101665.

(106) *Matériaux nanostructurés pour la conversion photovoltaïque*. France Culture. https://www.franceculture.fr/conferences/toulouse-iii-paul-sabatier/materiaux-nanostructures-pour-la-conversion-photovoltaique (accessed 2022-04-06).

(107) *Solar Photovoltaic Technology Basics*. https://www.nrel.gov/research/re-photovoltaics.html (accessed 2022-09-07).

(108) Wu, C.; Wang, K.; Batmunkh, M.; Bati, A. S. R.; Yang, D.; Jiang, Y.; Hou, Y.; Shapter, J. G.; Priya, S. Multifunctional Nanostructured Materials for next Generation Photovoltaics. *Nano Energy* **2020**, *70*, 104480. https://doi.org/10.1016/j.nanoen.2020.104480.

(109) El Zein, B. Growth and Characterization of Zinc Oxide (ZnO) Nanostructures for Photovotaic Applications. These de doctorat, Lille 1, 2012.

(110) *Chapter 1: Novel approaches for preparation of nanoparticles - Nanostructures for Novel Therapy [Book]*. https://www.oreilly.com/library/view/nanostructures-for-novel/9780323461481/xhtml/B9780323461429000013.xhtml (accessed 2022-04-08).

(111) *Nanoparticles: Properties, applications and toxicities | Elsevier Enhanced Reader*. https://reader.elsevier.com/reader/sd/pii/S1878535217300990?token=A69EB5D8C68AD67744F6BB735F0F2A546E6E76C18BA7583B91B2B71A19F1E453BB97DEB4AC0D297E17154A3DC57C1916&originRegion=eu-west-1&originCreation=20220406125644 (accessed 2022-04-06). https://doi.org/10.1016/j.arabjc.2017.05.011.

(112) Law, M.; Goldberger, J.; Yang, P. SEMICONDUCTOR NANOWIRES AND NANOTUBES. *Annu. Rev. Mater. Res.* **2004**, *34* (1), 83–122. https://doi.org/10.1146/annurev.matsci.34.040203.112300.

(113) Ross, F. M. Controlling Nanowire Structures through Real Time Growth Studies. *Rep. Prog. Phys.* **2010**, *73* (11), 114501. https://doi.org/10.1088/0034-4885/73/11/114501.

(114) Bagga, S.; Akhtar, J.; Mishra, S. Synthesis and Applications of ZnO Nanowire: A Review; Solapur, India, 2018; p 020004. https://doi.org/10.1063/1.5047680.

(115) Tan, E. P. S.; Lim, C. T. Mechanical Characterization of Nanofibers–a Review. *Composites Science and Technology* **2006**, *66* (9), 1102–1111.

(116) Dzenis, Y. Structural Nanocomposites. *Science* **2008**, *319* (5862), 419–420. https://doi.org/10.1126/science.1151434.

(117) Kang, D. H.; Kim, N. K.; Kang, H. W. High Efficient Photo Detector by Using ZnO Nanowire Arrays on Highly Aligned Electrospun PVDF-TrFE Nanofiber Film. *Nanotechnology* **2019**, *30* (36), 365303. https://doi.org/10.1088/1361-6528/ab2278.

(118) Lemma, S. M.; Esposito, A.; Mason, M.; Brusetti, L.; Cesco, S.; Scampicchio, M. Removal of Bacteria and Yeast in Water and Beer by Nylon Nanofibrous Membranes. *Journal of Food Engineering* **2015**, *157*, 1–6. https://doi.org/10.1016/j.jfoodeng.2015.02.005.

(119) Bielefeld University of Applied Sciences, Faculty of Engineering and Mathematics, Working Group of Textile Technologies, Interaktion 1, 33619 Bielefeld, Germany; Mamun, A. Review of Possible Applications of Nanofibrous Mats for Wound Dressings. *TEK* **2019**, *62* (2), 89–100. https://doi.org/10.14502/Tekstilec2019.62.89-100.

(120) Wehlage, D.; Blattner, H.; Sabantina, L.; Böttjer, R.; Grothe, T.; Rattenholl, A.; Gudermann, F.; Lütkemeyer, D.; Ehrmann, A. Sterilization of PAN/Gelatin Nanofibrous Mats for Cell Growth. *Tekstilec* **2019**, *62* (2).

(121) Zornitta, R. L.; García-Mateos, F. J.; Lado, J. J.; Rodríguez-Mirasol, J.; Cordero, T.; Hammer, P.; Ruotolo, L. A. High-Performance Activated Carbon from Polyaniline for Capacitive Deionization. *Carbon* **2017**, *123*, 318–333.

(122) Wortmann, M.; Frese, N.; Sabantina, L.; Petkau, R.; Kinzel, F.; Gölzhäuser, A.; Moritzer, E.; Hüsgen, B.; Ehrmann, A. New Polymers for Needleless Electrospinning from Low-Toxic Solvents. *Nanomaterials* **2019**, *9* (1), 52.

(123) Kim, J.-H.; Mirzaei, A.; Kim, H. W.; Wu, P.; Kim, S. S. Design of Supersensitive and Selective ZnO-Nanofiber-Based Sensors for H2 Gas Sensing by Electron-Beam Irradiation. *Sensors and Actuators B: Chemical* **2019**, *293*, 210–223.

(124) Zhen, H.; Wang, H.; Xu, X. Preparation of Porous Carbon Nanofibers with Remarkable Microwave Absorption Performance through Electrospinning. *Materials Letters* **2019**, *249*, 210–213.

(125) Abdel-Mottaleb, M. M.; Khalil, A.; Karim, S.; Osman, T. A.; Khattab, A. High Performance of PAN/GO-ZnO Composite Nanofibers for Photocatalytic Degradation under Visible Irradiation. *Journal of the Mechanical Behavior of Biomedical Materials* **2019**, *96*, 118–124.

(126) Yun, S. I.; Kim, S. H.; Kim, D. W.; Kim, Y. A.; Kim, B.-H. Facile Preparation and Capacitive Properties of Low-Cost Carbon Nanofibers with ZnO Derived from Lignin and Pitch as Supercapacitor Electrodes. *Carbon* **2019**, *149*, 637–645.

(127) Marcantonio, M. D.; Gellner, S.; Namanga, J. E.; Frohleiks, J.; Gerlitzki, N.; Vollkommer, F.; Bacher, G.; Nannen, E. Performance Enhancement by ZnO Nanoparticle Layer in Hybrid Ionic Transition Metal Complex-Light-Emitting Electrochemical Cells (ITMC-LECs). *Advanced Materials Technologies* **2017**, *2* (1), 1600215.

(128) Mohtaram, F.; Borhani, S.; Ahmadpour, M.; Fojan, P.; Behjat, A.; Rubahn, H.-G.; Madsen, M. Electrospun ZnO Nanofiber Interlayers for Enhanced Performance of Organic Photovoltaic Devices. *Solar Energy* **2020**, *197*, 311–316. https://doi.org/10.1016/j.solener.2019.12.079.

(129) Wu, H.; Pan, W. Preparation of Zinc Oxide Nanofibers by Electrospinning. *Journal of the American Ceramic Society* **2006**, *89* (2), 699–701. https://doi.org/10.1111/j.1551-2916.2005.00735.x.

(130) Sangkhaprom, N.; Supaphol, P.; Pavarajarn, V. Fibrous Zinc Oxide Prepared by Combined Electrospinning and Solvothermal Techniques. *Ceramics International* **2010**, *36* (1), 357–363.

(131) Siddheswaran, R.; Sankar, R.; Ramesh Babu, M.; Rathnakumari, M.; Jayavel, R.; Murugakoothan, P.; Sureshkumar, P. Preparation and Characterization of ZnO Nanofibers by Electrospinning. *Cryst. Res. Technol.* **2006**, *41* (5), 446–449. https://doi.org/10.1002/crat.200510603.

(132) Imran, M. *Fabrication and characterization of zinc oxide nanofibers for renewable energy applications - ScienceDirect*. https://www.sciencedirect.com/science/article/pii/S1878535213000257 (accessed 2022-04-23).

(133) Yun, S.; Lim, S. Improved Conversion Efficiency in Dye-Sensitized Solar Cells Based on Electrospun Al-Doped ZnO Nanofiber Electrodes Prepared by Seed Layer Treatment. *Journal of Solid State Chemistry* **2011**, *184* (2), 273–279.

(134) Xu, F.; Le, Y.; Cheng, B.; Jiang, C. Effect of Calcination Temperature on Formaldehyde Oxidation Performance of Pt/TiO2 Nanofiber Composite at Room Temperature. *Applied Surface Science* **2017**, *426*, 333–341. https://doi.org/10.1016/j.apsusc.2017.07.096.

(135) Watthanaarun, J.; Pavarajarn, V.; Supaphol, P. Titanium (IV) Oxide Nanofibers by Combined Sol–Gel and Electrospinning Techniques: Preliminary Report on Effects of Preparation Conditions and Secondary Metal Dopant. *Science and Technology of Advanced Materials* **2005**, *6* (3–4), 240–245. https://doi.org/10.1016/j.stam.2005.02.002.

(136) Kang, W.; Cheng, B.; Li, Q.; Zhuang, X.; Ren, Y. A New Method for Preparing Alumina Nanofibers by Electrospinning Technology. *Textile Research Journal* **2011**, *81* (2), 148–155. https://doi.org/10.1177/0040517510377831.

(137) Di Mauro, A.; Zimbone, M.; Fragalà, M. E.; Impellizzeri, G. Synthesis of ZnO Nanofibers by the Electrospinning Process. *Materials Science in Semiconductor Processing* **2016**, *42*, 98–101. https://doi.org/10.1016/j.mssp.2015.08.003.

(138) Li, Y.-Q.; Fu, S.-Y.; Mai, Y.-W. Preparation and Characterization of Transparent ZnO/Epoxy Nanocomposites with High-UV Shielding Efficiency. *Polymer* **2006**, *47* (6), 2127–2132. https://doi.org/10.1016/j.polymer.2006.01.071.

(139) Majumder, S. B.; Jain, M.; Dobal, P. S.; Katiyar, R. S. Investigations on Solution Derived Aluminium Doped Zinc Oxide Thin Films. *Materials Science and Engineering: B* **2003**, *103* (1), 16–25. https://doi.org/10.1016/S0921-5107(03)00128-4.

(140) Lee, D. Y.; Cho, J.-E.; Cho, N.-I.; Lee, M.-H.; Lee, S.-J.; Kim, B.-Y. Characterization of Electrospun Aluminum-Doped Zinc Oxide Nanofibers. *Thin Solid Films* **2008**, *517* (3), 1262–1267. https://doi.org/10.1016/j.tsf.2008.05.027.

(141) Turky, A. O.; Barhoum, A.; MohamedRashad, M.; Bechlany, M. Enhanced the Structure and Optical Properties for ZnO/PVP Nanofibers Fabricated via Electrospinning Technique. *J Mater Sci: Mater Electron* **2017**, *28* (23), 17526–17532. https://doi.org/10.1007/s10854-017-7688-6.

(142) Lotus, A. F.; Kang, Y. C.; Walker, J. I.; Ramsier, R. D.; Chase, G. G. Effect of Aluminum Oxide Doping on the Structural, Electrical, and Optical Properties of Zinc Oxide (AOZO) Nanofibers Synthesized by Electrospinning. *Materials Science and Engineering: B* **2010**, *166* (1), 61–66. https://doi.org/10.1016/j.mseb.2009.10.001.

(143) Morilhat, A. Synthese de Couches Minces Resistives Par Pulverisation Cathodique Magnetron Pour l'elaboration de Resistances Etalons Calculables En Courant Alternatif. These de doctorat, Belfort-Montbéliard, 2011.

(144) Binnig, G.; Rohrer, H.; Gerber, Ch.; Weibel, E. Surface Studies by Scanning Tunneling Microscopy. *Phys. Rev. Lett.* **1982**, *49* (1), 57–61. https://doi.org/10.1103/PhysRevLett.49.57.

(145) Rugar, D.; Hansma, P. Atomic Force Microscopy. *Physics Today* **1990**, *43* (10), 23–30. https://doi.org/10.1063/1.881238.

(146) *Dictionary of nanotechnology - Atomic Force Microscopy*. http://www.nanodic.com/Nanocharacterization/Atomic_Force_Microscopy.htm (accessed 2022-05-16).

(147) Jalili, N.; Laxminarayana, K. A Review of Atomic Force Microscopy Imaging Systems: Application to Molecular Metrology and Biological Sciences. *Mechatronics* **2004**, *14* (8), 907–945. https://doi.org/10.1016/j.mechatronics.2004.04.005.

(148) Vyas, S. A Short Review on Properties and Applications of ZnO Based Thin Film and Devices. *Johnson Matthey Technology Review* **2020**.

(149) Shin, P.-K.; Aya, Y.; Ikegami, T.; Ebihara, K. Application of Pulsed Laser Deposited Zinc Oxide Films to Thin Film Transistor Device. *Thin Solid Films* **2008**, *516* (12), 3767–3771. https://doi.org/10.1016/j.tsf.2007.06.068.

(150) Ellmer, K. Magnetron Sputtering of Transparent Conductive Zinc Oxide: Relation between the Sputtering Parameters and the Electronic Properties. *J. Phys. D: Appl. Phys.* **2000**, *33* (4), R17. https://doi.org/10.1088/0022-3727/33/4/201.

(151) Ergin, B.; Ketenci, E.; Atay, F. Characterization of ZnO Films Obtained by Ultrasonic Spray Pyrolysis Technique. *International Journal of Hydrogen Energy* **2009**, *34* (12), 5249–5254. https://doi.org/10.1016/j.ijhydene.2008.09.108.

(152) Zhang, S. Study of Fluorine-Doped Tin Oxide (FTO) Thin Films for Photovoltaics Applications. 225.

(153) Al Abdullah, K.; Awad, S.; Zaraket, J.; Salame, C. Synthesis of ZnO Nanopowders By Using Sol-Gel and Studying Their Structural and Electrical Properties at Different Temperature. *Energy Procedia* **2017**, *119*, 565–570. https://doi.org/10.1016/j.egypro.2017.07.080.

(154) Wang, J. T.; Shi, X. L.; Zhong, X. H.; Wang, J. N.; Pyrah, L.; Sanderson, K. D.; Ramsey, P. M.; Hirata, M.; Tsuri, K. Morphology Control of Fluorine-Doped Tin Oxide Thin Films for Enhanced Light Trapping. *Solar Energy Materials and Solar Cells* **2015**, *132*, 578–588. https://doi.org/10.1016/j.solmat.2014.09.043.

(155) Haddad, N.; Ben Ayadi, Z.; Mahdhi, H.; Djessas, K. Influence of Fluorine Doping on the Microstructure, Optical and Electrical Properties of SnO2 Nanoparticles. *J Mater Sci: Mater Electron* **2017**, *28* (20), 15457–15465. https://doi.org/10.1007/s10854-017-7433-1.

(156) Liu, Y.; Dong, Y.; Wang, G. Far-Infrared Absorption Spectra and Properties of SnO2 Nanorods. *Appl. Phys. Lett.* **2003**, *82* (2), 260–262. https://doi.org/10.1063/1.1535745.

(157) Hsu, N. E.; Hung, W. K.; Chen, Y. F. Origin of Defect Emission Identified by Polarized Luminescence from Aligned ZnO Nanorods. *Journal of Applied Physics* **2004**, *96* (8), 4671–4673. https://doi.org/10.1063/1.1787905.

(158) Kravets, V. G. Photoluminescence and Raman Spectra of SnOx Nanostructures Doped with Sm Ions. *Opt. Spectrosc.* **2007**, *103* (5), 766–771. https://doi.org/10.1134/S0030400X07110148.

(159) Castellanos, A. *Electrohydrodynamics*; Springer Science & Business Media, 1998.

(160) Haider, S.; Haider, A.; Alghyamah, A. A.; Khan, R.; Almasry, W. A.; Khan, N. *Electrohydrodynamic Processes and Their Affecting Parameters*; IntechOpen, 2019. https://doi.org/10.5772/intechopen.89929.

(161) Xue, J.; Wu, T.; Dai, Y.; Xia, Y. Electrospinning and Electrospun Nanofibers: Methods, Materials, and Applications. *Chem. Rev.* **2019**, *119* (8), 5298–5415. https://doi.org/10.1021/acs.chemrev.8b00593.

(162) Gilbert, W. *De Magnete*; Courier Corporation, 1958.

(163) Gray, S. V. A Letter to Cromwell Mortimer, M. D. Secr. R. S. Containing Several Experiments Concerning Electricity by Mr. Stephen Gray. *Philosophical Transactions of the Royal Society of London* **1731**, *37* (417), 18–44. https://doi.org/10.1098/rstl.1731.0005.

(164) Nollet, J. A. X. Part of a Letter from Abbè Nollet, of the Royal Academy of Science at Paris, and FRS to Martin Folkes Esq; President of the Same, Concerning Electricity. *Philosophical Transactions of the Royal Society of London* **1748**, *45* (486), 187–194.

(165) Rayleigh, Lord. XX. On the Equilibrium of Liquid Conducting Masses Charged with Electricity. *The London, Edinburgh, and Dublin Philosophical Magazine and Journal of Science* **1882**, *14* (87), 184–186. https://doi.org/10.1080/14786448208628425.

(166) Bailey, A. G. Electrostatic Spraying of Liquids. *Phys. Bull.* **1984**, *35* (4), 146–148. https://doi.org/10.1088/0031-9112/35/4/018.

(167) Cooley, J. F. Apparatus for Electrically Dispersing Fluids. US692631A, February 4, 1902.

(168) Morton, W. J. Method of Dispersing Fluids. US705691A, July 29, 1902.

(169) Formhals, A. Method and Apparatus for Spinning. *US patent* **1944**, *2349950*.

(170) *Disintegration of water drops in an electric field | Proceedings of the Royal Society of London. Series A. Mathematical and Physical Sciences*. https://royalsocietypublishing.org/doi/abs/10.1098/rspa.1964.0151?casa_token=pWO-Ps-nRMAAAAAA:aVOGlHkHumac9r5TpZB_cQ_FsBFNnp8pHoO5zhjaaMLONJPFIzyCXTpvkKj8ynX46eVekRprNh3G6kc (accessed 2022-03-25).

(171) Taylor, G. I.; Van Dyke, M. D. The Force Exerted by an Electric Field on a Long Cylindrical Conductor. *Proceedings of the Royal Society of London. Series A. Mathematical and Physical Sciences* **1966**, *291* (1425), 145–158. https://doi.org/10.1098/rspa.1966.0085.

(172) *Electrically driven jets | Proceedings of the Royal Society of London. A. Mathematical and Physical Sciences*. https://royalsocietypublishing.org/doi/abs/10.1098/rspa.1969.0205?casa_token=yRfWmr7pxyQAAAAA:aOsY7TI5cnZlmWuQLMF8hvlst9L00XZES0PW86GuIQ7sElkYBTX7r4H5vGtqYQg893PRbpjEL6WXJ74 (accessed 2022-03-25).

(173) Fong, H.; Chun, I.; Reneker, D. H. Beaded Nanofibers Formed during Electrospinning. *Polymer* **1999**, *40* (16), 4585–4592. https://doi.org/10.1016/S0032-3861(99)00068-3.

(174) Yarin, A. L.; Koombhongse, S.; Reneker, D. H. Bending Instability in Electrospinning of Nanofibers. *Journal of Applied Physics* **2001**, *89* (5), 3018–3026. https://doi.org/10.1063/1.1333035.

(175) Shin, Y. M.; Hohman, M. M.; Brenner, M. P.; Rutledge, G. C. Experimental Characterization of Electrospinning: The Electrically Forced Jet and Instabilities. *Polymer* **2001**, *42* (25), 09955–09967. https://doi.org/10.1016/S0032-3861(01)00540-7.

(176) *Bending instability of electrically charged liquid jets of polymer solutions in electrospinning: Journal of Applied Physics: Vol 87, No 9*. https://aip.scitation.org/doi/abs/10.1063/1.373532 (accessed 2022-03-25).

(177) Shin, Y. M.; Hohman, M. M.; Brenner, M. P.; Rutledge, G. C. Electrospinning: A Whipping Fluid Jet Generates Submicron Polymer Fibers. *Appl. Phys. Lett.* **2001**, *78* (8), 1149–1151. https://doi.org/10.1063/1.1345798.

(178) Larsen, G.; Velarde-Ortiz, R.; Minchow, K.; Barrero, A.; Loscertales, I. G. A Method for Making Inorganic and Hybrid (Organic/Inorganic) Fibers and Vesicles with Diameters in the Submicrometer and Micrometer

Range via Sol- Gel Chemistry and Electrically Forced Liquid Jets. *Journal of the American Chemical Society* **2003**, *125* (5), 1154–1155.

(179) Li, D.; Wang, Y.; Xia, Y. Electrospinning of Polymeric and Ceramic Nanofibers as Uniaxially Aligned Arrays. *Nano Lett.* **2003**, *3* (8), 1167–1171. https://doi.org/10.1021/nl0344256.

(180) Oh, E.; Park, H.; Sone, C.; Nam, O.; Park, Y.; Kim, T. Micro-Photoluminescence Study of InxGa1–XN/GaN Quantum Wells. *Solid State Communications* **2000**, *113* (8), 461–464. https://doi.org/10.1016/S0038-1098(99)00512-8.

(181) Viswanathamurthi, P.; Bhattarai, N.; Kim, H. Y.; Lee, D. R. The Photoluminescence Properties of Zinc Oxide Nanofibres Prepared by Electrospinning. *Nanotechnology* **2003**, *15* (3), 320–323. https://doi.org/10.1088/0957-4484/15/3/015.

(182) Shao, C.; Yang, X.; Guan, H.; Liu, Y.; Gong, J. Electrospun Nanofibers of NiO/ZnO Composite. *Inorganic Chemistry Communications* **2004**, *7* (5), 625–627. https://doi.org/10.1016/j.inoche.2004.03.006.

(183) Deitzel, J. M.; Kleinmeyer, J. D.; Hirvonen, J. K.; Beck Tan, N. C. Controlled Deposition of Electrospun Poly(Ethylene Oxide) Fibers. *Polymer* **2001**, *42* (19), 8163–8170. https://doi.org/10.1016/S0032-3861(01)00336-6.

(184) Dersch, R.; Liu, T.; Schaper, A. K.; Greiner, A.; Wendorff, J. H. Electrospun Nanofibers: Internal Structure and Intrinsic Orientation. *Journal of Polymer Science Part A: Polymer Chemistry* **2003**, *41* (4), 545–553. https://doi.org/10.1002/pola.10609.

(185) Sun, Z.; Zussman, E.; Yarin, A. l.; Wendorff, J. h.; Greiner, A. Compound Core–Shell Polymer Nanofibers by Co-Electrospinning. *Advanced Materials* **2003**, *15* (22), 1929–1932. https://doi.org/10.1002/adma.200305136.

(186) Park, J.-S. Electrospinning and Its Applications. *Adv. Nat. Sci: Nanosci. Nanotechnol.* **2010**, *1* (4), 043002. https://doi.org/10.1088/2043-6262/1/4/043002.

(187) Desai, K.; Kit, K. Effect of Spinning Temperature and Blend Ratios on Electrospun Chitosan/Poly(Acrylamide) Blends Fibers. *Polymer* **2008**, *49* (19), 4046–4050. https://doi.org/10.1016/j.polymer.2008.07.012.

(188) Sill, T. J.; Von Recum, H. A. Electrospinning: Applications in Drug Delivery and Tissue Engineering. *Biomaterials* **2008**, *29* (13), 1989–2006.

(189) Steele, B. C.; Heinzel, A. Materials for Fuel-Cell Technologies. In *Materials for sustainable energy: a collection of peer-reviewed research and review articles from Nature Publishing Group*; World Scientific, 2011; pp 224–231.

(190) O'Regan, B.; Schwartz, D. T.; Zakeeruddin, S. M.; Grätzel, M. Electrodeposited Nanocomposite n–p Heterojunctions for Solid-State Dye-Sensitized Photovoltaics. *Advanced Materials* **2000**, *12* (17), 1263–1267.

(191) Song, M. Y.; Ihn, K. J.; Jo, S. M.; Kim, D. Y. Electrospun TiO2 Electrodes for Dye-Sensitized Solar Cells. *Nanotechnology* **2004**, *15* (12), 1861.

(192) Kenawy, E.-R.; Bowlin, G. L.; Mansfield, K.; Layman, J.; Simpson, D. G.; Sanders, E. H.; Wnek, G. E. Release of Tetracycline Hydrochloride from Electrospun Poly (Ethylene-Co-Vinylacetate), Poly (Lactic Acid), and a Blend. *Journal of controlled release* **2002**, *81* (1–2), 57–64.

(193) Huang, L.; Apkarian, R. P.; Chaikof, E. L. High-Resolution Analysis of Engineered Type I Collagen Nanofibers by Electron Microscopy. *Scanning* **2001**, *23* (6), 372–375.

(194) Huang, L.; Nagapudi, K.; P. Apkarian, R.; Chaikof, E. L. Engineered Collagen–PEO Nanofibers and Fabrics. *Journal of biomaterials science, Polymer edition* **2001**, *12* (9), 979–993.

(195) Zong, X.; Kim, K.; Fang, D.; Ran, S.; Hsiao, B. S.; Chu, B. Structure and Process Relationship of Electrospun Bioabsorbable Nanofiber Membranes. *polymer* **2002**, *43* (16), 4403–4412.

(196) Liu, Y.; Zhang, H.; An, X.; Gao, C.; Zhang, Z.; Zhou, J.; Zhou, M.; Xie, E. Effect of Al Doping on the Visible Photoluminescence of ZnO Nanofibers. *Journal of Alloys and Compounds* **2010**, *506* (2), 772–776. https://doi.org/10.1016/j.jallcom.2010.07.067.

(197) Hajra, M. G.; Mehta, K.; Chase, G. G. Effects of Humidity, Temperature, and Nanofibers on Drop Coalescence in Glass Fiber Media. *Separation and purification technology* **2003**, *30* (1), 79–88.

(198) Bognitzki, M.; Czado, W.; Frese, T.; Schaper, A.; Hellwig, M.; Steinhart, M.; Greiner, A.; Wendorff, J. H. Nanostructured Fibers via Electrospinning. *Advanced materials* **2001**, *13* (1), 70–72.

(199) MacDiarmid, A. G.; Jones Jr, W. E.; Norris, I. D.; Gao, J.; Johnson Jr, A. T.; Pinto, N. J.; Hone, J.; Han, B.; Ko, F. K.; Okuzaki, H. Electrostatically-Generated Nanofibers of Electronic Polymers. *Synthetic metals* **2001**, *119* (1–3), 27–30.

(200) Norris, I. D.; Shaker, M. M.; Ko, F. K.; MacDiarmid, A. G. Electrostatic Fabrication of Ultrafine Conducting Fibers: Polyaniline/Polyethylene Oxide Blends. *Synthetic metals* **2000**, *114* (2), 109–114.

(201) Rutledge, G. C.; Shin, M. Y.; Warner, S. B.; Buer, A.; Grimler, M.; Ugbolue, S. C. A Fundamental Investigation of the Formation and Properties of Electrospun Fibers. *National textile center annual report* **2001**, *1*, 1–9.

(202) Schreuder-Gibson, H.; Gibson, P.; Senecal, K.; Sennett, M.; Walker, J.; Yeomans, W. Protective Textile Materials Based on Electrospun Nanofibers. *Journal of advanced materials* **2002**, *34* (3), 44–55.

(203) Khil, M.-S.; Cha, D.-I.; Kim, H.-Y.; Kim, I.-S.; Bhattarai, N. Electrospun Nanofibrous Polyurethane Membrane as Wound Dressing. *Journal of Biomedical Materials Research Part B: Applied Biomaterials* **2003**, *67B* (2), 675–679. https://doi.org/10.1002/jbm.b.10058.

(204) Fang, J.; Niu, H.; Lin, T.; Wang, X. Applications of Electrospun Nanofibers. *Chin. Sci. Bull.* **2008**, *53* (15), 2265–2286. https://doi.org/10.1007/s11434-008-0319-0.

(205) Huang, Z.-M.; Zhang, Y.-Z.; Kotaki, M.; Ramakrishna, S. A Review on Polymer Nanofibers by Electrospinning and Their Applications in Nanocomposites. *Composites Science and Technology* **2003**, *63* (15), 2223–2253. https://doi.org/10.1016/S0266-3538(03)00178-7.

(206) Varesano, A.; Carletto, R. A.; Mazzuchetti, G. Experimental Investigations on the Multi-Jet Electrospinning Process. *Journal of Materials Processing Technology* **2009**, *209* (11), 5178–5185. https://doi.org/10.1016/j.jmatprotec.2009.03.003.

(207) Khalf, A.; Madihally, S. V. Recent Advances in Multiaxial Electrospinning for Drug Delivery. *European Journal of Pharmaceutics and Biopharmaceutics* **2017**, *112*, 1–17. https://doi.org/10.1016/j.ejpb.2016.11.010.

(208) Liao, Y.; Loh, C.-H.; Tian, M.; Wang, R.; Fane, A. G. Progress in Electrospun Polymeric Nanofibrous Membranes for Water Treatment: Fabrication, Modification and Applications. *Progress in Polymer Science* **2018**, *77*, 69–94. https://doi.org/10.1016/j.progpolymsci.2017.10.003.

(209) Ibrahim, H. M.; Klingner, A. A Review on Electrospun Polymeric Nanofibers: Production Parameters and Potential Applications. *Polymer Testing* **2020**, *90*, 106647. https://doi.org/10.1016/j.polymertesting.2020.106647.

(210) Gupta, P.; Wilkes, G. L. Some Investigations on the Fiber Formation by Utilizing a Side-by-Side Bicomponent Electrospinning Approach. *Polymer* **2003**, *44* (20), 6353–6359. https://doi.org/10.1016/S0032-3861(03)00616-5.

(211) Jaworek, A.; Sobczyk, A. T. Electrospraying Route to Nanotechnology: An Overview. *Journal of Electrostatics* **2008**, *66* (3), 197–219. https://doi.org/10.1016/j.elstat.2007.10.001.

(212) Mehta, P. P.; Pawar, V. S. 22 - Electrospun Nanofiber Scaffolds: Technology and Applications. In *Applications of Nanocomposite Materials in Drug Delivery*; Inamuddin, Asiri, A. M., Mohammad, A., Eds.; Woodhead Publishing Series in Biomaterials; Woodhead Publishing, 2018; pp 509–573. https://doi.org/10.1016/B978-0-12-813741-3.00023-6.

(213) Zhang, S.; Liu, H.; Tang, N.; Yu, J.; Ding, B. Chapter 8 - Electronetting. In *Electrospinning: Nanofabrication and Applications*; Ding, B., Wang, X., Yu, J., Eds.; Micro and Nano Technologies; William Andrew Publishing, 2019; pp 249–282. https://doi.org/10.1016/B978-0-323-51270-1.00008-X.

(214) Nayak, R.; Padhye, R.; Arnold, L. Melt-Electrospinning of Nanofibers. In *Electrospun Nanofibers*; Afshari, M., Ed.; Woodhead Publishing Series in Textiles; Woodhead Publishing, 2017; pp 11–40. https://doi.org/10.1016/B978-0-08-100907-9.00002-7.

(215) Angammana, C. J.; Jayaram, S. H. Analysis of the Effects of Solution Conductivity on Electrospinning Process and Fiber Morphology. *IEEE Trans. on Ind. Applicat.* **2011**, *47* (3), 1109–1117. https://doi.org/10.1109/TIA.2011.2127431.

(216) Uyar, T.; Besenbacher, F. Electrospinning of Uniform Polystyrene Fibers: The Effect of Solvent Conductivity. *Polymer* **2008**, *49* (24), 5336–5343. https://doi.org/10.1016/j.polymer.2008.09.025.

(217) Baumgarten, P. K. Electrostatic Spinning of Acrylic Microfibers. *Journal of colloid and interface science* **1971**, *36* (1), 71–79.

(218) Sutanto, B.; Arifin, Z. STRUCTURAL CHARACTERISATION AND OPTICAL PROPERTIES OF ALUMINUM-DOPED ZINC OXIDE NANOFIBERS SYNTHESIZED BY ELECTROSPINNING. **2018**, *13*, 10.

(219) Sutanto, B.; Arifin, Z.; Suyitno; Hadi, S.; Pranoto, L. M.; Agustia, Y. V. Enhancement ZnO Nanofiber as Semiconductor for Dye-Sensitized Solar Cells by Using Al Doped. *AIP Conference Proceedings* **2016**, *1717* (1), 040006. https://doi.org/10.1063/1.4943449.

(220) Suyitno, S.; Purwanto, A.; Lullus Lambang G. Hidayat, R.; Sholahudin, I.; Yusuf, M.; Huda, S.; Arifin, Z. Fabrication and Characterization of Zinc Oxide-Based Electrospun Nanofibers for Mechanical Energy Harvesting. *Journal of Nanotechnology in Engineering and Medicine* **2014**, *5* (1). https://doi.org/10.1115/1.4027447.

(221) Madeira, A.; T. Papanastasiou, D.; Toupance, T.; Servant, L.; Tréguer-Delapierre, M.; Bellet, D.; A. Goldthorpe, I. Rapid Synthesis of Ultra-Long Silver Nanowires for High Performance Transparent Electrodes. *Nanoscale Advances* **2020**, *2* (9), 3804–3808. https://doi.org/10.1039/D0NA00392A.

(222) Lagrange, M.; Langley, D. P.; Giusti, G.; Jiménez, C.; Bréchet, Y.; Bellet, D. Optimization of Silver Nanowire-Based Transparent Electrodes: Effects of Density, Size and Thermal Annealing. *Nanoscale* **2015**, *7* (41), 17410–17423. https://doi.org/10.1039/C5NR04084A.

(223) Bergin, S. M.; Chen, Y.-H.; Rathmell, A. R.; Charbonneau, P.; Li, Z.-Y.; Wiley, B. J. The Effect of Nanowire Length and Diameter on the Properties of Transparent, Conducting Nanowire Films. *Nanoscale* **2012**, *4* (6), 1996. https://doi.org/10.1039/c2nr30126a.

(224) Preston, C.; Xu, Y.; Han, X.; Munday, J. N.; Hu, L. Optical Haze of Transparent and Conductive Silver Nanowire Films. *Nano Res.* **2013**, *6* (7), 461–468. https://doi.org/10.1007/s12274-013-0323-9.

(225) Bley, K.; Semmler, J.; Rey, M.; Zhao, C.; Martic, N.; Klupp Taylor, R. N.; Stingl, M.; Vogel, N. Hierarchical Design of Metal Micro/Nanohole Array Films Optimizes Transparency and Haze Factor. *Advanced Functional Materials* **2018**, *28* (13), 1706965. https://doi.org/10.1002/adfm.201706965.

(226) Chu, W.-P.; Lin, J.-S.; Lin, T.-C.; Tsai, Y.-S.; Kuo, C.-W.; Chung, M.-H.; Hsieh, T.-E.; Liu, L.-C.; Juang, F.-S.; Chen, N.-P. Using High Haze (> 90%) Light-Trapping Film to Enhance the Efficiency of a-Si: H Solar Cells. *Optics Communications* **2012**, *285* (15), 3325–3328.

(227) Giusti, G.; Consonni, V.; Puyoo, E.; Bellet, D. High Performance ZnO-SnO2:F Nanocomposite Transparent Electrodes for Energy Applications. *ACS Appl. Mater. Interfaces* **2014**, *6* (16), 14096–14107. https://doi.org/10.1021/am5034473.

(228) Zeman, M.; van Swaaij, R. a. C. M. M.; Metselaar, J. W.; Schropp, R. E. I. Optical Modeling of A-Si:H Solar Cells with Rough Interfaces: Effect of Back Contact and Interface Roughness. *Journal of Applied Physics* **2000**, *88* (11), 6436–6443. https://doi.org/10.1063/1.1324690.

(229) Krč, J.; Zeman, M.; Kluth, O.; Smole, F.; Topič, M. Effect of Surface Roughness of ZnO:Al Films on Light Scattering in Hydrogenated Amorphous Silicon Solar Cells. *Thin Solid Films* **2003**, *426* (1), 296–304. https://doi.org/10.1016/S0040-6090(03)00006-3.

(230) Müller, J.; Rech, B.; Springer, J.; Vanecek, M. TCO and Light Trapping in Silicon Thin Film Solar Cells. *Solar Energy* **2004**, *77* (6), 917–930. https://doi.org/10.1016/j.solener.2004.03.015.

(231) Minami, T.; Nanto, H.; Takata, S. Highly Conductive and Transparent Aluminum Doped Zinc Oxide Thin Films Prepared by RF Magnetron Sputtering. *Jpn. J. Appl. Phys.* **1984**, *23* (5A), L280. https://doi.org/10.1143/JJAP.23.L280.

(232) Caglar, M.; Caglar, Y.; Ilican, S. Electrical and Optical Properties of Undoped and In-Doped ZnO Thin Films. *physica status solidi c* **2007**, *4* (3), 1337–1340. https://doi.org/10.1002/pssc.200673744.

(233) Zhang, S.-T.; Vitrant, G.; Pernot, E.; Jiménez, C.; Muñoz-Rojas, D.; Bellet, D. Hazy Al2O3-FTO Nanocomposites: A Comparative Study with FTO-Based Nanocomposites Integrating ZnO and S:TiO2 Nanostructures. *Nanomaterials* **2018**, *8* (6), 440. https://doi.org/10.3390/nano8060440.

(234) Zhang, S.-T.; Foldyna, M.; Roussel, H.; Consonni, V.; Pernot, E.; Schmidt-Mende, L.; Rapenne, L.; Jiménez, C.; Deschanvres, J.-L.; Muñoz-Rojas, D.; Bellet, D. Tuning the Properties of F:SnO 2 (FTO) Nanocomposites with S:TiO 2 Nanoparticles – Promising Hazy Transparent Electrodes for Photovoltaics Applications. *Journal of Materials Chemistry C* **2017**, *5* (1), 91–102. https://doi.org/10.1039/C6TC04153A.

(235) Kim, H.-M.; Cho, S.; Kim, J.; Shin, H.; Jang, J. Li and Mg Co-Doped Zinc Oxide Electron Transporting Layer for Highly Efficient Quantum Dot Light-Emitting Diodes. *ACS Appl. Mater. Interfaces* **2018**, *10* (28), 24028–24036. https://doi.org/10.1021/acsami.8b04721.

(236) Tsay, C.-Y.; Fan, K.-S.; Lei, C.-M. Synthesis and Characterization of Sol–Gel Derived Gallium-Doped Zinc Oxide Thin Films. *Journal of Alloys and Compounds* **2012**, *512* (1), 216–222. https://doi.org/10.1016/j.jallcom.2011.09.066.

(237) Parihar, V.; Raja, M.; Paulose, R. A Brief Review of Structural, Electrical and Electrochemical Properties of Zinc Oxide Nanoparticles. *REVIEWS ON ADVANCED MATERIALS SCIENCE* **2018**, *53* (2), 119–130. https://doi.org/10.1515/rams-2018-0009.

(238) Dewei, C.; Sean, L. Growth and Electrical Properties of Doped ZnO by Electrochemical Deposition. *New Journal of Glass and Ceramics* **2012**, *2012*. https://doi.org/10.4236/njgc.2012.21003.

(239) Karimi PK, M. F. Characterization of Aluminum Doped Zinc Oxide (Azo) Thin Films Prepared by Reactive Thermal Evaporation for Solar Cell Applications. *J Fundam Renewable Energy Appl* **2015**, *05* (04). https://doi.org/10.4172/2090-4541.1000170.

(240) Koralli, P.; Fiat Varol, S.; Mousdis, G.; Mouzakis, D. E.; Merdan, Z.; Kompitsas, M. Comparative Studies of Undoped/Al-Doped/In-Doped ZnO Transparent Conducting Oxide Thin Films in Optoelectronic Applications. *Chemosensors* **2022**, *10* (5), 162. https://doi.org/10.3390/chemosensors10050162.

(241) Silva, R. F.; Zaniquelli, M. E. D. Aluminium-Doped Zinc Oxide Films Prepared by an Inorganic Sol–Gel Route. *Thin Solid Films* **2004**, *449* (1), 86–93. https://doi.org/10.1016/S0040-6090(03)01405-6.

(242) Bedia, A.; Bedia, F. Z.; Aillerie, M.; Maloufi, N.; Benyoucef, B. Morphological and Optical Properties of ZnO Thin Films Prepared by Spray Pyrolysis on Glass Substrates at Various Temperatures for Integration in Solar Cell. *Energy Procedia* **2015**, *74*, 529–538. https://doi.org/10.1016/j.egypro.2015.07.740.

(243) Yun, S.; Lim, S. Effect of Al-Doping on the Structure and Optical Properties of Electrospun Zinc Oxide Nanofiber Films. *Journal of Colloid and Interface Science* **2011**, *360* (2), 430–439. https://doi.org/10.1016/j.jcis.2011.05.022.

(244) Cho, Y.-Y.; Kuo, C. Optical and Electrical Characterization of Electrospun Al-Doped Zinc Oxide Nanofibers as Transparent Electrodes. *J. Mater. Chem. C* **2016**, *4* (32), 7649–7657. https://doi.org/10.1039/C6TC02586B.

(245) Sutanto, B.; Arifin, Z.; Suyitno; Hadi, S.; Pranoto, L. M.; Agustia, Y. V. Enhancement ZnO Nanofiber as Semiconductor for Dye-Sensitized Solar Cells by Using Al Doped. *AIP Conference Proceedings* **2016**, *1717* (1), 040006. https://doi.org/10.1063/1.4943449.

(246) Suyitno, S.; Purwanto, A.; Lullus Lambang G. Hidayat, R.; Sholahudin, I.; Yusuf, M.; Huda, S.; Arifin, Z. Fabrication and Characterization of Zinc Oxide-Based Electrospun Nanofibers for Mechanical Energy Harvesting. *Journal of Nanotechnology in Engineering and Medicine* **2014**, *5* (1). https://doi.org/10.1115/1.4027447.

(247) Yoshida, T. Leaching of Zinc Oxide in Acidic Solution. *Mater. Trans.* **2003**, *44* (12), 2489–2493. https://doi.org/10.2320/matertrans.44.2489.

(248) Siddiqi, K. S.; ur Rahman, A.; Tajuddin; Husen, A. Properties of Zinc Oxide Nanoparticles and Their Activity Against Microbes. *Nanoscale Res Lett* **2018**, *13* (1), 141. https://doi.org/10.1186/s11671-018-2532-3.

(249) Reguieg, F.; Ricci, L.; Bouyacoub, N.; Belbachir, M.; Bertoldo, M. Thermal Characterization by DSC and TGA Analyses of PVA Hydrogels with Organic and Sodium MMT. *Polym. Bull.* **2020**, *77* (2), 929–948. https://doi.org/10.1007/s00289-019-02782-3.

(250) Siddheswaran, R.; Sankar, R.; Ramesh Babu, M.; Rathnakumari, M.; Jayavel, R.; Murugakoothan, P.; Sureshkumar, P. Preparation and Characterization of ZnO Nanofibers by Electrospinning. *Crystal Research and Technology* **2006**, *41* (5), 446–449. https://doi.org/10.1002/crat.200510603.

(251) Lee, D. Y.; Cho, J.-E.; Cho, N.-I.; Lee, M.-H.; Lee, S.-J.; Kim, B.-Y. Characterization of Electrospun Aluminum-Doped Zinc Oxide Nanofibers. *Thin Solid Films* **2008**, *517* (3), 1262–1267. https://doi.org/10.1016/j.tsf.2008.05.027.

(252) Lin, C.-C.; Li, Y.-Y. Synthesis of ZnO Nanowires by Thermal Decomposition of Zinc Acetate Dihydrate. *Materials Chemistry and Physics* **2009**, *113* (1), 334–337. https://doi.org/10.1016/j.matchemphys.2008.07.070.

(253) López-Juárez, R.; Razo-Perez, N.; Pérez-Juache, T.; Hernandez-Cristobal, O.; Reyes-López, S. Y. Synthesis of α-Al2O3 from Aluminum Cans by Wet-Chemical Methods. *Results in Physics* **2018**, *11*, 1075–1079. https://doi.org/10.1016/j.rinp.2018.11.037.

(254) Ayral, A.; Droguet, J. C. Alumina Powders via a Controlled Precipitation of Aluminum Acetate. *J. Mater. Res.* **1989**, *4* (4), 967–971. https://doi.org/10.1557/JMR.1989.0967.

(255) *TIBTECH innovations: Metal properties comparison: electric conductivity, thermal conductivity, density, melting temperature*. https://www.tibtech.com/conductivite.php?lang=en_US (accessed 2022-08-19).